DYNABIOSOL : Bio-inspired design of a dynamic solar Photovoltaic envelope with evolving functionalities

Julie Ratovonkery

UNIVERSITÉ SAVOIE MONT BLANC

THÈSE

Pour obtenir le grade de

DOCTEUR DE L'UNIVERSITÉ SAVOIE MONT BLANC

Spécialité : **Génie Civil et Sciences de l'Habitat**

Arrêté ministériel : 25 Mai 2016

Présentée par

Julie RATOVONKERY

Thèse dirigée par **Christophe MENEZO**
et codirigée par **Ya Brigitte ASSOA**

préparée au sein des **Laboratoires LAM du CEA** et **LOCIE de l'Université Savoie Mont Blanc**
dans **l'École Doctorale SIE**

DYNABIOSOL: Bioinspired design of a dynamic solar Photovoltaic envelope with evolving functionalities

Thèse soutenue publiquement le **8 Septembre 2023**,
devant le jury composé de :
Stéphanie GIROUX-JULIEN
Professeure, INSA Lyon/ UCBL 1, Présidente de Jury
Marco FOSSA
Professeur, University of Genova, Rapporteur
Daniel AELENEI
Professeur associé, NOVA University Lisbon, Rapporteur
Christian INARD
Professeur, La Rochelle Université, Examinateur
Daniel ROUSSE
Professeur, Université de Québec, Examinateur
Rodolphe MORLOT
Docteur, ADEME, Examinteur
Christophe MENEZO
Professeur, Université Savoie Mont Blanc, Directeur de thèse
Ya Brigitte ASSOA
Ingénieure de recherche (Docteure), CEA, Co-directrice de thèse

Abstract

Climate change, growing energy demand and depletion of fuel resources have led to increasingly high energy and environmental ambitions. These ambitions aim for resilient, sustainable, zero carbon and positive energy buildings in the building sector. Radical innovation in building envelope technologies is paramount as it is a key element in building energy efficiency. Indeed, the envelope is often designed on the basis of static functionalities rather than an adaptive and multifunctional interface. However, in the latter case, it would interact with and benefit from the effects of its external environment to ensure a comfortable indoor environment and the production of the building operating energy.

In this context, this thesis consists in the design of an adaptive facade with integrated photovoltaic (PV) components. The adaptive functionalities are developed to improve both the thermal performance of the facade and the electrical production of the PV modules. Designing such an envelope element often requires complex mechanical and control systems to implement dynamic and adaptive functionalities. For this reason, a bioinspiration approach is adopted, and smart materials are used to achieve flexible and low-tech adaptation mechanisms.

The methodology involves the analysis of the thermal and electrical behaviour of a baseline photovoltaic facade. In this study, it comprises bifacial PV modules, a ventilated air gap and a multilayer wall from the outside to the inside. The principle is to identify the properties limiting that facade to static functionalities. From this step, biological mechanisms related to the identified properties, and that can overcome the limitations are explored. Afterwards, smart materials enabling to implement the identified bioinspired strategies into the facade are selected. Finally, the outline of the new concept is developed with the principles involved. The solution is validated through experimental studies on the samples of the selected materials and on a reduced-scale prototype of the facade. Numerical feasibility studies and energy performance analysis at the building scale are also carried out.

This approach results in the application of thermosensitive and reflective bilayer components on the multilayer wall behind the PV modules. Those components are thin rectangular slats applied opposite to the PV cells. They gradually bend upward when their temperature rises and return to their initial state as their temperature decreases to its initial value. This cyclic deformation allows the adjustment of the facade functionalities according to three principles. First, in summer, the curved bilayers provide sun shading to the wall and act like extended fins to cool the facade. Second, in winter, the relatively flattened bilayers limit the heat exchange surfaces in the air gap. In addition, either the air gap is closed to limit heat loss or solar thermal energy is recovered from the preheated air flowing through the open gap. Finally, the bilayers enhance the PV power output because of their high reflection of the irradiance to the backside of the bifacial PV modules. The experimental validation on the reduced scale prototype of the façade concept has shown a decrease in the external temperature of the wall of up to 10°C in the summer configuration. A case study of the façade integration on a tertiary building led to an increase of more than 12% in the electrical efficiency of the façade compared to a standard monofacial PV façade but a marginal gain in the overall thermal performance. These results drawn from both experimental and numerical evaluation show that the concept has a promising energy performance and constitute the main contribution to the field of this thesis work.

Keywords: *integrated photovoltaic, adaptive facade, bioinspiration, thermosensitive bilayer, numerical study, reduced scale prototype*

Résumé

L'urgence climatique, l'augmentation de demandes énergétiques et l'épuisement de ressources fossiles ont mené à des ambitions énergétiques et environnementales de plus en plus élevées. Dans le secteur de bâtiment, ces ambitions visent à des bâtiments résilients, durables, à faible impact environnemental et à énergie positive. L'innovation de l'enveloppe du bâtiment, qui est un élément clé de son efficacité énergétique, est donc primordiale. En effet, l'enveloppe est souvent conçue sur des bases de fonctionnalités statiques. Pourtant, elle devrait être comme une interface adaptative et multifonctionnelle, qui échange et exploite les effets de son environnement, afin d'assurer la qualité des ambiances intérieures et la production d'énergie de fonctionnement du bâtiment.

Dans ce contexte, cette thèse consiste à la conception d'une façade adaptative à composants photovoltaïques (PV) intégrés. Les fonctionnalités adaptives sont visées tant pour l'amélioration de sa performance thermique que pour la maximisation de la production électrique des modules photovoltaïques. L'obtention d'un élément d'enveloppe, muni de fonctionnalités dynamiques et adaptatives, fait souvent recours à des systèmes mécaniques et de contrôles complexes. Pour cette raison, une approche de bioinspiration et l'utilisation des matériaux intelligents sont choisies pour obtenir des mécanismes d'adaptation flexibles et intelligemment low-tech.

L'approche consiste à l'analyse thermique et électrique d'une façade photovoltaïque de base. Dans notre étude, elle est composée de modules PV bifaciaux, d'une lame d'air ventilée et d'un mur multicouche depuis l'extérieur vers l'intérieur. Le principe est d'identifier des propriétés limitant cette façade à des fonctionnalités statiques. De cette manière, les êtres vivants en lien avec les propriétés identifiées et pouvant franchir ses limitations sont explorés. Par la suite, les matériaux intelligents pouvant assurer les stratégies bioinspirées sont sélectionnés afin de développer le nouveau concept. Enfin, la solution est validée grâce à des études expérimentales sur les échantillons de composants intelligents choisis et sur un prototype à échelle réduite de la façade. Des études numériques de faisabilité et d'analyse de performance énergétique à l'échelle du bâtiment sont également réalisées.

Cette démarche a conduit à l'application de composants de bilames thermosensibles et réfléchissants sur le mur derrière les modules PV. Les bilames, en forme de lamelle rectangulaire sont disposés sur le mur en face des cellules PV. Ils fléchissent dans un sens avec l'augmentation de leur temperature, et retournent à leur état initial lorsque leur temperature retourne à sa valeur initiale. Cette déformation cyclique permet d'ajuster les fonctionnalités de la façade suivant trois principes. Premièrement, en été, les bilames déformés forment une protection solaire au mur et agissent comme des ailettes pour rafraichir la façade. Deuxièmement, en hiver, les bilames en forme plus aplatie limitent les surfaces d'échange thermique dans la lame d'air. Additionnellement, deux stratégies supplémentaires sont possibles en hiver : soit la limitation de la déperdition thermique par la fermeture de la lame d'air, soit la valorisation de l'air préchauffé circulant dans la façade ventilée. Enfin, la production électrique des modules PV est optimisée grâce à la réflexion des rayons solaires vers la face arrière des modules bifaciaux par les bilames. La validation expérimentale sur le prototype de la façade a conduit à une réduction de température de surface externe du mur de 10°C avec sa configuration en été. Un cas d'étude sur l'intégration de la façade à un bâtiment tertiaire a montré une augmentation de plus de 12 % de production électrique par rapport à une façade photovoltaïque monofaciale standard. Toutefois, le gain thermique global est marginal dans ce cas d'étude. Ces résultats qui sont issus à la fois d'une évaluation expérimentale et d'une évaluation numérique indiquent que le concept a une performance énergétique prometteuse et constituent la contribution principale de ce travail par rapport à la littérature.

Mots clés: *photovoltaïque intégré, façade adaptative, bioinspiration, bilame thermosensible, étude numérique, prototype à échelle réduite*

Nomenclature

Abbreviations

APA	Bilayer made of Aluminium- Plexiglas
BIPV	Building Integrated Photovoltaic
CHTC	Convective heat transfer coefficient
IPA	Bilayer made of Invar- Plexiglas
MAE	Mean absolute error
MBE	Mean bias error
PMMA	Polymethyl methacrylate (Plexiglas)
PV	Photovoltaic
RHTC	Radiative heat transfer coefficient
RMSE	Root mean squared error
UHPC	Ultra-high-performance fibre concrete

Symbols

A	Area	m^2
a	Curve slope	
b	Bifacial factor	
CP	Wind pressure coefficient	
Cp	Specific heat	$J.kg^{-1}.K^{-1}$
d	Thickness of the air channel	m
D, Dh	Hydraulic diameter	m
e	Thickness	m
E, P	Power	W
f	Friction coefficient	
$f\_, F\_$	View factor	
G	Irradiance	W/m^2
g	Gravity acceleration	$m.s^{-2}$
Gr	Grashof number	
H	Height	m
h	Heat transfer coefficient	$W.m^{-2}.K$
J	Radiosity	W/m^2
k	Thermal conductivity	$W.m^{-1}.K^{-1}$
K	Pressure drop coefficient	
L	Length/ thickness	m
Nu	Nusselt number	
P	Perimeter	m
P	Pressure	N/m^2
Re	Reynolds number	
Ri	Richardson number	
S	Area/ cross-section	m^2
T	Temperature (thermal)	°C or K
V, v	Velocity	m/s

y	Deflection	m
Z	Diffuse source of irradiation	W/m^2
$\dot{m}$	Mass flow rate	kg/s
M^0	Black body emittance	W/m^2
$q"$	Heat flux	W/m^2

Greek letters

Optic

α	Optical absorptivity
ξ	Transparency factor
ρ	Optical reflectivity
τ	Optical transmivitty

Thermal physical

α	Thermal expansion coefficient	$10^{-6}\ °C^{-1}$
α	Thermal diffusivity	m^2/s
φ	Heat flux	W/m^2
σ	Stefan-Boltzmann constant	$5.67.10^{-8}\ W.m^{-2}.K^{-4}$
θ	Incident angle	rad
β	Temperature coefficient	$/°C$
ρ	Density	$kg.m^{-3}$
ε	Emissivity	
μ	Dynamic viscosity	$kg.m^{-1}.s^{-1}$
ν	Cinematic viscosity	m^2/s

Other

$\sigma_{\_}$	Standard deviation of _	_
β	Tilt angle	rad
θ	Incident angle	rad
ϕ	Angle	rad
η	Efficiency	
$\Delta_{\_}$	Gradient or difference of	_
$\delta_{\_}$	Specific or relative error of	_

Subscripts/exponents

$cells$	Photovoltaic cells
$0, ref, r, \infty$	Reference
c	Characteristic
e	Effective
ext	Outdoor
int	Indoor
in	Inlet
out	Outlet
gr	Ground
rad	Radiative
$conv, c$	Convective
mod	Photovoltaic module

$g1$	Front surface of the module glass cover
$g2$	Rear surface of the module glass cover
f	Fluid
$M1$	External surface of the wall
$M2$	Internal surface of the wall
$insul$	Insulation
b	Bilayer
Dh	Hydraulic diameter
mix	Mixed turbulent and laminar flow
lam	Laminar flow
$turb$	Turbulent flow
nat	Natural convection
$forced$	Forced convection
dif, d	Diffuse radiation
dir, D	Direct radiation
th	Thermal
p	Of the layer
PV	Photovoltaic module
env	Environment

Table of contents

General introduction

Climate, energy, transport and taxation policies of the European Green Deal aim for a 55% reduction in greenhouse gas emissions by 2030, compared to the 1990 levels (European Commission, 2021).

In this sense, since 2017, at the One Planet Summits, one hundred and twenty-five (125) companies and large groups have committed to reducing their greenhouse gas emissions in favour of biodiversity by transforming their production processes and their value chains.

Moreover, in the building sector, the Energy Performance of Buildings Directive required European countries to ensure all new buildings to be nearly zero-energy by the end of 2020, while this requirement had to be applied to all new public buildings after 31 December 2018 (European Commission, 2016). A revision proposal of this directive was presented in December 2021, aiming to transform the building stock into zero-emission buildings by 2050, with a very low amount of energy required, fully covered by renewable energy sources and without on-site carbon emissions from fossil fuels.

In Europe, the building sector accounts for a significant share of total energy consumption (over 40%) and is responsible for 36% of CO2 emissions. In addition, the building stock is characterised by a very low turnover rate (1 to 2% per year, depending on the country). Energy demand is expected to double by 2050, when 75% of the world's population will live in cities. With increasing energy demand, limited fossil fuels and global warming, reliable, sustainable, environmentally friendly, and cost-effective energy sources, such as solar energy and technologies, are essential at the global level.

In France, the establishment of the RE2020 environmental regulation to design buildings with positive energy is part of these guidelines, and giant tenders have been launched to encourage photovoltaic addition or integration into buildings by 2050 to reach power installed between 35.1 GW and 44 GW in 2028.

In this promising context, the building envelope is the main area for the collection and local production of energy (solar photovoltaic, solar thermal) for the needs at the building and city levels. It also plays a major role in reducing energy consumption and more generally in improving energy efficiency in the context of the shift towards sustainable and energy-neutral buildings (Garde & Donn, 2014).

The building envelopes, especially facades, correspond to the interface between external environmental factors and the occupants' indoor requirements. However, the envelope is often designed on the basis of static functionalities with a limited potential to exploit and control the energy inputs of its environment. Advanced technological innovations with high energy efficiency are therefore highly expected in this sector, which is being pushed from a normative point of view towards strong sealing and thermal insulation. Thus, thanks to integrated and evolutive functionalities, the envelope could meet most of the needs of inhabited environment, namely: a protection of the indoor environment from outdoor climate but also a useful transfer (thermal energy, solar radiation, light, humidity, air) between them. More precisely, active and adaptive multifunctional building envelopes can significantly improve energy efficiency, sustainability, occupant comfort and the economic value of the construction sector.

Thus, this thesis aims to develop a breakthrough, flexible and multifunctional photovoltaic component for facade integration to optimise building energy performance, combining bioinspired strategies and smart material adapting the facade thermo-physical properties.

The design of this innovative facade gathered different challenges that had to be addressed and solved. First, the electricity production function is ensured by the integration of photovoltaic modules into the envelope that degrades the PV module operating conditions. Secondly, the energy management functions and the parameters that define the indoor environment (especially thermal comfort) had to be

adapted passively to changing climatic conditions. The passive and low-cost evolution of the innovative adaptive facade component had to be achieved while trying to control the complex operation of smart materials (here, thermosensitive bilayers). Finally, the application of the bioinspiration approach to photovoltaic modules for building integration had to be fully defined, considering the limited case studies existing in the literature.

The development of this concept has led to a manuscript containing six chapters. The first one presents a bibliographical study targeting state-of-the-art on each one of these challenges: building integrated photovoltaic (BIPV), adaptive facade solutions, smart materials and bioinspiration approaches. It highlights, more specifically, the advantages and limitations of the existing facade solutions and the bioinspiration method adapted for building envelope design.

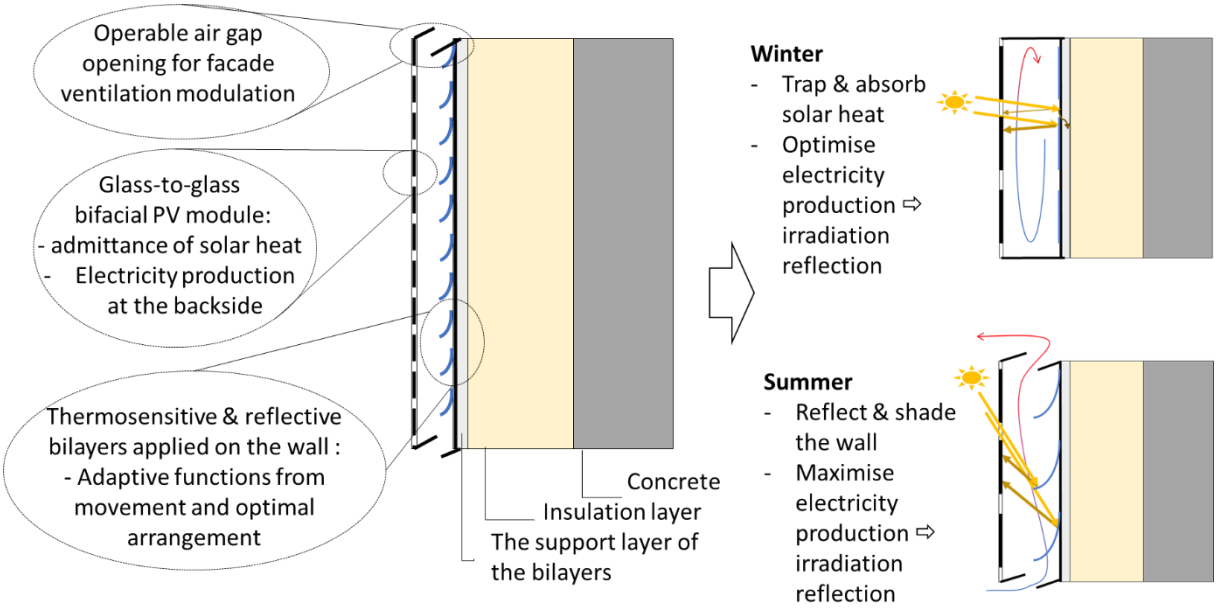

Figure 1: Illustration of the developed bioinspired adaptive PV facade

The bioinspiration method and its application to the facade design are addressed in the second chapter. More specifically, this method identifies the aspect of the standard baseline photovoltaic facade that should be adaptive toward the building energy requirement through a parametric study. The biological search and concept development are therefore based on this study. Therefore, the results of each design stage are detailed in this chapter, including the presentation of the innovative solution with the preliminary analysis of its feasibility.

The solution retained uses thermosensitive bilayers that dynamically adapt the facade function to outdoor temperature and solar irradiation (see Figure 1). The validation and the characterisation of the bilayer movement are presented in Chapter III. These investigations aimed at selecting and sizing appropriate bilayers, determining equations describing their deformation, and analysing their mechanical and thermal behaviour relevant to their application.

Experimental validation of the concept is undertaken on two reduced-scale prototypes of the designed facade. The experiments were conducted indoors using a solar simulator to validate the facade behaviour under different irradiation levels. This investigation provides more concrete proof of concept and the optimisation of the solution through numerous parametric studies on the prototypes. Details of this study are presented in Chapter IV.

The data collected during the experimentation are used to validate the developed thermal models detailed in Chapter V. These include the coupled thermal models of the standard photovoltaic facade and the designed bioinspired facade. Transient heat transfer in the standard PV facade is validated using a yearly period measurement. The experimentations on the reduced-scale prototype provide measurements for the validation of the steady-state thermal model of the two facades.

Finally, the last chapter outlines the energy performance assessment of the facade, considering its integration into the building. This numerical investigation also uses the developed thermal model in Chapter V. The yearly electricity production and conditioning energy gains from the bioinspired facade integration are evaluated and compared to standard building facades and photovoltaic facades in this chapter.

The results of all these investigations lead to the conclusions and perspectives provided at the end of this manuscript.

Chapter I. State of the art

I.1 Introduction

Building envelopes with responsive functionalities adjust to the change in their environment and ensure a comfortable indoor environment while minimising energy consumption. In Building Integrated Photovoltaic (BIPV), the adaptability and evolutivity of such envelope are also addressed for the optimisation of the electricity production of the photovoltaic (PV) components. Hence, a highly energy-performant and multifunctionality envelope element can be obtained. The development of such element is a breakthrough solution but a tremendous task, namely to ensure efficient and effective control of envelope responsiveness. To tackle this issue, this chapter critically analyses four thematics.

The first part analyses existing solutions for the optimisation of PV integration in the envelope, more specifically, the facade. The second part addresses the relevance of adaptive features in the envelope while highlighting the opportunities and challenges, especially for its thermal performance. The third part presents an overview of shape-changing smart material, which can be used to answer the problem of envelope responsiveness control. Finally, the last part describes the bioinspiration approach chosen here for the design of a flexible and low-tech adaptive PV facade.

I.2 Importance and challenges of solar photovoltaic integration in building

Solar energy is an essential solution for the implementation of renewable energy in buildings both for thermal and electrical load coverage. Photovoltaic (PV) technology is a fancy transformation of solar energy since electricity is the most versatile form of energy. It only can be used for lighting, electronic devices and motors. The application of photovoltaics is highly encouraged at the European level and has a huge potential in buildings, considering the extent of available surfaces on their envelopes, especially on the facades of high-rise ones.

There are two categories of PV applications in buildings: building-attached photovoltaic (BAPV) and building-integrated photovoltaic (BIPV). In the first category, solar panels are mounted on top of building elements and do not impact the integrity of the envelope functionality. In BIPV, the photovoltaic components replace conventional building materials such as tiles, windows and facade elements. In addition to electricity production, they should ensure at least the basic functionalities of the replaced element, such as energy economy through thermal and daylighting function, mechanical and acoustic function, as well as weather and fire protection (AFNOR, 2016). BIPV application leads to multifunctional building envelopes (Zanetti et al., 2017) as the PV components are also used to optimise the building functions, such as thermal efficiency, through an additional thermal insulation layer, for instance. However, this application remains a niche in overall solar PV applications, accounting for only 1% in 2017 based on estimation. Cost-effectiveness, power yield, technical implications and lack of favourable regulation are the drawbacks of its application over BAPV technology and traditional building materials (BIPVBoost, 2019).

In terms of application, roofing and rooftops are the dominant PV applications. Ensuring the multifunctionality of the envelope component is more complex for PV integration on the facade, especially in terms of aesthetics. Nonetheless, the BIPV application has a wide range of products offering more flexibility and aesthetic value than BAPV (Zanetti et al., 2020). Mutual shading between buildings (Vulkan et al., 2018) and important vertical temperature gradients in the module (Freitas & Brito, 2019) are among the parameters that can jeopardise electricity efficiency in the BIPV facade and should be considered closely. Furthermore, the vertical inclination is not optimal for PV applications.

However, the solar potential is higher on vertical surfaces than on flat roofs, considering the total integration of all the facade sides or on southern orientation (northern hemisphere) in winter in high-latitude regions (Freitas & Brito, 2019) (see Figure I-1). For this reason, with current energy ambitions in the building sector, PV integration on the facades should not be overlooked but deployed extensively.

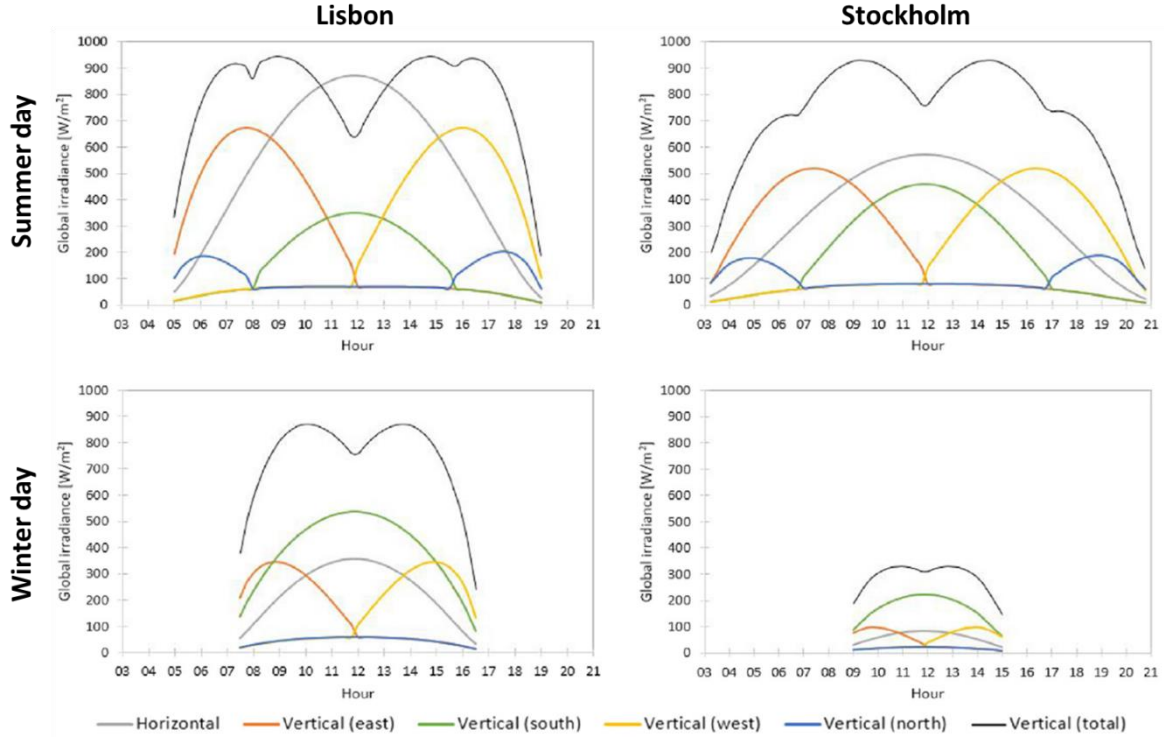

Figure I-1: Average global irradiance [W/m²] on horizontal and vertical planes for a summer day in two distinct latitudes: Lisbon (38°43'56"N) and Stockholm (59°20'6"N) (Freitas & Brito, 2019)

Considering the challenges and opportunities in PV application in the facades, the main focus is on this type of integration. For this, this section introduces firstly the generalities of PV technologies and their integration into the building. Secondly, optimisation solutions for PV integration are addressed more specifically for facade applications.

I.2.1 Overview of Photovoltaic elements for facade integration

I.2.1.1 Photovoltaic effect

A photovoltaic cell is a semiconductor component that converts light into electricity through the photovoltaic effect. When a semiconductor is exposed to light, the electrons in the upper bands of the material atoms are excited. If the energy of the photons (light particles) is high enough, the electrons are released. Therefore, hole-electron pairs are formed. Normally, these pairs recombine spontaneously, but doping the material negatively on one side and positively on the other creates an electrical field called p-n junction at the contact of the two layers. Thus, when the hole-electron pairs are formed, the electrical field induces the holes and electrons displacement towards specific directions. When an external circuit is connected to those layers, electrons flow through the circuit, and the system produces an electric current (Duffie & Beckman, 2006) (see Figure I-2).

I.2.1.2 Photovoltaic cell technology

There are several photovoltaic cell technologies. They are generally classified into three generations:

- ***Crystalline silicon-based cells*** are the first generation of solar cells. They constitute the largest market share and are the most mature technology. There are monocrystalline cells, which are

made from a single-crystal silicon wafer and polycrystalline or multi-crystalline cells, which are produced from metallurgical-grade silicon. Polycrystalline cells have lower efficiency and used to be known for their manufacturing cost.

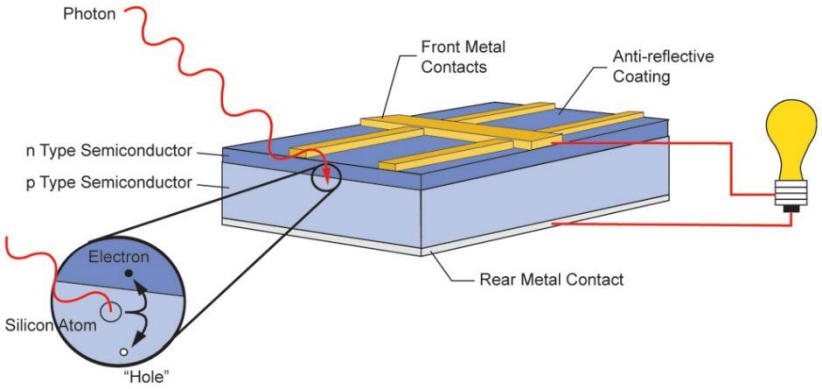

Figure I-2: Photovoltaic effect - silicon solar cell - Source: viridiansolar.co.uk

- The second generation of photovoltaic cells is composed of ***thin-film cells***. This technology aims to use less material while seeking to maintain the efficiency of first-generation technologies. They are generally cheaper than crystalline cells but have lower efficiencies. They are lightweight and flexible and can be incorporated into various substrates (curved, flat, flexible, rigid). Their transparency varies depending on the type of technology. There are amorphous silicon (a-Si), Cadmium telluride/sulphide (CdTe/CdS), and copper indium/gallium selenide (CIS/CIGS) cells (Shukla et al., 2016). A variety of chemical elements is used in thin film technology. They can be toxic and hazardous, especially the Cadmium in CdTe and CdS solar cells, or scarce, such as the telluride in CdTe and the Indium in CIS/CIGS. High power degradation is also observed in a-Si cells when exposed to sunlight (T. D. Lee & Ebong, 2017).
- Third-generation cells have a ***wide range of concepts***. They are often considered emerging because of their low market penetration. These technologies seek to address various challenges, including electrical conversion efficiency, material availability, manufacturing cost, other durability properties and environmental impacts. There are low-efficiency but low-cost cells, such as dye-sensitised cells and organic cells; significantly efficient but with low manufacturing costs, such as perovskite cells, and highly efficient but high-cost, such as multijunction cells and III-V technologies (Almosni et al., 2017).

Laboratory efficiency conversion of PV cells is constantly rising through the advancement of manufacturing and modification of the design structure. New concepts of solar cells, comprising hybrid inorganic-in-organics cells, are emerging and would constitute the fourth generation of PV technology (N. Kant & Singh, 2021). For crystalline cells, more advanced design and architecture significantly improve PV cell efficiency, including the Passivated Emitter Rear Cell technology (PERC) and Heterojunction with Intrinsic Thin layer cells (HIT).

In short, the PERC technology increases the light absorption from the solar cell by adding dialectric coating between the silicon and the aluminium at the backside. As part of irradiance of certain wavelengths surpasses the silicon without being absorbed, this layer reflects them back to the silicon. Hence, it increases the absorption of irradiance wavelength that would be wasted in conventional crystalline silicon technology. Meanwhile, HIT combines crystalline silicon and amorphous silicon to take advantage of both technologies. Hence, the solar cells consist of n-type crystalline silicon with deposition of intrinsic amorphous silicon and amorphous silicon of p-type and n-type (Mesquita et al., 2019).

An overview of the advancement of PV cell efficiency by technology is given in Figure I-3, according to the record efficiency reached in laboratories.

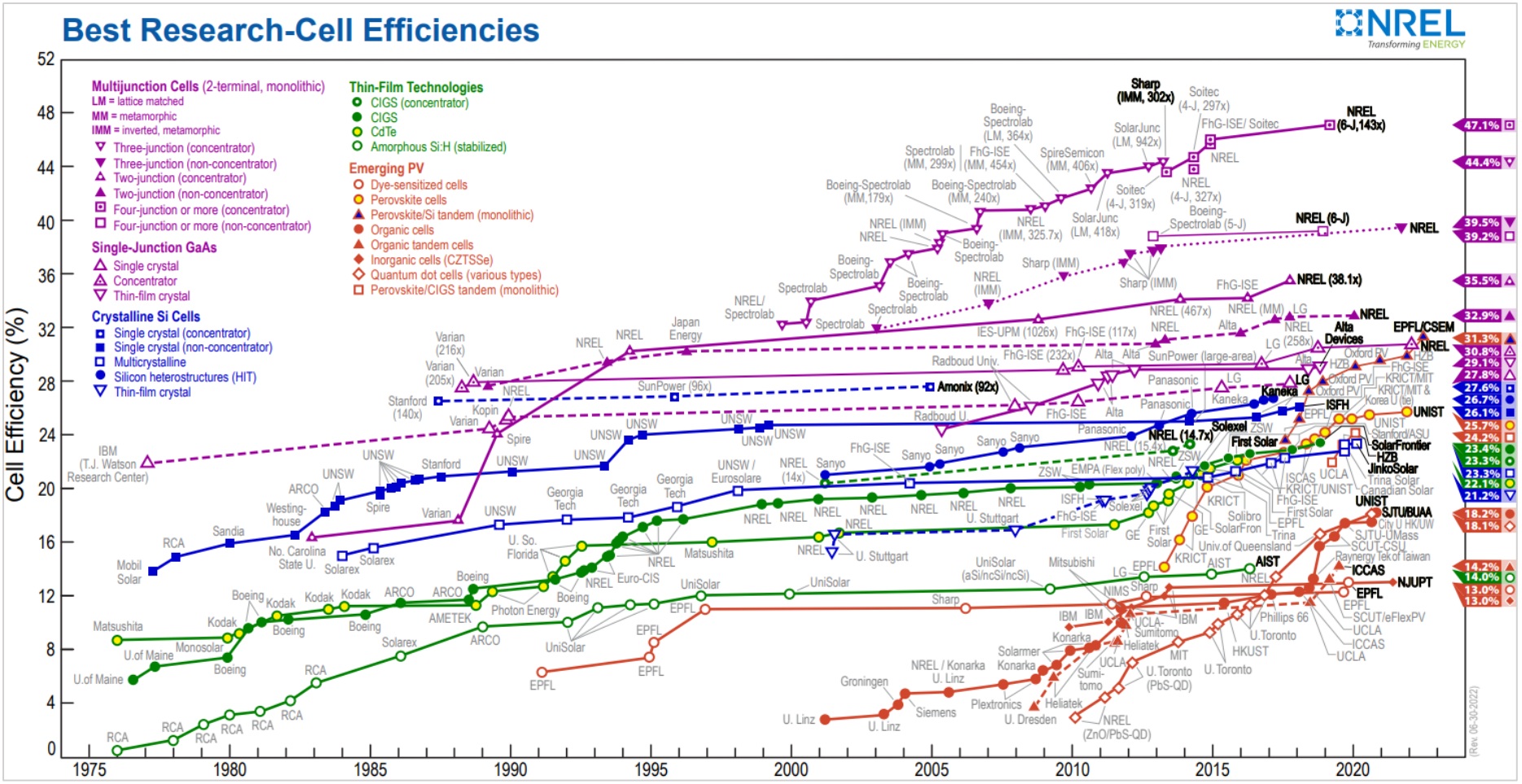

Figure I-3: Best research PV cell efficiencies – Source: NREL (https://www.nrel.gov/pv/cell-efficiency.html)

I.2.1.3 PV module structure

Photovoltaic cells are connected in series or parallel to modulate the voltage and current produced and form a photovoltaic module. In the most typical stack of rigid PV module structures, the assembly of solar cells is encapsulated by two polymer layers called encapsulants. One of the most used encapsulants is Ethylene-vinyl acetate polymer (EVA). The front surface is covered by glass or other thermoplastic resin. It is also called the front cover. This layer has a very high transmittance and can be texturised or combined with an anti-reflective coating, enhancing photon penetration to the cells. A polymer back sheet covers the rear surface for opaque PV modules. One of the most used is polyvinyl fluoride (PVF), commercially named Tedlar®. The whole can be framed with an aluminium structure or plastic profiles. In a semi-transparent module, the rear cover is made of glass. Hence, the module is denoted as "glass-to-glass" as the cells are covered by glasses on both sides (see Figure I-4). The encapsulation and coverage of solar cells provide them with mechanical and weather resistance, including protection from moisture, rain and ultraviolet radiation and electrical insulation (Oliveira et al., 2018). Those are basic PV module structures developed or modified according to the PV cell technology and the integration into various types of surfaces and applications.

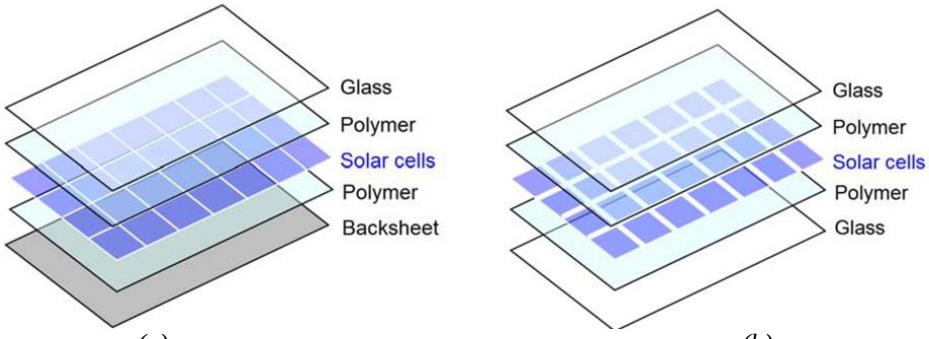

(a) *(b)*

Figure I-4: Two typical stacks of PV modules: (a) Opaque module (b) Glass-to-glass semi-transparent module (Infuso et al., 2014)

I.2.1.4 BIPV products and applications

The integration of PV in the building requires customising the PV module technology to meet the requirements (mechanical, thermal, acoustical, weather and fire protection, daylighting) of the replaced building elements (Kuhn et al., 2021). Therefore, there are numerous types of PV modules in the BIPV market:

- **Typical opaque flat and rigid PV modules**, with weather fitting, which are integrated into flat surfaces of facades, roofs and balconies;
- **PV foils and membranes** stick to diverse substrates such as metal panels or bulk building materials (see Figure I-5a);
- **PV modules of several tuned transparency** to replace transparent parts of the envelope such as windows, curtain walls, facade second skin, skylight, and atrium. They can be integrated into glazing units for their insulation. Their transparency is reached either by the use of thin film PV technology resulting in a relatively low transmittance coefficient but homogenous transparency (see Figure I-5b), or with semi-transparent crystalline silicon modules, where the cells do not cover the entire glass-to-glass modules and allow light to be transmitted through the interspaces (see Figure I-5c) (BIPVBoost, 2019).
- **PV slats, tiles and shingles** are usually used for roofing.
- **Diverse BIPV modules** are customised in size and colour to meet the aesthetic requirement of the envelope element (see Figure I-5b - d).

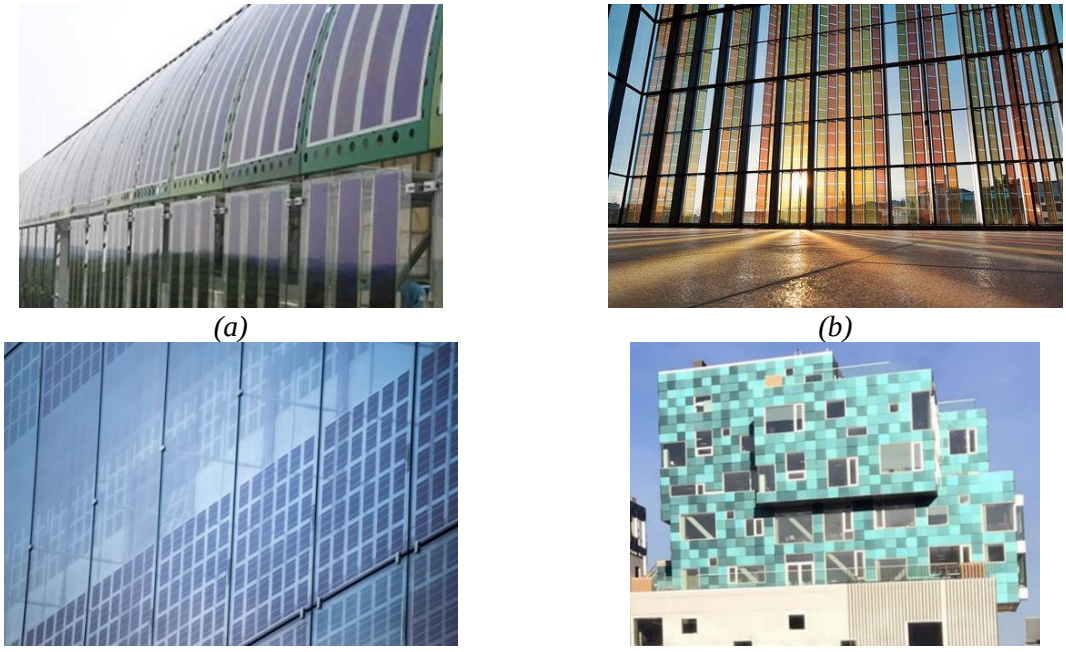

(a) *(b)* *(c)* *(d)*

Figure I-5: (a) Flexible PV module (source: Heliatek) (b) Transparent coloured PV module on the facade of SwissTech Convention Center, EPFL, Switzerland (source: Solaronix) (c) Semi-transparent PV module on double skin facade (source: Glassbel) (d) Opaque coloured PV module on the facade of Copenhagen International School (source: SolarLab)

Integration systems of PV modules into the building are classified into several categories. Some of the main BIPV systems are illustrated in Figure I-6. In the facade, there are two major types of integration:

- **Cold facade**: in a cold facade, the term "cold" refers to the cooling of the PV modules provided by the air circulation in the air gap on their back. Thus, cold facades are BIPV applications in opaque ventilated facades (rainscreen facades), double-skin facades and ventilated Trombe walls.
- **Warm facade**: the PV module is applied to replace conventional coating as in stick systems or the non-structural glazed wall as in a curtain wall system. In the latter application, it is also referred to as solar glazing. Warm facades are not ventilated (Frontini et al., 2015).

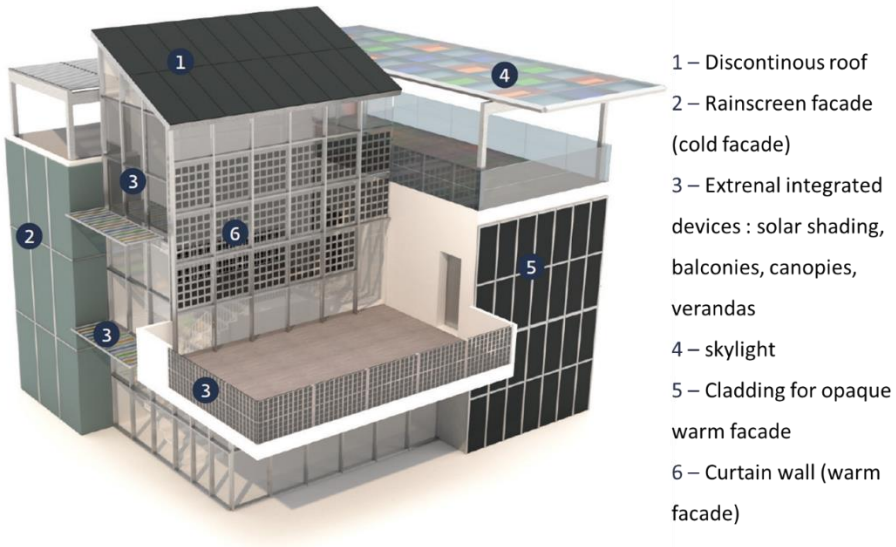

Figure I-6: Examples of BIPV application system in Building, Source: SUPSI (Zanetti et al., 2020)

Choices of the PV integration system, PV module and cell technology influence the PV power production efficiency and the initial requirements of the facade elements, including its energy

performance. In the following bibliographical study, the optimisation techniques for enhancing PV power output are addressed while considering the impact of those solutions on the facade thermal performances.

I.2.2 Optimisation of *BIPV facades electricity* production

Three axes are pinpointed here to enhance the PV power production: optimising the PV cell and module technology, cooling the PV to avoid excessive temperature increase and maintain its conversion efficiency and optimising the facade design to maximise the harvest of solar radiation.

I.2.2.1 Optimisation of photovoltaic technology: bifacial module

The selection of PV cell technology is one of the main aspects that ensure electricity production performance in BIPV applications. However, it is easily compromised by various requirements and integration constraints such as the aesthetic, the cost and the PV module weight (BIPVboost, 2019). Here, the bifacial PV technology is presented as an interesting option compared to monofacial glass-to-glass PV modules applied in curtain walls, solar glazing, and other facade systems.

- **Principle of bifacial PV cells**

Bifacial PV cells differ from standard monofacial ones in their ability to absorb and convert light from both the front and rear sides. This allows them to have higher electricity yields. Their capacity to absorb light on the rear side relies on their rear contact surface configuration. In detail, the contact surfaces are used to conduct electric current from the cell and are layered on the front and rear surfaces (as anode and cathode). The front contact surface in standard cells is grid-patterned and covers a very small cell area. Whereas the rear contact is applied as a coating and covers most of the cell area, which leads to the blockage of light absorption from this side. Hence, in short, the principle behind bifacial is to allow light penetration on the rear side by the modification of the rear contact configuration to a grid pattern (Frontini et al., 2019; Raina & Sinha, 2021) (see Figure I-7) and by the application of the cells in glass-to-glass module.

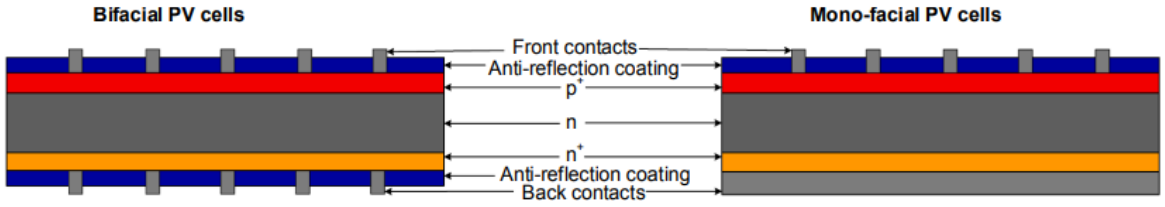

Figure I-7: Comparison of the cell architecture of monofacial and bifacial crystalline silicon PERC technology (Gu, Ma, Li, et al., 2020)

Nevertheless, the cell architecture is not symmetric. The conversion efficiency on the rear side is lower than on the front side. The ratio of the two efficiencies on each side is called the "bifaciality factor". It is about 70 to 80% with crystalline silicon PERC technology, one of the most popular bifacial cells. Heterojunction technology (HIT cells) provides more symmetric architecture and reaches a bifaciality factor superior to 95% (Frontini et al., 2019; Gu, Ma, Ahmed, et al., 2020).

- **Opportunities in bifacial cell application**

There are still very few studies addressing the integration of bifacial PV in the facade despite the potential of this technology. In the study of Tina et al. (2021), for instance, an increase of 2.9% is observed by comparing a ventilated facade with monofacial and bifacial modules. Those gains can be increased further through several integration optimisations such as:

- The application of the PV module in front of a reflective wall (C. Kim et al., 2021; Soria et al., 2016; Tina et al., 2021), which is reported to increase the electricity yields by 5.7% in the study of Tina et al. (2021) while considering a wall reflection coefficient of 0.7;
- The optimisation of facade geometry through the selection of appropriate airgap thickness, for instance (Assoa et al., 2021). This aspect is reported to enhance the power yield by 18% in the study of Soria et al. (2016) on a reduced-scale facade bench;
- The optimisation of PV module manufacturing, for example, the use of textured glass as cover layers to enhance light absorption, has led to a 25% energy gain in the study of Soria et al. (2016), considering other optimisation techniques.

- **Challenges in bifacial cell application:**

Some particular caution should be considered for the integration of bifacial PV on the facade. For instance, inhomogenous reflective properties of the surface on the back of the modules might induce hot spots, as investigated in the work of C. Kim et al. (2021).

In detail, hot spots occur when certain PV cells in the module are shaded or obstructed (by dust or other objects), leading to inhomogeneous illumination of the module and power mismatch. The current delivered from the series approaches that of the faulty cells, limiting the output power. However, the extra current produced by the unshaded cells is dissipated as heat to the faulty ones, resulting in localised overheating called "hot spot". This phenomenon is a typical problem in PV applications and can be solved by installing a bypass diode to disconnect the faulty array of cells from the output circuit.

In a bifacial facade, C. Kim et al. (2021) point out that this might occur additionally from non-uniformly distributed reflected light induced by different reflection coefficients on the back wall (from different wall painting colours, for instance). Clearly, uniformity of the back surface is required to resolve this issue. In addition, the influence can be lessened by using a diffused reflective back surface or by increasing the distance between the module and the wall.

As in all PV applications, the excessive temperature increase on the module also deteriorates the light conversion efficiency in bifacial modules. These issues are often addressed in the BIPV due to the lack of cooling of the back surfaces of the PV modules. The solutions addressing those aspects are presented in the following subsection.

I.2.2.2 PV cooling and its effect on the thermal performance of the facade

- **Importance of PV cooling: warm facade vs cold facade**

In the facade, the PV module can be integrated either with a ventilated air gap (cold facade) or without (warm facade) (see Figure I-8).

PV integration with ventilation is more attractive as the air circulation allows the back of the PV modules to be cooled to limit the loss of efficiency from high temperatures. The most common air circulation consists of air coming from outdoors and exhausted back outdoors. Numerous studies comparing the two integration modes were effectuated in the late 1990s and the early 2000s (Chow et al., 2003; Guiavarch & Peuportier, 2006; Jie et al., 2002; Yang et al., 2000). In summary, those studies reported an increase in the PV efficiency (from 12.7% to 14.7% in the study of Guiavarch and Peuportier (2006) on a social housing building in Paris), an increase in the PV power output and a decrease in the PV cells operating temperature, especially for mechanically ventilated air gap (respectively by 18°C and 8% in the study of Krauter et al. (1999)).

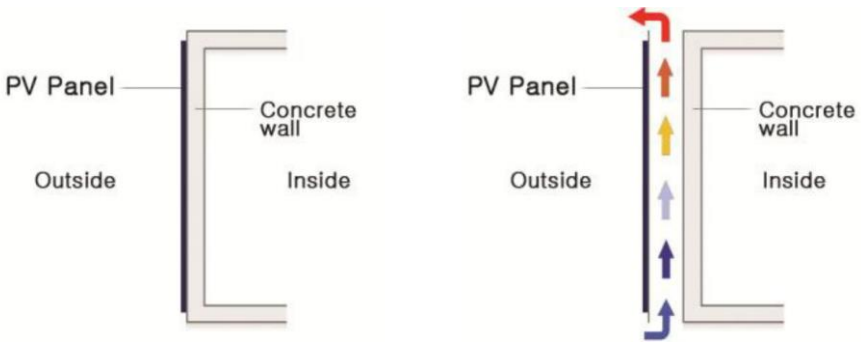

Figure I-8: Illustration of the PV facade without and with a ventilated air layer

This air circulation mode also enables the wall to cool down and reduce cooling loads in summer. For instance, Yang et al. (2000) reported a decrease in cooling load between 30% and 50% compared to a massive wall for a building implemented in China. However, this cooling effect induces heat loss and can potentially reduce the thermal performance of the facade in winter. Hence, the valorisation of the thermal energy dissipated can be considered by preheating the air supply of the building space. This application is called thermal BIPV or BIPV/T. In effect, various modes of facade ventilation enhance the facade thermal performance while cooling the PV module.

- **Air circulation mode for PV cooling and their thermal impact**

BIPV facade with a ventilated air gap is just one kind of ventilated facade with the additional functionality of producing electricity. Various types of air circulation in ventilated facades are depicted in Figure I-9 (T. Zhang et al., 2016). In general, the air enters the lower part of the facade and exhausts at the higher part.

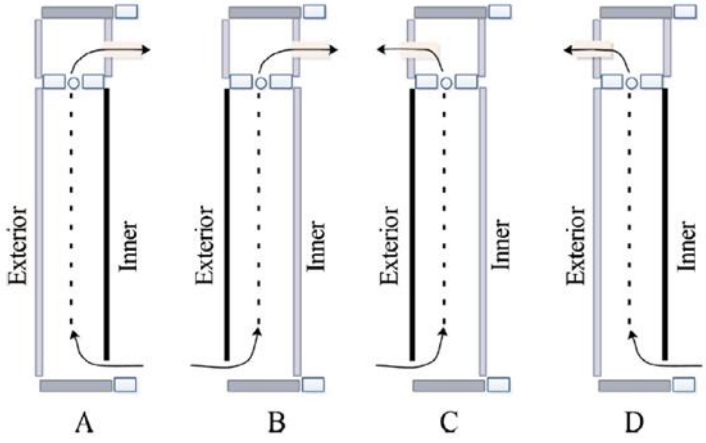

Figure I-9: Main air circulation modes in ventilated facades (T. Zhang et al., 2016)

For the facade cooling, there is external air circulation in which air comes and exhausts back to outdoors (Figure I-9C). It corresponds to the typical air circulation mode in PV cold facades, as presented before. This mode is often found in opaque ventilated facades (rainscreen facades) and double skin facades (facades that have glazing as a second skin). Its drawback is a possible increase in heating loads in winter due to excessive cooling of the facade (Ibañez-Puy, 2017). There is also the exhaust mode or chimney effect that corresponds to the air coming from indoors and is rejected outdoors (Figure I-9D). It is exploited to enhance natural ventilation in the building to reduce cooling loads. It suits hot and humid climates (Maghrabie et al., 2022).

For space heating and the preheating of air supply (to reduce the building heating loads), the cooling of the PV module is with air circulation in internal or in supply mode. The recovery of thermal energy from the air is reported to increase the overall performance of the facade by 0.6% to 1.9% in the work of

Guiavarch and Peuportier (2006), depending on the building implementation. In internal circulation mode, air comes from indoors and is directed to the supply unit (Figure I-9A). This mode is often found in solar walls such as the Trombe. This technology uses the greenhouse effect to trap shortwave solar radiation with the glazed second skin in the air gap and to store heat in a massive wall (Ahmed et al., 2020). In supply mode (Figure I-9B), the air comes from outdoors and is directed to the supply unit after the preheating in the gap. This mode can be found in double-skin facades and solar collectors such as transpired collector facades (in which the second skin is made of opaque modules and has multiple perforated air entrances for better air suction) (Athienitis et al., 2011).

This short overview of the ventilation mode in the facade shows that cooling PV modules with air to improve their electrical efficiency can also be exploited for cooling or heating of building space. Even though replacing the standard second skin material of the facade can reduce its thermal performance. For example, the lower transparency of the PV module can decrease heat harvest in the Trombe wall (Jiang et al., 2008). However, the shading from the PV cells can increase the thermal performance in summer due to additional solar protection from the cells. Thus, the PV facade should be optimised to identify the semi-transparency factor (the ratio of transparent surface uncovered by the PV cells to the surface of the module) of the glass-to-glass PV module and the geometric properties of the facade (such as air gap thickness) to improve its overall energy performance (thermal and electrical) (Saadon et al., 2016). Moreover, as each air circulation mode is for a specific function, switching from the space heating mode to space cooling mode is necessary to optimise the system, especially if there is no dominant cold or hot climate pattern in the building implementation region. Thus, a certain adaptability in the system is needed to not deteriorate the facade thermal performance in the cold or warm season according to the chosen ventilation system (G. Yu et al., 2021).

- **A glance at other media for PV facade cooling**

This overview of PV cooling mainly focuses on air circulation since air is already present in outdoor and indoor environments. Its circulation can be easily established passively through temperature gradient in the facade. This overcomes several issues, such as leakage, frost, and sensitive volume control linked to thermal expansion (G. Yu et al., 2021). However, apart from airflow, several other means of PV cooling are reported in the literature.

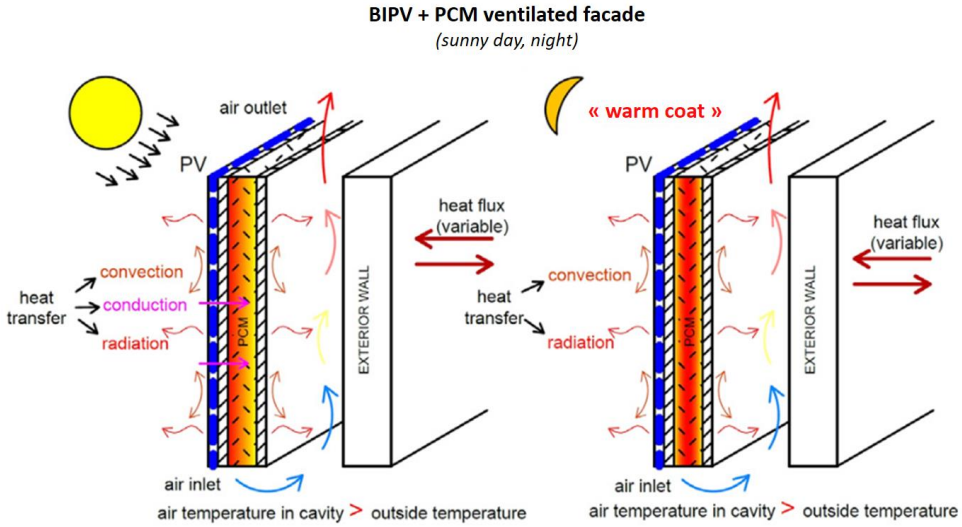

Figure I-10: Working principle of BIPV/PCM ventilated facades (Čurpek & Čekon, 2020)

For instance, water circulation behind the module can be an even more efficient alternative due to the thermal capacity and conductance of water. This method provides water heating for domestic hot water and can also help to cool down the wall in summer (Chow et al., 2009). PV Water cooling can be coupled with air circulation if the pipe is installed in the ventilated facade to provide warm water and warm air

(G. Yu et al., 2021) or alternate the systems between winter and summer according to the requirement (L. Xu et al., 2020). Water and air passive heat can be valorised further by using a heat pump (G. Yu et al., 2021).

Phase change material can also be used to regulate the PV temperature and the wall. The principle relies on the use of the material latent heat capacity to absorb excessive heat from the module during the phase change (more detail in subsection I.3.2.4). Hence, the PV module temperature would be maintained to the melting temperature of PCM, which should be ideally close to the PV nominal temperature. The heat stored from the PCM can be valorised or evacuated by coupling the system with air circulation (Čurpek & Čekon, 2020) or water circulation (Modjinou et al., 2019). An illustrated example of the application of PCM in a BIPV ventilated facade is given in Figure I-10. The evolution of functions between the two seasons is important in those systems to avoid overheating in summer.

I.2.2.3 Enhancement of PV cooling through geometrical design

- **Optimisation of the facade component dimension**

Regardless of the adopted method for the PV module cooling, the optimisation of the geometry has an important role in optimising the PV power output and facade thermal performances. For ventilated facades, those optimisations concern the air thickness, the height and length of the facade, and the number of air inlets.

In this scope, T. Zhang and Yang (2019) reported that the air gap thickness should not exceed 60 cm if the air gap is intended to improve ventilation capacity. However, the air gap thickness should be lower than 20 cm if the aim is to supply warm air from preheated air in the gap. Fossa et al. (2008) also reported that convective heat transfer is improved in the gap for a thickness of up to 10 cm. Above this distance, the temperature variation is not meaningful.

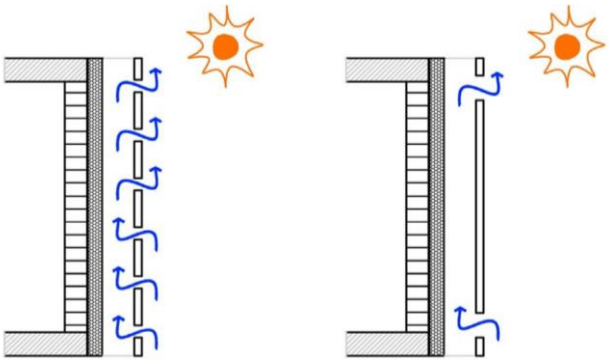

Figure I-11: Illustration of open joint ventilated facade vs closed joint ventilated facade (Ibañez-Puy, 2017)

The optimisation of the facade dimension is often linked to the ratio of the two given dimensions. W. Zhang et al. (2021) reported that a ratio of the air gap thickness and the module height leads to the most obvious drop in PV temperature (about 2°C from a change in the ratio from 0.05 to 0.15). In effect, limiting the air gap per floor or considering multiple air inlets is important to limit an excessive vertical temperature gradient in the facade (Athienitis et al., 2018; Rounis et al., 2016). An open joint configuration of the ventilated facade is also an option to increase the PV module cooling as the second skin consists of discontinuous panels leading to multiple air inlets and the increase the air suction (see Figure I-11) (Agathokleous & Kalogirou, 2016).

- **Addition of extended surfaces**

Else, the use of extended surfaces is also an efficient means for cooling BIPV facades as they enhance heat convection transfer through the increase of thermal exchange surface. In the investigation of Tonui and Tripanagnostopoulos (2007), the PV facade collector with extended fins attached to the back wall

is reported to provide a 5% increase in electrical power and exhibit the best performance compared to the typical solar collector and other configurations tested (see Figure I-12).

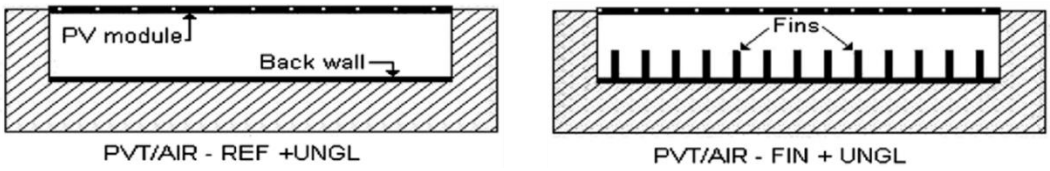

Figure I-12: Illustration of PV air-type unglazed thermal collectors with regular and optimised configuration with fins (Tonui & Tripanagnostopoulos, 2007)

However, extended surfaces and ribs can also reduce the airflow rate in the gap, especially if they are transverse to the flow. Therefore, it is necessary to optimise their spacing and shape to provide the cooling effect and to offset the reduction in air flow rate with the increase in convection exchange (from air turbulence induced by the fins) (Brinkworth & Sandberg, 2006). For example, in the work of Nghana et al. (2022), transverse ribs on the back of the PV modules are reported to reduce summer heat gain by about 35.5% for the optimal identified geometry consisting of triangular ribs.

I.2.2.4 Increase in incident radiation and its effect on the thermal performance of the facade

- **Geometrical design**

Being in a vertical plane is one of the main drawbacks of PV integration in the facade for buildings located in lower latitudes. Total solar irradiance is substantially higher on horizontal surfaces than on vertical surfaces (Freitas & Brito, 2019). Geometrical and architectural design is required in order to direct the maximum amount of solar irradiance from direct, diffuse, and reflected radiation on the PV components and improve their power production.

PV facade ZigZagSolar® tackles this geometric issue from its configuration consisting of prismatic prefab cassettes linked together to create a vertical zigzag facade outfit. The PV modules are on the top sides of the zigzag. The bottom sides are constituted by reflective panels. This configuration enables the modules to overcome the limitations of vertical inclination and to benefit from additionally reflected irradiation from the reflective panel on the bottom sides (see Figure I-13). The facade is reported to have a 126% energy yield if a standard inclined panel on a flat roof has 97% (ZigZagsolar, s. d.).

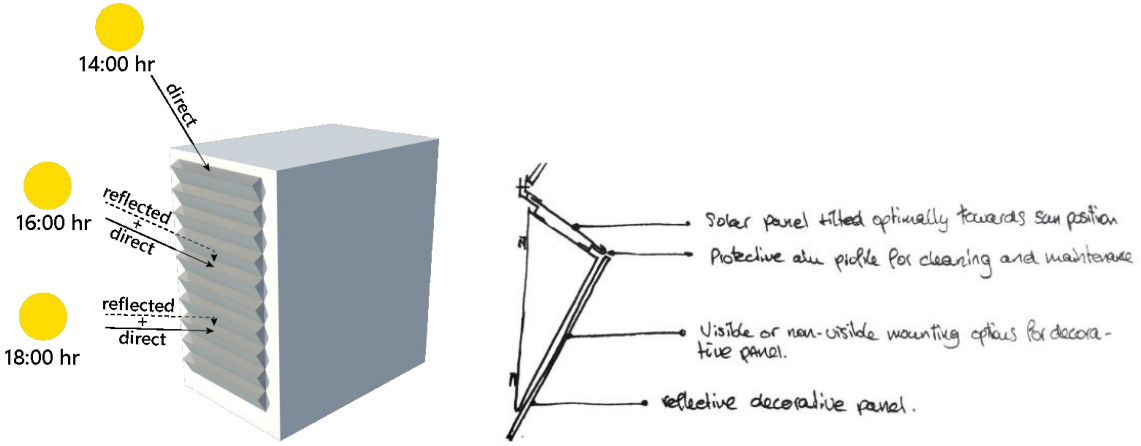

Figure I-13: Working principle of ZigZagSolar® - Source: zigzagsolar.com

- **Seasonal and dynamic solar tracking**

The possibility of being inclined toward the sun is indeed an effective solution to increase the PV power yield. It can be reinforced if the PV module can be modified to track the direction of the sun. In that scope, C. Lee, Lee, Choi and Yoon (2019) present operable opaque PV vents on the second skin of a double-skin facade. The vents are located at the top and bottom of a facade box comprising one building storey. The idea is to have the vent close in winter as the sun is low, and the vertical inclination of the panel does not lead to dramatic yield loss. In summer, the vent is opened and inclined with an optimum tilt angle to increase incident irradiance. This operation follows the thermal requirement as the closed vent in winter allows the second skin to act as a thermal buffer and reduce heat loss. The vent opening in summer reduces heat gain through natural ventilation with external air circulation by 10%.

This example shows the effectiveness of seasonal sun tracking for facade applications. However, dynamic tracking of hourly sun position can also be achieved in PV integration in the facade, as presented in the work of Hofer et al. (2016). In their study, the modules act at the same time as dynamic sun protection. They used units of PV panels to form either horizontal louvres rotating on the horizontal axis to track solar position from the horizon to the zenith, or vertical louvres for sun tracking from east to west or assemble in a diamond pattern for a bidirectional rotation allowing the tracking of effective sun position (see Figure I-14). From an electrical point of view, the main challenge is mutual shading between the modules, which leads to mismatch and power losses in the PV array and hot-spot heating (see subsection I.2.2.1). However, an optimised design according to module distancing, facade orientation and prevision of bypass diode to disconnect shaded module array would lead to more than 50% higher energy yield compared to uniform design strategies. The highest insolation per module is achieved with bidirectional tracking. Real-scale experimental investigations on this facade were undertaken on the HoNR building, ETH Zürich (Nagy et al., 2016) and NEST Hilo experimental building at Empa Research Centre in Dübendorf, Switzerland (Svetozarevic et al., 2019).

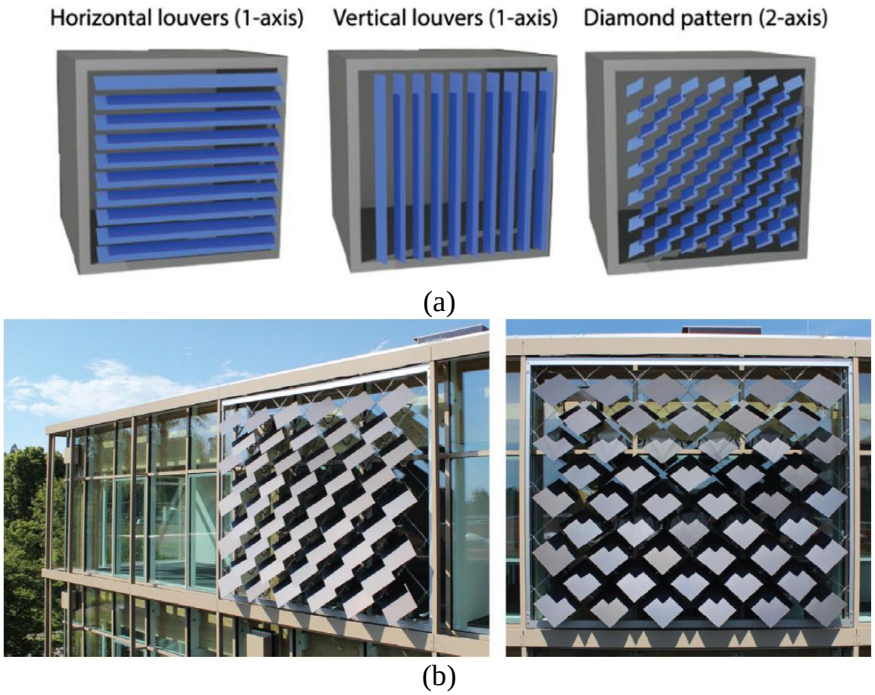

Figure I-14: Solar tracking PV facade louvres (a) Illustration of different patterns of louvres (b) Photograph of HoNR Building facade with Diamond pattern PV louvres

Dynamic sun tracking in the PV facade is an attractive and innovative solution that can be coupled with several facade functionalities. However, the effectiveness of this system in handling those multifunctionalities relies on an optimised and high-tech control system. Low-tech solutions can be achieved by using smart materials moving intrinsically according to a given trigger related to the solar

position. In this scope, Mazzuchelli et al. (2018) present a concept of PV facade element with self-oriented PV modules according to the sun elevation. The PV element consists of thin film solar cells attached to wooden slats that deflect with the variation of humidity. The temperature variation implicitly triggers the deformation of the slats because the relative humidity in the air is related to the ambient temperature. Thus, they would be flat (with a large curvature) with a vertical position at low temperatures or during winter. They gradually bend upwards as the temperature rises to be inclined in summer. This movement allows seasonal sun tracking and can provide an adaptive sun shading of the facade (see Figure I-15). However, there is no experimental proof of concept about the validity of the system yet.

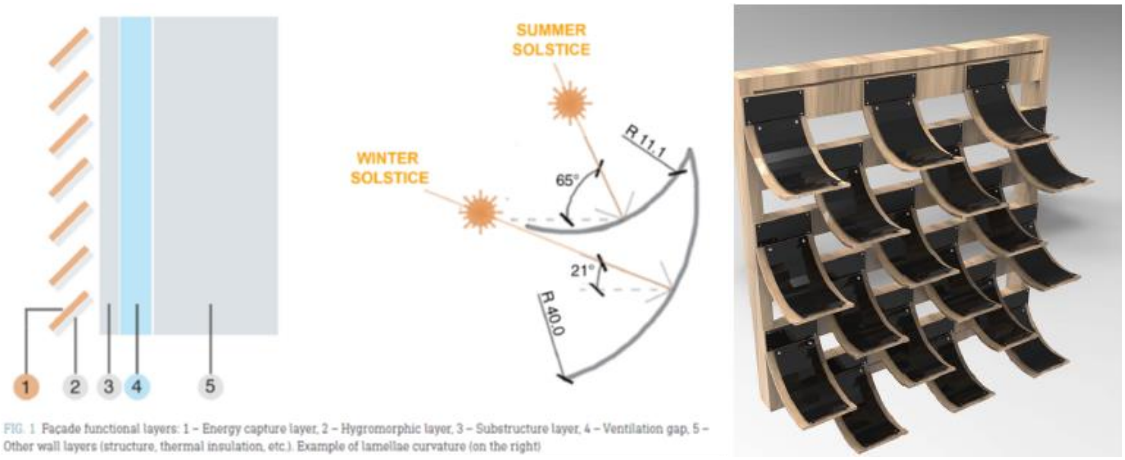

Figure I-15: Working principle of adaptive photovoltaic facade using hygromorph material (Mazzucchelli et al., 2018)

I.2.3 Conclusion on the optimisation of PV electricity yield

This state of the art on the optimisation of electricity yield in BIPV shows that, apart from the selection of the PV technology, the PV module cooling plays an important role and strongly impacts the facade thermal performance. This study focuses more deeply on cooling PV modules with air circulation, which can also be exploited for space cooling, heating, and fresh air preheating. The techniques are distinctively addressed here according to the thermal purpose. However, considering the alternation of cold and warm periods, adopting a solution adapted for only space heating leads to overheating and degradation of thermal performance in summer. The opposite situation occurs if the adopted solutions only target the cooling of PV modules or the facade. Hence, adaptive functionality is required in the facade and can be achieved by varying air circulation modes by closing and opening air vents.

In addition, directing a maximum solar irradiance on the PV components significantly improves the power yield. This can be achieved with reflective coatings and by optimising the inclination of PV modules, especially through seasonal or dynamic solar tracking. These strategies address the adaptability of the PV module configuration according to the variation of the sun's position in its hourly and seasonal pattern.

The adaptive and evolutive solutions that enable the adjustment of PV facade functionality to ensure thermal and electrical requirements are primordial to achieving a highly performant PV facade. This necessity for adaptive features is even more relevant regarding the thermal performance of the facade, which is strongly influenced by the variation of climatic conditions and the change of seasons. Therefore, in the second part of this bibliographic study, the requirement of adaptive and evolutive features of the building envelope is presented regarding the management of the thermal behaviour of the facade.

I.3 Relevance and challenges of Adaptive facades

I.3.1 Need for adaptation in building envelope functionalities

The building envelope should ideally act as an interface regulating the energy exchange between indoors and outdoors by benefiting from available heat gain or dissipating excess heat according to the thermal comfort need. In contrast, it is often designed as a barrier or a shield limiting those exchanges (Badarnah, 2017) as insulation is the main leverage for the improvement of the building energy saving. Certainly, this solution is primordial. However, its impact alone is very limited (Chesné, 2012), considering the current energy ambitions. It leads to static functionalities of the envelope while the conditions of the external environment are dynamically evolving (López et al., 2017; Shahin, 2019). Hence, energy systems are required to maintain the thermal comfort of the occupants as a consequence.

The idea of an envelope that can exploit the conditions of its environment is not new. It is the basis of passive strategies and bioclimatic design. Many traditional buildings are based on passive cooling and heating strategies such as natural ventilation (chimney effect), evaporative cooling, solar heating (solar collector), use of the greenhouse effect and thermal storage (massive and Trombe wall) (Aflaki et al., 2015; Bhamare et al., 2019). Nevertheless, passive strategies used for given climatic conditions often contradict the opposite. Thus, even with passive technologies, the building performance is limited to the nominal operating conditions of the design. With the current context of climate change and considering a temperate climate with two opposing seasons, building design should take into account multiple functionalities dealing with a wide range of climatic conditions, enabling the building to adapt, evolve and be resilient. Modulating airflow in ventilated facades is one of the ways to implement this adaptability, but many other envelope concepts exist in the literature to reach this goal.

In 2014, the COST Action TU1403 was launched to harmonise, share and disseminate knowledge on adaptive envelopes, specifically the facade. From this programme, an adaptive facade is defined as being able to change its functions, features or behaviours over time in response to changes in building performance requirements or boundary conditions, to improve the overall performance of the building (Aelenei et al., 2016; Loonen et al., 2013, 2015). Loonen (2015) stated that it acts "*as a climate mediator, negotiating between comfort needs and what is available in the ambient environment*". By taking benefits from its environment, an adaptive envelope minimises HVAC needs to ensure comfort requirements (Attia et al., 2018). As many existing technologies can meet this definition, adaptive facades are often associated with several other terms, such as responsive, active, kinetic, smart, intelligent, interactive, reversible, transformable, or movable (Romano et al., 2018). Several types of adaptability can be developed according to the targeted responsive functions of the envelope. Therefore, in the following subsections, the functions developed and adaptive facade technologies are presented considering thermal performance management in the building.

I.3.2 Overview of adaptive facade for thermal management

I.3.2.1 Responsive functions and process control

Thermal requirements in buildings change, first, mainly with a seasonal pattern from winter, summer, and mid-seasons, and second, with the alternation of day and night, where the occupant activity and comfort requirements fundamentally differ. This latter is accompanied by hourly fluctuations of temperature that can be approximated daily with a sinusoidal pattern. There are more dynamic fluctuations in environmental conditions like wind speed and direction variations and the sky cover (Loonen et al., 2013). However, the variation of the climatic conditions is strongly linked to solar radiation and position (height, azimuth). The envelope element develops opposite functions to opposite conditions to adjust its functionality. The adaptations are processed gradually or on and off. Towards solar heat management, those functions can be:

- to transmit or prevent could be linked with transparent and opaque features or exposed and shaded features;
- to collect or reject could be linked to the absorptive and reflective optical properties;
- and finally, to store and redistributing heat could be established with the exploitation of the envelope inertia.

Other media, such as air, are used to distribute, redirect or dissipate the thermal energy depending on the requirement. The establishment of one function is triggered by a change in one or many parameters of the indoor or outdoor environments, such as temperature, air humidity and insolation. The adjustment might be from an intrinsic change in the envelope material properties at a microscopic level. For example, the material becomes more reflective when its temperature rises. Either way, an extrinsic adaptation is established by using a subordinate control system directing the envelope to change its features, geometry or operation mode in response to the requirements. The adaptation is, therefore, at a macroscopic level. Movement is one of the most exploited responses in this kind of adaptation (Aelenei et al., 2016; Loonen et al., 2013, 2015).

To address the technologies dealing with those responsive functions, the next subsection presents facades employing kinetics adaptation, modulations of optical properties and energy storage and redistribution in the following subsection.

I.3.2.2 Kinetic envelopes

Building envelopes that move integrally or a part of their elements are called kinetic envelopes. This type of adaptation is one the most exploited and realised in numerous operational buildings or at a higher stage of prototype experimentation. According to Moloney (2011), four basic movements characterise the change in form or morphology: translation, rotation, scaling and deformation. Combining these motions results in complex movements, leading to complex morphology patterns in the building elements.

- **Extrinsic kinetic envelopes with rigid motion**

Extrinsic kinetic envelopes use automated and mechanised systems to enable the movement of the facade elements. They are often controlled by intelligent systems comprising sensors for perceiving environmental triggers, a processor unit that controls if an operation should be launched, and an actuator that launches the operation. In highly responsive and interactive systems, the users can also give feedback and information as input to the process control (Capeluto & Ochoa, 2017). Hence, input operational energy is necessary and should be lower than the energy gained through the adaptation for the effectiveness of the system. However, due to their complexity (from the control, motor and actuator), the drawbacks of those envelopes lay in their risk of failure and the high cost of maintenance and installation (López et al., 2017). Though, those additional costs and the potential gain in the life cycle of those envelopes are hardly discussed in the literature.

Most of these technologies develop adaptive features based on solar availability, management of heat gain, daylighting and solar protection. For instance, at the building scale level, the heliotropic buildings rotate to orientate the room that requires solar heat and light toward the sun as the building has a cylindric shape. The idea is to track the position of the sun with the rotary motion to adjust thermal and visual performances and to optimise energy production from the components installed in the building (Loonen et al., 2013; Ramzy & Fayed, 2011).

(a) (b) (c) (d)

Figure I-16: Examples of dynamic facades (a) Rotating sunshade (Al Dakheel & Tabet Aoul, 2017) *(b) Campus Kolding, Kolding (Denmark) (c) Kiefer Technic Showroom (d) Abu Dhabi Al Bahar Tower* (Romano et al., 2018)

At the scale of facade elements, the strategy is to tune the facade from transparent to opaque or semi-opaque to limit solar heat gain and glare without blocking daylighting. Thus, the facade usually comprises two skins: a static glazed wall and kinetic opaque or partially opaque blinds. Either daylight or temperature often triggers the motion. In general, there are :

- Rotating blinds like those installed on the facade of the Campus Kolding and Thyssen Krupp Quarter building (Romano et al., 2018); the rotation can be on a horizontal axis or vertical axis (Al Dakheel & Tabet Aoul, 2017);
- Folding blinds as in the Kiefer Technic Showroom building (Romano et al., 2018; Wang, 2014);
- Elements that scale up by combining basic movements, such as in the Al Bahar Tower in Abu Dhabi and the Arab World Institute in Paris (Romano et al., 2018) (see Figure I-16).

- **Extrinsic kinetic envelopes with flexible motion**

Previous examples of facades use rigid movement, leading to the assembly of numerous mechanical parts. Exploiting the reversible deformation of material provides flexible movements and lowly mechanised structures. The domain of soft robotics and inspiration from movement found in nature are pathways to reach those systems.

Figure I-17: Prototype of the facade shading system Flectofin® (Lienhard et al., 2011)

For instance, one soft pneumatic actuator is capable of generating bidirectional rotation movement of solar tracker photovoltaic modules that are also used as blind in the work of Hofer et al. (2016); Nagy et al. (2016); Svetozarevic et al. (2019). Besides, in the field of bioinspiration, Flectofin® and the facade of the One Ocean Pavilion are one of the well-documented bioinspired facades that exploit flexible movement for their adaptation. The Flectofin® is a real-scale sunshade prototype inspired by the reversible movement of the Strelitzia reginae flower (commonly known as Bird of Paradise) (see Figure

I-17). It is comprised of hingeless louvres opening through an elastic bending (Lienhard et al., 2011). As the actuating forces can be external or from thermal expansion, the concept can also be adapted to provide intrinsic movement. The One Ocean Pavilion project was initially an attempt to scale up the Flectofin® prototype to a facade. However, due to the difficulty of this attempt, the facade is inspired by the movement of plants. Both concepts aim to improve visual and thermal comfort in buildings (Knippers & Speck, 2012).

- **Intrinsic kinetic envelopes**

To overcome the failure risks from highly mechanised and extrinsic intelligent systems, the implementation of lowly mechanised or "low-tech" systems can be achieved by using shape-morphing smart materials and lead to intrinsic kinetic facades. Shape-changing materials change shape by deforming when triggered by certain stimuli such as temperature, humidity and electric current. They can be either the skin of the facade itself or a component of the facade that acts as a sensor and actuator (Vazquez et al., 2019). Despite the pertinence of the technology, the use of those materials in buildings is still recent. Most of the designs are still at the concept and prototype level. Adaptive motions are mostly targeted to modulate air gap circulation mode, enhance natural ventilation, or provide solar protection. More details about those materials and their application in the facade are given in section I.4.

I.3.2.3 Modulation of optical properties for heat gain management

Apart from kinetic features, controlling heat gain through modulation of the optical properties of the facade can also be achieved by fluid movement or the use of chromogenic material.

- **Modulation of optical properties from liquid flow**

Most applications exploiting fluid flow in the facade are to collect and dissipate heat (Biyik et al., 2017; Ibrahim et al., 2017). However, it can also be exploited to change optical properties and modulate heat gain, as present in the work of Baumgärtner et al. (2017); Ritter et al. (2015) about Fluidglass. In detail, Fluidglass consists of triple glazing. A coloured fluid circulates between the chambers of the first and third glazings. The fluid contains particles whose concentration gives the colour and thus tunes the transmittance of the glazing. This concentration is controlled according to the sunlight level and the indoor temperature. In addition, this fluid circulation also allows passive cooling and can act as a thermal collector. As in other adaptive facades assisted by subordinated systems, the main challenges are ensuring optimised operation control and offsetting the energy needed for fluid pumping (see Figure I-18).

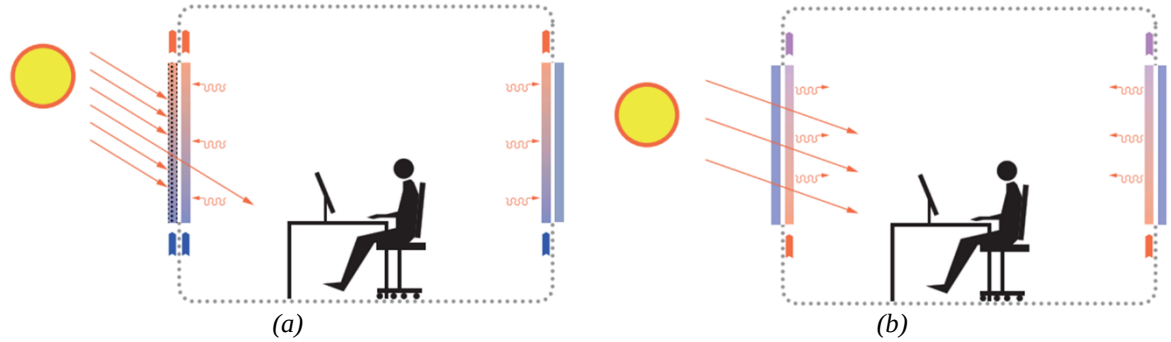

Figure I-18: Basic operation in Fluidglass (a) Summer: lowly transparent glass with a high concentration of particles in the fluid (b) Winter: lowly concentration of particles in the fluid to admit solar heat gain

- **Modulation of optical properties with chromogenic material**

Change of optical properties to module heat gain can also be reached using chromogenic smart material in glazings or opaque materials.

Several types of glazings switch on and forth from clear to tinted states in response to given stimuli. There are:

- Passive adaptive glazings which operate without input energy, such as thermochromic and photochromic glazings, respectively stimulated by the temperature and sunlight;
- And active adaptative glazings, such as electrochromic and gasochromic, are triggered respectively by current-voltage and gas injection; liquid crystal and suspended particle glazings are clear under current voltage due to the rearrangement of their constituent particles (Khaled & Berardi, 2021).

The main drawback of most chromogenic glazings is the increase of their absorptance coefficient in their tinted state to offset the decrease in their transmittance. Therefore, the absorbed heat can still be conducted indoors. However, effective chromogenic glazing would decrease its transmittance by increasing reflectance to avoid excess heat (Aste et al., 2018; Khaled & Berardi, 2021; Tällberg et al., 2019). Passive adaptive glazings are attractive since they do not require any control system and operational energy. However, their active peers outperformed them despite the use of electricity due to the maturity of the technology. In effect, the effectiveness of passive chromogenic glazing relies on the advanced material process to tune the transition temperature from tinted to a clear state. Their drawbacks (such as in the case of Vanadium oxide glass) also include the long-term stability of the material and the cost of the process, which are reported to be hard to improve simultaneously (Aburas et al., 2019).

The optical properties can be adjusted for opaque facades by using thermochromic coatings as in thermochromic glazing. Those coatings comprise pigments that have dark colours and, therefore, a low reflection coefficient at low temperatures. The pigments become lighter, and their reflection coefficient increases when the temperature exceeds a specific threshold. Thermochromic coatings offer a promising adaptive solution, especially for energy-storing envelopes such as Trombe walls (Perez et al., 2019). However, the main obstacle to the use of this technology is the loss of its thermochromic property over time due to UV radiation and some visible light (Karlessi & Santamouris, 2015). The coating can be protected with filter glasses. Though, this solution decreases the energy harvest performance of the wall by blocking parts of the solar spectrum (Perez et al., 2019).

This small glance at available technologies for the modulation of optical properties shows that input energy and extrinsic operation control are still needed for their effectiveness. Passive technologies are promising but still need more research in material science for their reliability and effectiveness.

I.3.2.4 Energy storage and redistribution

The technologies presented so far allow responding to immediate thermal needs. However, considering the intermittence of solar availability in diurnal patterns, for instance, forecasting future needs is also important in multifunctional building envelopes. This is achieved with a massive wall with high thermal capacity in a conventional facade. However, phase change material (PCM) can also be used to store thermal energy as latent heat (Souayfane et al., 2016).

Solid-liquid PCMs are the most used for building applications. At high temperatures, PCMs absorb heat without exceeding their phase change temperature until completely melted. The absorbed heat is released when the temperature decreases. This process is exploited in winter to store heat when the sun is available and to release heat at night for space heating. In summer, it helps to maintain the peak temperature within the comfort range during the day, but the store heat should dissipate at night. For this purpose, PCMs are incorporated into building materials through direct incorporation, impregnation in porous materials, macro-encapsulation, micro-encapsulation or in a stabilised form in a composite material. Encapsulation is the most preferred technique as it would prevent leakage issues during the liquid phase (Suresh et al., 2022).

The effectiveness of a PCM for thermoregulation or thermal storage depends on several parameters. First, the phase change temperature should be around the operational temperature of the building;

between 18 and 30°C is the most efficient. Potential candidates are paraffin, fatty acids, hydrated salts and eutectic composites (Zhou et al., 2012). PCMs should also have a high thermal diffusivity to allow for their activation. The crystallisation-melting cycles must be well controlled. Otherwise, they may remain in a liquid state without being able to solidify, leading to a high risk of overheating in summer. Night ventilation or free-cooling can be considered to establish these cycles (Ascione et al., 2016).

A wide range of applications of PCMs can be found in the literature: in opaque facade elements within the envelope masonry (Vicente & Silva, 2014) or micro-encapsulated in concrete (Zhou et al., 2012). In glazed elements, PCMs can fill the space between a double-glazing unit, but this solution degrades the transmittance of the glazing (Goia et al., 2014; D. Li et al., 2020). Various reviews on PCM applications focus on the prevention of overheating in double-skin facades and ventilated facades (de Gracia et al., 2013; Diarce et al., 2013; Y. Li et al., 2019) or to help to maintain PV components temperature in BIPV facade (Čurpek & Čekon, 2020; Modjinou et al., 2019). Furthermore, for winter performance, de Gracia et al. (2013) suggest that a ventilated facade with PCM acts like a Trombe wall during cold periods because of its heat storage capacity. As the application of PCMs in a Trombe wall enhances its thermal inertia, higher performance can be achieved with a thinner wall layer (Duan et al., 2021; Zalewski et al., 2012).

I.3.3 Challenges in adaptive facade design

This overview of adaptive technologies for thermal performance management provides examples of envelope modulating the functions of transmission, collection, prevention, rejection, storage, and dissipation of heat gain.

Most of the operational adaptive envelopes involve the use of input energy, rely on a high-tech intelligent system for effective process control or are dependent on highly mechanised systems. Those aspects challenge the effectiveness of adaptative envelopes. Certainly, energy-consuming adaptations are designed to save more energy than input. However, few studies exhaustively evaluate the energy performance of highly adaptive facades such as kinetic ones. The impacts of maintenance and end-of-life costs within the life cycle of the solution are hardly addressed in most designs. Further studies should be undertaken to develop tools and perform a thorough performance evaluation of adaptive facades.

Concerning the design process, bioinspiration approaches and smart materials are leading pathways to overcome challenges in adaptative facade design. On the one hand, a multitude of systems in nature exhibits the adaptive strategies sought in the buildings to maintain comfort while minimising energy consumption. On the other hand, smart materials would lead to low-tech and lowly mechanised solutions because of their self-adjustment capacity. Nevertheless, most applications in buildings are still recent. Especially for kinetic facades, most of the solutions are still in the design concept stage or reduced scale prototype stage. Therefore, a comprehensive investigation of designs using smart materials is necessary while considering thorough proof of concept and performance evaluation. For this reason, the following section gives more details about shape-changing smart materials and their application in adaptive facades.

I.4 Shape-changing smart materials

There are several types of shape-changing materials. For facade design application, Vazquez et al. (2019) reviewed the use of shape-memory alloys, shape-memory polymers, thermo-bimetals, bilaminar composites, hydrogels, and electroactive materials and wood. Most of these materials are stimulated by temperature, except for wood, which reacts to humidity, and electroactive materials, which are stimulated by electric current.

I.4.1 Shape memory materials

I.4.1.1 Shape memory alloys (SMA)

Shape memory alloys (SMA) are ferroelastic alloys that return to their original shape when the temperature exceeds a given threshold. This reversible deformation is due to the shape memory effect from the thermomechanical behaviours in which a series of crystalline deformation occurs to memory and recover their original geometry (Yi et al., 2020). The most widely used SMA is called Nitinol (Ni-Ti). This material offers interesting characteristics, including its corrosion resistance, ductility, high recovery after deformation and biocompatibility (Formentini & Lenci, 2018). For facade applications, SMAs were used in the form of wires (Formentini & Lenci, 2018) or springs that act as sensors and actuators (Jun, 2017; M. Kim et al., 2023; Verma & Devadass, 2013; Yi et al., 2020; Yi & Kim, 2021b).

As an example, Formentini and Lenci (2018) present a prototype of a ventilated facade equipped with SMA wires attached underneath a flexible skin. The wires bend the facade element to create a ventilation opening during warm periods (see Figure I-19). Thus, alternating bent and flattened configurations modulate the facade ventilation according to the cooling requirement. Nonetheless, this work is still at a proof-of-concept stage, and a validation of their impact on the building thermal performance is not reported.

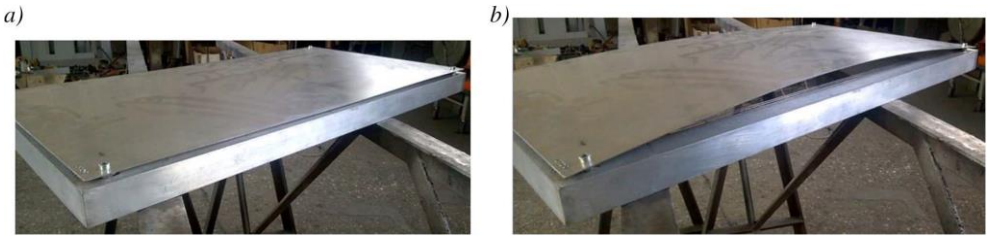

Figure I-19: Prototype of a smart facade element with SMA actuators (a) Closed air gap (b) opened air gap (Formentini & Lenci, 2018)

For thermal purposes, SMA spring actuators enable the motion of kinetic shading devices. In the reduced scale prototyping work of Yi & Kim (2021), motorised shading devices with an extrinsic intelligent system are compared with the shading with the same geometry actuated by SMA. The results of their study show better performance than the intelligent system in terms of lowering the indoor temperature in the tested climate. However, they reported slower mechanical responses.

I.4.1.2 Shape memory polymer (SMP)

Shape memory polymers (SMPs) have more or less the same principles as SMAs. However, they can be stretched up to 800%, though the deformation capacity of SMPs is just 4 to 6% (M. Kim et al., 2023). Manufactured through moulding or 3D printing, their properties can be customised to the requirements and according to the polymer composition (Vazquez et al., 2019).

In 2018, Yoon (2018) presented design concepts using SMPs as kinetic facade skin and an actuator for adaptive sunshading triggered by the temperature in a glazed facade. In the basic proposed configuration, the polymer acts as an actuator partially attached to a circular blind. The flapping motion of the actuator changes the blind gravity centre and leads to its rotation and gradual opening at low temperatures or closing of the blinds at high temperatures. In other configurations, the polymer forms a skin that opens and closes like a venus fly flap (Coelho & Zigelbaum, 2011), or by a scaling movement inspired by Kirigamis and Origamis (Ning et al., 2018), or by a venus folding movement (see Figure I-20). Therefore, the concept aims to enhance the thermal and visual performance of the facade.

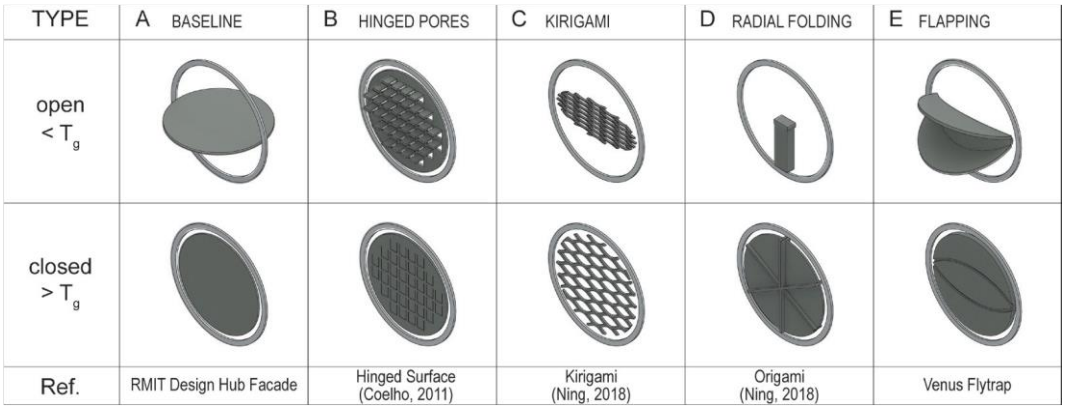

Figure I-20: Prototypes of facade blinds with SMP actuators and skins (Yoon, 2018)

I.4.2 Bilayers

Bilayers are composed of two materials of the same or different nature with different expansion properties (thermal or hygroscopic) and laminated to each other. The material with a high coefficient of expansion is called the active material. And the one with a lower coefficient of expansion is the passive material. Under the increase of the parameter concerned by the expansion property (temperature or humidity), the active material should expand, but as the passive material blocks this expansion, the whole assembly bends (Foged & Pasold, 2015) (see Figure I-21). Several types of smart materials exploit this principle to change shape: thermo-bimetal or thermostat metal, wood bilayer and wood composites and bilayer composites.

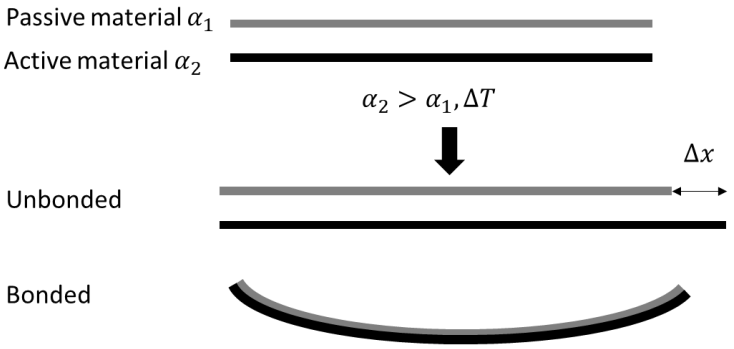

Figure I-21: Bilayer working principle - responding to change in temperature

I.4.2.1 Thermo-bimetal or thermostat metal

Thermo-bimetals bend with the increase in temperature as they are composed of two metals with different coefficients of thermal expansion (Vazquez et al., 2019). In 2016, Doris Kim Sung employed this material to modulate openings in a facade skin in order to enhance natural ventilation and thermal comfort (López et al., 2017). The facade prototype comprises bimetal slats that deform according to each respective temperature. Their deformations can create ventilation openings in the envelope, leading to a responsive cooling of a building without any input operational energy. The same principle as in thermo-bimetal can be used by laminating two different materials of different thermal expansion to obtain any kind of thermosensitive bilayer.

I.4.2.2 Wood bilayer and wood composites

Lamination of two different types of wood or wood slats composed of two different tissues results in hygromorphic material bending with the increase of moisture (Holstov et al., 2015). Since the absolute air humidity containment depends on the temperature, these materials are implicitly triggered by the

temperature variation. In the literature, the use of wood as a smart material mostly came from the inspiration of the constriction and expansion of pinecones. In 2015, Reichert et al. (2015) presented two large-scale prototypes of facades called “Hydroskin” and “Hygroscope”. The concept aims to regulate the humidity and provide space cooling from ventilation induced by the closing and opening of the wooden skin system (see Figure I-22). Holstov et al. (2015, 2017) presented a closely similar concept which provides natural ventilation during dry conditions. Their studies mainly show the efficiency of the movement generated according to the flexibility and thickness ratio of the active and passive materials.

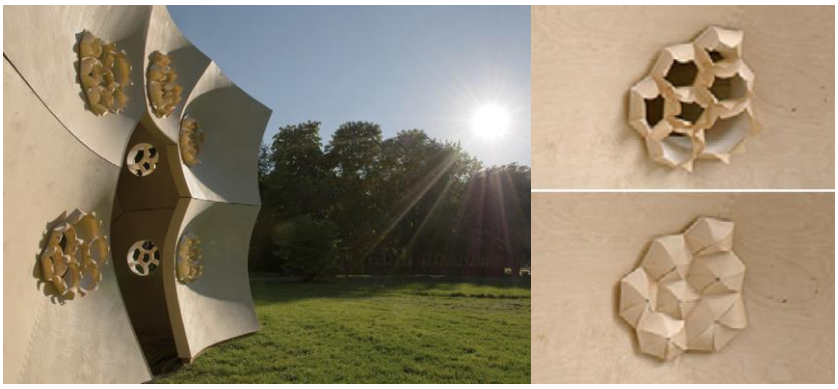

Figure I-22: Prototype de HydroSkin (Reichert et al., 2015)

I.4.2.3 Bilayer composites

Bilayer composites are constituted of two materials of different natures, whose stimuli can vary depending on the nature of the active material (Vazquez et al., 2019), where each blade has a specific function. For instance, the composition of a wood slat and aluminium sheet results in adaptive responses to both temperature (through the aluminium) and humidity (through the wood) (El-Dabaa, 2019). This composition is interesting since the concept aims to respond to a wider range of stimuli and climatic conditions. However, the system is still in the early phase of experimentation. The suggested application is the intrinsic opening and closing of facade louvres, but details on the effectiveness of the design are not reported in the study.

The work of Mazzucchelli et al. (2018), mentioned earlier in subsection I.2.2.4, is also included in this category. It consists of the lamination of a photovoltaic cell on wooden bilayers in order to exploit the wood movement for solar tracking, sun shading and cooling of the PV components. The design is still in the conceptual phase.

I.4.3 Challenges and opportunities in shape-changing materials application in the facades

This short overview of shape-changing smart materials shows that their applications in buildings are still recent. Hence, most works are still in the proof of concept or early prototyping stage. Many scientific barriers still need to be explored before an effective or systematic deployment of most smart materials on full-scale adaptive facades. A thorough study is needed to optimise their properties and geometry to substantially enhance the building thermal performance and outperform the intelligent kinetic facade. In effect, an understanding of the thermomechanical properties of those materials is primordial as they undergo a cyclic deformation, which results in their fatigue and deterioration. Due to their recent application, their mechanical reliability and operational lifecycle remain important domains of inquiry (Yi & Kim, 2021b). Other challenges include the cost of manufacturing, which can be significant for SMP due to 3D printing despite the inexpensiveness of polymers (Yi & Kim, 2021a). As for bilayers, the cost can be relatively low, depending on the process and the material used to form the layering.

Nonetheless, shape-changing materials can overcome the challenge of failure linked to complex mechanical systems and operational costs (linked to energy consumption and maintenance) of intelligent kinetic facades. They allow the envelope to self-adapt to its environment. Furthermore, they are targeted for bioinspired and biomimetic design. In effect, smart materials provide more flexible motion and can respond to environmental stimuli similar to those of live species (such as temperature and humidity). In that scope, the stretching of plant cells due to changes in their pressure (M. Kim et al., 2023), the opening of plant stomachs (Yi & Kim, 2021a), and plant movement are some biological strategies (Holstov et al., 2015; Mazzucchelli et al., 2018; Reichert et al., 2015) taken as models for these applications. For further exploration of bioinspiration, the following section addresses the method, relevance and challenges of this approach for facade design.

I.5 Relevance and challenges of bioinspiration approaches

I.5.1 Definition of bioinspiration

Bioinspiration is a design approach that takes nature as a generator of ideas for the development of a technical solution. It is a broad term to designate this process of getting inspired by nature (Kuru et al., 2019). Other terms like “biomimetics” and “biomimicry” are used when the process is integrated with a comprehensive method, and the targeted natural strategy is closely analysed, modelled and abstracted before its transfer and implementation in the technology. Details of these processes can be found in the norm ISO 18458:2015 (2015). In this manuscript, the term bioinspiration is used. The purpose of this work is not to develop a solution solely based on natural strategy but to learn from natural adaptive strategies to design a new facade concept that also relies on existing innovative solutions.

I.5.2 Relevance of bioinspiration for the design of adaptive PV facade

Bioinspiration is a relevant approach for the design of adaptive PV envelope elements since multitudes of living species respond to external stimuli of their environment and adapt their function. Similarly to the buildings, they are subject to changes in their environmental conditions. They should constantly seek tolerable internal or physiological conditions for their survival. This notion of maintaining physiological equilibrium, equivalent to comfort in the building, is called ‘homeostasis’ (Breed & Moore, 2016). It consists of self-regulatory processes where a living organism develops several strategies to maintain the states of various parameters such as body temperature, blood pH and oxygen saturation, fluid balance, and nutrient concentration (McEwen, 2016). Therefore, they collect energy and undergo several types of exchanges with their environment for this purpose. Homeostasis then implies the adaptation of living beings to their environment and is closely analogous to the need for adaptation in buildings. The convergence of the requirements in the building and the strategies employed by living beings then allows the design of an innovative bioinspired building (Badarnah Kadri, 2012).

I.5.3 Biological strategies for the envelope design

I.5.3.1 Relevant biological strategies

Getting inspired by biological adaptation strategies related to climate effect mitigation would allow the development of PV envelope solutions that optimise both the electricity production, their thermal performances, and the comfort of the occupants. For PV in general, light-synthesising bacteria and plants and the nanostructured interface (cuticle) of insects are among the relevant sources of inspiration for enhancing light absorption and conversion efficiency (Soudi et al., 2020). Plants can also be a source of inspiration for buildings, given that both are fixed to their implementation and perform their adaptation

in that state (López et al., 2017). Moreover, the building envelope is often compared to the skin, which is the interface of exchange in live species.

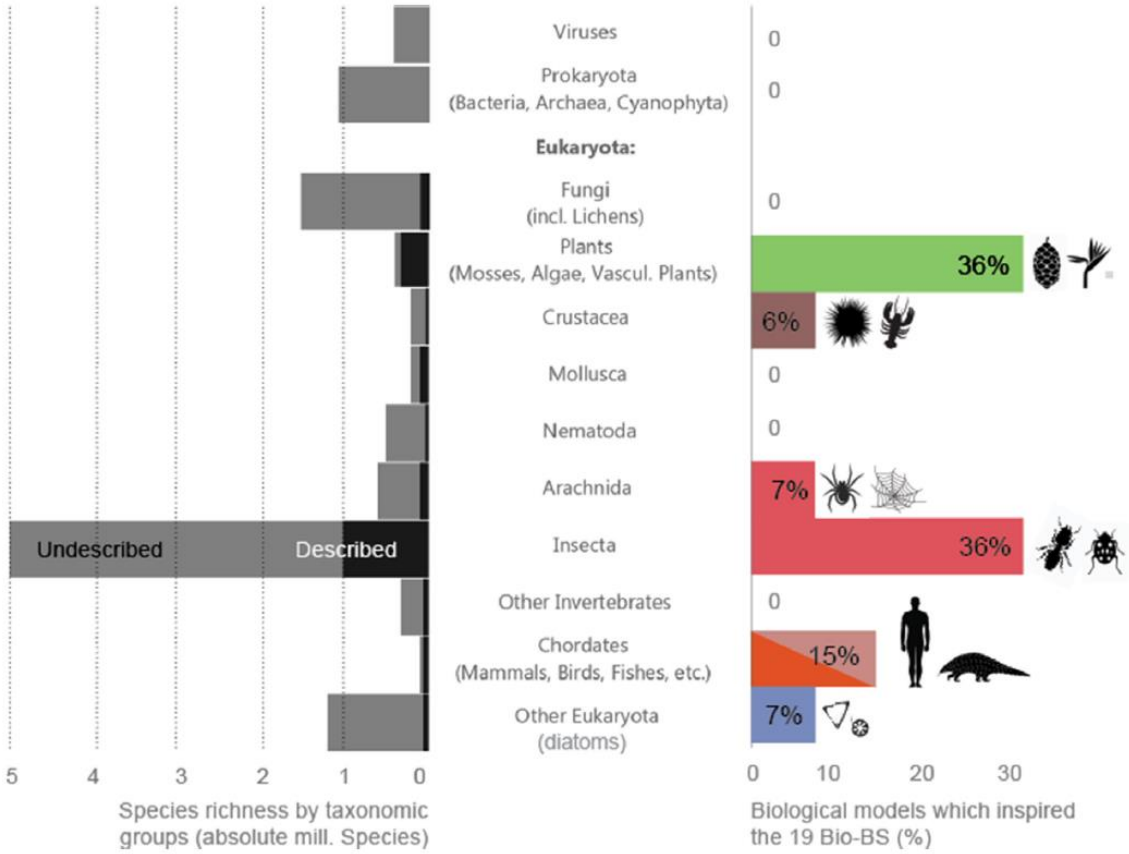

Figure I-23: Distribution of the major groups of biological models which inspired the bioinspired building skins analysed by Cruz et al. (2021) according to the distribution of estimated species on earth (Cruz et al., 2021)

This short identification of potential candidates for bioinspiration joins the results of the comparative analysis effectuated by Cruz et al. (2021) on the design process of biomimetic building skins. In effect, they identified that most biological models for bioinspiration are often from animal or plant kingdoms (see Figure I-23). They point out that this might be because those kingdoms are visible in our daily lives, and other kingdoms can be hard to scale up. In this study, the ease of access to the available and understandable resources with the help of biologists is one of the drivers to target those kingdoms. Furthermore, among the building elements studied by Cruz et al. (2021), the challenge of developing flexible and low-tech mechanisms is addressed in most solutions, even if the evolution of the energy performance is reported only in a few designs. An overview of adaptation solutions in living organisms is discussed in the following subsection to guide the exploration of biological strategies.

I.5.3.2 Adaptation solutions in live species

Adaptation strategies are most noticeable in organisms living in extreme conditions such as deserts and environments with extreme radiation, temperature and pressure. These organisms then develop particular adaptations regarding their physiology, morphology and behaviour (Badarnah Kadri, 2012; López et al., 2017).

Morphological or structural adaptation concerns the appearance, structure, shape and geometry of the organism to develop better functions fitting with its environment. Many examples of morphological adaptation can be found in desertic environments. In cacti, spines and ribs on their stems protect them from high temperatures and diurnal temperature variations by influencing convective and radiative

exchanges (Nobel, 1978). Desert silver ants have triangular prismatic hairs that enhance the reflection of solar radiation and allow these organisms to live in a hot and dry environment (Willot et al., 2016).

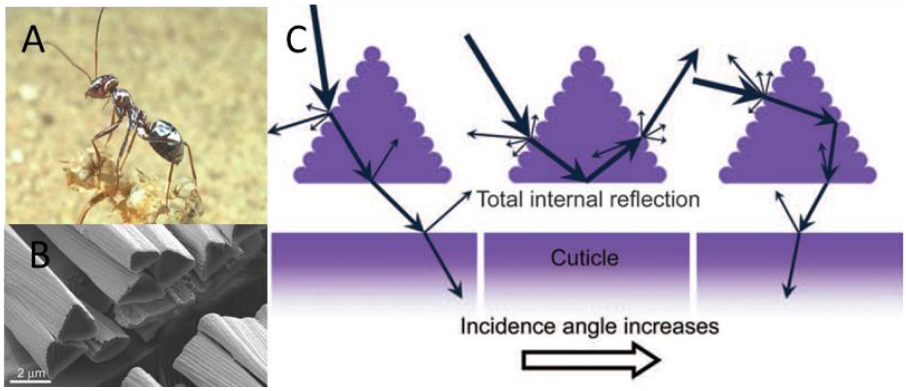

Figure I-24: Photograph of a silver ant - a cross-sectional view of hairs of silver ants- the principle of heat reflection through the triangular morphology of the hair of silver ants

Physiological adaptation is related to chemical processes within the living being. This adaptation mode represents the response of the organism to an external stimulus to maintain homeostasis (Badarnah Kadri, 2012). For example, photosynthesis CAM (Crassulacean Acid Metabolism) is an adaptive process allowing plants in arid environments to use water efficiently by limiting water loss through transpiration and storing water (Lüttge, 2004).

Finally, behavioural adaptation consists of actions taken by the organism. These are responses that allow the organism to interact with its environment. For example, penguins gather during severe winter to reduce their exchange surface and decrease their heat loss (Gilbert et al., 2006).

Regarding those types of adaptations, the form, function and process of living organisms are the sources of inspiration. Imitating forms is the most direct type of bioinspiration. It does not necessarily incorporate the function linked to the morphology. Getting inspired by the function attempts to transfer the mechanism developed in the live being. It can be directly transferred to the technology or indirectly as an abstraction step is involved. Hence, the function imitated does not always perform with the same purpose as in the natural model. The imitation of process addresses the adaptation of organisms as a system and is mainly applicable at urban and inter-building scales (Loonen, 2015). Furthermore, adaptation in nature also occurs from a molecular level to an inter-organism level, and the responses can be in the range of seconds, hours, days, seasons and long-term evolution. Those spatial and temporal responses can also be analogous to building element adaptation.

I.5.4 Overview of bioinspiration approaches

The transfer of mechanisms found in nature can be complex. Direct replication of natural strategies to technology is rarely successful. An abstraction phase, i.e. interpreting or translating biological phenomena to technology, is often required (Vincent et al., 2006). This transfer might imply a creative approach but also knowledge of natural science (López et al., 2017). However, biological and technical fields are far apart, and biological databases are very large. The problem of scaling biological models to technology and conflicts between needs in design (e.g. between functions and aesthetics) are among the difficulties of bioinspiration (Badarnah Kadri, 2012). Hence, there is no general method applicable to the bioinspiration approach. However, according to the literature, existing methods can be classified into two approaches:

- Biology-to-technology (Baumeister et al., 2014), bottom-up, biology push (Speck & Speck, 2008), inductive bioinspiration (Gebeshuber & Drack, 2008) or solution-based approaches (Helms et al., 2009) are initiated by the observation of natural phenomena for the development

of a new technological solution. These approaches are described as biology push in this document;

- Technology to biology (Baumeister et al., 2014), top-down, technology pull (Speck & Speck, 2008), bioinspiration by analogy (Gebeshuber & Drack, 2008) or problem-based approaches (Helms et al., 2009) are methods where the first step is to define the technical problems in existing technology to improve with biological strategies. These approaches are described as technology pull here.

Many tools and processes are proposed for each of these approaches. In general, technology pull methods consist of the following:

- Problem definition consists of problem identification and formulation and concerns the technical domain;
- Exploration, investigation and abstraction of biological models involve finding biological solutions corresponding to the problems, their analysis and their transfer to the technology. Those steps mainly concern the biological domain and the bridge between biology and technology;
- And finally, a solution development step consists of the design of the concepts and their validation, thus the analysis of the bioinspired solution (Badarnah Kadri, 2012) (see Figure I-25).

The processes of biology push methods are constituted by investigations in the biological domain as a first step, a transfer phase from biology to technology and finally, the transcription of the biological principle to technology. Both bioinspiration approaches describe similar processes, especially in the biology-to-technology transfer phase. However, a biology push approach might require a longer investigation time since a thorough biological search might be needed to find interesting phenomena that can be used to develop a new technical solution. Furthermore, the bioinspiration approach often leads to iterative processes. Particularly for technology pull approaches, many attempt loops of biological transfer might be required to identify the right biological model for the technical problem (Speck & Speck, 2008).

I.5.5 Details of bioinspiration method processes

For each stage of bioinspiration, many researchers have developed particular processes that address how to define the technical problem and biological solutions, conduct biological research, develop biological models and transfer them to the technology. This section then presents the methods of answering these questions by combining interesting processes that can be applied to various problems. Since each approach is different even within their steps, summaries of some methods are given in Appendix A1.

I.5.5.1 Problem definition

Problem definition is the first step in problem-based approaches. Most methods suggest defining problems by identifying the desired functions in verbal form (e.g. avoid, transmit, protect) (Shu et al., 2011). In the BID (Biologically inspired design) method, to define problems, Vattam et al. (2007) propose four techniques: making assumptions that define the problem, decomposing complex functions into subfunctions, defining functions in the form of an optimisation problem and posing a criterion for design success. Badarnah Kadri (2012) proposes to identify functions in terms of challenges. Those challenges are divided into four categories in that research: heat, air, water and light. The problem definition is accompanied by the definition of the context and objectives of the study. Reformulation of the problem can be required to ease the biological search as the terms used in technical fields to describe function might differ in biology (Helms et al., 2009).

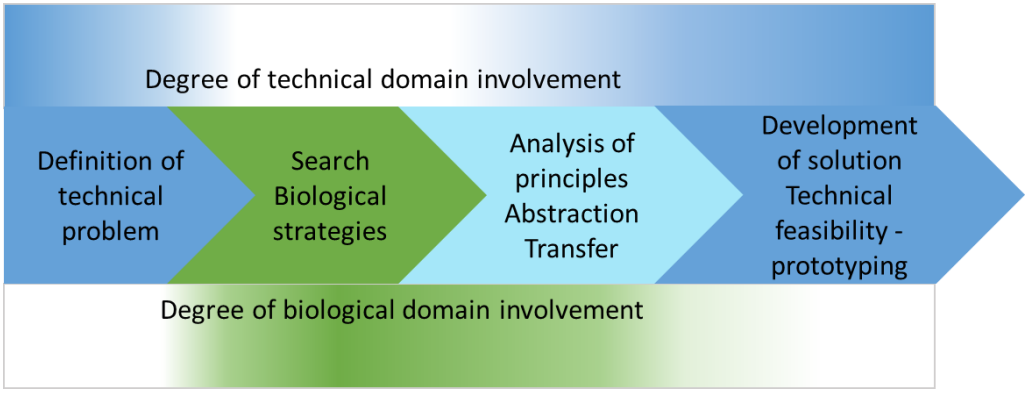

Figure I-25: Technology pull bioinspiration process, inspired by the works of (Badarnah Kadri, 2012; Cruz et al., 2021; Speck & Speck, 2008)

I.5.5.2 Biological research

Biological research can be performed by cooperating with biologists or browsing available databases. It can be a rigorous task considering the size of all existing databases. To ease the process, Helms et al. (2009) propose four techniques :

- Change the constraints: to broaden the search scope, for example, instead of searching for "keeping cool", the term "thermoregulation" can be used;
- Find organisms that adapt to extreme conditions or "champion adapters" like those surviving in the desert;
- Find organisms in the same family as those facing the same problems might not always perform the same strategies;
- Search for multifunctional organisms.

Because of the difference in terms used in engineering and biology, Chiu and Shu (2007) developed an algorithm to generate understandable keywords in the biology domain from the technical keywords. This method allows engineers to search in the biology domain without being experts. In the same perspective, the biomimicry taxonomy developed by The Biomimicry Institute can also be used to find keywords to easily perform the biological search (Baumeister et al., 2014).

I.5.5.3 Exploration and analysis of biological data for the transfer of principles to technology

The analysis of biological data consists of the understanding, extraction, classification, and abstraction of biological principles for their transfer to the technology. The decomposition of biological strategy functions as the decomposition done in the problem definition can be undertaken (Helms et al., 2009). For a detailed analysis of the biological strategies, Badarnah Kadri (2012) proposes to classify the organisms according to the challenges they are facing, their function, the processes performed, and, finally, adaptation factors. In her methodology, the biological principles extracted for the design combined all strategies that respond to design objectives from various organisms. In the same sense, López et al. (2017) classify plant adaptation data according to climate, type of strategy (dynamic or static), adaptation scale, structural system, and environmental constraints. To develop the design concept, the analysis of the classified data consists of answering the following three questions: "What kind of adaptation is developed? Why is this plant adapting? How did it develop these specific functions?". Finally, modelling the behaviour of the organism with computer-aided design (CAD) and simulation tools is an effective way to understand kinetic adaptations (Schleicher et al., 2015).

I.5.5.4 Development of bioinspired solutions

As the last step, solution development includes the development of the concepts and their transformation into a product through prototyping and experimental and numerical assessment. Concept development consists of investigating the technical implementation potentials of the selected biological solutions (Speck & Speck, 2008). It is not a direct copy of biological adaptation. It consists in transferring or translating the abstracted biological model to the technology. Brainstorming ideas, modelling the principles of a particular structure and making sketches are some of the methods used in this phase. Afterwards, experimental prototypes at various scales and numerical modelling are necessary to validate the design concept (Badarnah Kadri, 2012; López et al., 2017).

I.5.6 Tools for bioinspiration design

There are various tools available for bioinspiration design. Some of them are linked to a specific bioinspiration methodology, as in the case of BioTRIZ, which is the extension of the TRIZ methodology applied to biological data. In detail, TRIZ comes from a Russian acronym meaning "theory of inventive problem solving" and is a collection of tools and techniques developed by Genrich Altshuller and Rafik Shapiro to help define a technological problem and guide the development of an inventive solution. This tool is known for its ability to transfer inventions and solutions found in one engineering domain to another domain (Vincent et al., 2006). The principle is to formulate a factual problem in a conceptual problem. And then finding the conceptual solution sets corresponding to the problem in the TRIZ database. The conceptual solution can then be transformed into a factual solution (Ilevbare et al., 2013).

Bioinspiration tools are classified in the works of Fayemi et al. (2017) and Wanieck et al. (2017) according to the steps of the bioinspiration process involved. There are:

- **The analysis and abstraction tools** involved in the analysis phase and abstraction of the technical problem or the biological solutions. In this category, the tool DANE (Design Analogy to Nature Engine), an interactive toolbox gives access to biological SBF ("Structure-Behaviour-Function") models and engineering systems. Those models describe the structure, behaviours and functions of a system. The structure represents studied systems with the components, the substance contained in the components and their connections. Behaviours are represented as schema representing a series of states and the transitions between them. The functions are the consequence of behaviours. Their representative schema specifies what triggered the behaviours and what their outcomes are (Goel et al., 2009; Vattam et al., 2011).

- **the transfer tools** which are used to transpose technical functions to biology (transfer tools), namely through the use of the biomimicry taxonomy, which translates the technical problem into biological terms (Baumeister et al., 2014);

- **the application tools** which are used for the identification and implementation of the biological model. For biological search, various biological database exists; in this work, for instance, AskNature (https://asknature.org/) was used for a quick browse of biological strategies. It is an open biological database provided by The Biomimicry Institute and includes more than 1700 biological strategies. The strategies can be browsed in verbal form according to the function sought, for instance, "absorb energy", and according to the Biomimicry taxonomy.

I.5.7 Conclusion in bioinspiration approach

This quick overview of bioinspiration aimed to understand the adaptation process in living organisms and the methods and tools for getting inspired by those strategies. In the scale of buildings, the most explored are the inspiration of form and function found in nature and concern mostly animal and plant

kingdoms. Building technology is well established even if continuous improvement is needed. This is why a technology-pull approach might be more convenient to conduct. This approach defines the limitations in existing technology and seeks natural strategies to overcome those limitations.

This overview of bioinspiration tools and methods aims to present a glimpse of some available tools in the fields. In this project, they are combined to develop the method adopted, described in the next chapter. Hence, none of the presented methods is integrally used in this project, but their investigation aims to select the process adapted for the investigation purpose. Namely, the decomposition of problems and analogy proposed by the BID method helps to identify the function needed in a PV facade and make an analogy with living species, AskNature and the Biomimicry taxonomy to initiate the search for biology and analogy principles.

I.6 Conclusions

With the aim of designing a bioinspired PV facade with evolutive functionalities, four themes were addressed in this bibliographic study: building integrated photovoltaic (BIPV), adaptive building envelopes, smart materials and bioinspiration approach. In the analysis of BIPV facade systems, this study has pointed out the existence of trade-offs for PV integration in the facade, namely the PV electrical performance, the facade thermal performance and its aesthetic value. An optimisation process is primordial for selecting PV technology and the facade design in terms of its geometry, PV inclination and integration mode.

Developing adaptive features can lessen those trade-offs. For the PV electrical performance, adaptive features can be implemented through solar tracking, modulation of properties, or the flow of a media cooling the PV modules. This latter solution is strongly linked to the thermal performance of the facade. As an aside, most adaptive solutions for facade thermal management involve solar flux harvest and control. Thus, developing adaptive functionalities for PV components and facade thermal performance goes hand in hand. Nevertheless, there are multitudes of adaptive facade technologies. The most developed ones contain highly mechanised and intelligently controlled systems that are costly, energy-consuming, and prone to failure. Getting inspired by natural strategies is reported to overcome those issues by developing flexible motion through the use of smart materials. Envelope elements adopting those principles are still at a low state of technology readiness, though. Nonetheless, this design is oriented in this direction in order to develop a low-tech solution.

Since the subject concerns BIPV facades which are well described in the literature, the technology pull approach of bioinspiration is more adapted for the design objective. The review of the BIPV enables the selection of the starting point or the product to be improved. This baseline is a naturally ventilated PV facade with an opaque wall, one of the most current PV integration modes in the facade. Additionally, as a first step in the optimisation of the thermal and electrical performances of the facade, semi-transparent and bifacial PV modules are chosen. The challenge is then to find the biological strategies to optimise the PV module cooling and solar harvest and for the thermal management of the facade. Details of the design processes inspired by methods found in the literature are given in the next chapter.

Chapter II. The bioinspired facade concept development

II.1 Introduction

This chapter details the development stages of the bioinspired photovoltaic facade. In brief, the bioinspired approach applied in this study consists of questioning what should be adaptive in an ordinary photovoltaic facade to improve its functionalities. The responses to this question are the pathway for the biological search and the application of strategies to obtain an optimised facade. A numerical study on the feasibility of the concept is then conducted before further validation. From the bibliographic study and given the available data that can be exploited, the starting point of the design is a ventilated photovoltaic facade composed of semi-transparent bifacial modules.

The first part of this chapter details the method developed to improve this facade technology with a bioinspired approach. In the second part, parametric studies are conducted on the facade to identify the parameters that influence its electrical and thermal performances and should be adaptive. The third part presents some biological strategies selected according to the parameters identified. The last parts of this chapter present the designed bioinspired facade and a preliminary study of the design feasibility.

II.2 Presentation of the developed method

A bioinspiration method was developed based on existing approaches (see the summary of some of them in Chapter I and Appendix A1) and on the design purposes. This method is a technology pull approach consisting of four steps: problem definition, biological search, analysis of biological strategy and solution development. Figure II-1 gives the summary of this method.

- **Problem definition: which parameters in the PV facade should be adaptive?**

The problem definition consists of identifying the targeted functions in the design. In this study, they are well defined in the state of the art on BIPV and building facades in general:

- From the PV side, those functions are linked to the maximisation of solar radiation collection and the PV components cooling.
- From the thermal performance side, the problem is mainly about how to move from the desired functions during cold periods (avoidance of heat loss and collection, storage, distribution, and admission of heat gain) to the desired functions during warm periods (rejection, dissipation and protection from thermal intake).

To tackle these problems, the main parameters that influence and induce conflicts between electrical and thermal performances, especially in two opposite climatic conditions, should be identified. Those are the facade thermo-physical and geometrical properties that should be adaptive. Their identification is conducted through parametric and multiobjective optimisation studies on the starting point facade.

- **Biological search: which biological organisms are related to those parameters?**

The search for biological strategies is based on the results of the parametric study. In this method, the relevant biological strategies are those linked to the functions (e.g. heat collection or rejection) related to the identified parameters. Thus, this step consists of general exploration and selection of relevant organisms. Motions found in nature are also explored because this strategy is an effective way to change properties without necessarily changing the intrinsic properties of the material used.

- **Analysis of biological strategies: which strategies are relevant and how to apply them?**

In this step, a comprehensive analysis of a few selected organisms is performed to extract adaptation principles. An Analogy between the facade problem and the biological solution is undertaken to transfer the strategy found. Application ideas are brainstormed and sketched. The end of this stage involves the search for the material or system that can be used to apply the strategy.

- **Development of the solution**

This stage consists of the final sketching of the concept by taking into account the explored biological mechanisms and relevant existing solutions. A simple assessment of the design potential is realised to evaluate the feasibility of the concept. If the potential of the concept is confirmed, a parametric study is undertaken for the preliminary sizing of key elements of the facade. A proof of concept study is conducted with test benches at different scales to develop and validate a numerical model of the innovative solution.

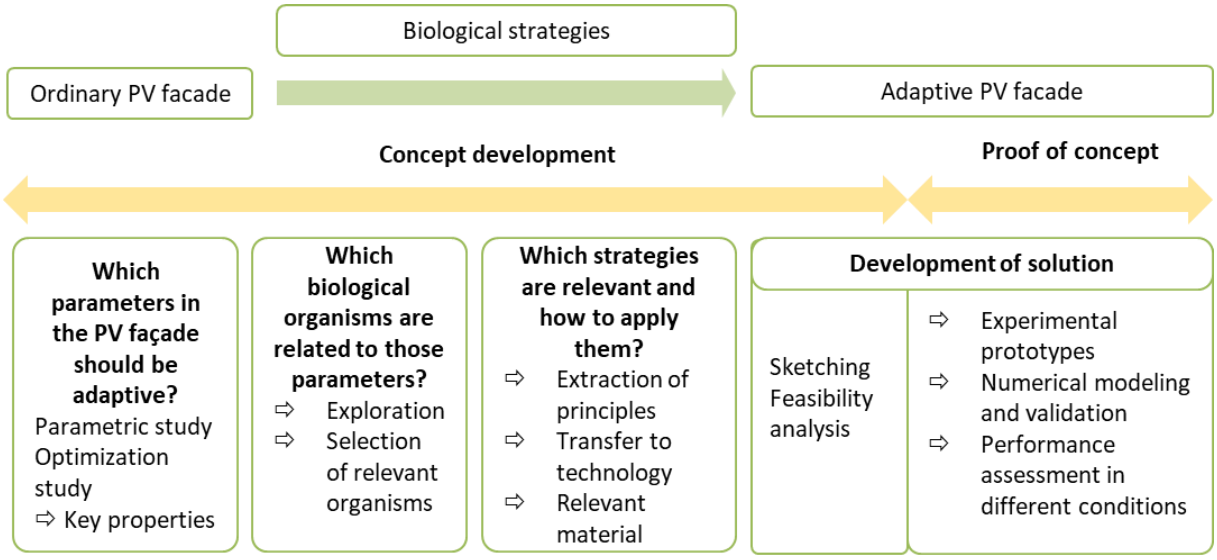

Figure II-1: Summary of the method processes for the design of the bioinspired PV facade

This chapter presents the application of this method from the problem definition to the preliminary sizing. The steps, including the proof of concepts, are presented in the following chapters.

II.3 Problem definition: Definition of influencing parameters

In this part, the initial BIPV facade is presented. The influence of its thermo-physical properties on the cooling and heating loads and electricity production is studied in order to select the ones that should vary in the adaptive facade to be developed. Main heat transfers in interaction within a BIPV facade were analysed, namely: the convective and radiation heat exchanges between the facade and its surrounding environment elements, the convective and radiation heat exchanges in the facade air gap and the conductive heat exchange in its constitutive layers.

II.3.1 Presentation of the selected initial BIPV facade

The baseline of the current design is a photovoltaic facade composed of monocrystalline silicon heterojunction (HET) glass-to-glass bifacial photovoltaic modules, a ventilated air gap and a multilayer wall (see Figure II-2). A facade with glass-to-glass PV modules is taken as a reference since glass-to-glass PV modules are relatively more aesthetically appealing. They permit the transmission of solar radiation (according to their semi-transparency ratio). Thus, they can be optimised to increase the

thermal performance of the facade (Saadon et al., 2016). Accordingly, bifacial PV modules are chosen in the reference facade since they would provide higher electrical performance than monofacial ones considering glass-to-glass to PV modules according to their semi-transparency factor (Assoa et al., 2021; Soria et al., 2016; Tina et al., 2021). This choice is also because of the purpose of exploring more this technology. Moreover, the PV technology must be defined from the beginning of the process since the parametric study results and the façade requirements might differ if the PV facade has either monofacial or bifacial PV cells.

Naturally ventilated air gap with external air circulation has been chosen since it is the most exploited in ordinary PV facades (the air comes and exhausts outdoors). The particularity of this facade is that it is an open joint ventilated one, in which different air gap outlets and inlets exist between the PV modules. The facade has four (4) rows and two (2) columns of PV modules. The air enters the first two openings at the bottom and is exhausted in the two last openings at the top. The bificiality of the PV is already an optimised solution regarding the PV facade electrical performance. The facade configuration was developed and validated in the framework of the Life European project CONIPHER (project reference: LIFE14 CCM/FR/000954) involving CEA INES (Assoa et al., 2021). This facade was selected in this study since it corresponds to the initial configuration requirements and disposes of a database of its thermal and electrical measurements.

In the initial facade, the multilayer wall is composed of 2 cm thick ultra-high performance fibre concrete (UHPC) panels, 20 cm thick rock wool insulation blocks and a 20 cm thick concrete wall. The air gap is 2 cm thick. The PV module covers comprise 3 mm thick tempered glasses on the front and rear sides. Each module has a transparency of 61.6% and an electrical efficiency of 20% at the standard test conditions (STC, corresponding to an irradiance of 1000 W/m², an ambient temperature of 25°C and an air mass coefficient of 1.5).

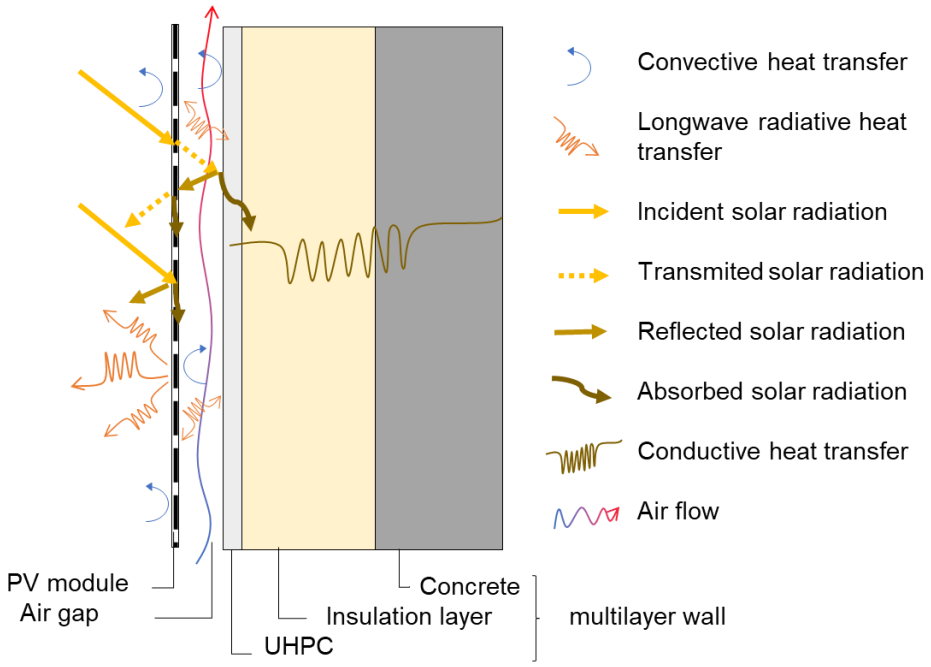

Figure II-2: Illustration of PV facade composition with main heat transfers in interaction

The BIPV system is mounted on the southern facade of a test cell of the experimental building FACT (Facade Tool) located at Le Bourget du lac (40°38'44" N, 5°51'33" E). Each test cell of FACT is a highly insulated cubic volume of 2.3m wide, 3.9m in length and 3.3m in height. The indoor air temperature is conditioned with a CLIMACIAT AIRTECH 25 dual-flow air handling unit from CIAT, with a dual setpoint of nearly 21°C in the heating and 26°C in the cooling seasons. For parametric

studies, the thermal loads are calculated for an indoor space with a geometry corresponding to the test cell of FACT.

II.3.2 Parametric studies

II.3.2.1 Thermal analysis of the BIPV facade

The parametric study is conducted by coupling the energy model of the cell integrating the facade and the dynamic thermal and electrical model of the facade itself. The software EnergyPlus is used for the building energy modelling of the cell to calculate its thermal loads (cooling and heat loads), which are the thermal performance indicators. The facade model is based on a nodal (or resistance-capacitance) approach and is developed separately in Python to have a better understanding of heat exchanges (see Figure II-2) in the system (details are given in Chapter V). This model gives the produced electric power, which is the electrical performance indicator. The simulation has been conducted for one year period using an hourly typical weather file of Lyon, France (45°43'48" N, 5°4'48") (the closest site with an available weather database from enrgyplus.net/weather). Although the climate of Lyon is slightly different from the one of Le Bourget du Lac, both have temperate semi-continental climates (but Le Bourget du Lac has mountain climate influence).

A PV facade comprises several layers with their respective functions and various properties that might relatively influence the thermal behaviour, the electrical performance of the facade and the thermal comfort in the building space. In order to reduce the number of relevant thermo-physical properties to consider during the parametric studies, a preliminary thermal analysis of the facade has been performed based on the literature, considering radiation, convective and conductive heat transfers.

- **Choice of parameters related to radiation heat transfer**

Solar radiation is the main responsible for the facade heat gain and PV power production. Therefore, the optical properties of the PV modules and the external surface of the wall should be investigated for its consideration.

For the PV modules, the semi-transparency factor (the ratio of transparent surface uncovered by the PV cells to the surface of the module) is an essential parameter for their thermal and electrical performance and is more straightforward to optimise than other optical properties. In fact, the absorption, transmission and reflection coefficients are interdependent and complementary. The variation of one of these coefficients entails the variation of at least one other. Consequently, studying the optical properties of PV glasses and encapsulants would lead to considering numerous parameters. In addition, highly transparent covers on both sides of the bifacial modules would increase the incident irradiation on their cells. In this regard, the study of the semi-transparency factor alone would allow simultaneously analysing the impact of the optical properties of the modules from their two sides and on the wall. Furthermore, this parameter is reported to be a source of a trade-off between electrical and thermal performance in the literature. This parameter is analysed mostly in the range of 10% to 90% semi-transparency (Jiang et al., 2008; Saadon et al., 2016; S. Xu et al., 2014).

As for the wall, the absorptivity (which is complementary to the reflectivity) is studied. Its variation would induce considerable conflict between the need for a reflective wall to enhance the PV power output (Tina et al., 2020) and the wall cooling in summer and the need for an absorbing wall to reduce the heating load in winter. An absorption coefficient ranging from 0.84 (black paint) to 0.09 (white paint) has been studied in the work of Kim et al. (2021) for the assessment of the PV current output in the bifacial PV facade.

- **Choice of parameters related to convective heat transfer (in the air gap)**

The airflow in a naturally ventilated facade depends on the air temperature gradient, the temperature of the boundary surfaces of the gap, the effect of the wind and the geometry of the gap, i.e. its height, thickness and the characteristics of its openings. The study of the influence of geometric properties on convective heat exchange is straightforward, as the other parameters depend on the meteorological data. The air gap thickness and height are widely studied in the literature for the effectiveness of heat dissipation and regarding the importance of the vertical temperature gradient in the facade (Agathokleous & Kalogirou, 2016, 2018b). As the current study is more about a modular element of the building facade, the focus is only on the air gap thickness as a first step. Investigation of the impact of the air gap height is the most relevant in multi-story building applications (Athienitis et al., 2018).

The ranges of air gap thickness studied in the literature are large, as the air gap can be beyond 1m thick in the case of double-skin facades. Since the aim is to valorise the preheated air potentially, the analysis is undertaken on a narrow gap. For natural ventilation, the maximum thickness corresponding to that application is about 20 cm (T. Zhang & Yang, 2019).

- **Choice of parameters related to conductive heat transfer**

Increasing thermal resistance through insulation material is one of the major solutions in buildings to limit heat loss in winter and heat gain in summer. In warm conditions, a highly insulated wall might lead to high temperatures on its exterior side and influence the electrical efficiency of the PV module. For this reason, the effect of the insulation layer thickness on the electrical and thermal efficiency of a PV facade is analysed. In the literature, this effect is reported in cases where the insulation material is directly attached to the PV module. For instance, Li et al. (2019) studied the variation of insulation thickness between 0 and 50 cm, considering a thermal conductivity of 0.0263 W/m K. Their results show considerable decreases in electrical efficiency and heat gain from the facade.

Besides insulation, the study of the thermal inertia (heat capacity) of the facade is also relevant to address the parameters related to conductive heat transfer. However, as the facades are ideally implemented on tertiary buildings, immediate responses to external thermal constraints (such as protecting, rejecting, admitting and collecting) could be more relevant than the functions of heat storage and redistribution. Those latter functions are more exploited in residential buildings due to the need for temperature dephasing related to the building occupancy schedule.

Therefore, the considered parameters in the parametric and optimisation study are :

- the transparency factor ξ of the PV module, which is the ratio of the total surface uncovered by the PV cells and the surface of the PV module:

$$\xi = 1 - \frac{S_{cells}}{S_{mod}} \quad \text{(II-1)}$$

- the absorption coefficient of the front wall α_{M1},
- the depth of the air channel d,
- and the thickness of the wall insulation L_{insul}.

Table II-1 gives the reference and bound values of each of those parameters.

Table II-1: References and bound values of the selected parameters

	Low bound	High bound	Reference
ξ [-]	0	1	0.34
α_{M1}[-]	0.12	0.91	0.65
d $[m]$	0.02	0.20	0.02
L_{insul} $[m]$	0.10	0.30	0.20

II.3.2.2 Results and discussion of the parametric study

The thermal loads and PV power output determined as a function of the selected parameters are obtained from the thermal model of the PV facade described in Chapter V and our research paper (Ratovonkery et al., 2020). They are presented in Figure II-3 according to each parameter variation. Since the objective is to minimise the thermal loads and maximise the PV power output, the y-axis for the assessment of PV power output is inverted to ease the graph reading. This way, the optimal value of all indicators corresponds to the bottom of each axis.

- **Results of the transparency factor ξ investigation**

The study of the transparency factor ξ is presented in Figure II-3a. As seen from this figure, the transparency factor has a great influence on both the thermal and electrical performances of the facade. On the one hand, as expected, there is a conflicting influence of ξ on the heating and cooling loads. When the transparency factor increases, the quantity of solar radiation reaching the wall increases. Thus, the heating load decreases while the cooling load becomes more significant. With the considered bound values of ξ, 4 % decrease in the heating energy rate is observed, while the cooling energy rate rises to 15 %.

On the other hand, the increment of the transparency factor decreases the electric power produced. Since the bound values correspond to the opaque module and ordinary glazing, the power varies from zero to the maximum power yields obtained with an opaque PV module. Hence, at least for the reference value of the other parameters, the module bifaciality does not contribute to maximising the power yield since the maximum electrical output is obtained from an opaque module.

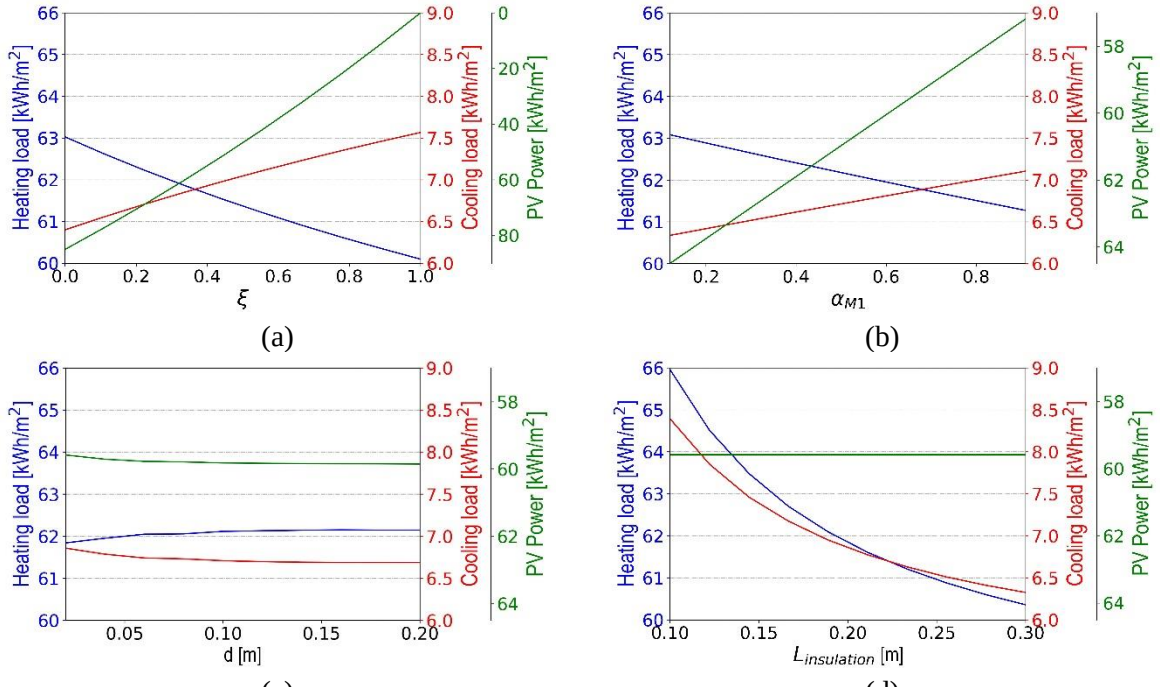

Figure II-3: Parametric studies results (a) Study of the transparency factor (b) Study of the wall absorption coefficient (c) Study of the air gap thickness (d) Study of the wall insulation thickness (Ratovonkery et al., 2020)

- **Results of the wall absorption coefficient α_{M1} investigation**

According to the results of the wall absorption coefficient analysis (α_{M1}) shown in Figure II-3b, the increment of the absorption coefficient enhances the heating performance while deteriorating the cooling performance. The variations are respectively 4% and 10% in the heating and cooling loads. Since the

module is bifacial, the rise of the absorption coefficient decreases radiation reflected by the wall. Thus the electricity produced by the module also decreases by 10 %. All energy performances vary linearly with the wall absorption coefficient. The general trends of the three curves are similar to the results of the transparency factor ξ.

- **Results of the air gap thickness d investigation**

The presence of the air gap has a cooling effect on both the wall and the PV modules. Therefore, its increment deteriorates the heating performance. The result of the air gap thickness analysis is illustrated in Figure II-3c. Compared to previously investigated parameters, the influence of the air gap variation is small. Changes in cooling and heating energy rates are just 0.3 % and 1.5 %, respectively. And the variation in PV module power is 0.2 %. The result may be linked to the performance of the thermal model used. The correlations for the approximation of convective heat transfer are limited by the gap geometry. Hence, a more detailed model might be needed to thoroughly analyse this parameter. In addition, its effect can be noticed only on the $10\ cm$ first centimetres variation of the gap thickness.

- **Results of the wall insulation thickness L_{ins} investigation**

The result of the study of the wall insulation thickness is given in Figure II-3d. The variation of insulation has the greatest influence on the thermal indicators among the studied parameters. This result confirms the thermal insulation predominance in thermal performance enhancement solutions. Variations in cooling and heating loads observed are 6 % and 17 % respectively. However, this parameter has a negligible effect on the electrical performance (PV module power varies by 0.004%). Moreover, optimising the heating and cooling performance likely converges to the same value of insulation thickness. Therefore, this parameter does not induce any conflict but should only be optimised to minimise thermal loads.

- **Partial conclusion on the parametric study**

The overall results suggest that conflict-inducing parameters on the thermal loads are the transparency factor ξ, the absorption coefficient $\alpha_{M1}$and the air gap thickness d. In effect, the transparency factor and absorption values determine the solar intake admittance from the wall. The air gap thickness determines the capacity of the air to dissipate heat. The optimal value of those parameters differs in heating and cooling seasons since the requirements also differ. Therefore, developing adaptive features in those properties can be considered. The facade functions needed for maximising power yields are likely similar to those for minimising cooling performance. However, there is also a conflict between the heating load and the PV power optimisation. However, since the contradiction is in the same climatic conditions, the adaptive feature should be developed to adjust the facade towards the best trade-off.

II.3.2.3 Limit of the parametric study

In the parametric study, varying the parameters one by one and keeping reference values of the others is an effective approach to obtaining a global insight into the influence of each parameter on the performance indicators. Nevertheless, it is hard to determine the real impact of one parameter as the reference values of the others can change, and their influence taken together can add up or offset. This issue can be overcome if the study is conducted with an adimensional model or as an optimisation problem. For this reason, multiobjective optimisation is performed on the model to confirm the parametric study result, which is discussed in the next section.

II.3.3 Parametric optimisation

II.3.3.1 Principle of the multiobjective optimisation

A multiobjective optimisation problem (MOP) consists of identifying the optimal solutions responding to at least two objectives, which are formulated as *objectives functions*. For the design purpose, those

objectives are minimising the thermal loads of building space and maximising the PV power output. The consideration of those objectives with the same importance does not lead to a unique solution. Instead, several solutions representing the essential trade-offs among the objectives are obtained. This is why this investigation aims to analyse the variation of the selected parameters throughout those optimal solutions.

Formally, a multiobjective optimisation problem (MOP) is defined as:

$$\begin{aligned} &minimize\ \mathbf{f}(\mathbf{x}) = [f_1(\mathbf{x}), f_2(\mathbf{x}), \ldots, f_k(\mathbf{x})\ ]^T \\ &subject\ to\ \mathbf{x}\ \in \chi \subseteq \mathbb{R}^n \end{aligned} \tag{II-2}$$

$\mathbf{f}(\mathbf{x})$ the objective vector is composed of k scalar *objective functions* $f_i : \mathbb{R}^n \longrightarrow \mathbb{R}\ (i = 1, \ldots, k; k \geq 2)$. The vector $\mathbf{x}$ is formed by n *decision variables*, which are the values of the selected parameters in the *feasible decision variable space* χ and included in the decision space $\mathbb{R}^n$.

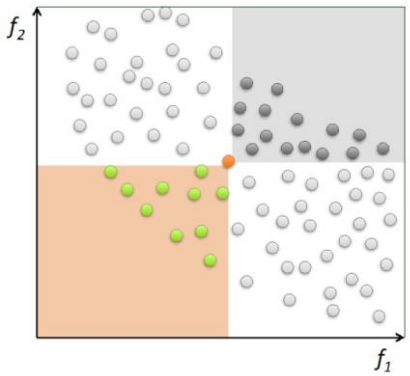

Figure II-4: Illustration of Pareto dominance relation for double objective optimisation in the objective function space – the orange point dominates the dark grey points and is dominated by the green points. (Armand Decker, 2015)

The optimal solutions are obtained by comparing the objective vectors. This process is according to the Pareto dominance relation, which suggests that an objective vector $\boldsymbol{z}^1$ Pareto-dominates another vector $\boldsymbol{z}^2$ (symbolised $\boldsymbol{z}^1 \prec_{Pareto} \boldsymbol{z}^2$), if none of the objective functions in $\boldsymbol{z}^1$ is worse than those in $\boldsymbol{z}^2$, and at least one objective function in $\boldsymbol{z}^1$ is better than the vector $\boldsymbol{z}^2$(see illustration in Figure II-4). This is formally written as

$$\forall i \in \{1, \ldots, k\}: z_i^1 \leq z_i^2\ and\ \exists j \in \{1, \ldots, k\}: z_j^1 < z_j^2 \tag{II-3}$$

Therefore, an objective vector is considered optimal if none of its objective function components can be improved without deteriorating at least one of the others. This optimality means that a decision vector $\mathbf{x}^* \in \chi$ is Pareto optimal if there does not exist another solution $\mathbf{x} \in \chi$ such that $\mathbf{f}(\mathbf{x}) \prec_{Pareto} \mathbf{f}(\mathbf{x}^*)$. Hence, $\mathbf{f}(\mathbf{x}^*)$ is a non-dominated or Pareto optimal objective vector. However, the Pareto order $\prec_{Pareto}$ is not a total order. Some objective vectors might be incomparable. Thus, there can be several Pareto optimal solutions considering the feasible variable spaces χ. The set of those solutions (decision variables) is called Pareto optimal set, and their corresponding images are a subset of non-dominated objective vectors forming the so-called Pareto Front (see Figure II-5). Hence, the output of a MOP is the non-dominated objective vectors of the Pareto front and the Pareto optimal set corresponding to the set of optimal decision variables.

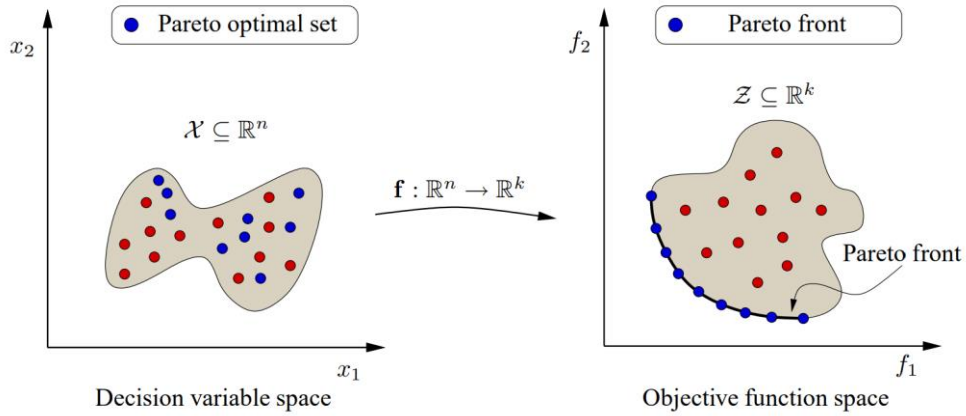

Figure II-5: Illustration of Pareto optimal set and its image the Pareto front (López Jaimes et al., 2011)

II.3.3.2 Methods available for multiobjective optimisation

Several methods exist to solve MOP problems. For a problem with a continuous decision variable, as in the case of this study, available methods can be classified into three groups: descent-order, heuristics and derivative-free optimisation algorithms.

- In the **descent order algorithm**, the objective function vector must be continuously differentiable. The principle is to find a decision variable satisfying a given criterium in the looping evaluation of the objective functions. The renewal of the decision variable is according to a descent direction which depends on the gradient of the objective function vector. The main drawback of this method is that it generates only one non-dominated solution for a given starting point.
- In the **heuristics methods**, several sets of decision variables, often called population (in Evolutionary algorithms), are evaluated from the start of the loop. The population interacts with each other through some defined parameters and renewed over the iteration through mutation and selection supposedly toward some Pareto optimal solutions. The advantages of those methods are that the objective functions do not need to be derivable. They can be applied to many kinds of problems but are more costly in time, deal badly with constraints and are difficult to scale with a large number of variables. The number of potential solutions is also limited by the population size.
- **Exact black-box and derivative-free optimisation methods** are very similar to heuristics. They also start with a population of points and update them towards iterations. However, it does not make any restrictions on the size of the population and convergence analysis is deterministic. Those methods are efficient but less dominant than the heuristic methods regarding available algorithms (Salomon, 2021).

Given the fact that many available algorithm tools deal with heuristic optimisation, a genetic algorithm NGA 2, an evolutionary algorithm, is selected to solve the problem. For this, the problem was solved using the Python package Deap, which contains several useful predefined functions for the programming of the algorithm.

II.3.3.3 Results and discussion of the multiobjective study

Using the thermal model described in Chapter V and in the paper (Ratovonkery et al., 2020) ,the resolution of the MOP enable to identify a Pareto Front with 37 non-dominated solutions (see. Figure II-6a). The analysis of those solutions is presented in Figure II-6b, where the histogram bars represent non-dominated solutions, the optimised thermal load and the PV power output. The y-axis for the PV

power output variation is also inverted as in the parametric study. The graph lines represent the variation of each optimised parameter in respect of their bound values.

As in the parametric study, the transparency factor ξ of the PV module has an important influence on the non-dominated solution. Its value varies from the lower to upper bound from one solution to another.

In the lower value of the transparency factor, the absorption coefficient α_{M1} seems to vary significantly (from 0.57 to 0.9). This is probably because, in that range, the PV module is almost opaque. Hence, the model is no longer sensitive to the variation of the absorptivity, leading to the instability of the solution. The study of wall absorption is relevant if the module is transparent enough. Therefore, by observing the absorptivity variation for the transparency factor above 30%, a variation from 0.77 to 0.9 is obtained. Against the minimal value, this variation is about 17%. Those obtained optimal values correspond to a wall with a high absorption property. This indicates the predominance of the heating load requirement in the thermal load given the selected climate (region).

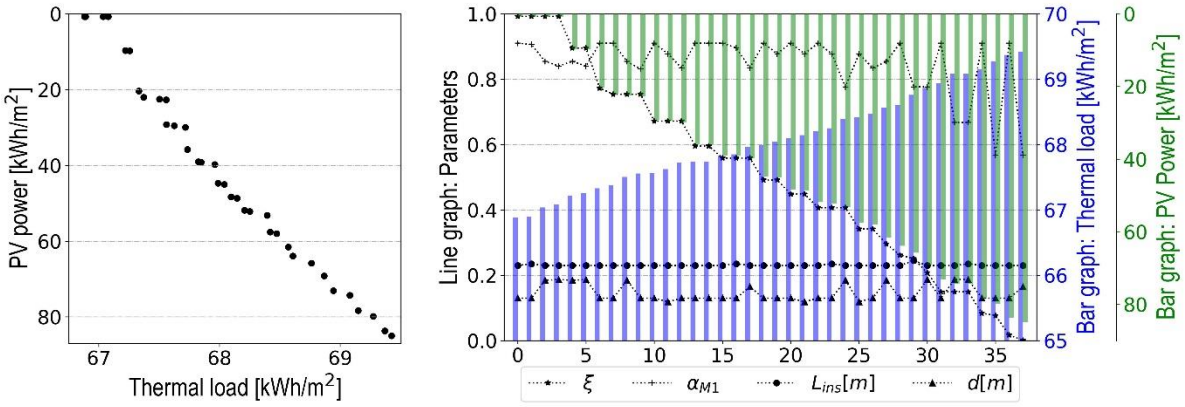

(a) (b)

Figure II-6: Results of the optimisation study (a) Pareto Front (b) Non-dominated solutions analysis according to each parameter (Ratovonkery et al., 2020)

The transparency factor variation curve has a staircase trend. Each step is characterised by different values of wall absorptivity and air gap thickness d. This might be because the thermal load is an add-up of heating and cooling loads and showcases the compensating effect of the two parameters. The air gap thickness varies significantly from 11 cm to 18 cm, corresponding to a 57% variation, taking the minimal value as a reference.

Lastly, it can be seen that the optimised values of insulation thickness L_{ins} are almost constant throughout the solutions. They are between 23 cm to 24.5 cm. This result confirms the result of the parametric study deducing that this parameter does not need to be adaptative but just optimised to improve the thermal efficiency.

II.3.4 Conclusions

The parametric study results and the multiobjective optimisation both show that the most influential and conflict-inducing parameters on both thermal and electrical performances are the transparency factor of the module, the thermal absorption coefficient of the wall and the air gap thickness. Those parameters are linked to radiative and convective heat transfer in the air gap. Thus, the biological search should focus on strategies related firstly to solar heat intake regulation and, secondly, to the dissipation, the harvest of thermal power and the modulation of convective heat transfer through air circulation. The design challenge is also to establish the best compromise between thermal and electrical performance in winter, given their contradictory requirements and the control of the air circulation to provide both cooling and heat recovery.

II.4 Search - analysis and application of biological strategies

Various biological strategies that might respond to the problems were explored to provide the targeted functions of the facade. However, this section presents only the strategies analysed to design the facade. Those are the adaptations in the skin blood vessels, in cactus and plant movements, which can be used as a bridging mechanism between two opposing functions.

II.4.1 Adaptation strategy in human skin: Blood Vessel

The skin is the interface between the body and the surrounding environments and has a major role in body temperature regulation. Since blood flows all over the body cells to deliver oxygen and nutrients, its circulation also distributes heat and contributes to thermoregulation (Arens & Zhang, 2006). Blood vessels at the skin level exhibit the first level of adaptations to heat constraint and can be a source of inspiration for building envelopes with fluid circulation.

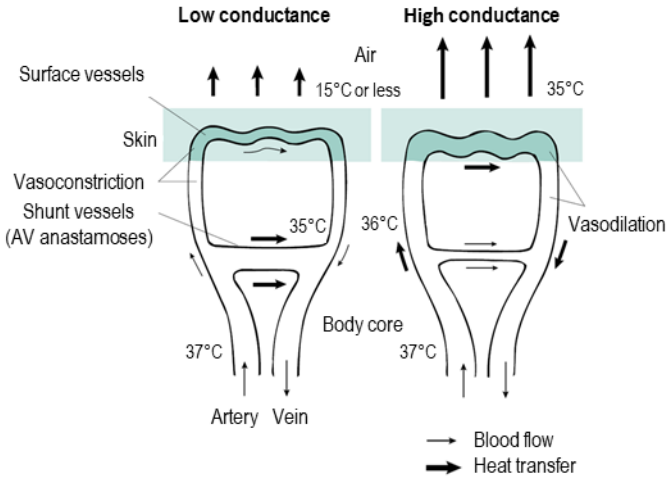

Figure II-7: Illustration of Vasoconstriction and vasodilation mechanisms (Willmer et al., 2005)

The core temperatures of the human body should be maintained at approximately 37°C with a fluctuation of 0.5 to -1°C (Kellogg, 2012). In a neutral environment (environment temperature within the comfort range), the skin blood flow is about 250 ml/min. When the body is exposed to cold stress, it is reduced to retain heat through a mechanism called vasoconstriction. In this circumstance, the inner diameters of blood vessels are also reduced. In contrast, the blood vessels dilate, and the flow increases under heat stress through a mechanism called vasodilation. This latter is usually accompanied by sweating for evaporative cooling. For highly exposed areas such as the hand, fingers, feet and ears, there are blood vessels called arterio-venous anastomoses (shunt vessels) that enhance the regulation mechanisms. They enable blood to shunt either into superficial vessels (capillaries) to dissipate heat or to the deeper vessels (directly from the arterioles to the venules) to retain heat (see Figure II-7). The flow rate at peripheral skin blood vessels can range from almost zero to 8 l/min, respectively to severe cold and heat constraints (Arens & Zhang, 2006; Charkoudian, 2010; Willmer et al., 2005).

Skin temperature and internal temperature perceived by sensory nerves triggered the mechanisms of vasodilatation and vasoconstriction. Those sensory inputs are transmitted to the central nervous system, which activates the nerves responsible for the adaptation mechanisms (Kellogg, 2012). If vasoconstriction is triggered at the set point of 37°C, sweating and vasodilation are already activated at 0.2°C above. Additional mechanisms occur with the increasing heat stress, like shivering and behavioural adaptations (Arens & Zhang, 2006).

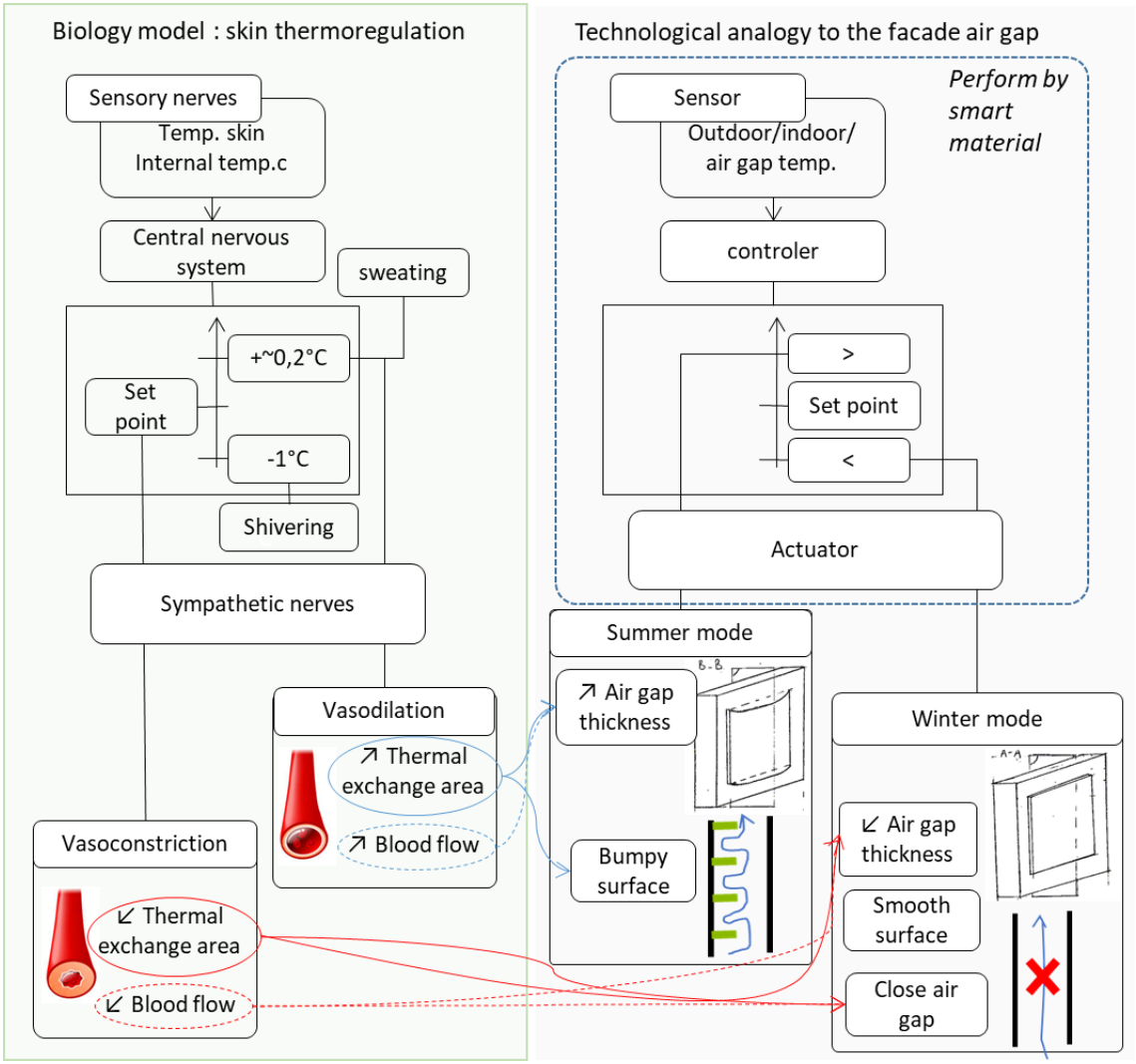

Figure II-8: Schematic analogy of the skin thermoregulation and the strategy application in the facade air gap

An analogy with the blood vessel adaptation and air circulation in a ventilated PV facade is established by considering the blood and the air as media of heat regulation. Two interesting principles that are achieved simultaneously in a biological organism are extracted. The first one is thermoregulation through the modulation of blood flow rate. It can be applied, for example, with controlled airflow in a mechanically ventilated PV facade or operation of air gap opening and closing (which is largely exploited in double skin facades). The second is the modulation of the surface of the exchange, which can be achieved in a facade with different manners:

- A mechanised system allowing the expansion of the air gap thickness;
- Application of dynamic irregularities in the air gap surface layers such as folding or curling ribs and fins. The idea is to have a smooth surface for heat loss reduction purposes and additional extended surfaces for heat dissipation (see Figure II-8).

The use of kinetic adaptation can be then involved, especially in the application of the second principle, which in the facade is targeted to be achieved with smart materials.

II.4.2 Adaptation strategy in cacti

Technical solutions for optimising radiative heat transfer related to solar protection can be achieved by getting inspired by organisms living in a hot climate with high insolation. Desert cacti have several adaptation strategies to withstand extreme heat stress. Their surrounding air and ground temperatures can exceed respectively 45°C and 70°C (Franco & Nobel, 1989). Protection from solar irradiance is crucial in this kind of environment. In fact, shortwave radiation is reported as the most important environmental variable affecting their maximum temperatures. 70% reduction in shortwave radiation by shading can lower the stem surface temperature by 17°C in dwarf cacti of 2 cm diameter (Nobel et al., 1986).

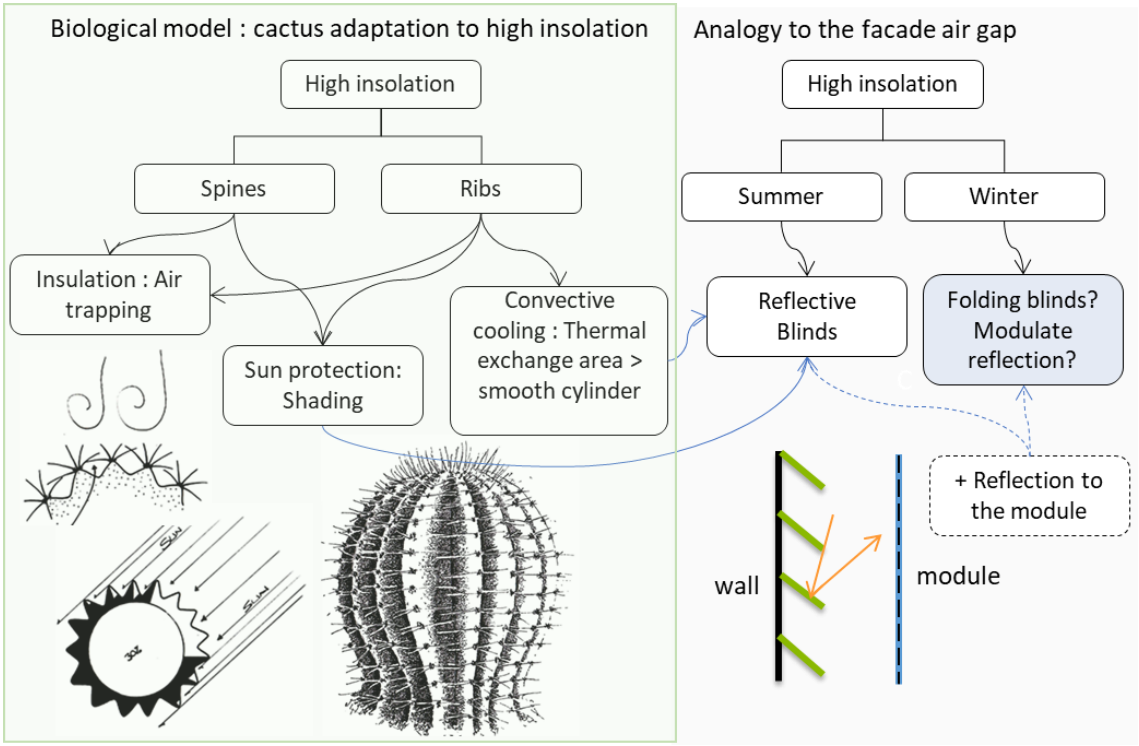

Figure II-9: Schematic analogy of cactus adaptation to high radiation and the strategy application in the facade wall – cactus images source: boucingideas.wordpress.com

The presence of spines and ribs provides self-shading in barrel and columnar cacti (Drezner, 2011, 2017; Lewis & Nobel, 1977; Nobel, 1978). In detail, those cacti have accordion-like ridges and furrows with spines present on the top of the ribs. The spines intercept solar radiation coming to the stem and can lead to 60% shading in densely covered Mammillaria cacti. Their removal in this kind of cactus can increase the maximal average temperature by 3 to 6°C.

Parallel ribs on the stem also affect the self-shading. Closely spaced and deep ribs reduce exposure to direct sunlight (Nobel, 1980). Therefore, morphology adjustment towards solar availability is observed along the circumference of the plants. Ribs are closely spaced on the south-facing side (Drezner, 2017). Nonetheless, reported temperature reductions from the ribs are mostly related to convective heat transfer. Per unit area, this coefficient is estimated to be 44% greater than on a smooth surface due to inducing turbulence from the irregular pattern. Moreover, they increase the area of convective heat exchange leading to higher heat dissipation. Nonetheless, the air-trapping effect can reduce local heat convection in the deep furrows and under the spine.

The principles extracted from the presented strategies are the effectiveness of self-shading for solar protection. Shading elements can contribute to an increase in surface exchange for better heat

dissipation. The application joins the previously presented idea by using wall surface irregularities (ribs, fins, blinds) to control shortwave radiative heat transfer in the air gap. The illustration of the analogy between the biological strategy and the technical problem is given in Figure II-9.

II.4.3 Strategies for generating flexible motion

As plants move without muscles, their motion strategies are relevant for designing lowly mechanised systems. An overview of their movements is undertaken to develop the motion of extended surfaces in the air gap. In plants, tropic movements result from directional stimuli such as light and gravity, and nastic movements result from non-directional triggers such as temperature, humidity and touch. Those motions are for several reasons, such as optimisation of photosynthesis, growth, prey trapping and dispersal of seeds. Despite the diversity of purposes, three general mechanisms are found to generate folding, bending and clapping motions:

- **Growth-related movement**:
  - In phototropic plants induced by unidirectional light, the privileged flow of auxin (responsible for plant growth) toward the shaded part results in the plant bending toward the light direction;
  - Some organs like leaves, petals and sepals have different cell structures between the upper side (adaxial) and lower side (abaxial). This results in unequal growth and leads to bending or closing movement depending on the plant (see Figure II-10a).

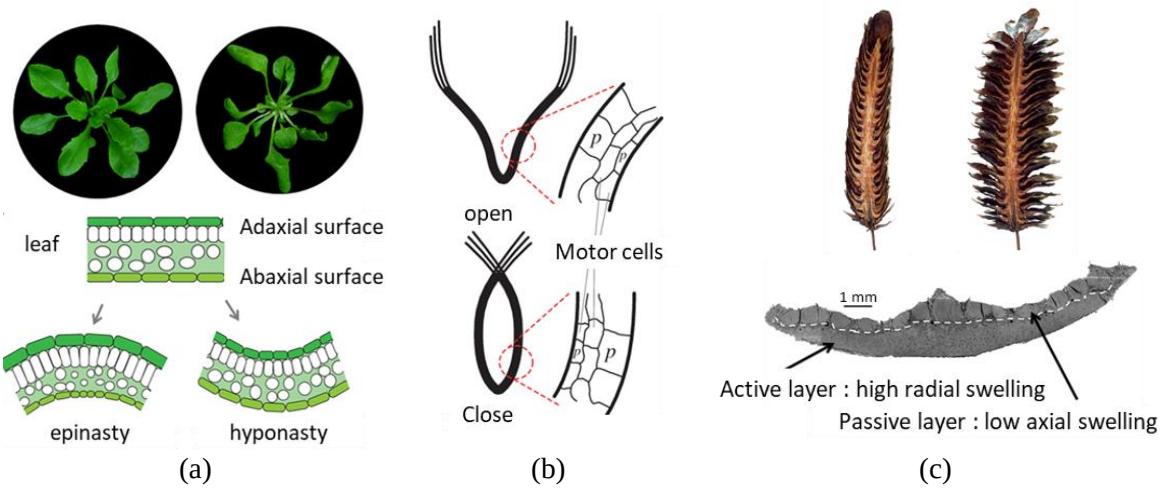

Figure II-10: Illustration of bending principle in plants (a) Growth-related movement according to differential cell structure in leaf (Romero-Puertas et al., 2011) *(a) Turgor-mediated movement in venus flytrap(Li & Wang, 2015) (c) Motion in response to moisture fluctuation from differential cell structure* (Duigou & Castro, 2016; Reichert et al., 2015)

- **Turgor-mediated movements** (exploited in Venus flytrap) result from the change in turgor or hydrostatic pressure in plant cells. In this category, the motor organs often have two regions which exchange turgor. A loss of turgor in the upper part of the motor organ leads to a gain of turgor in the lower part and a bending toward the upper part (see Figure II-10b).

- **Differential properties in layering tissues**:
  The two previous movements are related to living plants and their metabolism. For seed dispersal, some movements are solely from structural differences in tissue layers, which induces a differential moisture response on the inner and outer fibres. For example, in a mature pinecone, the outer layers shrink in a dry environment, enabling the cone to expand and deliver its seeds. When the humidity rises, the fibre swells, resulting in closing movement. The reversible movement continues in a cycle with moisture fluctuation (Reichert et al., 2015; Sisodia & Bhatla, 2018) (see Figure II-10c).

Differential expansion or contraction from tissue layers is identified as a major plant movement driver. The trigger and motor of the movement are diverse. However, the principle is similar to that in bilayer materials. Thus, from this analysis and regarding the stimuli identified in the previous analogies (temperature and irradiance), thermosensitive bilayers can be used to perform the movement in the facade concept. Thermosensitive bilayers exhibit bending movement because of differential thermal expansion of their constituting layers.

II.5 Presentation of the adaptive PV facade concept

The exploration and analysis of biological strategies show the need for:

- modulation of the airflow and area for thermal exchange to adjust convective heat transfer in the air gap, as in the skin blood vessels and the presence of ribs and furrows on cacti stems;
- shading of the building wall to limit heat gain under heat stress, as in cacti plants;
- flexible motions to change the geometry as in several types of plants according to bilayer principles and to adjust the facade function.

From those strategies, the final solution retained has the same configuration as the ordinary BIPV facade but with bilayer components mounted on the external side of the multilayer wall and the possibility of closing and opening the facade air gap. The purposes are to modulate thermal exchange surface and shading from the use of the bilayers and to modulate the airflow from the control of the air gap opening. Details of the facade principles are presented in the following subsections according to the modulated heat transfer. The illustration of the concept depicting all the operation modes of the facade is given in Figure II-11.

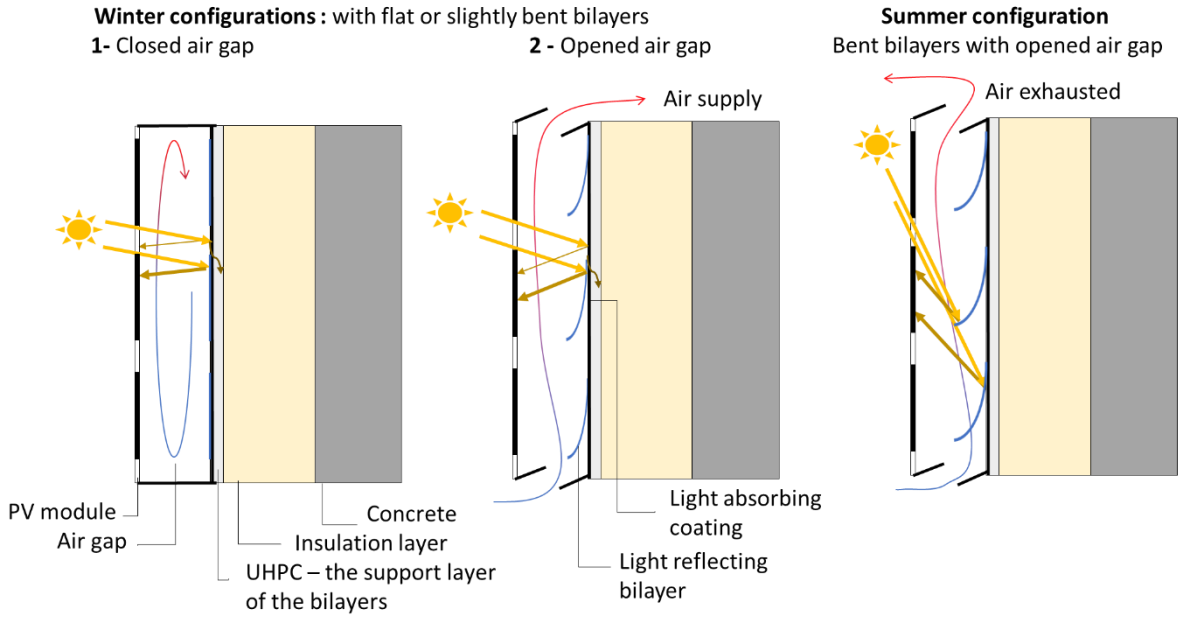

Figure II-11: Scheme of the bioinspired adaptive PV facade concept detailing operation modes in winter and summer

II.5.1 Adaptive functions related to the convective heat exchange

For convective heat transfer, the principle is to have smooth air gap surfaces in winter by applying bilayers with a flat configuration at low temperatures. Since the requirement of heat dissipation increases with the irradiance and outdoor air temperature, a gradual increase in surface exchange is achieved in parallel with the progressive deformation of the bilayers with their respective temperature. The bending is also targeted to provide airflow turbulence to enhance convection between the air, the back surface of

the module and the wall surface. Thus, those functionalities are the application of the increase of thermal exchange area from vasodilation in blood vessels and from the ribs of cacti. They are targeted for PV modules and wall cooling in summer.

During the cold period (winter), various operations of the air circulation can be considered. Closing the air gap to use the air as a thermal buffer provides heat retention and is privileged in a cloudy period. This operation can also be considered in a sunny period, assuming that the greenhouse effect allows solar heat gain to be accumulated and a part of this heat gain to be transmitted to the building space (despite the wall insulation). However, opening the air gap and valorising preheated air for space heating can also be considered in the sunny period.

The deformation of the bilayers toward the passive slats normally occurs when their temperature is below the reference temperature. However, they are assumed to remain flat as the wall blocks the bilayers from deforming in this direction.

II.5.2 Adaptive function related to radiative heat exchange

The cyclic movement of the bilayers with their temperature fluctuations is exploited to shade the wall in summer. However, to absorb a part of solar radiation in winter, the bilayers should be flat and positioned only behind the PV cells. They have the same length as the PV cells. The idea is to allow the absorption of the solar irradiance transmitted through module transparency to the part of the wall that is not covered by the bilayers. In contrast, this uncovered part of the wall is shaded in summer since the bilayers are bent. Nonetheless, this strategy is possible only for a facade oriented to the south, with bilayers bending around the horizontal axis and low and high solar elevations, respectively, in winter and summer.

The presented strategies are mostly related to the management of thermal performance. For the module power output enhancement, reflective bilayers are used to increase incident solar radiation on the back surface of the bifacial module. From this perspective, the difference from a uniformly reflective wall is that:

- A compromise between heat absorption and irradiance reflection is achieved in winter by privileging the heating needs. The uncovered part of the wall still harvests solar irradiance. Even if incident irradiance on the bilayers is likely small because the sun is low, this part is reflected in the module.
- The bilayers reflect solar radiation to the back surface of the module in winter while ensuring solar protection on the wall in summer.

Therefore, the absorptive wall and reflective bilayers provide adaptive thermal functions in the opposite seasons and a viable trade-off between thermal and electrical performances in winter.

II.6 Preliminary feasibility study and preliminary sizing of bilayer components

II.6.1 Potential temperature reduction and PV power output gain from the summer operation

The main feature differencing the developed concept from an ordinary PV facade is the bilayer operations exploited in summer. Those operations are heat dissipation through the increase of the heat exchange surface, solar protection through deflection of the bilayers and their reflective properties and PV power output optimisation through the solar flux reflection. The impact of those operations should be assessed to check the feasibility and the potential of the concept. Thus, a parametric study on the

numerical model of the optimised facade is developed to check that the bilayers effectively reduce the wall temperature in summer and enhance PV power production. The facade model is developed by considering the bilayers as (see Figure II-2):

- Extended rectangular fins for the convection and conduction heat transfer modelling;
- Diaphragms for the determination of the air mass flow rate;
- Diffuse flat Venetian blinds for the modelling of shortwave radiative heat transfer.

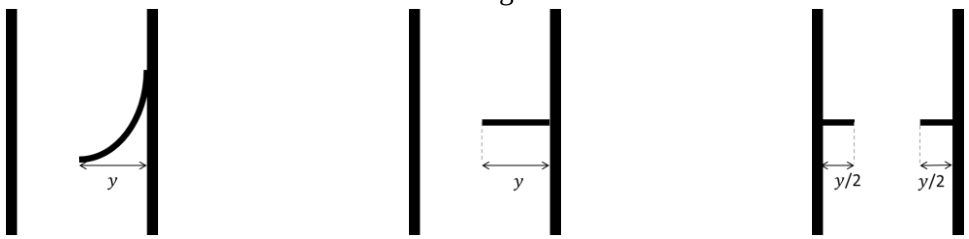

Figure II-12: Simplification of the modelling of the bilayers from the modification in the convective heat transfer and airflow calculation (a) Real configuration of a deformed bilayer in the air gap (b) Approximation of the bilayers as rectangular fins with a characteristic length y (the deflection) (c) Approximation for the calculation of the pressure drops as diaphragms narrowing the thickness of the air gap by a distance equal to the deflection y.

More details on the modelling are presented in Chapter V. The simulations are realised with the typical climate of Lyon as in the parametric study considering the three summer months (from June 21st to September 21st). The same PV facade as in the parametric study is considered, but an airgap thickness of 10 cm and a PV module semi-transparency of 30% (transparency factor in which the effect of the wall absorptivity becomes more relevant) are considered.

II.6.1.1 Heat dissipation potential through the increase of exchange surface

Since the first investigation focuses on heat dissipation through convection, the bilayers are considered to have the same absorption coefficient as the wall (which $\alpha_b = 0.65$). According to the concept, they are positioned behind the PV cells and have the same length as the PV cells (which is assumed to be approximately 15.5 cm). Their deflection is fixed and varied from 0 to 9 cm. The value zero (0) corresponds to the ordinary PV wall without bilayers. The thermal conductivity of the bilayers is varied from 0.035 W/mK corresponding to an insulating material, 2.32 W/mK equal to the thermal conductivity of the UHPC on the external layer of multilayer wall, and 23.2 and 232 W/mK for hyper conductive layers.

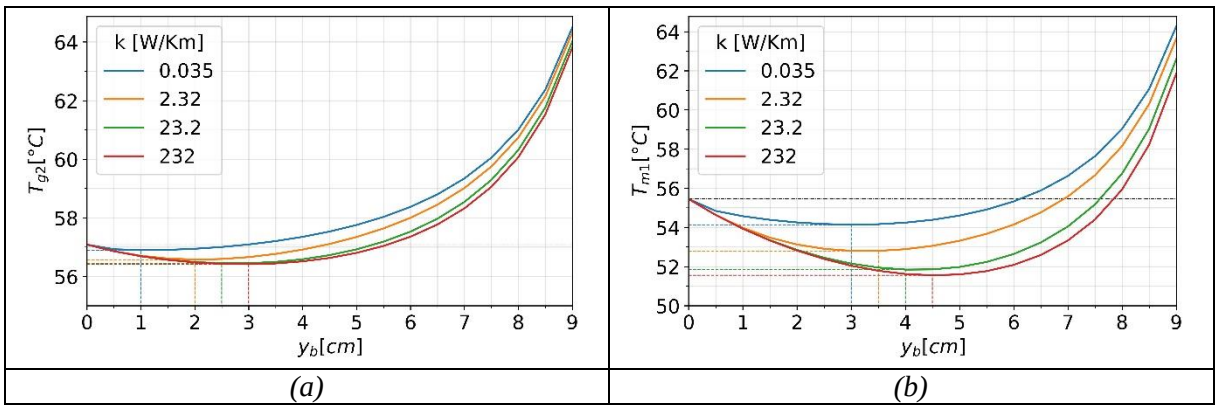

Figure II-13: The maximum temperature reached on the back surface of the module (a) and the external surface of the wall (b) during the summer period according to the variation of the bilayer deflection

The maximum temperatures reached on the wall and the PV module according to the variation of the deflection and the thermal conductivity of the bilayers are presented in Figure II-13. The results show that there are optimum values of deflections leading to the maximum temperature reduction on each surface. Those optimum values correspond to a given temperature difference ΔT_b in the bilayers, which

is the temperature difference between the final and initial state of the bilayers. Above these values, the surface temperature rises and becomes higher than that of the ordinary wall from a certain threshold. The convex trend of the temperature curves indicates that a balance is required between the capacity of bilayers to act as an extended surface to dissipate heat and the pressure loss induced by their deflection (which reduces the airflow rate).

Table II-2: Estimation of the specific deflection δy_b to reach the optimum deflection considering thermally conductive bilayers, the maximum temperature difference ΔT_b and the optimum deflection y_{opt}

	PV module temperature			Wall		
$k_b\ [w/mK]$	2.32	23.2	232	2.32	23.2	232
ΔT_b [°C]	33.13	32.45	32.04	32.80	31.85	31.55
$y_{opt}\ [cm]$	2	2.5	3	3.5	4	4.5
$\delta y\ [mm/°C]$	0.60	0.77	0.94	1.07	1.25	1.43

For the same deflection value, the temperature reductions on the wall and PV modules increase with the thermal conductivity of the bilayers. In addition, the optimum deflection y_{opt} for a given bilayer also increases with its conductivity and is inferior on the PV module compared to the wall. Nonetheless, at the optimum deflection for the wall, the PV module temperature remains under the threshold except for the bilayers made of insulation material. The temperature reduction on the PV module is not significant. It is just 0.70°C for the most efficient bilayers (with the thermal conductivity $k_b = 232\ W/m^2$). On the wall, the maximum temperature reduction from heat dissipation is 3.90°C. The bilayers are then proven to reduce the facade temperature if they are thermally conductive. If the bilayers deflection is linear to the temperature difference, the specific deflection δy (the deflection for a temperature variation of 1°C) required should be between 0.60 mm/°C to 1.43 mm/°C to reach the optimum deflection, for a thermal conductivity between 2.32 W/mK and 232 W/mK (see Table II-2). Those values are obtained assuming the bilayers are flat at 20°C.

II.6.1.2 Effect of bilayer reflectivity for the wall solar protection and PV power output

In the second investigation, the capacity of the bilayers for solar protection and enhancement of the produced electricity is investigated. For this, the reflectivity of the bilayers is varied from 0.05 to 0.75, considering they have the same conductivity as the UHPC panel (2.32 W/mK). The range of their specific deflection δy_b (adapted for this conductivity) is from 0.6 mm/°C to ~1.0 mm/°C.

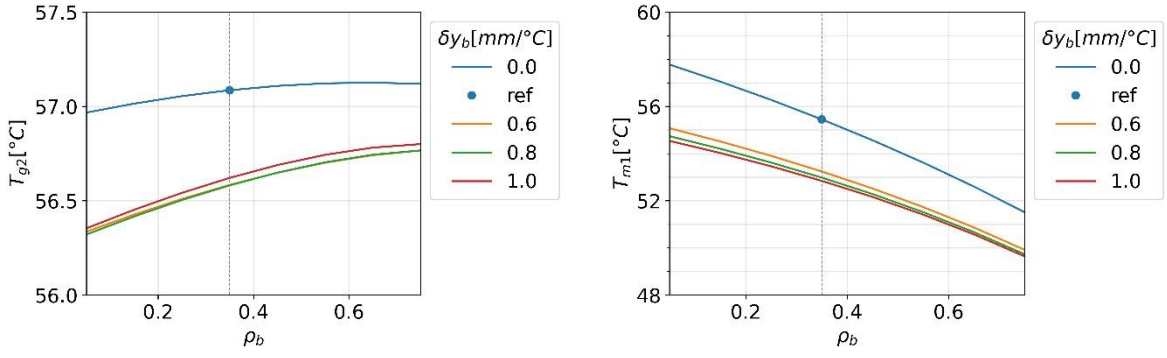

(a) *(b)*

Figure II-14: The maximum temperature reached on the back surface of the module (a) and the external surface of the wall (b) during the summer period according to the variation of the reflection coefficient ρ_b and the specific deflection δy_b of the bilayers

The maximum temperature reached on the back surface of the PV module and the external surface of the wall according to the variation of those parameters are given in Figure II-14. The temperature of the

PV module increases with the increase of the reflectivity as more incident solar radiation is reflected on the module. As for the wall, the reflective property of bilayers reduces its temperature. The difference between the wall temperature with flat bilayers or without bilayers ($\delta y_b = 0\ mm/°C$) and with bent bilayers ($\delta y_b > 0\ mm/°C$) decreases with the rise of the reflectivity. In effect, the heat dissipation effect from the bilayers is dominated by the effect of the radiation reflection. Nonetheless, the bending of the bilayers leads to lower PV module and wall temperature than a reflective wall with flat bilayers or without bilayers. There are no substantial differences in the results from the bilayers of different specific deflections both for the PV module and the wall, especially at a high reflection coefficient. Compared to the reference wall with a reflectivity of 0.35 (an absorptivity of 0.65), the temperature reduction from the reflective bilayers of 0.75 of reflectivity and 1.0 mm/°C of specific deflection is negligible on the PV module (0.29°C) and is about 5.8°C on the wall. The bilayers effectively constitute solar protection for the wall.

The maximum PV power reached according to the reflectivity of the bilayers and their specific deflection is plotted in Figure II-15. For the same reflectivity of the bilayers and the wall, the potential of the bilayers to increase the power output is more perceptible at lower reflection due heat dissipation effect. Nonetheless, the bent bilayers have relatively the same power output as the flat bilayers at a high reflectivity. Thus, the bent bilayers would act as an ordinary reflective wall in terms of PV power production for the bifacial PV module. However, it has a higher potential of dissipating the wall heat. Compared to the reference wall with a reflectivity of 0.35 (or absorptivity of 0.65), a gain of about 7% is obtained in the power output.

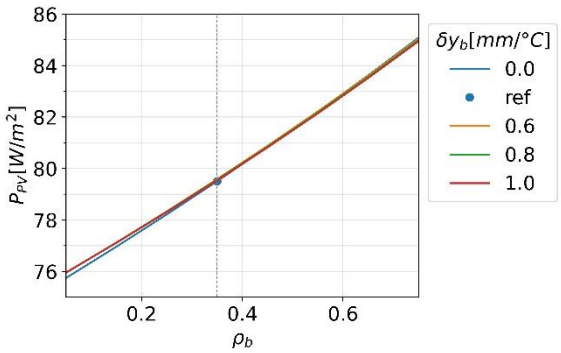

Figure II-15: The maximum PV power output reached during the summer period according to the variation of the reflection coefficient ρ_b and the specific deflection of the bilayers δy_b

II.6.1.3 Conclusion and the bilayers selection criteria

The results indicate a promising potential for the facade concept to effectively reduce thermal loads and increase PV power output compared to ordinary PV walls. The developed innovative facade operations in summer are feasible. This preliminary study indicates that the bilayers should be:

- thermally conductive to promote heat dissipation in their deformed state;
- have a significant difference in thermal expansion to obtain a specific deflection between 0.6 mm/°C and 1.43 mm/°C considering a length of 15.5 cm and a reference temperature of 20°C at flat state;
- and as they are exposed to solar radiation, their material should withstand visible and UV radiation.

II.6.2 Selection of the appropriate bilayers

II.6.2.1 Calculation of the bilayer deformation

To select the bilayers according to the capacity to deflect, several models exist in the literature for deflection calculation. The Timoshenko analytical model is used in this study (Timoshenko, 1925). It is given in equation (II-4) for a bilayer fixed at one end and free at the other end (see Figure II-16).

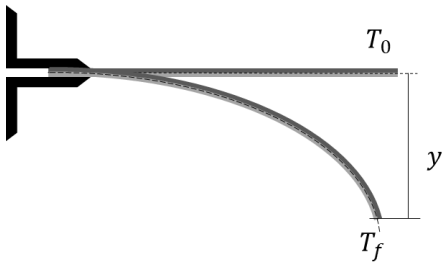

Figure II-16: Illustration of deflection of a bilayer fixed at one end and free at the other end

$$y = \frac{\kappa L^2}{2} \tag{II-4}$$

With L the length of the bilayer and κ its curvature is given by :

$$\kappa = \frac{6(1+m)^2}{3(1+m)^2 + (1+mn)(m^2 + \frac{1}{mn})} \frac{(\alpha_2 - \alpha_1)(T - T_0)}{H_1 + H_2} \tag{II-5}$$

Considering that the bilayer is flat at the reference temperature T_0 and bent at the temperature T. α_1 and α_2 are respectively the thermal expansion coefficients of the passive and the active slats. H_1 and H_2 are the thicknesses of the passive and active slats, their value should be optimised according to the ratio in the thickness $m = H_1/H_2$ and the ratio of the Young modulus $n = E_1/E_2$. In effect, there are pairs of m and n that provide the maximum curvature for a bilayer of total thickness H to the below expression:

$$\kappa = \frac{3}{2} \frac{(\alpha_2 - \alpha_1)(T - T_0)}{H} \tag{II-6}$$

II.6.2.2 Calculation of the effective thermal conductivity

An effective thermal conductivity should be determined to select the bilayers according to the thermal properties. For this, the effective thermal conductivity in series and parallel are considered.

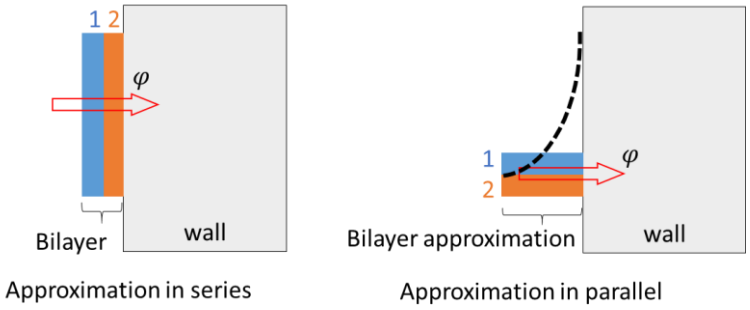

Figure II-17: Illustration of the approximation of the effective thermal conductivity of the bilayers according to the direction of the heat flow φ in the wall – Approximation in series for flat bilayer and approximation in parallel for deformed bilayer assumed as rectangular fin

The effective thermal conductivity in series represents the lower bound of their possible thermal conductivity value. It also represents the bilayer properties in their flat state, considering the heat flux direction in the wall. The effective thermal conductivity in parallel represents the higher bound of their

possible thermal conductivity value. It is representative of the bilayer properties in their deformed state in respect of the heat flux and the approximation of the bilayers as extended rectangular fins (see Figure II-17).

$$k_{series} = \frac{e_1 + e_2}{\frac{e_1}{k_1} + \frac{e_2}{k_2}} \quad \text{(II-7)}$$

$$k_{parallel} = \left(\frac{1}{e_1 + e_2}\right)(e_1 k_1 + e_2 k_2) \quad \text{(II-8)}$$

The expression for the approximation of thermal conductivity in series is given in Equation (II-7), and the approximation in parallel is in Equation (II-8). In those equations, e_i is the thickness of the slat i and k the thermal conductivity.

II.6.2.3 Selection of the materials composing the bilayers

Considering the criteria of thermal expansion, thermal conductivity and resistance to solar radiation, four materials made of polymer and metal alloy are selected to potentially form the bilayers from their pairing. They are Aluminium, Invar, Polymethyl methacrylate (PMMA, commercially known as Plexiglas) and Polytetrafluoroethylene (PFTE, commercially known as Teflon) (see Table II-3 for their physical properties). The ease of handling and manufacturing, polymers of 1 mm thick and metal alloys of 0.25 mm thick are considered to obtain enough deflection and take into account available materials thicknesses.

Table II-3: Physical properties of the selected material

Material	Thermal expansion $[10^{-6}/°C]$	Young modulus $[GPa]$	Thermal conductivity $[W/mK]$
Aluminium	23.5	70.6 – 75.6	237
Invar	1.7-2	140 – 150	13
PMMA	70 – 77	2.4 – 3.3	0.19
PTFE	100 – 160	0.3 – 0.8	0.24

The specific deflection of 15.5 cm length bilayers and their equivalent thermal conductivity are calculated to evaluate all the possible pairs from the selected materials. The results are presented in intervals to consider all possible values regarding the range of material properties for the deflection calculation. For the effective thermal conductivity, the lower bound corresponds to the approximation in series, and the higher bound is the approximation in parallel (see Table II-4).

Table II-4: Specific deflection δy_b and effective thermal conductivity k_b in series and parallel of the selected bilayers

	Slat 1 / Salt 2	Aluminium	Invar	PMMA	PTFE	
	Aluminium		24.65 – 125	0.24 – 47.55	0.30 – 47.60	k_b $[W/mK]$
δy_b [mm/°C]	Invar	0.75 – 0.76		0.24 – 2.75	0.30 – 2.80	
	PMMA	0.66 – 0.77	0.90 – 1.04		0.21 – 0.22	
	PTFE	0.71 – 1.71	0.65 – 1.65	0.13 – 0.75		

Considering the criteria of thermal conductivity and deflection capacity (ideally between 0.6 mm/°C and 1.43 mm/°C), Table II-4 shows that the pairs Aluminium-Invar, Aluminium-PMMA and Invar-PMMA can potentially be adapted for the application presented in this work. The pair Aluminium-Invar is a

good candidate regarding those criteria. However, its thickness is very thin (0.5 mm), making it more delicate to handle in manufacturing and mounting on the wall (for not to fold the resulting bilayer). The pairs metal-polymers (Aluminium-PMMA, Invar-PMMA, Aluminium-PTFE, Invar-PTFE) have a low thermal conductivity in their lower bound. However, this characteristic can be interesting since it is applied when the bilayers are flat or at low temperatures. Thus, low thermal conductivity can contribute to the insulation of the wall. The pair PMMA-PTFE is discarded because of its low thermal conductivity and its low value of specific deflection at its lower bound. The bilayers with metal-PTFE are discarded because the higher bound of possible deflection is very high and might potentially induce the opposing desired effect. Moreover, PTFE has a very low surface tension, which may hinder bilayer manufacturing if bonding is chosen as a manufacturing option. Therefore, the bilayers Aluminium-PMMA and Invar-PMMA are selected for further experimental validation of the concept and more detailed numerical studies, which are presented in the next chapters.

II.7 Conclusions

This chapter presented the development of the bioinspired PV facade concept from the definition of the technical problem to a preliminary numerical study for the confirmation of the feasibility of the concept and the selection of the materials. Convective and radiative heat transfer modulation is identified as a pathway to develop adaptive features in the ordinary PV facade. Adaptive biological strategies linked to those types of heat transfer are explored. Three main strategies are retained: the modulation of thermal exchange area, modulation of airflow in the facade air gap, and solar protection through shading and reflective properties of the wall. Thermosensitive bilayers bending with the rise of temperature are applied on the wall surface to implement those strategies.

The developed concept takes advantage of the reversible deformation of the bilayers and mainly differs from ordinary PV facades when the bilayers are deformed at high temperatures. Thus, the feasibility study is conducted on the facade configuration in summer. The results indicate a promising potential of the design to reduce the wall temperature and increase the PV module power output. This is with the condition that the implemented bilayers are thermally conductive and have optimised deflection capacity between 0.6 mm/°C to 1.43 mm/°C for an air gap of 10 cm thick and bilayer length of 15.5 cm. Bilayers made Aluminium-PMMA and Invar-PMMA respect those conditions and are selected for further investigation. Hence, the following chapters consist of the experimental study for the characterisation of the deflection properties of those bilayers to validate their adequacy for further prototyping.

Chapter III. Characterisation and sizing of the thermosensitive bilayers

III.1 Introduction

Reflective thermosensitive bilayers are applied on the external wall of the BIPV facade in this work to manage the thermal behaviour of the wall and optimize the electrical performance of the PV modules. The previous chapter has proven the potential of the design and allowed the selection of two bilayer candidates made of Aluminium-PMMA and Invar-PMMA. However, that preliminary study is conducted considering the bilayers are assembled without any bonding material and with uniform heating and temperature for their deflection calculation with an analytical model. Hence, it is necessary to understand how and to which extent those bilayers deform, considering their manufacturing process and the temperature conditions to which they are subjected.

For this, this chapter presents an experimental measurement of the bilayer deflection in order to:

- Choose the assembly method of the bilayers;
- Validate and observe their behaviour in real operating conditions;
- Determine the equation of their deflection as a function of the applied temperature variation $y = f(\Delta T = T - T_0)$. The obtained equation would be exploited to study the effect of their heating method and the influence of their geometry. It also allows the approximation of their deflection in further numerical study or experimentation for the facade prototyping without using displacement or strain measuring devices like strain gauges.
- Select suitable bilayers for the application.

III.2 Methodology of deflection determination

The deflection of the bilayers was measured considering that one of their ends is fixed and the other free (see Figure III-1).

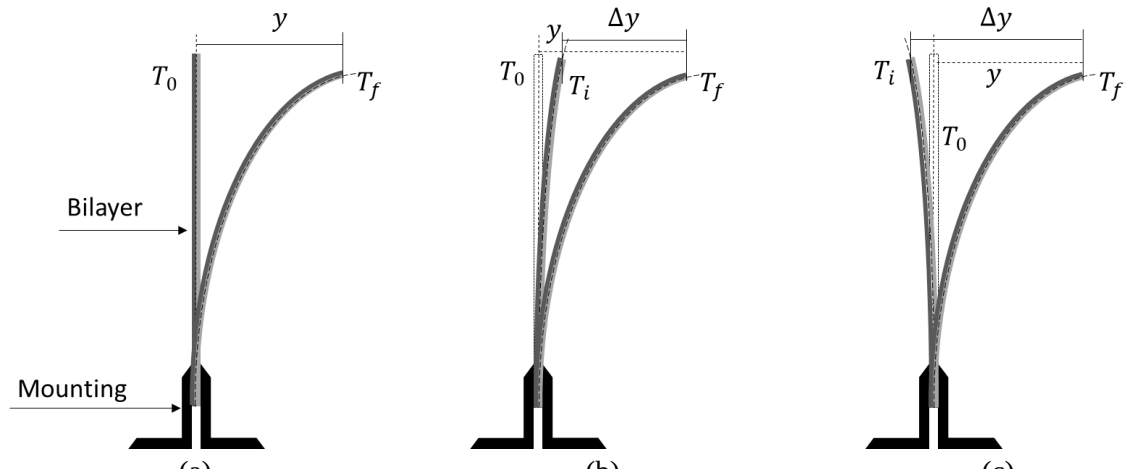

Figure III-1: Illustration of the bilayer sample with its mounting and its deformation during the experiment

As in a cantilever beam, the deflection is defined as the vertical displacement (if the beam is horizontal) of any point along the neutral axis from an unstressed (flat) state to a stressed state. Hence, it is a function of the temperature difference between its heated state T_f and its flat state T_0 in the elastic zone of its deformation ($y = f(\Delta T = T_f - T_0)$) (see Figure III-1a).

However, the samples can be slightly bent either toward the passive (see Figure III-1b) or active layer (see Figure III-1c) at the beginning of the test. Thus, the total displacement ($\Delta y = f(\Delta T = T_f - T_i)$) is considered as a function of the bilayer final temperature T_f and its initial temperature T_i (the temperature at the start of each experiment regardless of the state of the bilayer sample). Depending on the initial state of the bilayer, the deflection y can only be retrieved if the bilayer was bent towards the active layer at the beginning of the test (see Figure III-1c). Either way, the test can not be exploited in terms of deflection determination. Nonetheless, for comparison purposes of two different bilayers, all tests can be analysed as a specific displacement (deflection) δy, i.e. the deformation corresponding to a temperature rise of 1°C, is determined:

$$\delta y = \frac{\Delta y}{T_f - T_i} \tag{III-1}$$

In the same direction, both the deflection y and the total displacement Δy are approximated by a linear model through the regression of all the data for a given bilayer considering several ranges of temperature differences:

$$y = a(T - T_0) \tag{III-2}$$

$$\Delta y = a'(T - T_i) \tag{III-3}$$

The two equations (III-2) and (III-3) are then compared to check if a single equation can determine the displacement of bilayers regardless of their initial state. Furthermore, a comparison with the analytical equation used in Chapter II is undertaken to check if the selected bilayers deform in the range of the desired deflection (allowing them to reach the thermal and electrical performance determined in the feasibility study).

Hence, the general process of the experiment consists of knowing the initial position of the bilayer, increasing its temperature to a given value, measuring the corresponding displacement at its free end and finally cooling it down until it recovers its initial configuration. For this purpose, the bilayers need to be manufactured, and a heating device, a displacement measurement device and temperature sensors are required for the measurement. Those are detailed in the following sections.

III.3 Presentation of bilayer samples and the experimental setup

III.3.1 Presentation of the bilayer samples

The bilayers made of Invar and PMMA, denoted IPA, and of Aluminium and PMMA, denoted APA, were used in the experiment. Several sizes of those bilayers are considered. The Invar and Aluminium were sliced from raw flat metal sheets and the PMMA from clear and transparent plates to obtain the desired geometry.

Several thicknesses of the bilayer APA were tested, from a total thickness of ~1.25 mm to 2.5 mm. Three different widths were considered for all bilayers: 2.5 cm, 5 cm and 7.5 cm to investigate the effect of the geometry. All bilayers tested had a total length of 16.5 cm and an effective length (actual length that is not fixed and is effectively deforming) of 15.5 cm.

Table III-1 summarises all the bilayer samples tested with their corresponding means of assembly, the thickness of their constituents and their width. The thicknesses were measured with a calliper with 10^{-2} mm accuracy, and the width and length with the graduated ruler with a minimal graduation of 0.5 mm.

Table III-1: List and sizes of the bilayer samples

Bilayer	Bond	Metal thickness [mm]	PMMA thickness [mm]	Total thickness [mm]	Adhesive thickness [mm]	Width [cm]
APA	Epoxy*	0.361	1.942	2.396	0.093	2.5
	Double-coated tape 1**	0.361	1.942	2.353	0.050	2.5
	Epoxy	0.502	1.942	2.56	0.116	2.5
	Double-coated tape 1	0.502	1.942	2.494	0.050	2.5
	Epoxy	1.031	0.191	1.248	0.026	2.5
	Double coated tape 2***	1.031	0.191	1.258	0.036	2.5
	Epoxy	1.031	0.191	1.245	0.023	5
	Epoxy	1.031	0.191	1.36	0.138	7.5
IPA	Epoxy	1.031	0.222	1.271	0.034	2.5
	Double coated tape2***	1.031	0.222	1.32	0.067	2.5
	Epoxy	1.031	0.222	1.29	0.037	5
	Epoxy	1.031	0.222	1.28	0.027	7.5

* Epoxy LOCTITE EA 3479A, ** Double coated tape 3M 9425HT, *** Double coated tape 3M 467MP

III.3.2 Manufacturing of the bilayers

The challenge in manufacturing the bilayers is to choose the appropriate assembly method that enables their cyclic deformation without making them crack or detach through delamination or local buckling (Holstov et al., 2017). Here, adhesives are chosen to assemble the bilayer used to ensure that the interface of the two layers is entirely bonded. However, it leads to three-layer materials. For this reason, selecting the adhesive is important and involves identifying the adhesive that is sufficiently thin and able to transfer the stress between the two layers for the composite to be assimilated as a “bilayer”.

Three types of adhesives were tested: epoxy adhesive from LOCTITE with the reference EA 3479A, two types of double coated tapes from 3M with reference 9425HT and 467MP. The epoxy adhesive was chosen as its effectiveness has already been reported in the work of Matthieu Bouchaud (2015), in which bilayer components were tested for their implementation in adaptive facade opening elements. Double-coated tapes are tested for their common use as transfer adhesives in many technical applications. They are easy to apply and provide uniform adhesive thickness along the bilayer.

The manufacturing of the bilayers consists of four steps:

- First, the sheets were sliced to the desired size.

- Second, the surfaces of the substrates were abraded with sandpaper to enhance their physical adherence (see Figure III-2a), except that of Invar, whose dust is hazardous in case of inhalation.
- Third, the substrates were thoroughly cleaned with an air jet to sweep the abrasion dust and with isopropanol (see Figure III-2b). The PMMA sheets were dried in an oven for 24 hours at 55°C to eliminate any traces of moisture (see Figure III-2c).
- Finally, the bilayers were assembled.

The epoxy adhesive was applied using a spatula to obtain a very thin layer (see Figure III-2d). As for the 9425HT tape, since it had different adhesion strengths on the two sides, two layers of tape, 25 µm thick each, have been applied. The higher tack sides were applied to the substrates, and the lower tack sides were bonded to each other. For the 467MP tape, only one layer was applied since this tape had the same adhesive strength on both sides. This tape was also 25µm thick.

(a) (b) (c) (d) (e)

Figure III-2: Images sequence of the bilayer manufacturing (a) Abrade (b) Clean (c) Dry (d) Bond (e) Compress

After applying the adhesive (epoxy or tape), the bilayers were held under a press for 24 hours, the minimum curing time of those adhesives (see Figure III-2e). The experiment was undertaken at least 48 hours after the adhesive application.

III.3.3 Presentation of the experimental setup

Three methods were applied to heat the samples during deflection measurement indoors: uniformly in a thermal chamber (under controlled conditions), on the active or passive side with a heat gun and a radiant lamp. As for the outdoor experiment, in which the bilayers were subjected to their real operating conditions, their passive sides were heated by the sun. For each of those heating methods, the instrumentation of the bilayers evolved throughout the investigation. Therefore, the following paragraphs address only the setup employed in the majority of the tests.

III.3.3.1 Indoor experiments

a) Heating devices and temperature measurement

TC direct thermocouples of type T are used to measure the temperature of the bilayers and the air during the heating process. They were connected to a Graphtec mini logger 8420 acquisition system to record the temperature every second. The measurement uncertainties are ± (0.5% on the reading + 0.5)°C.

- **Heating setup in the thermal chamber**

A thermal chamber of the brand Venticell is used in the first experiments to heat the bilayers. Inside the thermal chamber, the bilayers were clamped vertically on a metallic stand. Four thermocouples measured the temperature of each bilayer, two on each side and at 1 cm from each end. Thermocouples

measuring the air temperature in the thermal chamber were also positioned at the same levels as those of the bilayers on their sides and between them (Figure III-3). The initial temperature of the oven is 25°C. It was increased to a final temperature of 65°C, which was maintained for 15 minutes to reach a steady state. The chamber was then cooled back to its initial temperature to observe the recovery of the bilayers to their initial position.

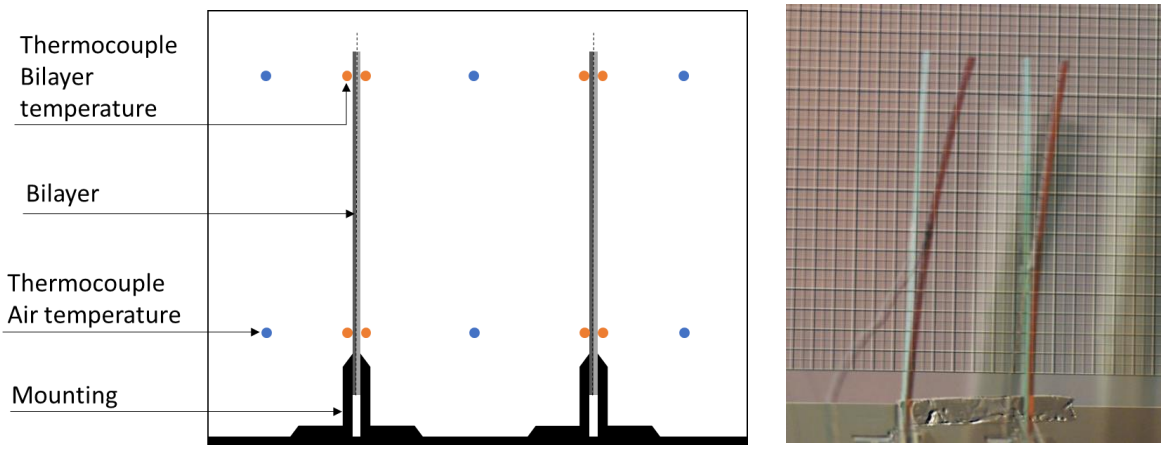

Figure III-3: The experimental setup inside the thermal chamber (a) Illustration of the bilayers mounting and the thermocouple positions (b) Superposition of the bilayer pictures at initial and deformed states inside the thermal chamber

- **Heating setup with the heat gun**

The second heating setup involves using a heat gun Bosch GHG 600CE to heat the bilayer from one of its sides (from the passive or active layer). The heat gun has a power of 2000W. It blows hot air with a temperature of 600°C at its mouth and a flow rate of 350 l/min. The heat gun was positioned in front of the bilayer at a distance that allowed the temperature of the heated side to be as homogenous as possible (at around 65 cm). The bilayers were tested one by one and instrumented with ten thermocouples, with five on each side at 1, 4.5, 8, 11 and 14.5 cm from the fixed end. The ambient air temperature, the air temperature between the heater and the sample and the air temperature behind the sample were also measured (see Figure III-4).

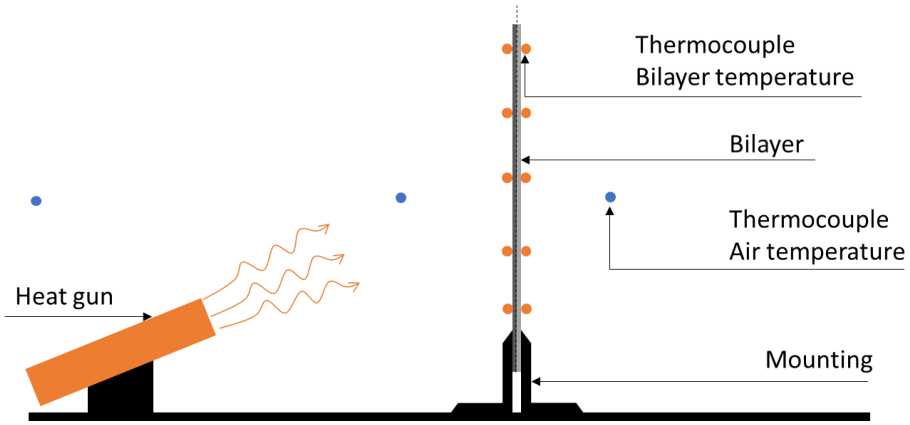

Figure III-4: Illustration of the experimental setup for the heating with a heat gun

The tests were conducted in a room with an ambient temperature regulated around 20°C. At the beginning of the test, the sample had a temperature close to that of the room. It was heated for 10 minutes, allowing it to reach a temperature of up to 65°C (if the PMMA side was heated). The cooling of the bilayer was accelerated by using a fan.

- **Heating setup with radiant lamp**

In the third heating setup, a radiant lamp was employed to heat the bilayer from one side, as in the second setup with the heat gun. A 260 W halogen lamp and a 1500 W infrared lamp were used. The infrared lamp enabled obtaining a higher level of temperature. The lamp was placed in front of the sample, which was mounted vertically on its support.

In this method, the homogeneity of the bilayer temperature was less sensitive to the distance from the lamp since the height of the lamps was greater than the length of the sample. Thus, to impose different final temperature values, the distance between the lamp and the bilayer was varied from 60 to 130 cm by sliding the sample from its mounting bench (see Figure III-5). The same instrumentation configuration as in the heating with the heat gun was used.

b) Displacement measurement setup

The deflection measurement was carried out by analysing images taken during the test. A fixed camera took pictures of the axis of the bilayer every 10s. The pictures taken over two sequences (e.g. at the beginning and the end of the test) were overlaid to measure the displacement of the free end of the bilayer. The timer on the temperature data logger and the camera were synchronized to associate the position of the bilayer given by the picture and the corresponding temperature.

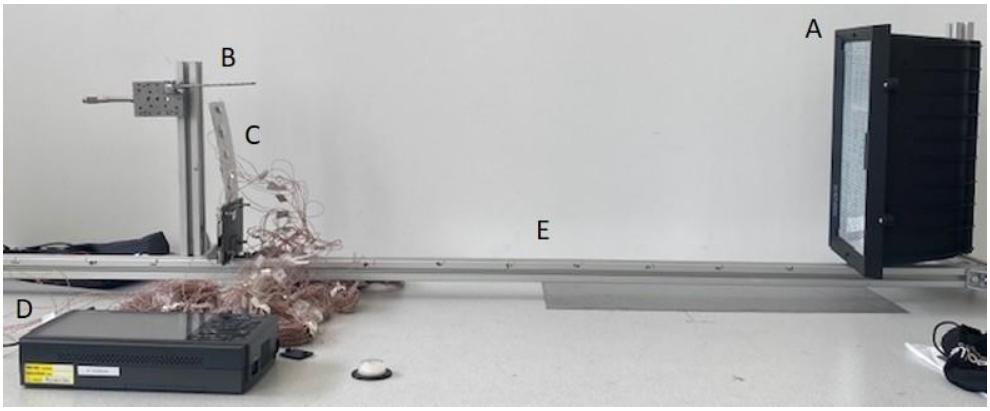

Figure III-5*: Photograph of the experimental setup with radiant lamp showing (A) The radiant lamp (B) the reference rod with translation stage (C) the bilayer sample (E) the graduated mounting bench*

An object with a known size was mounted in the same plane as the bilayer and used as a reference to convert the pixels on the images into a metric unit. In the experiment with the radiant lamp, a rod that can be translated in the axis of the displacement of the bilayer was used for this reference and also as an additional measuring device. The rod was mounted on a linear translation stage, translating when the adjustment screw was rotated. Graduation on the device links the rotation of the screw and the translation of the rod (see Figure III-5). This manual measurement was conducted to verify the measurement acquired through image processing. It has an uncertainty of 0.2mm.

I also attempted to read the displacement directly with graph paper. However, this method was ineffective because the perspective effect distorts the reading of the image, leading to significant inaccuracy.

c) Comparison of the three heating methods

Table III-2 summarises and compares the three experimental setups with their advantages and drawbacks. Most of the experiments were performed with the radiant lamp setup because it allowed heating the bilayer from one side as in its real operating condition. In addition, several temperature difference ranges can be applied since the bilayer temperature uniformity was less sensitive to the

distance with the lamp in this setup. Nonetheless, the temperature obtained was significantly more heterogeneous than in the thermal chamber. The average temperature in the bilayer was considered in the approximation of the deflection. Nonetheless, the reliability of the approximation was linked to the uniformity of the bilayer temperature.

Table III-2: Comparison of the heating devices for indoor experiments

Heating method	Advantages	Drawbacks
Thermal chamber	Temperature uniformity ($\sigma(T) < 0.5°C$) leads to a coherent comparison with the analytic model.	Difficulty in processing the images due to the low image quality (low luminosity inside the thermal chamber and blurring from the thermal chamber glass).
Heat gun	Good image quality, Possibility to verify the deflection from the image processing with manual measurement, Heating from one side as in real operating conditions.	The temperature uniformity was sensitive to the distance between the heat gun and the bilayer.
Radiant lamp		Low-temperature uniformity compared to the thermal chamber (at best $\sigma(T) = 0.56°C$ and up to $\sigma(T) = 2°C$)

III.3.3.2 Outdoor measurement

As for the field test, the bilayer strip was placed horizontally on concrete support. The metallic side (the passive side) of the bilayer was exposed to solar radiation. The data acquired from the CEA-INES meteorological platform helped determine the test conditions, which include the ambient air temperature, the global horizontal irradiation, and the wind speed. The temperature of the heated side was measured using a type K thermocouple with an uncertainty of ± 1.5°C. During the field test, since the bilayer was fixed in a horizontal plane, the displacement of the bilayer was measured directly with a graduated ruler with ½ mm of accuracy.

III.4 Selection of the assembling method

The first experiment was carried out to select the suitable adhesive allowing the bilayer to deform freely. The investigation was undertaken on the 2.37 mm and 2.5 mm thick and 2.5 cm wide aluminium-PMMA (APA) bilayer samples bonded with epoxy adhesive and 3M 9425HT adhesive tape. They were heated with the heat gun. Only a single thermocouple fixed in the middle of the heated side was used to measure their temperature. Two tests were carried out on each sample, one to heat the sample from the PMMA side (active material) and the other to heat it on the metal side (passive material).

Figure III-6 shows the results of tests for samples heated by their active face (PMMA) with overlaid images of their initial and final states. In general, the adhesive tape prevents the bilayer from deforming. When the temperature is very high, the strips are detached. For the 2.37 mm bilayer, the free end of the bilayer appears to move slightly in the final state. However, by zooming in on the image, a local buckling can be seen in the middle of the sample (see Figure III-6a). Figure III-6c clearly shows the delamination of the bilayer at high temperatures for the 2.5mm thick APA.

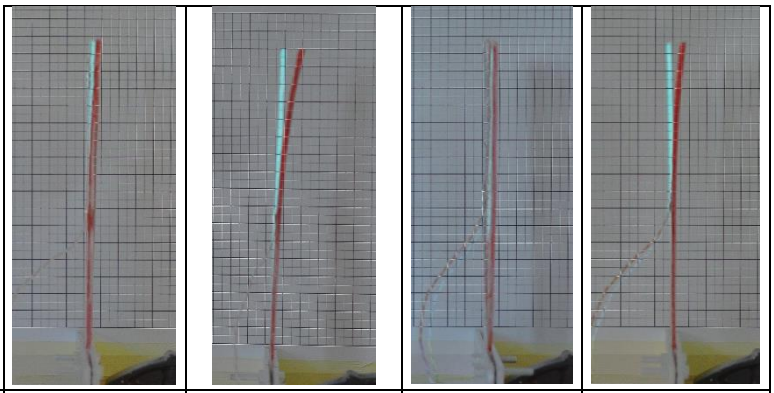

	(a)	(b)	(c)	(d)
Bilayer	APA 2.37 mm		APA 2.5 mm	
Bond	9425HT tape	Epoxy adhesive	9425HT tape	Epoxy adhesive
ΔT [°C]	30.93	26.77	44.22	30.13
Total displacement Δy [mm]	2.34	9.40	-	9.84
Specific displacement δy [mm/°C]	0.07	0.35	-	0.33

Figure III-6: Comparison of the displacement of the 2.37 mm and 2.5 mm thick aluminium-PMMA bilayers (APA) according to their assembly method - 9425HT tape and LOCTITE EA 3479A epoxy adhesive

Those results correspond to the tests conducted at the early stage of this work. The bilayer thicknesses were selected mostly from their high availability in common markets. This is why even if the bilayer bent with the epoxy adhesive, the obtained specific deflection (δy = 0.33 mm/°C and 0.35 mm/°C) was lower than that required (minimum 0.6 mm/°C) according to the study in Chapter II.

Given the inadequacy of the 3M 9425HT tape, another type of double-coat tape was used. It was 3M 467MP tape. The experiment was carried out with an Aluminium-PMMA bilayer of 1.2 mm thickness, whose thickness was supposed to lead to the range of required specific deflection determined in the previous chapter.

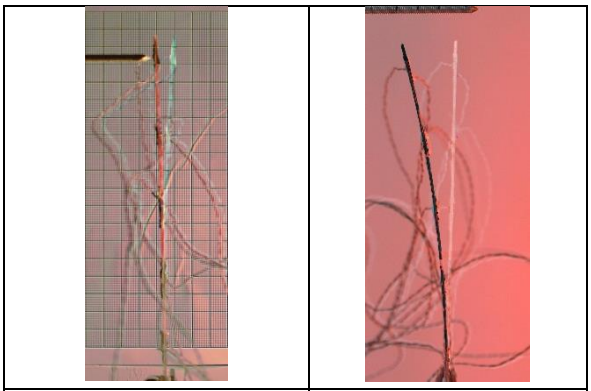

	(a)	(b)
Bilayer	APA 1.2 mm	APA 1.2 mm
Bond	467MP tape	Epoxy adhesive
ΔT [°C]	27.66	23.83
Total displacement Δy [mm]	9.16	23.40
Specific displacement δy [mm/°C]	0.33	0.98

Figure III-7: Comparison of the deformation of the 1.2 mm thick aluminium-PMMA (APA) bilayers according to their assembly method - 3M 467MP tape and LOCTITE EA 3479A epoxy adhesive

The results show that the deflections of the samples assembled with 3M 467MP tape remained low compared to those assembled with epoxy adhesive (see Figure III-7). The bilayer with the epoxy

provided the required specific deflection ($\delta y = 0.98\ mm/°C$, requirement: $0.60 < \delta y < 1.43 mm/°C$). Details of all the physical properties of the bonding materials were provided on the technical sheet. However, the observed behaviours would indicate that the adhesive tape is very flexible and elastic, enabling it to absorb the differential expansion of the materials it bonds and preventing the intended bending.

These results led to the choice of epoxy adhesive for assembling the bilayers. However, since the adhesive was applied manually, the thickness of the adhesive in the sample could be variable among different bilayers. A variation of deflection in the bilayers of the same properties can occur. Indeed, if the adhesive is very thick, it can also limit the strip deformation. Delamination was observed for bilayers with very thin adhesive. For this reason, the compression stage is very important to expand the adhesive uniformly. Therefore, the compared bilayers were assembled by the same operator and compressed in the same press to limit this thickness variability and assume their thickness was relatively equal.

III.5 Bilayer behaviour in situ experiment

Outdoor experiments were conducted to determine if the bilayers could deform under real operating conditions. The 2.5 mm and 2.37 mm thick aluminium-PMMA bilayers assembled with epoxy adhesive were used in the experimentation. These thicknesses are not yet optimized as these tests were among the first experiments conducted. The measurements were carried out on four (4) sunny days in May 2021. The ambient air temperature was between 12.3°C and 27.7°C, the wind speed was between 0.09 and 4.55 m/s, and the global horizontal solar radiation was between 33 and 1064 W/m2 during the days considered. The maximum deflections observed were 7.5 mm and 8.5 mm, respectively, for the 2.37 mm and 2.5 mm thick samples.

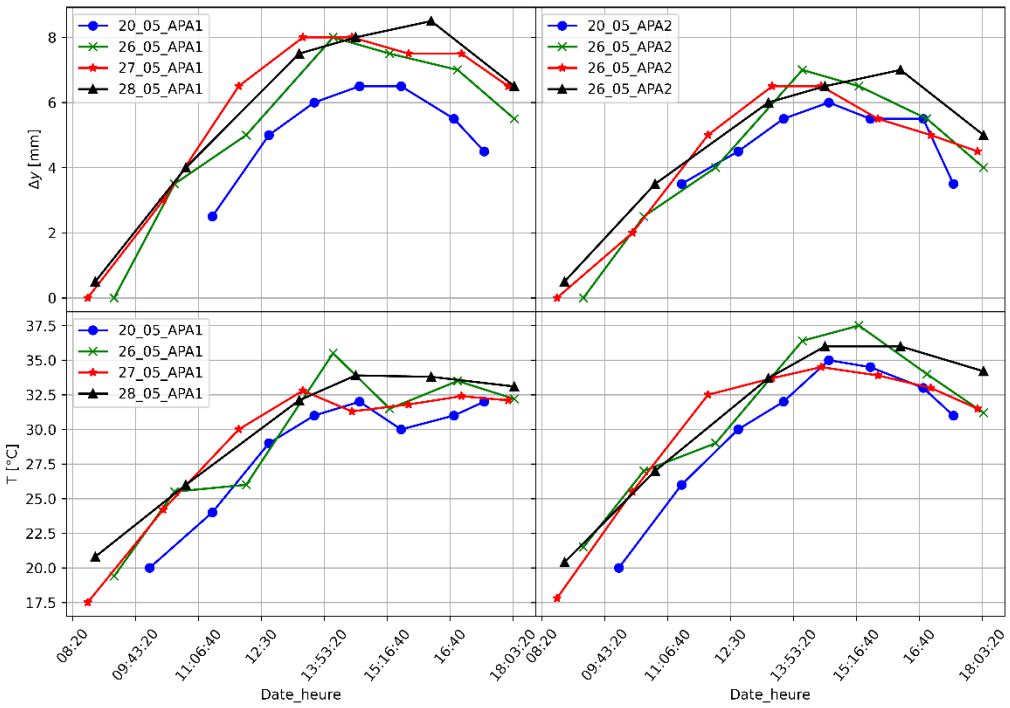

Figure III-8: Evolution of the displacement of the Aluminium-PMMA (APA) bilayers and their temperatures during the days of outdoor testing - APA1 bilayer 2.37 mm thick - APA2 bilayer 2.50 mm thick

Figure III-8 shows the evolution of the displacement of the samples and their temperature during the test days. The curves have the trend of the daily temperature and sunshine evolution. This result shows that the bilayer sheets also respond to slower temperature loads than those of the experimental heating

devices. These deformations have confirmed the possibility of applying the bilayers under real conditions. However, they are not sufficient to obtain an optimal fin effect. Consequently, the following sections present only the results obtained from the thinner bilayer samples.

III.6 Determination of the deflection equation as a function of the temperature variation

The approximated equation of the deflection y and the total displacement of the bilayers Δy are determined in this section. The formulas obtained would be exploited to compare the effect of the heating method, the effect of the bilayer width and the comparison of the bilayers of different natures. The investigation was undertaken on the 1.2 mm thick Aluminium-PMMA bilayers and the 1.25 Invar-PMMA bilayers. 29 measurements were conducted on the Aluminium-PMMA bilayer and 16 measurements on the Invar-PMMA bilayer, though respectively 25 and 11 of them can be exploited to obtain the deflection from the flat state of the bilayer (see Table III-3). Most of the tests were carried out on the 7.5 cm bilayers as this width corresponds to about half of a photovoltaic cell, the minimum targeted size in this application.

Table III-3: Number of the measurements of the deflection and total displacement according to the bilayer type and geometry

Bilayers	Test number	Possibility of deflection estimation	
		Yes	No
Aluminium – PMMA 1.2 mm thick – 2.5 cm width	3	2 (flat)	1
Aluminium – PMMA 1.2 mm thick – 5 cm width	2	2 (1 flat)	0
Aluminium – PMMA 1.2 mm thick – 7.5 cm width	24	21	3
Invar – PMMA - 1.25 mm thick – 2.5 cm width	4	1 (flat)	3
Invar – PMMA - 1.25 mm thick –5 cm width	2	1	1
Invar – PMMA - 1.25 mm thick – 7.5 cm width	10	9	1

III.6.1 Study on Aluminium-PMMA bilayer

III.6.2 Aluminium-PMMA of 7.5 cm width

III.6.2.1 Effect of the heating method: passive or active side

To determine the approximated equations of the bilayer deflection and total displacement, the temperature of the bilayer sample is assumed to be homogenous (at the initial and final states), which is not the case in real conditions. The bilayers are likely heated by the sun from their passive side, and their mounting influences the temperature at their fixed ends. Therefore, the temperatures are different at their sides and can be heterogeneous along their length (see Figure III-9). The average temperature in

the bilayer was used in the approximation to keep this assumption of temperature uniformity. Nevertheless, it is interesting to determine if the bilayer behaviour changes according to the heated side.

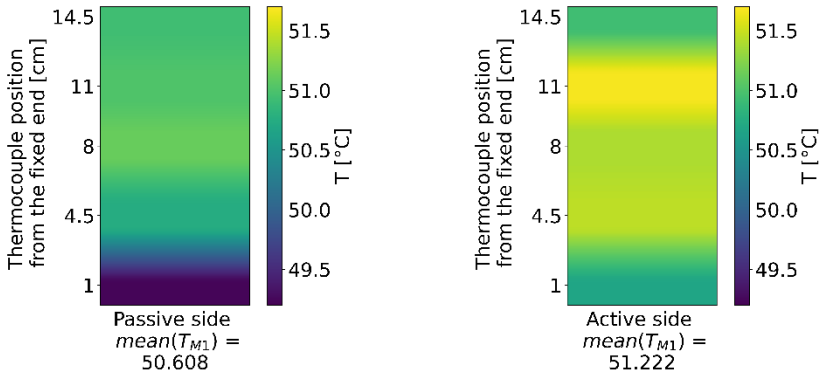

Figure III-9: Illustration of the temperature repartition on the bilayer surfaces from a sample heated on the active side with the radiant lamp

The results of the displacement measurement of the bilayer Aluminium-PMMA for 7.5 cm width are analysed to investigate this aspect. The bilayer displacements against the temperature variation are plotted in Figure III-10a according to its heated side. The data points 'P' design those retrieved from the heating on the passive side (aluminium), and the points 'A' from the heating on the active side (PMMA). The trend lines of data according to the heated side and the global trend of overall data are also traced.

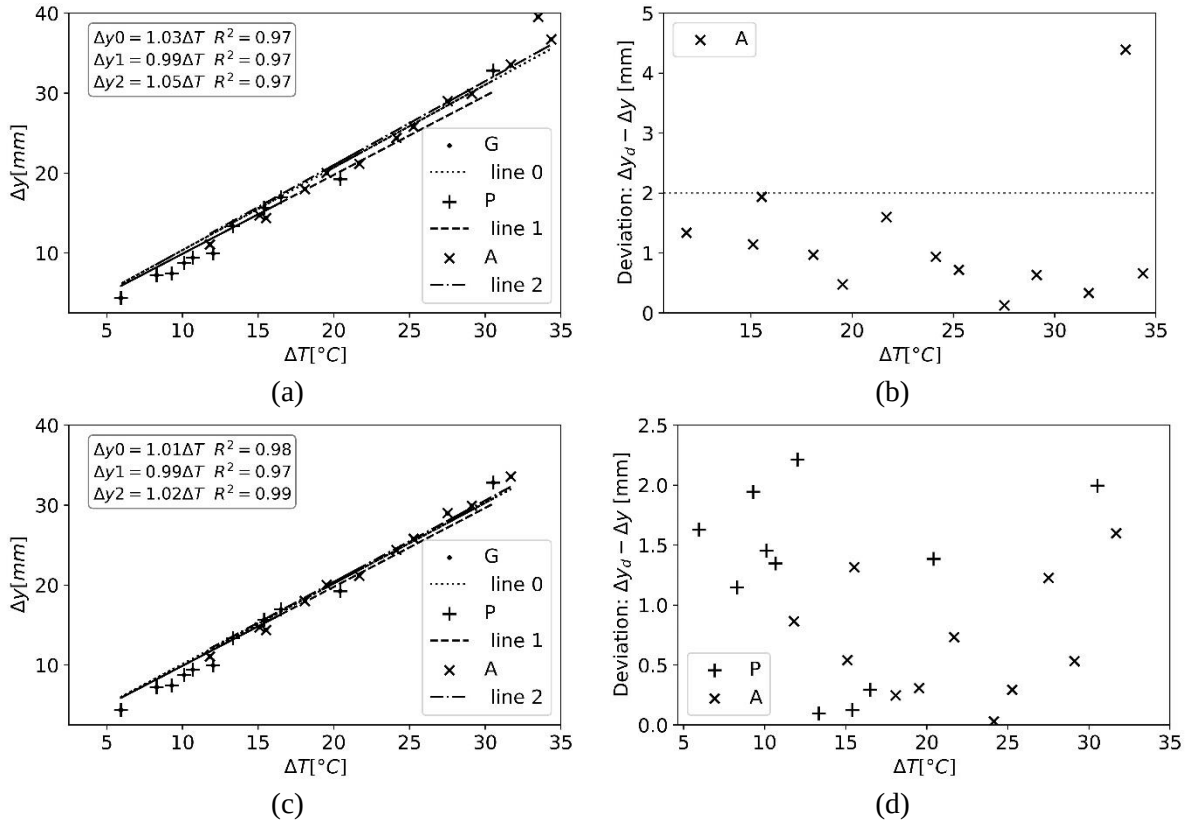

Figure III-10: Analysis of displacements of the bilayer against the increase in their temperature depending on the heated side - P: heating on the passive side (Aluminium) - A: heating on the active side (PMMA) - G: Global results (a) Displacements and their linear regression according to the heated side (b) Deviation of the displacements from the predicted line for heating on the active face (c) Displacements and their linear regression in the elastic zone (d) Deviation of the displacement from the global predicted line

The equations $\Delta y_{1(P)}$ and $\Delta y_{2(A)}$ have been obtained respectively through the regression of the data from heating on the passive (aluminium) and the active side(PMMA):

$$\Delta y_{1(P)} = 0.99\ \Delta T\ [mm] \quad \text{(III-4)}$$

$$\Delta y_{2(A)} = 1.05 \Delta T\ [mm] \quad \text{(III-5)}$$

ΔT is the temperature difference between the final and initial states of the bilayers. The equations (III-4) and (III-5) show that there is just a small difference in their slopes:

$$a_{2(A)} - a_{1(P)} = 0.06\ [mm/°C] \quad \text{(III-6)}$$

The difference between the measurement and the obtained linear equation from the bilayer heated on the active side was plotted in Figure III-10b. There is a point particularly distant from the others. It corresponds to a temperature difference of $\Delta T = 33{,}50°C$. This can be from the plasticizing of the bilayer beyond the yield temperature increase. In effect, a nonlinear increase in the deformation can be observed at a certain temperature threshold. During this test, when the sample was cooled down, it did not return to its initial shape. A residual deformation occurred, and the elastic zone of the bilayer seemed to expand. Hence, the deviation of the measurement conducted afterwards was linear to those conducted in the initial elastic zone even if the temperature difference was higher $\Delta T = 34{,}37°C$.

If the measurements with temperature loading exceeding the elastic zone are discarded, the graph in Figure III-10c is obtained. The trends of the bilayer heated on the passive side become closer to the one heated on the active side. The equation from the overall data is:

$$\Delta y_0 = 1.01\ \Delta T\ [mm] \quad \text{(III-7)}$$

The difference in the data from this global equation is rather scattered, but no point is particularly far from the others (see Figure III-10d). In conclusion, the data can be analysed without considering which side of the bilayer is heated.

III.6.2.2 Effect of the initial state of the bilayer

Among 24 measurements performed on the Aluminium-PMMA bilayer 7.5 cm wide, displacement from the flat state or the deflection can be measured in 21 of them. Since the bilayers are not programmed to be flat at a given temperature, it is important to find out if the equation of the deflection y can be approximated with the equation of the displacement Δy.

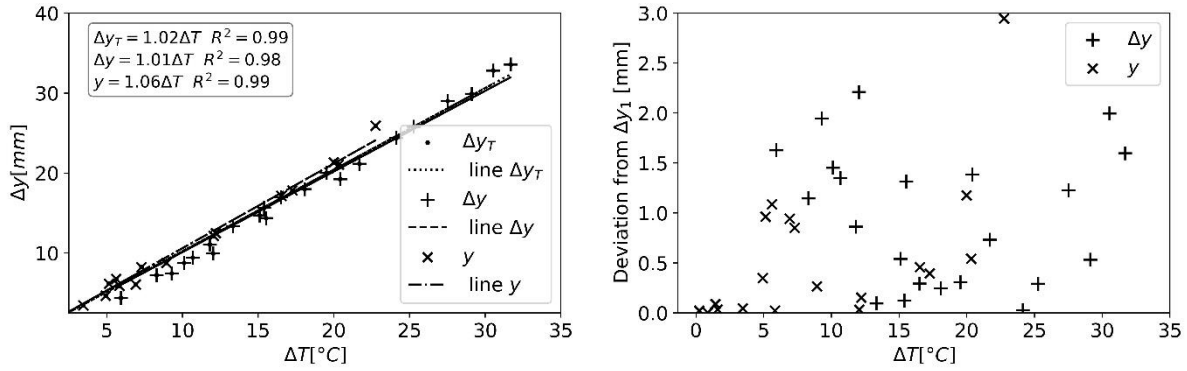

(a) (b)

Figure III-11: Analysis of displacements of the bilayer against the temperature variation depending on the initial state of the sample with Δy_T for overall data – Δy for the measurement of the total displacement - y for the measurement of the deflection (a) Displacements and their linear regression (b) Deviation of the displacements from the predicted line of the total displacement data Δy

As in the previous investigation, the data and the linear predictions from the two kinds of measurements are shown in Figure III-11a according to the temperature variation. The linear model from overall data is also traced (Δy_T). The results obtained show that the slopes of Δy and y are very close, with a difference of $0.05\ mm/°C$.

Considering only the equation of the total displacement Δy, Figure III-11b shows that the overall data (corresponding to the total displacement and the deflection) are not far from the trend line obtained. 98.07% of the data from the deflection measurement y can be retrieved from the equation of the displacement:

$$\Delta y = 1.01 \Delta T\ [mm] \quad \text{(III-8)}$$

This indicator is satisfactory and enables to conclude that the deflection can be approximated with the equation of the total displacement. Furthermore, in the measurement of the deflection, the temperature T_0 was not always at a steady state (if the sample was not flat at the beginning of the test, T_0 was retrieved from the analysis of the image sequence). Therefore, it is more accurate to rely on the equation of the displacement since both T_i and T_f correspond to a steady state of temperature.

III.6.2.3 Effect of the width of Aluminium-PMMA bilayer

In Timoshenko's analytic model (see Chapter II), the bilayer deflection is from a one-dimensional model, as the length is significantly more important than the width. In this application, the bilayer size would be at least half a PV cell. Thus, the length is just twice larger than the width.

Additional measurements on the sample of 2.5 cm and 5 cm width were performed to investigate the effect of width on the Aluminium-PMMA bilayer.

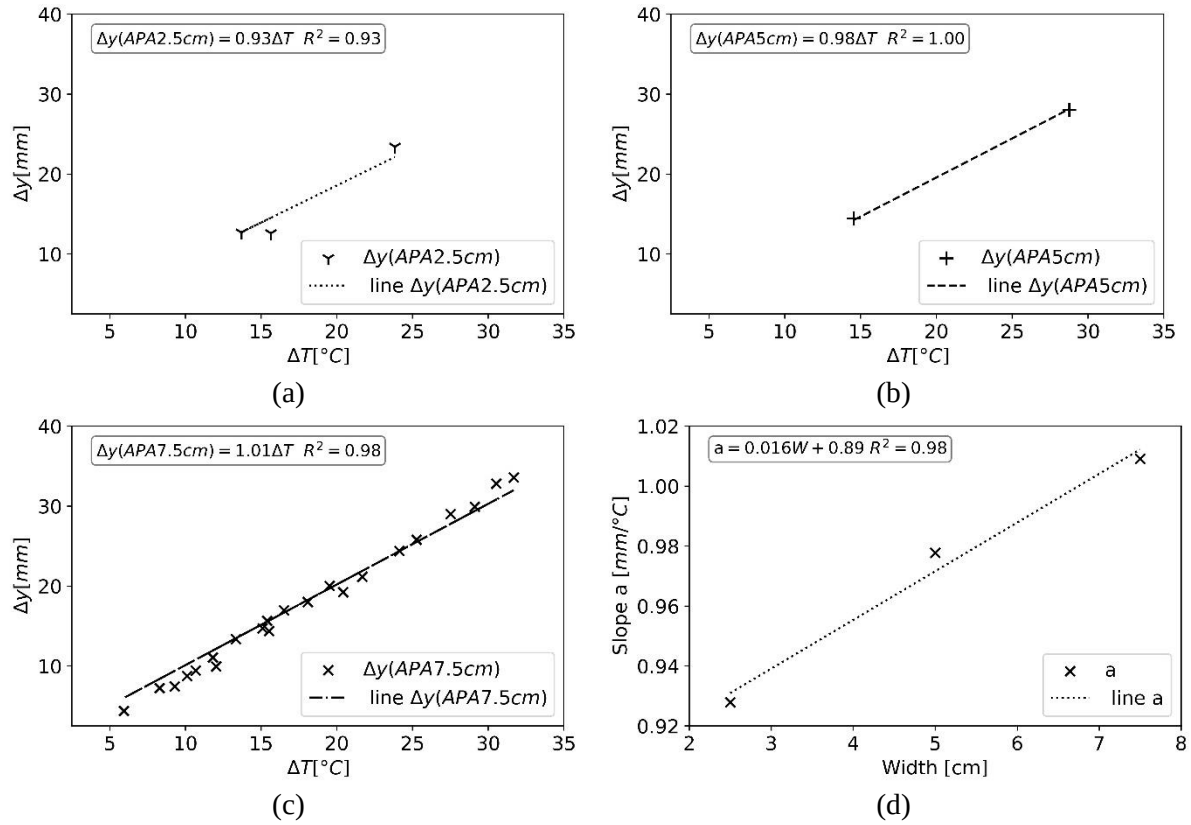

Figure III-12: Analysis of the effect of the width of the Aluminium-PMMA (APA) bilayer - Displacements and their linear regression of samples of (a) 2.5 cm in width (b) 5 cm in width, and (c) 7.5 cm in width – (d) Variation of the slope according to the width of the bilayer

The approximative equations of all the samples (for 2.5 cm to 7.5 cm width) are compared by plotting the displacement against the temperature variation (see Figure III-12a to c). From the obtained results, the deflection slope increases with the increase of the width (see Figure III-12d). However, this increase is small, and more measurements should be undertaken on the samples of 2.5 cm and 5 cm in width to draw a firmer conclusion. Nevertheless, the equation of the slope variation can be estimated to approximate the deflection from a sample of random width. Thus, a global deflection equation can be written as follows:

$$y = (0.016W + 0.89)\Delta T\ [mm] \tag{III-9}$$

With W the width of the bilayer is expressed in cm.

The displacements obtained from equation (III-9) ($\Delta y = f(a)$) are compared with the overall measured data and their predicted trend line in Figure III-13a. The result shows that displacements depending on the slope equation are close to the measurements. It enables the retrieval of 97.97% of the data, while the equation from the regression from all data retrieves 97.62% of them. Therefore, the deformation of the Aluminium-PMMA bilayer is not sensitive to the width, at least in the range studied here. Thus, a one-dimensional approximation of the bilayer deformation is valid for this case.

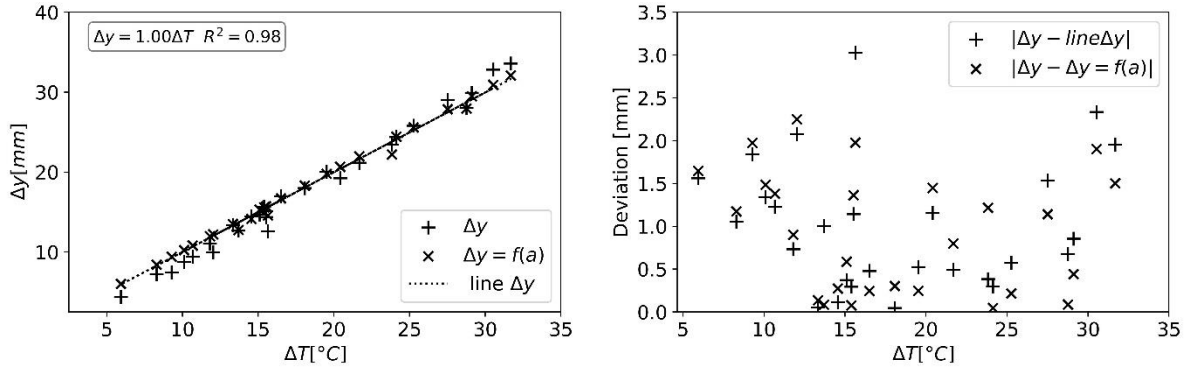

(a) (b)

Figure III-13: Comparison of the displacement measurement with the approximation depending on the width of the Aluminium-PMMA bilayer (APA) (a) Displacements against the temperature variation (b) Deviation of the displacements Δy and the approximated displacement $\Delta y = f(a)$ from the general trend line

III.6.3 Study on Invar-PMMA bilayer

The determination of the displacement and the investigation of the effect of width are also undertaken with the bilayer Invar-PMMA. The variation of displacement against the temperature variation is shown in Figure III-14 for each bilayer.

Similarly to the bilayer Aluminium-PMMA, the result from the 7.5 cm width sample shows that the bilayer plasticizes when the temperature variation ΔT is above 38°C (Figure III-14c). Thus, the measurements above this temperature variation are not considered to determine the trend line. However, in contrast to the previous study, there is no linear trend in the deflection slope according to the width, but the slope variation is very small according to the width (see Figure III-14d).

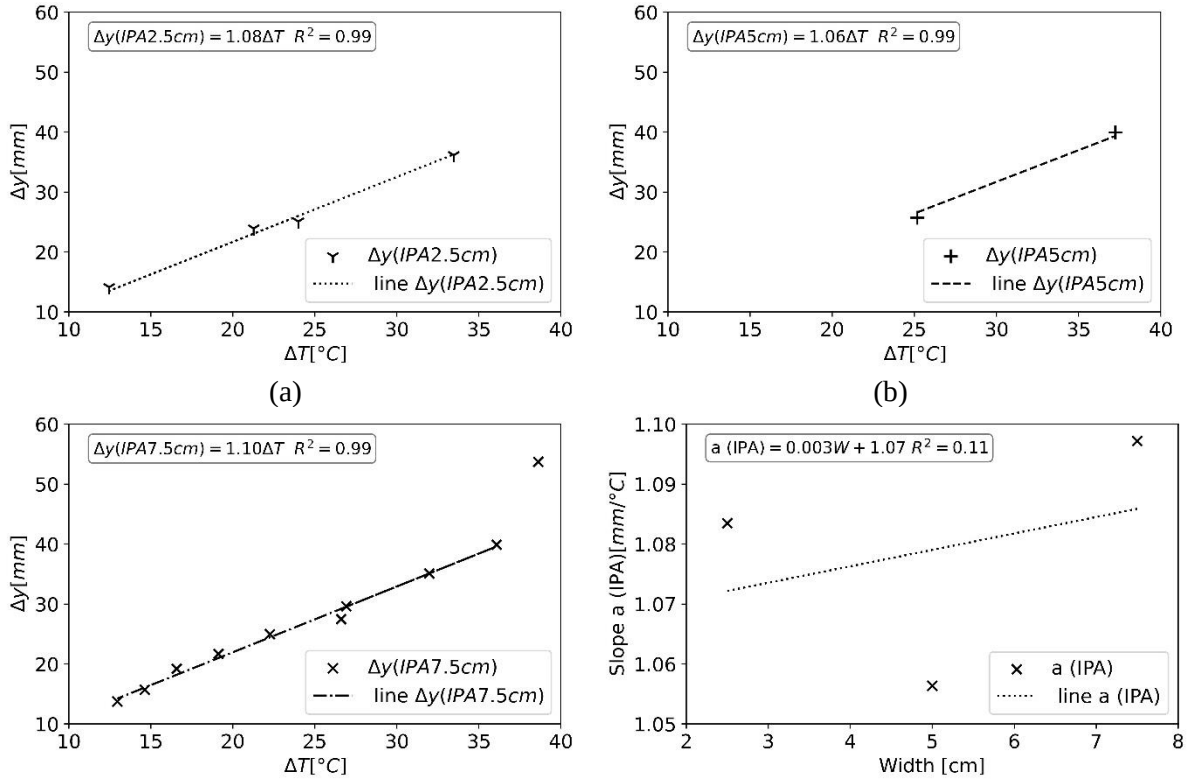

Figure III-14: Analysis of the effect of the width of the Invar-PMMA (IPA) bilayer - Displacements and their linear regression of samples of (a) 2.5 cm in width (b) 5 cm in width, and (c) 7.5 cm in width – (d) Variation of the slope according to the width of the bilayer

Hence, both the measured displacements and those approximated with the slope equation are aligned with the general trend equation (see Figure III-15). This comparison with the equation with the slope ($\Delta y = f(a)$) is conducted just to compare with the previous study, even though determining the displacement with the slope equation is not relevant here since its coefficient of determination R^2 is very low.

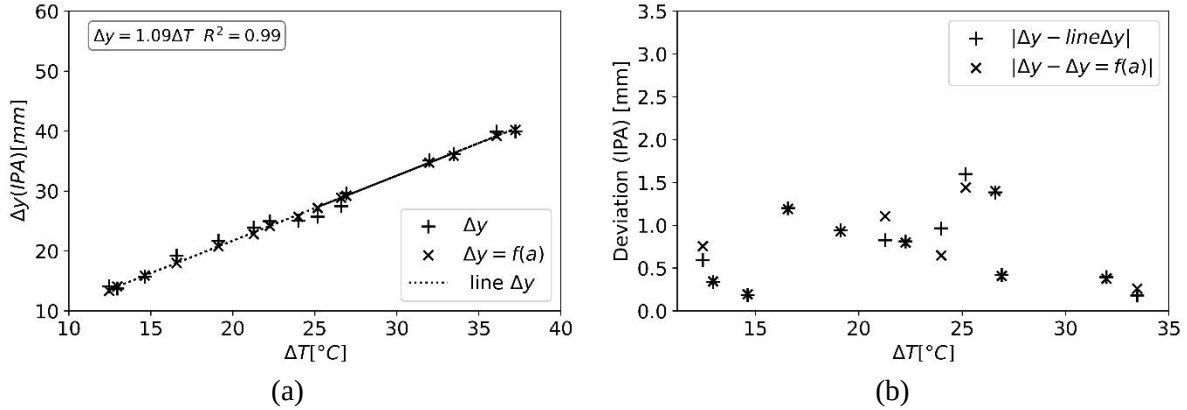

Figure III-15: Comparison of the displacement measurement with the approximation depending on the width of the Invar-PMMA bilayer (IPA) (a) Displacements against the temperature variation (b) Deviation of the displacements Δy and the approximated displacement $\Delta y = f(a)$ from the general trend line

For the bilayer Invar-PMMA, it is more interesting to consider the general trend of all data (III-10) than to establish an approximation depending on the width.

$$\Delta y = 1.09 \Delta T \; [mm] \qquad \text{(III-10)}$$

The results suggest that the width has little effect on the behaviour of the Invar-PMMA and that its deflection can also be approximated with a one-dimensional equation. Though, by performing the same experiment, different behaviour was observed with an Invar and PMMA sliced from different batches of material (a rolled metal sheet instead of flat metal for the Invar). The deformation of the newly tested sample was not uniform along the width. Apart from the displacement according to the length axis, displacement along the width axis was also observed. This displacement was not symmetric, probably because the strip was fixed at the end (see Figure III-16). Hence, the deformation no longer corresponds to a beam deflection but to the plate deflection. However, the previously presented analysis can be applied if the displacement of the bilayer is only according to the length axis.

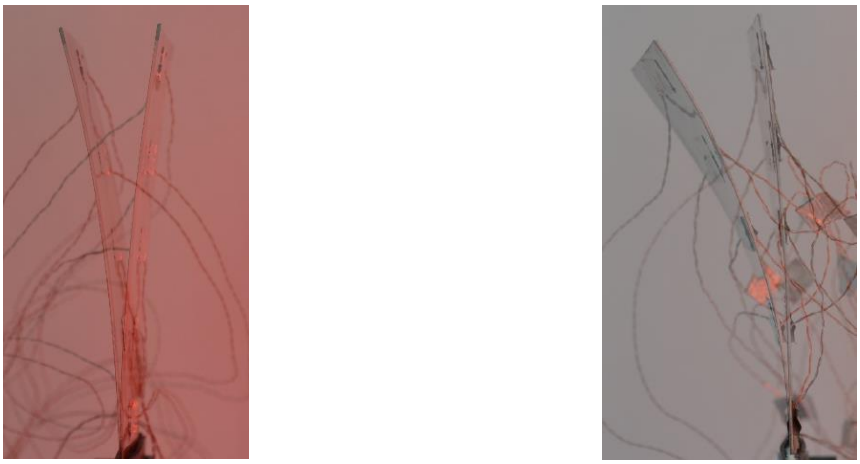

(a) (b)

Figure III-16: Illustration of different behaviour observed in the Invar-PMMA bilayer (a) Displacement according to the length axis (b) Displacement according to both the length and width axis

III.6.4 Comparison of the experimental model and analytical model

Considering the application of adhesive to assemble the bilayer, the resulting material is not a bilayer but a three-layer material. This is why the adhesive should be thin and able to transmit the stress from one layer to another to ensure the behaviour found in a bilayer. This subsection confronts the experimental result with the simulated displacement from the analytical model presented in Chapter II of this manuscript to validate and evaluate this behaviour. The input of this model is given in Table III-4 according to the technical data provided by the manufacturer.

Table III-4: Physical properties of the materials forming the bilayers

Parameter	Aluminium	Invar	PMMA
Coefficient of thermal expansion (CTE) $[10^{-6}\ °C^{-1}]$	23.5	1.7 – 2.0	70 – 77
Young modulus $[GPa]$	70.6 – 75.2	140 – 160	2.4 – 3.3

The measured displacement with their general trend and the simulated data are plotted in Figure III-17a for the Aluminium-PMMA bilayer and Figure III-17b for Invar-PMMA with one dimension behaviour. The simulated curve is an envelope curve. As the properties of the materials are given with an interval in the manufacturing data sheet, the higher curve is from the properties allowing to obtain the maximal deflection. The lower curve is from the properties allowing to obtain minimal deflection. If the bilayers have the behaviour of the ideal bilayer from the model, the measured displacement should be in the envelope curve.

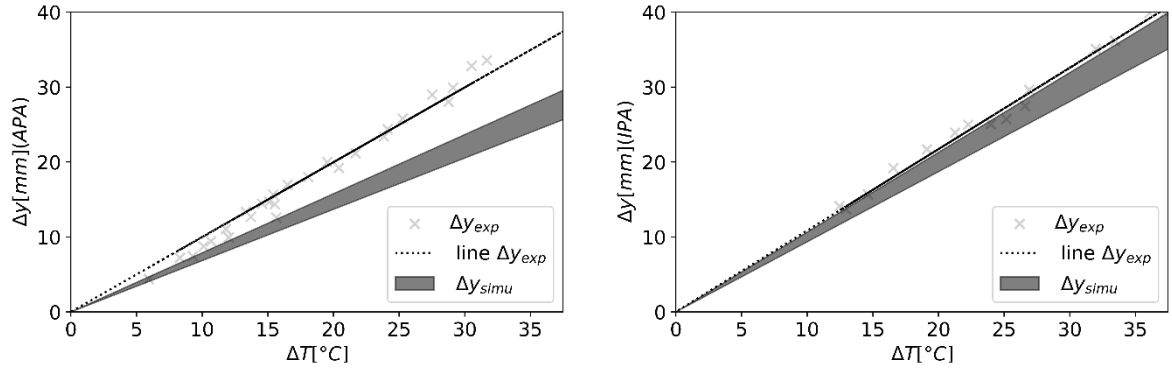

(a) (b)

Figure III-17: Comparison of measured displacement and simulated deflection (a) Aluminum-PMMA (APA) bilayer (b) Invar-PMMA (IPA) bilayer

Figure III-17a shows that the deformation of Aluminium-PMMA is more important than the one predicted in the simulation. Some measurements with small temperature differences are closer to the higher bound of analytical results. The differences between the slope of the analytical model (simulation) and the linear regression of the measurement are $0.31\,mm/°C$ and $0.21\,mm/°C$ respectively from the inferior and superior curves. Hence, the deviation from the analytical model is between 4.2 mm to $9.2\,mm$ lower than measured delfection at $\Delta T = 30°C$, which is $y_{exp} \approx 30\,mm$. Therefore, the manufactured sample does not behave as predicted. Nonetheless, its specific deflection is in the range of the required deflection for the concept to be effective.

As for the bilayer Invar-PMMA, the measurement is close to the higher curve of simulated data (see Figure III-17b). The differences between the slope of the linear regression from the experiment and analytical model are $0.15\,mm/°C$ and $0.02\,mm/°C$ respectively from the inferior and superior curves. At $\Delta T = 30°C$, the analytical model gives a deflection y between 0.6 mm to 4.5 mm lower that the measurement (where $y_{exp} \approx 32.56\,mm$). Hence, the behaviour of the Invar-PMMA is close to the ideal bilayer behaviour as long as the sample only deformed along the bilayer length.

In conclusion, this confrontation of the measurements with the analytical simulation demonstrates the necessity of experimental determination of the bilayer deformation. The presence of the adhesive has a significant influence on the behaviour of the bilayer.

III.7 Comparison of deformation of the aluminium-PMMA and the Invar-PMMA

According to the analytic model, the slope of the deflection of Invar-PMMA should be around 35% higher than that of the Aluminium-PMMA (see Chapter II). However, the difference in deformation between the two bilayers is reduced to 9% while taking into account the approximative equations from the overall displacement measurements, as the deformation of the bilayer Aluminium-PMMA is greater than predicted.

The width of the bilayer has little influence on their deflection in the range of width considered in this study. Nonetheless, particular attention is required in the selection of the material composing the bilayer. Even from bilayers of the same nature, different behaviours can be obtained regarding longitudinal (along the length axis) and transversal deformation (along the width axis). A one-dimensional approximation of the bilayer displacement is not accurate if there is a significant displacement along the width. This issue is encountered in some samples of the Invar-PMMA bilayer and not in the Aluminium-PMMA samples. Hence, this method of deformation estimation is more suited for the Aluminium-PMMA sample, which is an important advantage regarding the desired behaviour in the facade concept.

Nonetheless, the elastic zone of the Invar-PMMA bilayer is wider in terms of temperature than the Aluminium-PMMA, allowing the sample to be used in cyclic temperature constraints in a larger range of thermal conditions.

III.8 Conclusions

In conclusion, this study shows that the selected bilayers are suitable for application in the designed bioinspired facade. As expected, they exhibit a cyclic deformation and can operate in real conditions.

The effectiveness of their deformation strongly depends on their manufacturing method. In this study, the epoxy adhesive provides satisfactory bilayer deformation and is selected for assembling the samples.

The bilayer deflection is linear in the elastic zone of the deformation and is not very sensitive to the width of the sample for the Aluminium-PMMA strips. In contrast, for the invar-PMMA strips, a deformation along the width axis can also be observed depending on the variety of the constituent materials. Contrary to the analytical model, the Aluminium-PMMA samples have deformation as important as the Invar-PMMA. Therefore, the Aluminium-PMMA bilayer was selected considering its one-dimensional behaviour, its deflection capacity and its higher thermal conductivity. Moreover, aluminium is more available, less hazardous, and more easily recyclable than Invar. Nevertheless, a further comparison is conducted to confirm this choice in an experimental study on the facade prototype.

In effect, the next step of the facade design is validating the facade performance through reduced-scale prototyping. The deflection equation determined in this chapter is used to approximate the deformation of the bilayer in this prototyping. Therefore, this study enables to avoid using displacement measuring devices that can disturb the bilayer deformation in further experimentation. Only their temperature data is needed for their deflection determination. The deflection model can also be implemented in the thermal model of the adaptive facade.

Chapter IV. Experimental study of the facade prototypes

IV.1 Introduction

This chapter presents the experimental evaluation of the relevance of the developed innovative facade concept in controlled radiation conditions. For this purpose, different experimental parametric studies have been performed indoors on an elementary component of the designed BIPV facade using a solar simulator. The facade element comprises a photovoltaic module, a naturally ventilated air gap, and an insulated concrete wall bearing a bilayer assembly referenced as the support layer.

As a first step, a configuration of the facade noted, “prototype 1”, comprising an ordinary glass layer instead of the PV module, has been studied and used as a reference for comparison. First, the impacts of the component thermal behaviour of different parameters were investigated, namely the application of different bilayer assemblies and support layer materials, the air gap thickness, the nature of the ventilation, and the shading effect from dummy PV cells.

In the second step, both the thermal and electrical performances of the design were assessed, considering the effect of photoconversion and the addition of the PV module on the BIPV facade. This investigation was undertaken on the second prototype, noted as “prototype 2”.

The bioinspired facade differs from ordinary ones and displays most of its innovative features when the bilayers are bent. In that state, it simultaneously acts as a heat sink, solar shading, and irradiance reflector for the PV modules. For this reason, the experimentation was conducted considering the summer configuration, in which the bilayers deformed at their maximum, and the air gap is opened. The synthesis of the experimentation results in this configuration would forecast its behaviour in winter and mid-season. However, additional experimentations are needed to determine the actual behaviour in those seasons and constitute one of the perspectives of this study.

This chapter is composed of a description of the experimental setup, the test plan and the analysis of the results of the experimental parametric studies.

IV.2 Validation of the concept under a solar simulator

IV.2.1 Objectives and parameters considered

The prototyping aims to validate, size and propose the best materials and configurations of the innovative PV facade to confirm the feasibility study in Chapter II. Most of the investigations were performed on prototype 1 to discard the effect of the PV module and focus on the impact of the bilayers on the facade thermal behaviour. Therefore, the following test plan has been considered:

- **Test 1** evaluates the impact of the arrangement of the bilayers on their support layer by comparing the configurations without bilayers (corresponding to an ordinary facade), with a staggered bilayers arrangement, and with complete coverage of bilayers arranged in line. For this, the effect of solar radiation and the air velocity in the gap is highlighted throughout the analysis. Even if the bioinspired facade is designed with a naturally ventilated air gap, mechanically ventilated configurations are also analysed to highlight the performance of the bilayer application over the use of mechanically ventilated systems. Implementing a

mechanically ventilated air gap efficiently cools down a BIPV facade but requires operating electrical energy. Hence, this comparison would highlight the thermal performance of this active solution over the current passive solution in terms of energy usage.

- **Test 2** aims to select the most optimum bilayers by comparing the effect of bilayers characterised in Chapter III (Aluminium-PMMA and Invar-PMMA bilayers) while considering the configuration with complete coverage of bilayers arranged in line.
- **Test 3** focuses on the impact of the material composing the support layer to highlight the influence of its thermal properties on heat dissipation through areas with and without bilayers.
- **Test 4** aims to study the influence of the airflow rate by varying the airgap thickness.
- **Test 5** assesses the relevance of bilayers, considering that the PV cells also provide shading on the wall. For this, dummy PV cells have been applied to the glass layer.
- **Test 6** assesses the relevance of bilayer application in the PV facade prototype by considering the experimentations on prototype 2. The facades with and without bilayers are compared according to their thermal and electrical performances. The relevance of implementing the bilayers over the use of mechanical ventilation is also highlighted here, considering the electrical performance of the PV module.

With the results of Test 6, the forecast of the PV facade performance in winter and mid-season is discussed by considering the experimental result from low and mid solar radiation. One test per configuration and testing constraints was conducted on prototype 1. Whereas in prototype 2, two tests were performed per configuration and testing constraint to confirm the repeatability of the experiment.

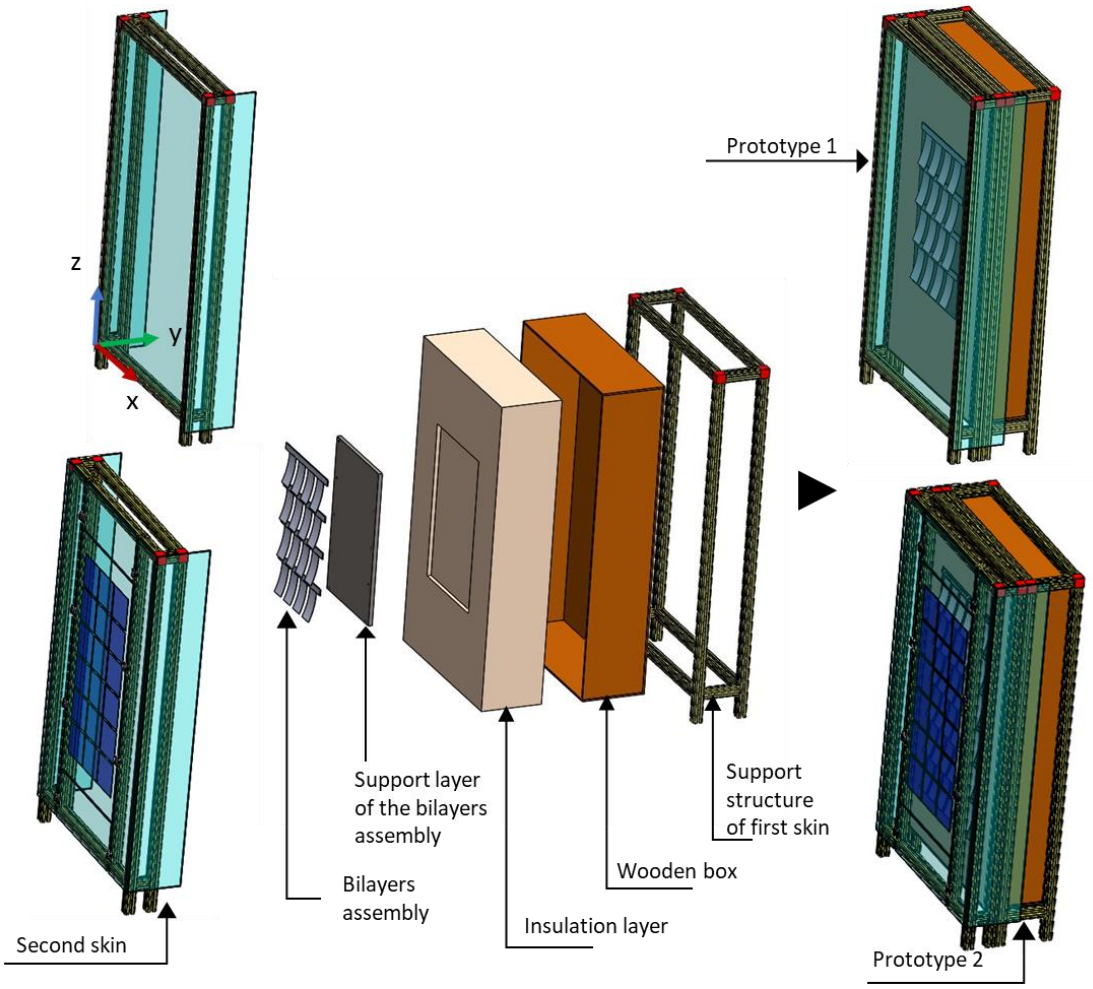

Figure IV-1: Composition of the prototypes

IV.2.2 Description of prototypes

The prototypes are facade elementary components highly insulated on the supposed interior surface and are composed of two parts.

The first part is the facade first skin. It represents the multilayer wall and is constituted by an insulation layer extruded on its centre to receive the concrete wall supporting the bilayer assembly (the bilayers and their mounting components). These are enclosed in a wooden box and mounted into a parallelepiped aluminium structure. The second part is the second skin. It also consists of a parallelepiped aluminium structure, closed on the left, right and front sides by glazings. In prototype 2, the centre of the front glazing is extruded and contains the PV module.

The two parts of the prototypes are nested together to form the facade with an air gap opened at the bottom and top sides (see Figure IV-1). A fan is installed below the second skin unit to blow air from the bottom to the top of the gap to study the impact of the air velocity while considering the configuration with a mechanically ventilated air gap (see Figure IV-2). The air velocity is regulated by changing the voltage supply of the fan.

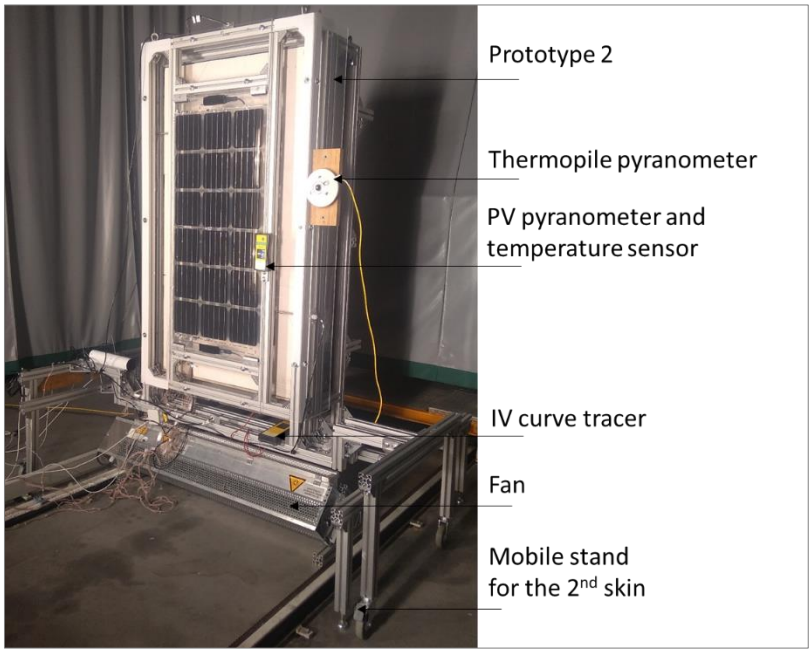

Figure IV-2: Photograph of the prototype

The compositions of the prototypes and the sizes of their elements are given in Table IV-1. The main difference between the two prototypes is the clear glazing instead of a PV module as a second skin in prototype 1. Apart from that, a larger size of the support layer and more bilayers are studied in prototype 2, as given in Table IV-1.

In detail, the PV module used in prototype 2 is a glass-to-glass frameless bifacial module of 55 cm x 115 cm in size. It is composed of 3 mm tempered glass covers on the front and back sides, front and back layers of 600 µm ethylene vinyl acetate (EVA) encapsulants, and 18 monocrystalline PERC (Passivated Emitter Rear Cell) bifacial PV cells arranged in rows of six (6) and columns of three (3) cells. Each cell has a size of 16.4 cm x 16.4 cm and 20% of efficiency. The PV module weighs 10.3 kg and is 7 mm thick. It has a transparency factor of 24% with an active area of 0.49 m². Considering a 10% contribution from the PV bifaciality, the module has 98Wp nominal power, an open circuit voltage of Voc = 12.1V, a short circuit current of Isc = 9.44A and a 77.3% fill factor.

Table IV-1: Compositions and size of the prototype elements

Parts	Materials	number	Height (z) [mm]	Width (x) [mm]	Thickness (y) [mm]	Prototype
Prototype	-	-	1720	960	354 + air gap thickness	1 & 2
First skin						
Insulation layer	Extruded polystyrene	1	1500	850	300	1 & 2
Support layer	Concrete (default material)	1	750	450	20	1
			1060	550	20	2
Bilayers	Aluminium/ PMMA	16 (4x4)	170	70	1.2	1
	Invar/ PMMA				1.25	
	Aluminium/ PMMA	36 (6x6)			1.2	2
Second skin						
Air gap	-	-	-	-	100/150/200	1 & 2
Front and side glazings	Plexiglas (PMMA)	-	1500	Front: 960 Sides: 250	8	1 & 2
PV module	Layers of Glass/ EVA encapsulant/ PV cells/ EVA encapsulant/ Glass	1	1150	550	7	1 & 2

IV.2.3 Description of the bilayer assembly considered

The bilayers considered for testing with the two prototypes have been characterised in Chapter III and are w_b = 7 cm wide and L_b = 17 cm long, with an effective length of L_e = 15.5 cm (the length that is deforming). Their assembly was obtained by clamping them per row with screws between two rectangular thin aluminium plates that were screwed to the support layer (see Figure IV-3).

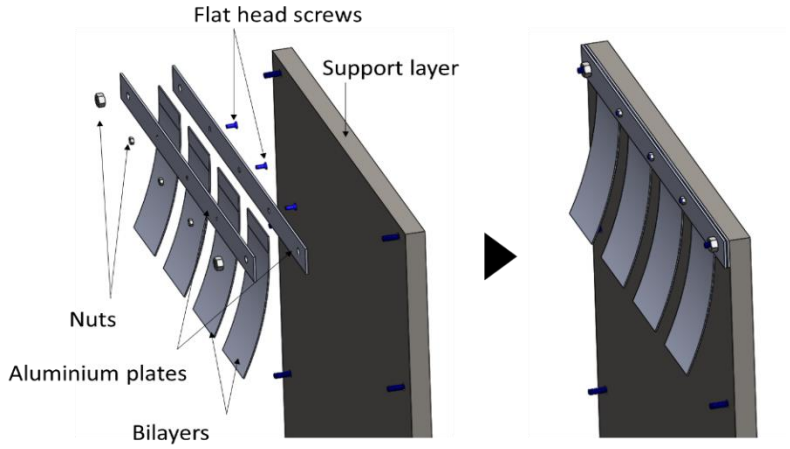

Figure IV-3: Mounting procedure of the bilayers on the support layer

In prototype 1, sixteen bilayers, in total, have been arranged on the support layer in rows and columns of four (4). A staggered bilayer assembly of eight (8) elements has also been built. In prototype 2, the bilayers were mounted in rows and columns of six (6), resulting in 36 bilayers. These assemblies have been arranged in order to have two bilayers behind each PV cell.

Figure IV-4(b) and (c) present the different bilayer assemblies built.

(a) (b) (c)

Figure IV-4: Photograph of the concrete support layer (a) without bilayers (W) (b) with the staggered arrangement (S) (c) with the in line arrangement (C)

IV.3 Description of the experimental setup

IV.3.1 Positioning of the solar simulator

A solar simulator was positioned vertically in front of the facade (parallel to the facade). It comprises eight incandescent lamps of 4000 W, which irradiate up to 1200 W/m² when all lamps are switched on. Its radiation is sufficiently representative of solar radiation. The spectral energy distribution of the solar simulator at 1000 W/m² and that of the sun at the same irradiation value with an air mass coefficient of 1.5 (AM 1.5G) are shown in Figure IV-5.

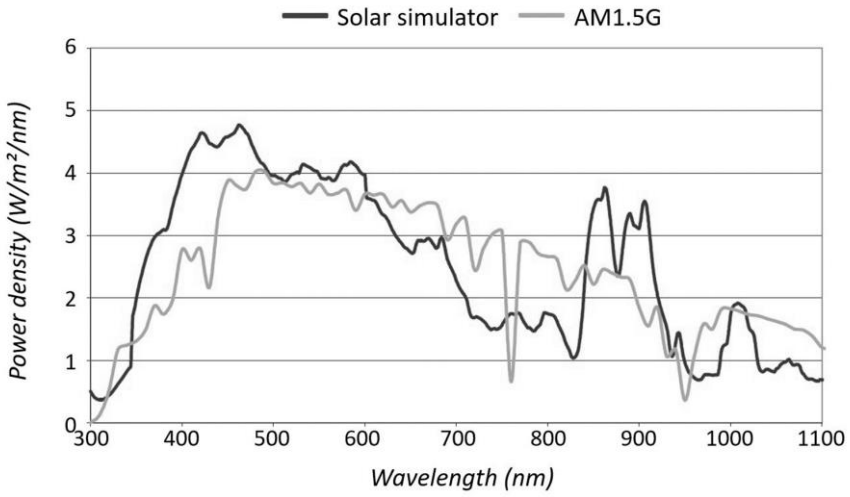

Figure IV-5: Comparison of the spectral energy distribution of the solar simulator and the sun at AM1.5G

This figure shows that the two power densities are close. The simulator provides lower energy than the sun above 1000 nm, but this range represents only 0.93% of total solar energy at 1000 W/m² and AM1.5. It covers the spectral (300 nm to 1100 nm) range suitable for investigating the PV module thermal and

electrical behaviour (Assoa, Sauzedde, et al., 2017). Moreover, the simulator contained double glazing that can be cooled to represent a cold sky with a temperature of 17°C in front of the lamps.

The lamps are in rows of four and columns of two. In this experiment, only 4 lamps at the bottom, which were in front of the facade, were used (see Figure IV-6). Their positions within the simulator were set in a way to obtain a disparity of irradiation inferior to ±10% on the prototype. For this, irradiation mapping was performed by measuring the incident global radiation at four corners and in the middle of the support layer with a pyranometer (positioned on the same plane as the facade second skin). The intensity of the lamps was tuned at the beginning of the experiment to deliver the desired irradiation value.

Figure IV-6: Photograph of the vertical position of the solar simulator set for the test campaign

IV.3.2 Description of the prototype instrumentation

The prototypes have been instrumented with T-type thermocouples of TC-Direct measuring the surface temperature of its layers with an accuracy of ±0.5°C in the range of -40° to 125°C and an accuracy of around ±0.2°C after calibration. The main thermocouples were positioned on the front and back surfaces of the glazing and the support layer. The front surface of the support layer was highly instrumented to observe the temperature disparity induced by the application of the bilayers on it. Thus, thermocouples were placed behind and on the interspaces of bilayers according to the transversal (axis x) and longitudinal (axis z) directions of the prototype (rows and columns of bilayers). Two thermocouples measured the temperature of each instrumented bilayer at its two ends in prototype 1. In prototype 2, only one thermocouple was used at its free ends. The thermocouple at the mounting (the aluminium plate) also enabled to determine the temperature at the fixed end.

With the assumption of a symmetric pattern of temperature distribution along the system, only one-half of the prototype was instrumented with thermocouples. On the other half, two fluxmeters (FQA018C from Ahlborn) were fixed at the top and bottom of the support layer interior surface. Their calibration accuracy was 5% with -0.12%/K of temperature coefficient aside from a nominal temperature of 23°C.

The air velocity and temperature in the gap were measured with anemometers and thermocouples. They were positioned on the inlet and outlet of the air gap in the middle of its width and thickness. Two others were on the bottom and the top of the support layer, respectively, on the left and right sides. Those sensors were positioned diagonally so that the disturbance of the airflow induced by the first anemometer at the bottom is not strongly perceived by the one positioned on the top. The anemometers are air velocity transducers of TSI. The one on the top of the support layer was omnidirectional of 8475 model, with an accuracy of more or less 3% of the reading plus ±1% of the selected full scale. The others were the 8455

models. They have an accuracy of 2% of reading plus ±0.5% of the full scale. There was no particular reason behind the use of the two different models of anemometers. They were chosen according to their availability. Nonetheless, the omnidirectional air velocity transducer was positioned at the top bilayers support layer as the airflow might be the most disturbed at this level.

The positions of the mentioned sensors are given in Figure IV-7 and Figure IV-8, respectively, for the first and second prototypes.

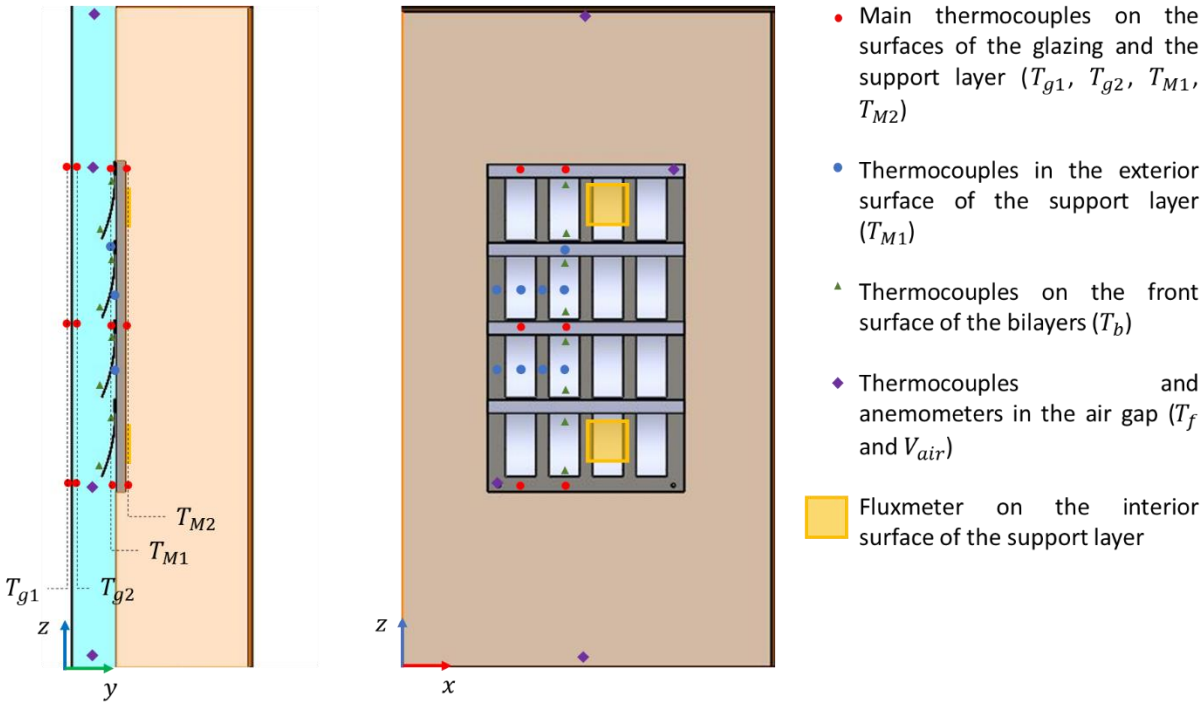

Figure IV-7: Instrumentation of Prototype 1

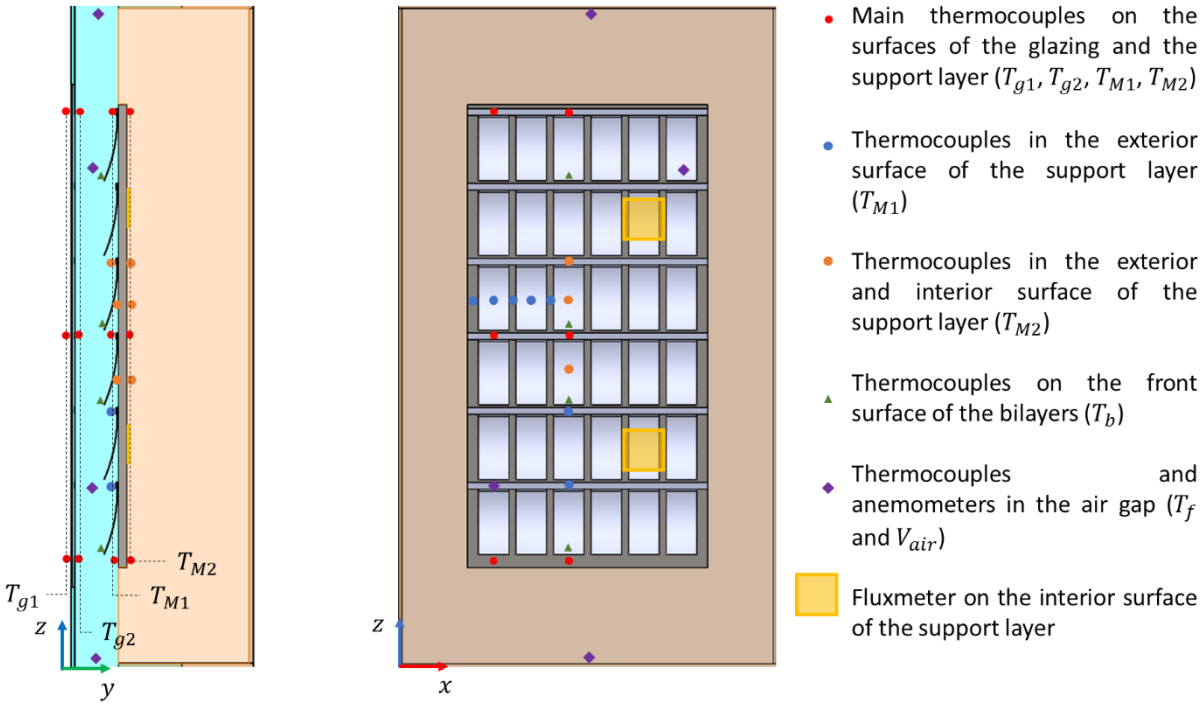

Figure IV-8: Instrumentation of Prototype 2

Two T-type thermocouples measured the indoor ambient air temperature beside and behind the prototypes to determine the testing conditions. A pyranometer CMP11 of Kipp & Zonen was hung on the same plane as the glazing to measure the solar global radiation with an accuracy of ±1.4%.

All the sensors have been connected to an Agilent 34972A data logger collecting the data with a 10-second time step. Labview software has been used to pilot the data collection, invert the raw measurement output (voltage and current) and append the calibration correction to the temperature measurements.

For the bilayer deformation analysis, the initial deflection at each of their free end was measured with a graduate ruler (with ½ mm graduation) punctually at the beginning of each series of tests. Their final deflection at a steady state is estimated with the approximative equation determined in Chapter III.

The electrical characteristics of the PV module were also measured punctually using an IV curve tracer of the brand TRI-KA (www.tri-ka.com). It provides values of open circuit voltage, short circuit current and electrical voltage, current and power at the maximum power point in standard test conditions (STC: with 25°C of PV module temperature and at 1000 W/m² of solar global radiation). It has an accuracy of ±1% of the reading on the voltage and current. It was connected through radiowave to a device called TRI-SEN device of the same brand, which provides the module temperature and the solar global radiation incident (through a photovoltaic pyranometer) on the PV module plane with accuracies of ±3% and ±5%, respectively. The position of the pyranometer CMP11 of Kipp & Zonen and the TRI-SEN device on the prototypes can be seen in Figure IV-2.

IV.3.3 Principle of application of the test plan

For each configuration that had been tested, the prototype was subjected to three (3) levels of irradiation G and air velocity V_{air}. Those irradiations correspond to the intensity of lamps of 50%, 70% and 95% which permit obtaining around 400, 600 and 850 W/m² average on the support of prototype 1 and 350, 550 and 800 W/m² for prototype 2. The average irradiations on prototype 2 were smaller, given its bigger size. Nonetheless, they were close to 400, 600 and 850 W/m² at the centre of prototype 2. Therefore, those three values were used as references to present the results from the three irradiations and were considered to forecast the behaviour of the prototype in winter (corresponding to the low irradiation 400 W/m²), mid-season (600 W/m²) and summer (850 W/m²). The selected air velocities are 2 m/s and 1 m/s at the entrance of the air gap, and experimentations with natural ventilation (through the buoyancy effect) are also performed.

The testing constraints were applied in series on the prototype, beginning from the constraints providing the lowest temperature (400 W/m² and 2 m/s) to that leading to the highest temperature (850 W/m² and natural ventilation). The constraints were modified when the steady state was considered to be reached, more precisely, when all temperatures did not vary by more than 0.5°C in ten minutes. As a result, the temperature on each node has a staircase evolution. The last measurement at each step corresponds to the temperature at the steady state for the given constraints (see Figure IV-9). Only those measurements at steady state were examined, except for the analysis of the impact of the support layer material in which the transient heat transfer regime measurements were considered.

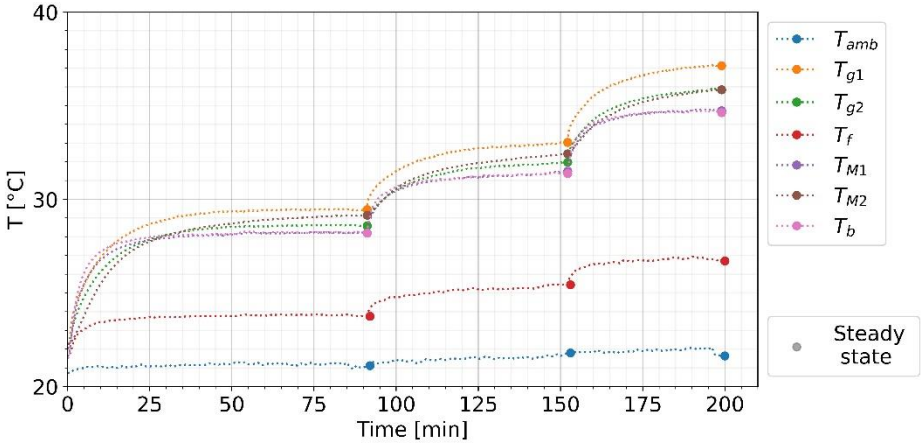

Figure IV-9: Staircase mean temperature evolution at each surface with the value at steady state - series of tests on prototype 1 with insulation support layer at $V_{air} = 2\ m/s$ and $G = 400\ W/m^2$, $600\ W/m^2$, $850\ W/m^2$ on each step

IV.4 Results and discussion of the experimental parametric study

The results of the experimental parametric study are presented and discussed in this section. Although the experiments were conducted indoors, ambient air temperatures varied significantly from one series of tests to another. Hence, the comparative study between configurations is limited to those with ambient temperature differences inferior to 1°C $\left(\left|T_{amb,Test\ 1} - T_{amb,Test2}\right| < 1°C\right)$. Considering the difference in the ambient temperature and the incertitude of the measurements, an uncertainty of around ±1°C is assumed in the comparison. In effect, the resulting temperature evolutions are collinear while comparing two tests with the same configuration and assuming little variation in the heat transfer exchange (convective and radiation) coefficients. However, the temperatures on the surfaces are shifted by the difference in the ambient temperatures if they are stable throughout the tests.

A minimum threshold of temperature difference on each surface was also considered to assume that the bilayer application is impactful. For the glazing, considering the model of bilayer efficiency according to the temperature difference (see Chapter V), the bilayer application should decrease the temperature by at least 2.5°C to increase the PV module efficiency by 1% (with a temperature coefficient of 0.004/°C). For the support layer, the difference in temperature T_{M1} should be at least 5°C to reduce the flux gain by 1W/m² considering a wall thermal resistance of 5 (K.m²)/W.

IV.4.1 Impact of the arrangement of the bilayers: Test 1

The analysis of the bilayers arrangement (Test 1) was conducted on prototype 1 without bilayers (prototype 1 W), with bilayers arranged in staggered (prototype 1 S) and in line (complete coverage) (prototype 1 C) with concrete and wood support layers (see Figure IV-4).

IV.4.1.1 Impact on the external surface of the support temperature

The temperature map on the external surface is analysed to highlight the desired effects of the two bilayer arrangements. For this, temperature maps on the first half of the support layer surface are established for the three configurations in Figure IV-10. Each region in the map is considered to have a uniform temperature and corresponds to the longitudinal and transversal interspaces between the bilayers and the parts that are supposed to be behind the bilayers in the in line arrangement. The results

were from the irradiation $G = 850\ W/m^2$ and naturally ventilated (buoyancy effect) air gap, which provided the most extreme case of temperature disparity in the support surface.

As expected, the temperature along the support layer height (axis z) increases uniformly from bottom to top in prototype 1 W (without bilayers). The temperatures on the same height level are sensibly equal. Whereas, for the cases with bilayers (in prototype 1 S and prototype 1 C), the temperature increment along the support height is observed only while considering the shaded and unshaded surfaces separately. The temperature of the shaded surface (or the surface behind the bilayers) is lower than that of interspaces or the parts that are not shaded. The application of the bilayers leads to a high temperature disparity on the support surface because of heterogenous shading. The interspaces between the bilayers and the edges have a higher temperature than the part behind them. On prototype 1 S, the temperature gradient at the same height level is up to 8°C due to the staggered arrangement. This difference increases with irradiation and the decrease of airgap ventilation, with a minimum of about 2°C at the minimum irradiation $G = 400\ W/m^2$ and maximum air velocity $V_{air} = 2\ m/s$. The longitudinal edges have the highest temperatures in the prototypes with bilayers according to the height level since the unshaded insulation influences the edges.

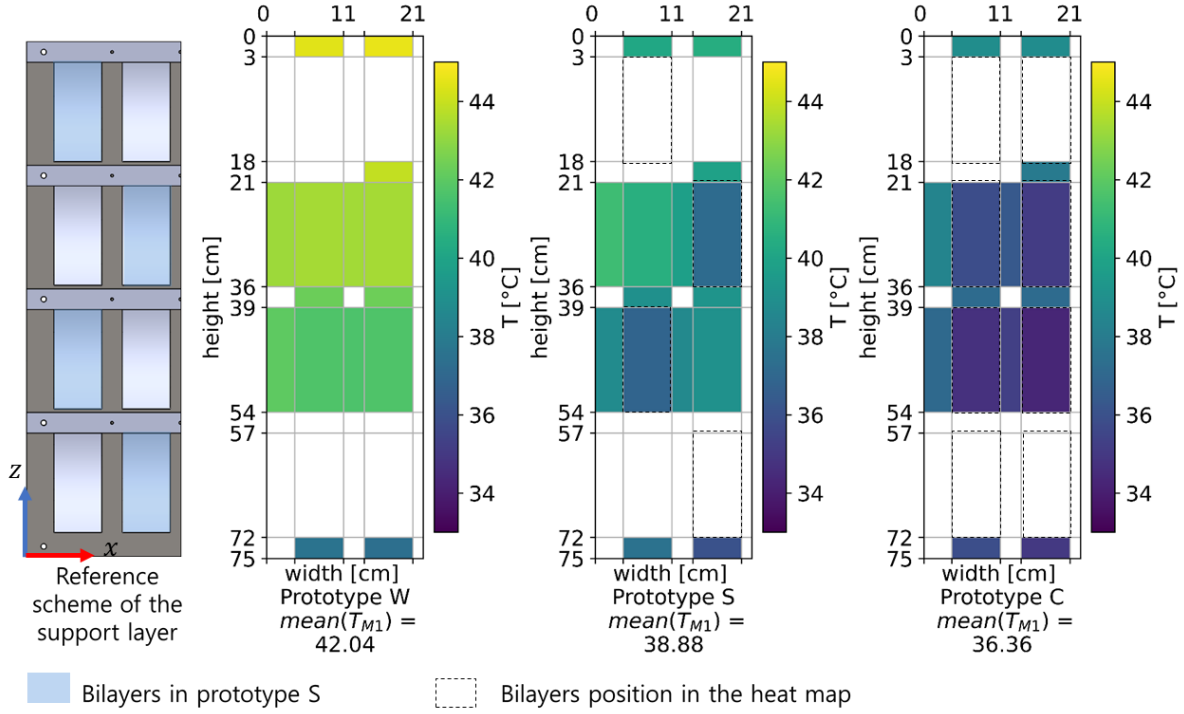

Figure IV-10: Temperature map of the external surface of the support layer according to the arrangement of the bilayers at $G = 850\ W/m^2$ and naturaly ventilated air gap on prototype 1

Globally, the temperature range in prototype 1 C is the lowest, while the one without bilayers (prototype 1 W) is the highest. The magnitude of the difference in temperature between the three configurations is discussed further in the following subsection. This first investigation confirms the cooling effect from the bilayers. Shading is the main component in this cooling. When the bilayers are bent, they induce turbulence and increase the convective heat transfer. This effect would also contribute to the cooling and is showcased by the study of the staggered arrangement (prototype 1 S).

IV.4.1.2 Impact on the temperature on each surface of the prototype

The mean temperature at the surface layers is studied for a global investigation. The first analysis was with the lowest irradiation $G = 400\ W/m^2$. The temperature observed at each layer for the naturally ventilated air gap is plotted in Figure IV-11a. The focus is on the temperatures of the interior side of the

glazing T_{g2} and the exterior side of the support layer T_{M1} which are directly impacted by the bilayers. In the support layer, the temperature reduction from the presence of the bilayers can be easily noticed. It is up to 6°C and 3°C, respectively, from the in line and staggered arrangements (prototype 1 C and prototype 1 S). However, considering these irradiation and air ventilation constraints, the bilayer application has no cooling effect on the glazing. The temperature differences are all inferior to 1°C.

The investigation of the test performed with $V_{air} = 2\ m/s$ shows that heat dissipation is enhanced with forced ventilation, leading to lower facade temperature, which is consistent. The impact of the in line arrangement in prototype 1 C is relatively the same as in natural ventilation on the support layer and the glazing compared to prototype 1 W (without bilayers). The difference in T_{M1} is 6°C. It remains negligible in T_{g2} (see Figure IV-11b). Whereas the performance of prototype 1 S with the staggered arrangement increases with mechanical ventilation. On the glazing, a slight temperature reduction is observed ($\Delta T_{g2} = 1\ °C$) compared to the prototype 1 W. Though, this remains small considering the value of uncertainty in the result comparison (±1°C).

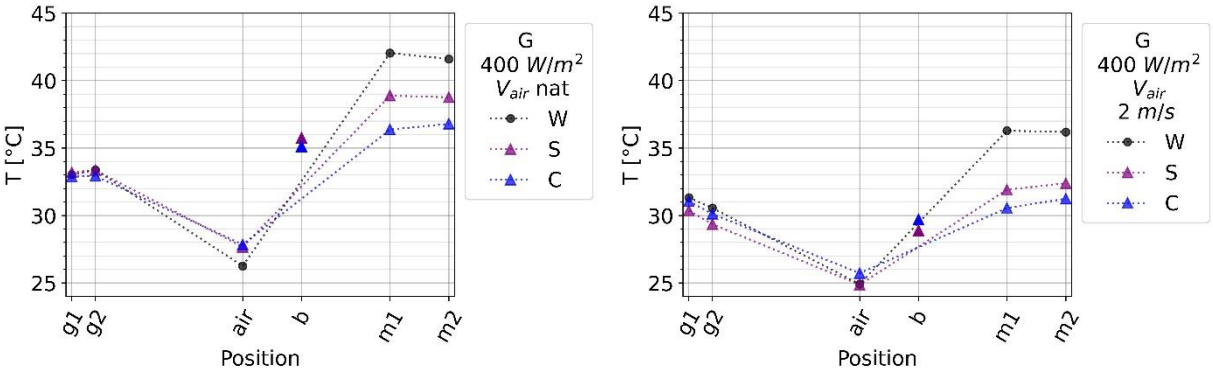

(a) *(b)*

Figure IV-11: Temperatures in prototype 1 according to the bilayers arrangement for $G = 400\ W/m^2$ (a) naturally ventilated air gap (b) air velocity at the entrance is $V_{air} = 2\ m/s$

The improvement brought by the staggered arrangement in prototype 1 S is perceptible by comparing it with prototype 1 C with the in line arrangement of bilayers. On the support layer, the difference in T_{M1} between the two prototypes (1 S and 1 C) is 3°C with natural ventilation and becomes 1°C with $V_{air} = 2\ m/s$ at the air gap entrance. This decrease in temperature difference is also observed with $G = 600\ W/m^2$ and $G = 850\ W/m^2$ if only the naturally ventilated façade and the air velocity $V_{air} = 2m/s$ are compared. On the glazing, it can be suggested that prototype 1 S has the same performance as prototype 1 C except at high irradiation and natural ventilation with $G = 850\ Wm^2$, conditions in which the bilayer application is the most impactful, as shown in previous results (see Table IV-2).

Table IV-2: Comparision of temperatures at the interior side of the glazing T_{g2} and the exterior side of the support layer T_{M1} in prototype 1 S with straggered arrangement and prototype 1 C with the in line arrangement of bilayers

$G\ [W/m^2]$	400			600			850		
$V_{air}\ [m/s]$	nat	1	2	Nat	1	2	Nat	1	2
$\Delta T_{g2} = T_{g2}(S) - T_{g2}(C)[°C]$	<1	<1	-1	<1	2	0	3	2	<1
$\Delta T_{M1} = T_{M1}(S) - T_{M1}(C)[°C]$	3	2	1	5	5	3	5	6	4

Those results indicate that the desired turbulence enhancement from the staggered arrangement is achieved only with significant air velocity in the gap, thus with mechanical ventilation. Its effect remains

inferior to prototype 1 C and is reduced at high irradiation. The staggered arrangement can be considered a midway compromise between prototype 1 W and prototype 1 C, considering the other properties of the prototypes.

The temperatures from the three configurations are shown in Figure IV-12 at $G = 850\ W/m^2$ with natural ventilation to highlight the bilayer effect at high irradiation. Compared to the prototype without bilayers, the temperature reductions are respectively $\Delta T_{M1} = 15°C$ and $\Delta T_{M1} = 11°C$ on the external side of the support layer from prototype 1 C and prototype 1 W. Those reductions are from the shading and fin effects of the bilayers on the wall. In addition, they are also because of bilayers' reflective properties, which reduce the absorbed radiation on the wall. According to the thermal model validated in Chapter VI, the radiation absorbed on the wall decreases by up to 50% due to the presence of the bilayers.

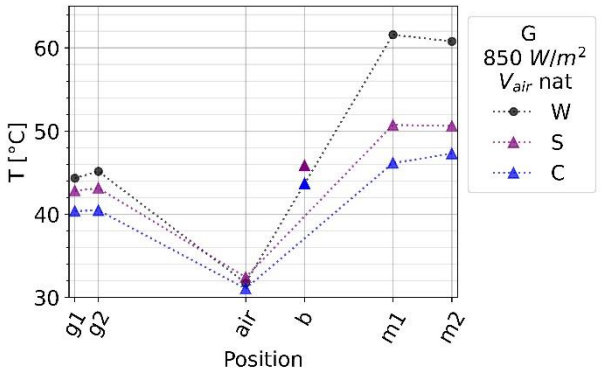

Figure IV-12: Temperatures in prototype 1 according to the bilayers arrangement for $G = 850\ W/m^2$ in naturally ventilated air gap

A more tangible temperature reduction can be observed on the glazing, with $\Delta T_{g2} = 4°C$ and $\Delta T_{g2} = 2°C$ from the comparison of prototype 1 W respectively with prototype 1 C and prototype 1 S. High irradiation leads to higher bilayer temperature and bending. Thus, it can be suggested that heat convection on the glazing is increased due to disturbance of the airflow that turns out to be turbulent. This increase is estimated at up to 20%, considering the thermal power transmitted to the air. Nonetheless, the temperature decrease can also be linked to the low emissivity of aluminium ($\varepsilon_{Al} = 0.09$) leading to a low radiative exchange between the warmer wall and colder glazing. To conclude, the bilayer impacts are more tangible at high irradiation, which corresponds to the purpose of its integration for heat management in summer.

IV.4.1.3 The relevance of the bilayer application over the use of mechanical ventilation

The relevance of the bilayer application in a BIPV facade over the implementation of mechanical ventilation for facade cooling is investigated in this part. For this, Figure IV-13 compares the temperature from prototype 1 W at $V_{air} = 2\ m/s$ with the prototype 1 C at natural ventilation. Here, the prototype with a wooden support layer is studied as the tests conducted at different air velocity levels are comparable according to the testing ambient temperature conditions with this support. For both $G = 400\ W/m^2$ and $G = 850\ W/m^2$, prototype 1 W with mechanised ventilation leads to lower temperatures at T_{g2}, with temperature differences of about $\Delta T_{g2} = 2$°C. Though, this decrease is only from the interior side of the glazing. Whereas on the support layer, the support with bilayers always leads to a lower temperature, with the difference increasing with the irradiation. Those temperature differences are $\Delta T_{M1} = 2°C$ and $\Delta T_{M1} = 5°C$ respectively for $G = 400\ W/m^2$ and $G = 850\ W/m^2$.

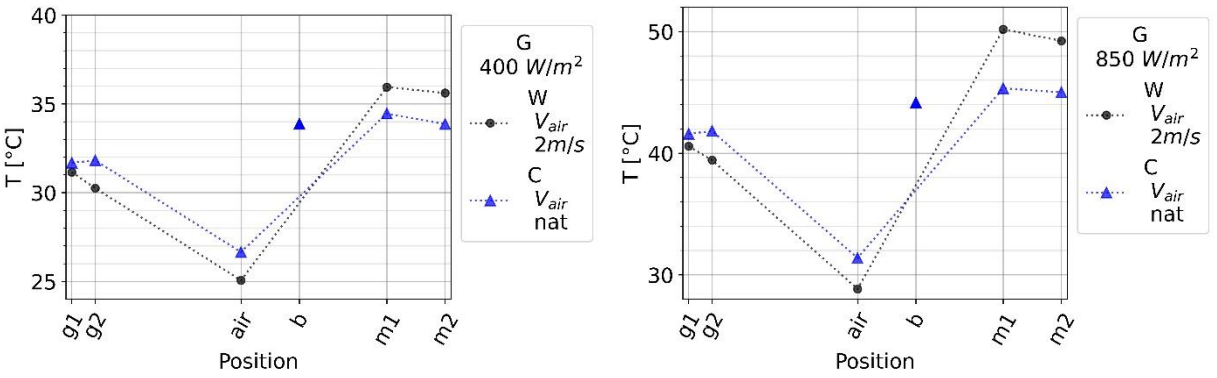

(a) *(b)*

Figure IV-13: Temperatures in prototype W (without bilayers) at $V_{air} = 2\ m/s$ and the prototype C (with bilayers arranged in line) at natural ventilation with a wooden support layer (a) for $G = 400\ W/m^2$ (b) for $G = 850\ W/m^2$

Therefore, the application of the reflective bilayers arranged in line can compete with the installation of mechanical ventilation in airgap for the cooling of the wall. However, for the glazing, forced ventilation remains more efficient for its cooling. On this layer, the bilayer effect at natural ventilation is small and can be observed only at high irradiation.

IV.4.2 Selection of the appropriate bilayers: Test 2

Thanks to the results from Test 1, the study of the impact of the bilayers arrangement, an in line arrangement on prototype 1 (C) can be taken as a reference to select the most optimised bilayers among Aluminium-PMMA (APA) and Invar-PMMA (IPA). The comparison is undertaken from the tests performed with $G = 400\ W/m^2$ and $G = 600\ W/m^2$ (irradiation levels in which comparable results were obtained) and a concrete support layer. The bilayers have considerably the same initial deformation in those compared experiments.

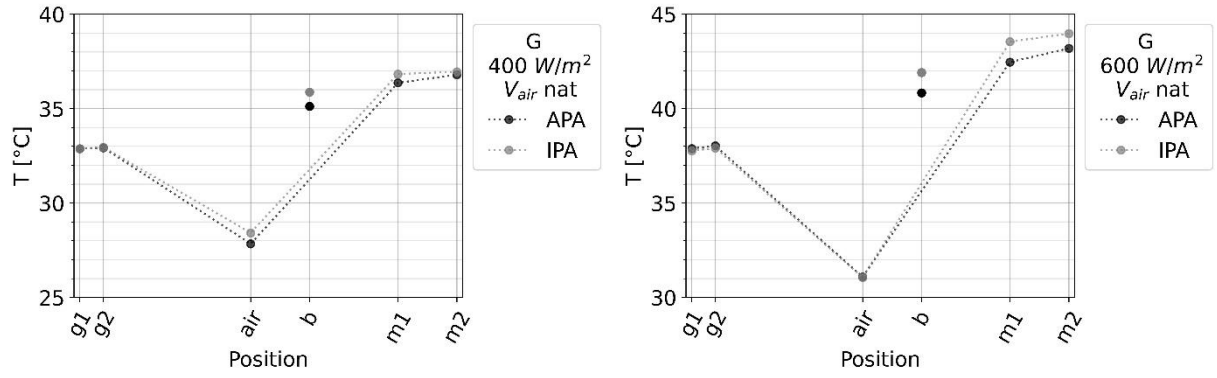

(a) *(b)*

Figure IV-14: Temperatures in the prototypes with Aluminium-PMMA bilayers and with Invar-PMMA bilayers with natural ventilation and (a) $G = 400\ W/m^2$ (b) $G = 600\ W/m^2$

Figure IV-14 shows that the prototype temperatures from the two configurations are very close for the test conducted with natural ventilation. At $G = 600\ W/m^2$, the temperature in the prototype Invar-PMMA seems to be slightly higher at the bilayers and the support layer by $\Delta T_b = \Delta T_{M1} = 1°C$. Nevertheless, this difference is negligible. Table IV-3 shows that the same range of temperature difference was obtained in the prototype with forced ventilation.

Table IV-3: Temperature differences between the prototypes with Aluminium-PMMA (APA) bilayers and with Invar-PMMA bilayers (IPA) at $G = 400\ W/m^2$ and $G = 600\ W/m^2$

$G\ [W/m^2]$	400			600		
$V_{air}\ [m/s]$	Nat	1	2	nat	1	2
$\Delta T_{g2} = T_{g2}(IPA) - T_{g2}(APA)[°C]$	<1	<1	-1	0	0	-1
$\Delta T_b = T_b(IPA) - T_b(APA)[°C]$	1	1	-1	1	1	-1
Expected $\Delta y_b = y_b(IPA) - y_b(APA)[mm]$	2	2	-1	3	2	-1
$\Delta T_{M1} = T_{M1}(IPA) - T_{M1}(APA))\ [°C]$	1	0	-1	1	0	-1

The expected difference in the deformation of the bilayers Invar-PMMA and Aluminium-PMMA is also negligible, at most $\Delta y_b = 3\ mm$ at $G = 600\ W/m^2$ (according to the deflection equations determined in Chapter III). In this result, the deflection in the Invar-PMMA is considered uniform along their length. Thus, the expected higher convection enhancement from those bilayers is not observed. Considering the similarity of the two bilayers' performance against the disadvantages of the couple Invar-PMMA, the bilayer Aluminium-PMMA is chosen for further investigation. Indeed, Invar is more costly and less available. It contains Nickel, which is a rare metal. Also, the deflection of the couple Invar-PMMA is difficult to evaluate with a one-dimensional approximation.

IV.4.3 Impact of the support layers: Test 3

Concrete was the default support layer of the bilayer assembly as it is one of the most commonly used materials in buildings. However, this choice does not allow the dissociation of the effect of convective and radiative heat transfer. In effect, radiative exchange in the air gap is complex, considering the shadowing of the wall from the bilayers and the difference in reflectivity properties between the support layer and the bilayers. Moreover, the impact of thermal conductivity and heat capacity of the support layer on the facade thermal performance should also be investigated for its material selection. For these reasons, prototype 1 was studied with support made of:

- concrete which is thermally conductive and has high thermal capacity;
- wood which has low thermal conductivity but high thermal capacity;
- extruded polystyrene insulation with low thermal conductivity and low thermal capacity;
- and the superposition of aluminium sheet, which has very high thermal conductivity and thermal capacity (see Table IV-4), with the insulation, noted the composite support layer. As both this support and the bilayers are composed of aluminium on their external side, this investigation enables to focus on heat dissipation through convective heat transfer by simplifying the radiative phenomena in the air gap.

Table IV-4: Thermal properties of the tested support layers

Support material	Thermal conductivity $[Wm^{-1}K^{-1}]$	Thermal capacity $[MJK^{-1}m^3]$	Thermal diffusivity $[10^{-6}m^2/s]$
Concrete*	1.40	1.32	1.04
Wood*	0.19	1.16	0.16
Extruded polystyrene *	0.036	0.34	0.82
Aluminium sheet (+ polystyrene)	237	2.43	97.53

*Measured value with Hot Disk TPS 2200

Table IV-5 presents the stabilisation time and the mean surface temperatures (at the interior surface of the glazing T_{g2}, the bilayers T_b, the exterior and interior surface of the support layer T_{M1} and T_{M2}) at steady state considering the four tested support layers and an irradiance $G = 400\ W/m^2$ and $V_{air} = 1\ m/s$. These irradiance and air velocity are common testing constraints applied at the beginning of the test series for all of the support layers tested. Hence, they permit the observation of the temperature stabilization time at the first temperature step of the test series. Table IV-5 shows that the concrete support layer takes the longest time to reach a steady state, followed by the wood, the composite support (aluminium sheet + insulation) and finally the insulation.

Table IV-5: Temperature stabilization time and surface temperatures at steady state according to the support layer at $G = 400\ W/m^2$ and $V_{air} = 1\ m/s$

Support material	Stabilization time	$T_{g2}\ [°C]$	$T_b[°C]$	$T_{M1}\ [°C]$	$T_{M2}\ [°C]$	$T_{M1} - T_{M2}[°C]$
Concrete	1h54min	30	30	31	31	0
Wood	90 min	30	30	31	31	0
Extruded polystyrene	54 min	29	30	30	30	0
Aluminium sheet (+ polystyrene)	70 min	30	31	32	30	2

There are no significant differences in the prototype mean surface temperatures for the considered irradiance. However, the temperature gradient in the composite aluminium and insulation support layer is significant compared to the others. This is probably because, in prototype 1, the thermocouples at the interior side of the support are aligned to the unshaded interspaces of the bilayers. The aluminium sheet allows to uniformise the temperature at the exterior side of the support. On the one hand, aluminium reflectivity is high, reducing the difference in the absorbed heat at the shaded and unshaded parts of the support. On the other hand, the high thermal conductivity of the aluminium sheet reduces vertical temperature stratification along the support. Consequently, the thermocouple at the interior side of the support perceives the effect of the shaded (low temperature) and unshaded (high temperature) surfaces. Whereas in the other support material, only the effect of the unshaded part of the exterior surface of the support is likely perceived by the thermocouples at the interior surface of the support; thus, the measured mean temperature T_{M1} and T_{M2} are around the same temperature (I rounded the results in the table to consider the comparison uncertainty).

To confirm the previous observation, the temperature maps of the exterior side of the support layers at a steady state are shown in Figure IV-15 according to the nature of their material. The results from $G =$

$850\ W/m^2$ and naturally ventilated air gaps are presented as these conditions provide the highest temperature disparity in the surface of the support layer. The mean temperatures achieved at the exterior side of the support are also close for the four materials. The insulator support has the lowest mean temperature but the highest temperature gap between the shaded and unshaded surfaces. At the same height level, the shaded temperature can be as low as 35°C while the unshaded longitudinal edge is 47°C, leading to a temperature difference of 12°C. This alternation of high and low temperatures might create an air vortex trapped under the bilayers. This phenomenon is not intended in the application.

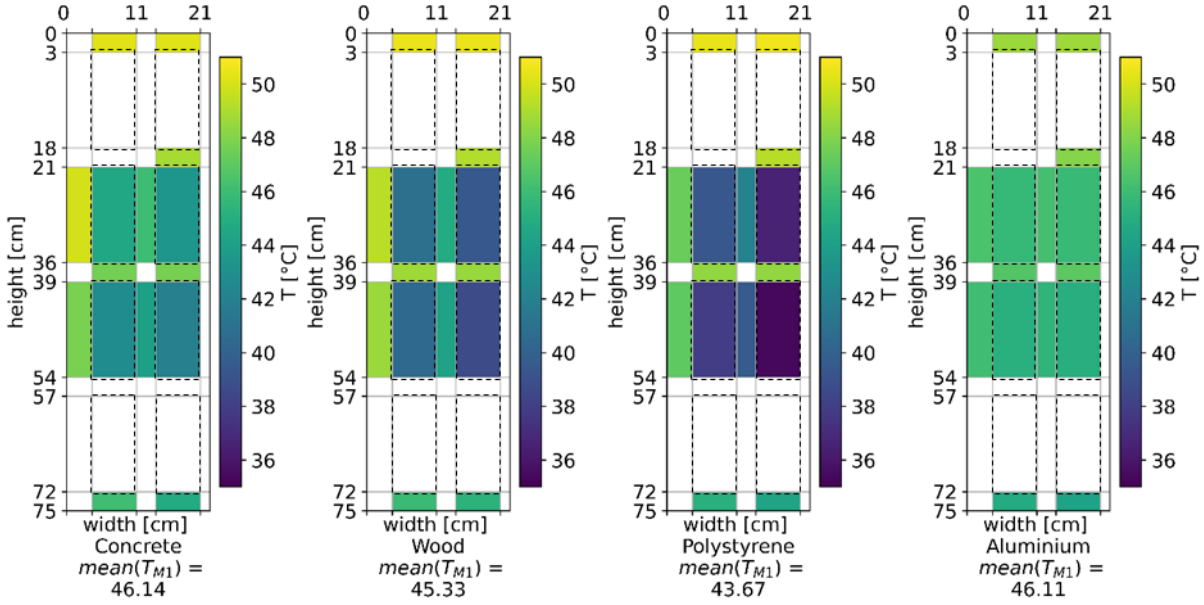

Figure IV-15: Temperature repartition on the exterior side of the support layer according to the support material $G = 850\ W/m^2$ and naturally ventilated air gap

A high disparity of surface temperature is also observed on the wooden support layer, with temperature differences up to 10°C at the same height level. The differences are up to 7°C on the concrete support layer and as low as 1°C on the support with the aluminium sheet at the same height level. Even though the vertical temperature gradient was still observed in the support layer with the aluminium sheet, it can be suggested that this support layer configuration can help direct the airflow upward without inducing air trapping beneath the bilayers. Nonetheless, since the shading effect is likely minimized with this support layer, prototype 1 with this support should be compared, considering the configuration without bilayers but with the aluminium wall. In effect, validating that heat dissipation through bilayers still significantly reduces the facade temperature is necessary considering these two configurations. This investigation was not addressed in this study and is one of its outlooks. A concrete support layer was still used for the remaining study, given its common use in buildings.

IV.4.4 Impact of the air gap thickness: Test 4

The effect of the air gap thickness variation is studied in this subsection by comparing air gap thicknesses of prototype 1 from 10, 15, to 20 cm, noting that the air gap of 10 cm is taken as reference as the bilayers are sized to perform at this airgap size. The results of the tests performed with $G = 600\ W/m^2$ and with natural ventilation in the air gap are analysed.

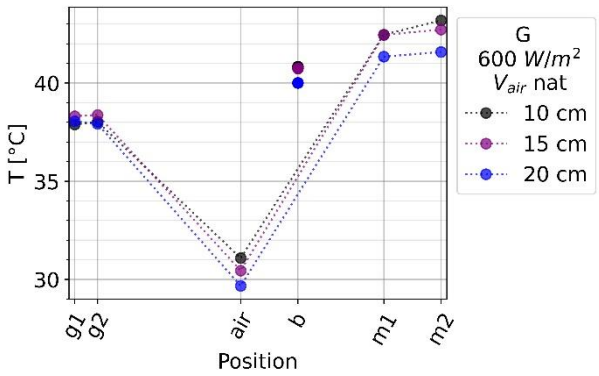

Figure IV-16: Temperatures in prototype 1 for the study of airgap thickness at $G = 600\,W/m^2$ and naturally ventilated air gap

The comparisons of the mean temperature at each node of the prototype are given in Figure IV-16. As shown in the graph, there is no significant temperature difference in each layer. Especially in the glazing, the differences between the three configurations are less than 1°C. On the exterior side of the wall, the temperature values of the prototype with the 10 cm air gap and the 15 cm air gap are similar. More noticeable gaps are observed compared to the 20 cm air gap thickness. This configuration is 1°C and 2°C cooler than the cases with a 10 cm air gap on the exterior and interior sides of the support layer. Those results indicate that increasing the air gap thickness enables, as expected, cooling down the facade. However, the cooling enhancement is insignificant and concerns only the wall.

IV.4.5 Impact of the dummy PV cells: Test 5

During test 5, dummy PV cells made of black PFTE sheets were glued on the external surface of the glazing of prototype 1 to precast the effect of the PV cells shading on the wall. Each sheet is 17 cm x 16.5 cm in size. They result in a glazing semi-transparency factor of 34% according to the support layer size (see Figure IV-17). The experiments are undertaken with $G = 600\,W/m^2$ and a naturally ventilated air gap with a thickness of 15 cm. The comparison of temperatures from the prototypes with and without the dummy PV cells is presented in Figure IV-18.

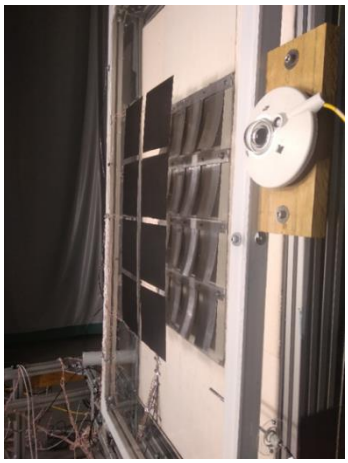

Figure IV-17: Photograph of prototype 1 with dummy PV cells

The additional shading provided by the dummy PV cells decreases both the external surface of support and bilayer temperatures by 5°C. The general trend of the temperature distribution is modified since the effective absorptivity at the glazing has increased, leading to decreased irradiance to the wall. Therefore, a substantial rise in the glazing temperature is observed, up to 16°C and 13°C, respectively, on the

external and internal glazing. The temperature gradient in the glazing also increases significantly. The internal temperature is 2°C lower than the external one. It indicates that heat transfer in the air gap becomes more important for the cooling of the glazing, both from the radiative exchange with the wall and convective exchange with the air.

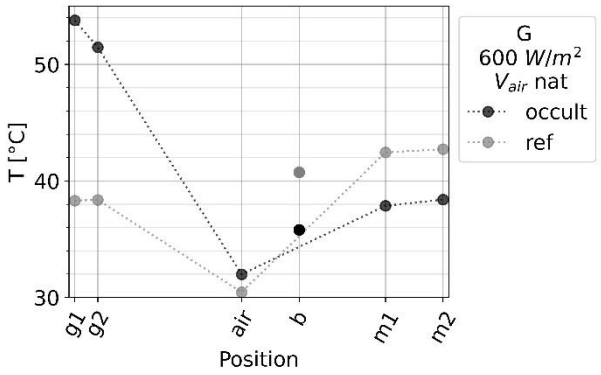

Figure IV-18: Temperatures in prototype 1 with and without dummy PV cells (occultations) for $G = 600\ W/m^2$ and naturally ventilated air gap of 15 cm thick

The investigation shows the change in the facade thermal behaviour by adding the dummy PV cells and confirms their additional solar protection on the wall. However, this study should be completed by comparing the prototype with dummy PV cells but without bilayers. This way, the bilayer application's relevance can be evaluated, considering that the dummy cells also provide shading. Those studies are addressed directly on the investigation of prototype 2 to assess the influence of the bilayers on the PV output power.

IV.4.6 Impact of the bilayer application on the PV facade: Test 6

The experiment conducted on prototype 2 consists of comparing the PV facade prototype with and without bilayers. The bilayers are arranged in line and fully cover the support layer. Considering that two tests per configuration are undertaken with this prototype, the repeatability of the experience has been confirmed. From two tests with the same configuration and under close indoor temperatures, a maximum difference of the measured temperatures of only $\Delta T = 0.7°C$ is obtained in the prototypes.

IV.4.6.1 Impact on the temperature on each surface of the prototype

To address the impact of the bilayers on the facade thermal behaviour, the temperatures measured at steady state from prototype 2 with and without bilayers are plotted in Figure IV-19, considering the irradiations $G = 400\ W/m^2$ with naturally ventilated air gap and $G = 850\ W/m^2$ with the three levels of air velocity.

Similar trends of temperature evolution are obtained in prototype 2 compared to the test with dummy PV cells in prototype 1. However, the temperature on the glazing and the support layer are less important, about 6 and 4°C inferior, respectively, considering the in-line arrangement of bilayers. For the glazing, this is because the PV cells are less absorptive than the PTFE sheets and convert part of the irradiation into electricity. For the support layer, this is linked to a smaller transparency factor of the PV module and a more packed arrangement of bilayers with narrow interspaces both transversally (axis x) and longitudinally (axis z) (see Figure IV-18 and Figure IV-19b).

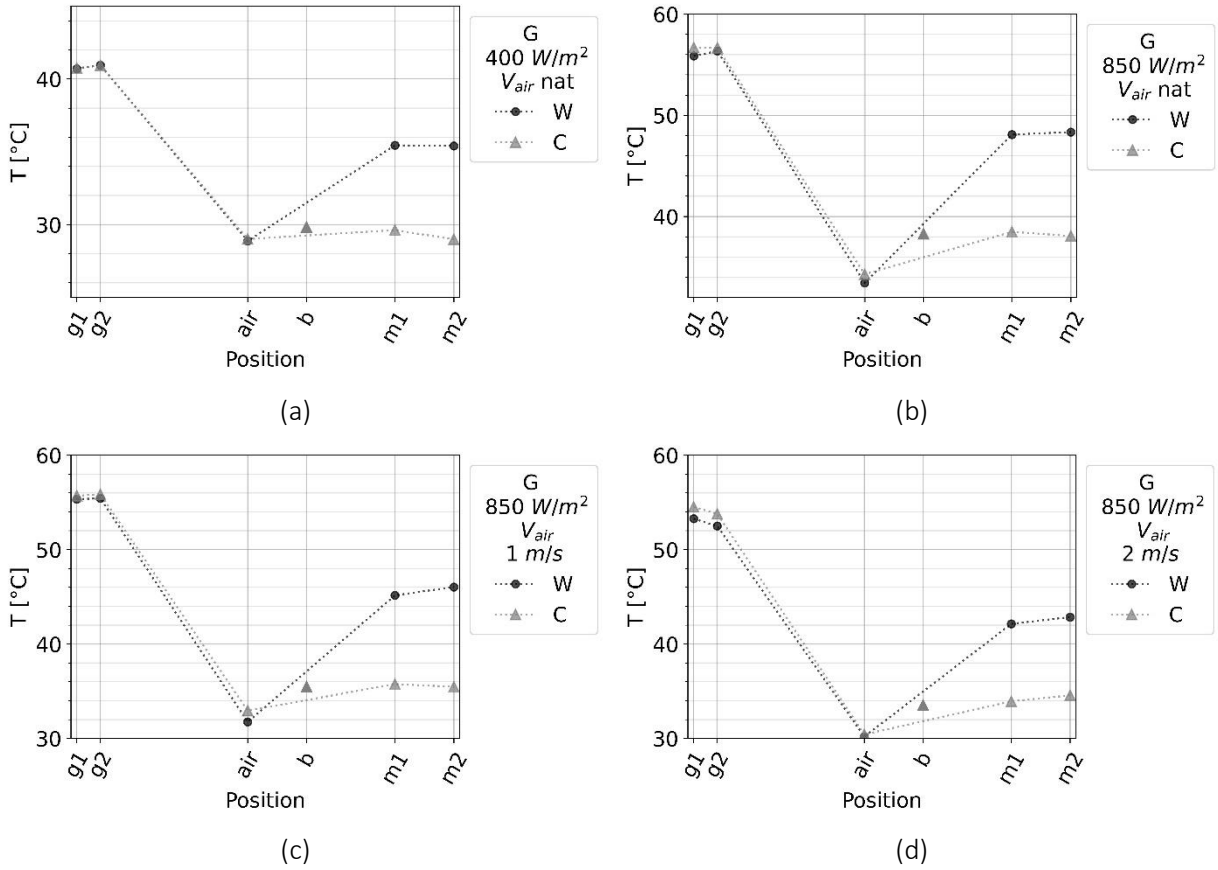

Figure IV-19: Temperatures in prototype 2 considering the configurations without bilayers (W) and with bilayers arranged in line (C) (a) with $G = 400\ W/m^2$ and naturally ventilated air gap (b-c-d) $G = 850\ W/m^2$ (b) and natural ventilation, (c) $V_{air} = 1\ m/s$ (d) and $V_{air} = 2\ m/s$

In prototype 2, the results in Figure IV-19 and Table IV-6 show that the presence of the bilayers does not influence the PV module temperature considering natural ventilation or low air velocity (1 m/s) in the air gap regardless of the irradiation level. With $V_{air} = 2\ m/s$, the prototype with bilayers has slightly higher temperatures with magnitude differences around 1°C at T_{g2} (see Table IV-6). This difference is small but can be linked to pressure losses in the air gap due to the more packed arrangement of the bilayers. It would not affect the PV module performance.

Table IV-6: Comparision of temperature interior side of the glazing T_{g2} and the exterior side of the support layer T_{M1} in prototype 2 without bilayers W and with bilayers arranged in line C

$G\ [W/m^2]$	400			600			850		
$V_{air}\ [m/s]$	Nat	1	2	Nat	1	2	Nat	1	2
$\Delta T_{g2} = T_{g2}(W) - T_{g2}(C)[°C]$	0	-1	-2	0	-1	-1	0	0	-1
$\Delta T_{M1} = T_{M1}(W) - T_{M1}(C)[°C]$	6	4	3	8	6	6	10	9	8

As in prototype 1, important temperature differences are observed between the two configurations on the support layers. Those differences increase with the irradiation and decrease with the rise of air velocity in the gap. Yet, shading is still the main component of wall cooling and has an important role,

especially with high irradiation. In effect, with $G = 850\ W/m^2$, the gap between the two configurations is important. However, the variation of air velocity hardly affects this temperature difference.

IV.4.6.2 Impact on the PV power production

The PV power produced with the prototype with and without bilayers according to the air velocity and the irradiation is given in Table IV-7. As predicted, power production increases with the increase in air velocity. The prototype with bilayers produces more electricity than the configuration without. Nevertheless, the production difference is very small, less than $1\ W$ or $1.6\ W/m^2$ if reported to the PV module area. In effect, the uncertainty in the measurement is ±2% of the power reading, and the reported differences are around the range of the measurement uncertainty (from $\pm 0.6\ W$ to $\pm 1.2\ W$ according to the power measured). However, since the measurements are consistent by always giving the same range of power differences, we conclude that the bilayers have an effect but are small. They have no cooling effect on the PV module, and the power gains are likely related to the reflection properties of the bilayers compared to the support layers made of concrete. An increase in electricity production would probably occur on the back side of the module.

Table IV-7: Comparison of the PV power produced between prototype 2 without bilayer W and with bilayers arranged in line C

$G\ [W/m^2]$	400			600			850		
$V_{air}\ [m/s]$	nat	1	2	Nat	1	2	Nat	1	2
P (Without bilayers W) [W]	27.9	28.6	29.0	42.6	42.9	43.4	57.1	57.6	58.6
P (With bilayers C) [W]	28.8	29.1	29.4	43.3	43.7	44.1	57.7	58.0	59.1
$\Delta P = P(W) - P(C)[W]$	-0.9	-0.5	-0.4	-0.7	-0.8	-0.7	-0.6	-0.4	-0.5
$\Delta P/S_{PV}\ [W/m^2]$	-1.4	-0.8	-0.6	-1.1	-1.3	-1.1	-0.9	-0.6	-0.8

IV.4.6.3 The relevance of the bilayer application over the use of mechanical ventilation

As for prototype 1, the relevance of the bilayer application is investigated by comparing the behaviour of the prototype with bilayers and natural ventilation with the mechanically ventilated prototype without bilayers. Table IV-7 provides the PV power output for this comparison. However, considering the staircase pattern of the test execution, only the tests performed with $G = 400\ W/m^2$ can be compared considering the similarity of the indoor conditions. The result shows that the naturally ventilated prototype with bilayers outperforms the one without bilayers with $V_{air} = 1\ m/s$. It has lower performance compared to prototype W, with $V_{air} = 2\ m/s$. Nonetheless, the power output differences are under the magnitude of the measurement uncertainty (around ±2% in the most pessimistic estimation).

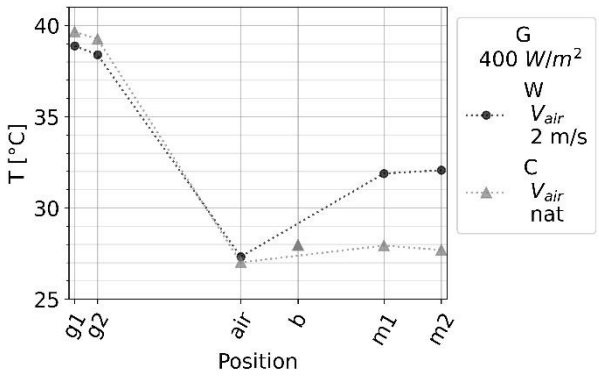

Figure IV-20: Evolution of temperature in prototype 2 without bilayers (W) at $V_{air} = 2\ m/s$ and the prototype with bilayers (C) at natural ventilation for $G = 400\ W/m^2$

The comparison of temperature from this comparable testing constraint ($G = 400\ w/m^2$) is given in Figure IV-20. The temperature of the PV module is very close in the two configurations ($\Delta T_{g2} = 1°C$, the prototype with bilayers having the higher temperature). At the support, a gap of $\Delta T_{M1} = 4°C$ is observed. This confirms that the bilayers permit cooling the wall more than mechanical ventilation, considering the studied air velocity range.

IV.4.7 Precast of winter and mid-season performance according to the impact of the irradiance

All the results presented so far show that applying the bilayer components leads to a cooler wall regardless of the irradiation and air velocity level in the air gap. However, during winter and mid-season, in which the level of solar irradiation is around $400\ W/m^2$ and $600\ W/m^2$, the wall should not dissipate or reject heat but either store heat for the night or transmit heat indoors. This is why, in the concept, closing the air gap at low outdoor temperatures would accumulate solar heat gain in the facade through the greenhouse effect. However, keeping the air gap open can be considered if the preheated air is valorized.

Table IV-8: Study of the heat transmission to the air in the gap of prototype 2 and the heat flux passing through the support in prototype 2 with and without bilayers

$G\ [W/m^2]$	400					
$V_{air}\ [m/s]$	0,4		1		2	
Arrangement	W	C	W	C	W	C
$T_{air,out}\ [°C]$	31	32	30	30	27	27
$T_{air,in}\ [°C]$	28	27	26	26	26	26
$T_{air,out} - T_{air,in} [°C]$	4	5	4	4	2	2
$V_{air,mean}\ [m/s]$	0.28	0.29	0.62	0.61	1.20	1.21
$P_{th}\ [W]$	106	137	242	263	195	225
η_{th}	0.2	0.3	0.5	0.6	0.4	0.5
$\varphi_{M1M2}\ [W/m^2]$	5	3	4	2	4	2
$G\ [W/m^2]$	600					
$T_{air,out}\ [°C]$	35	36	33	34	30	31

$T_{air,in}$ [°C]	28	28	27	27	27	27
$T_{air,out} - T_{air,in}$ [°C]	7	8	6	7	3	3
$V_{air,mean}$ [m/s]	0.37	0.35	0.71	0.65	1.23	1.24
P_{th} [W]	242	280	409	447	408	429
η_{th}	0.4	0.4	0.6	0.7	0.6	0.6
φ_{M1M2} [W/m^2]	6	4	6	3	4	2

To investigate this solution, I have calculated the mean air velocity measured in the gap $V_{air,mean}$ and the temperature difference in the outlet and inlet $T_{air,out} - T_{air,in}$, the thermal power transmitted to the air P_{th} and the mean heat flux passing through the support layer φ_{M1M2}. The thermal efficiency η_{th} of heat transmission to air is also calculated (it is the ratio between the heat transmitted to the air P_{th} and solar irradiation incident on the prototype surface) (see Table IV-8).

The comparison of the prototype with and without bilayers shows that the difference in the air velocity is negligible. The air temperature variation $T_{air,out} - T_{air,in}$ from the prototype with bilayers is likely higher than the one without when the temperature in the gap is increasing, meaning at low air velocity (natural ventilation or $V_{air} = 1\ m/s$) or with a higher irradiation range ($G = 600\ W/m^2$). This result shows a better heat transmission to the air and can be explained by the increase of exchange surface because of bilayer bending. Nonetheless, the difference obtained is very small (about 1°C). However, those slight differences in the temperature gradient in the air gap can lead to a more significant difference in the thermal power (P_{th}) transmitted to the air. The thermal efficiency gap $\Delta\eta_{th}$ varies up to 10%.

On the one hand, considering the comparison uncertainty, the heat transmitted to air in the configuration with bilayers would be at least the same amount as in the prototype without bilayers. On the other hand, regarding the amount of power needed to raise the air temperature by 1°C, it can be precast that more important power transmitted to the air can compromise the decreased heat gain coming through the wall (heat flux φ_{M1M2}) if the preheated air is valorized. Hence, the proposed solution might not increase the thermal performance of the facade in winter but can potentially be equivalent to an ordinary PV facade without bilayers.

IV.5 Conclusions

The evolutive PV facade designed here aims to protect from or dissipate solar heat gain in summer and harvest or admit heat in winter while maximising the PV power production through the application of thermosensitive bilayers. The experimental study effectuated on two reduced-scale facade prototypes was conducted to validate those functionalities.

The results show that the bilayers effectively enable the wall to cool down when the facade is subjected to high solar irradiation. The highest temperature reduction on the wall is obtained when the bilayers are arranged in line, as their main function is to reinforce the sun shading on the wall. Nevertheless, they have a negligible thermal impact on the PV module, but a little reduction of temperature is obtained with the prototype with transparent glazing. A slight temperature rise is observed with the lowly semi-transparent PV module but does not affect electricity production. On the contrary, using reflective bilayers is confirmed to increase the PV power output.

The two selected bilayers have a negligible difference in their thermal effect on the facade. The bilayers Aluminium-PMMA were selected because of their cost, uniform deflection on their length, and the availability and sustainability of the constituent materials. The choice of the support layer of those

components can vary according to the design purpose. A conductive and reflective sheet on the support layer limits the temperature disparity due to the shading. It can also limit air vortexes trapped beneath the bilayers. However, the impact of the shading is minimised in this case, and further investigation is needed to understand the relevance of this configuration. As for the air gap thickness, an increase from 10 cm to 20 cm does not substantially enhance the facade performance, as the bilayers are designed to perform with an air gap thickness of 10 cm.

Finally, the addition of bilayers can always compete with the use of mechanical ventilation with air velocity in the magnitude of 2m/s in terms of support temperature reduction. This finding validates the summer thermal performance intended from the design. In winter, the design can compete with ordinary PV facades only if the preheated air can be valorized when the air gap is open.

The results in this experimental study showed more impact on wall surface temperature reduction than PV power production increase from the bilayers in this experimental scale. This observation is not conclusive regarding the facade behaviour once integrated into the building envelope. For this reason, the measurements are used to validate the numerical model of the facades, which is presented in the following chapter. Then, the facade thermal and electrical performances are assessed in the last chapter considering a building with the bioinspired PV facade.

Chapter V. Thermal modelling of BIPV and the bioinspired facades

V.1 Introduction

Two major numerical investigations are conducted for the design of the bioinspired PV facade. The first one is the study of an ordinary ventilated PV facade aiming at identifying the aspects that should be adaptive (see Chapter II). The second study assesses the feasibility and performance of the newly designed facade with thermosensitive bilayers (see Chapter II and Chapter VI). To carry out those studies, models coupling the assessment of the heat transfer, airflow in the facade gap and PV power output are necessary for each of those facades.

The model is developed with Python through a nodal or resistance-capacitance approach. The basic model denotes the one corresponding to the facade without bilayers. This model is adapted to consider the bilayers deformation, whose estimation formula is given from the experimental study presented in Chapter III.

This chapter presents the development of this basic model, the modifications brought to it from the integration of the bilayers and the validation of the models in the last part.

V.2 Modelling of the facade without bilayers

V.2.1 Presentation of the basic thermal model

An ordinary ventilated PV facade is composed of rows of PV modules, an air gap and a multilayer wall (see Figure V-1). For the cooling of the PV modules, the outdoor air mostly enters at the bottom and is exhausted back at the top of the gap. In this study, semi-transparent bifacial PV modules are considered.

The basic model is developed according to the thermal network presented in Figure V-1, with the occurring convective, radiation, and conductive heat transfer. The PV module is discretized in three nodes of temperatures: the front glass is represented by the temperature T_{g1}, the PV cells by T_{PV} and the back glass by T_{g2}. The air temperature in the gap is T_f. The multilayer wall is described by the temperatures T_{M1} and T_{M2} respectively on the exterior surface and the interior surface of the wall. The temperature nodes in the middle of each layer of the wall are noted in alphabetic order from T_{Ma}, T_{Mb} to T_{MX} the last layer. Hereby hypotheses are considered for the modelling :

- One-dimensional heat conduction through the section of the wall. The temperature on each surface layer is considered uniform.
- The external convective heat transfer coefficient (CHTC) $h_{c:ext,g1}$ depends on the wind velocity V_{wind}.
- The CHTC inside the air gap and between the wall and indoor air are calculated according to the nature of the boundary layer through Nusselt correlations.
- External and internal environments are assumed to behave like a black body. Their radiant temperatures are, respectively T_{env} and $T_{r,int}$.
- The rear surfaces of PV modules and the exterior surface of the wall are approximated as two infinite parallel plates for the estimation of radiation heat exchange.

- Incident solar radiation is uniform on the facade and is assumed to be absorbed in each layer of the PV module (the front glass G_{g1}^a, the PV cells G_{PV}^a and the rear glass G_{g2}^a) and on the external surface of the wall (G_{M1}^a).
- The multiple reflections of solar radiation in the air gap are approximated by a single reflection of the radiation from the wall surface.
- The thermal capacity of the PV modules is neglected.

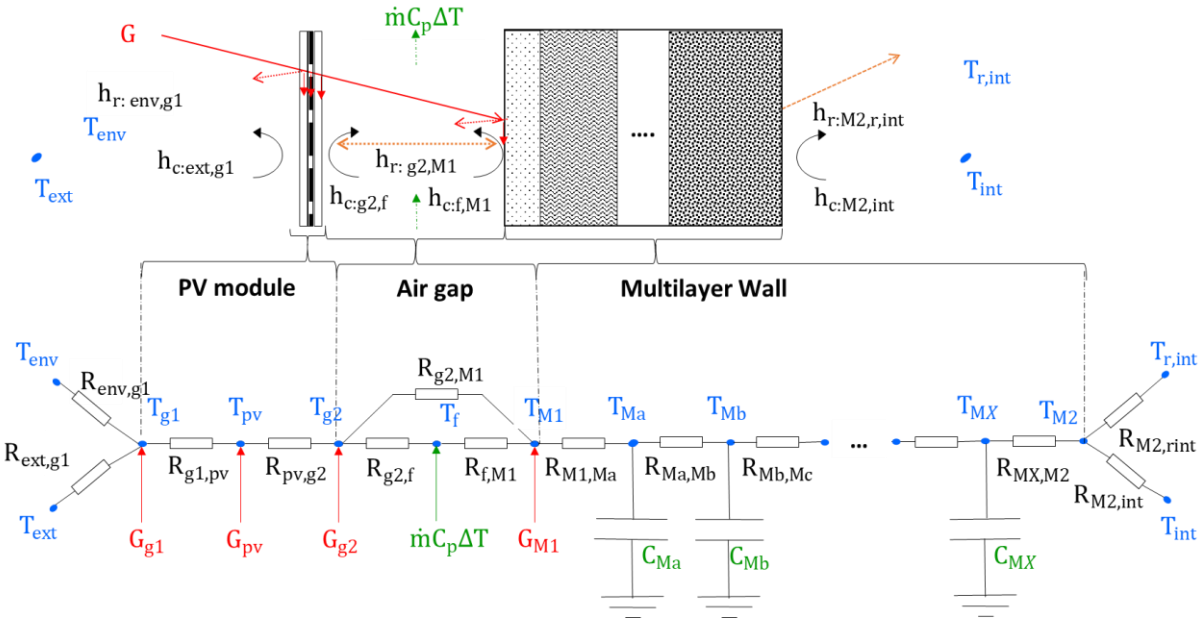

Figure V-1: Thermal network of the ordinary PV facade for the basic thermal model

The convective, radiation and conductive heat transfer coefficients are noted, respectively, by $h_{c:i,j}, h_{r:i,j}$ et $h_{i,j}$, where i,j are the concerned nodes. $\dot{m}$ is the airflow rate and C_{pair} is the thermal capacity of the air. A is the surface area of heat exchange on each surface. The thermal capacity of each wall layer is noted C_i. The time step for the transient heat transfer is Δt. T_{M_i0} is the temperature of the layer in the previous time step. The energy balances for each node are written as follows (see Figure V-1):

$$(T_{g1}):\quad h_{c:ext,g1}(T_{ext}-T_{g1})+h_{r:env,g1}(T_{env}-T_{g1})+G_{g1}^a=h_{g1,PV}(T_{g1}-T_{PV}) \tag{V-1}$$

$$(T_{PV}):\quad h_{g1,PV}(T_{g1}-T_{PV})+G_{PV}^a=h_{PV,g2}(T_{PV}-T_{g2}) \tag{V-2}$$

$$(T_{g2}):\quad h_{PV,g2}(T_{PV}-T_{g2})+G_{g2}^a=h_{r:g2,M1}(T_{g2}-T_{M1})+h_{c:g2,f}(T_{g2}-T_f) \tag{V-3}$$

$$(T_f):\quad h_{c:g2,f}(T_{g2}-T_f)+h_{c:f,M1}(T_{M1}-T_f)=\frac{\dot{m}C_{pair}}{A}(T_{f,out}-T_{f,in}) \tag{V-4}$$

$$(T_{M1}):\quad h_{r:g2,M1}(T_{g2}-T_{M1})+h_{c:f,M1}(T_f-T_{M1})+G_{M1}^a=\ h_{M1,Ma}(T_{M1}-T_{Ma}) \tag{V-5}$$

$$(T_{Mi}|i=\{a,b,c,\dots,X\}):\quad h_{M_{i-1}M_i}(T_{M_i}-T_{M_{i-1}})-h_{M_iM_{i+1}}(T_{M_i}-T_{M_{i+1}})=\frac{C_{M_i}}{A}\left(\frac{T_{M_i}-T_{M_i0}}{\Delta t}\right) \tag{V-6}$$

$$(T_{M2}):\quad h_{MXM2}(T_{MX}-T_{M2})=h_{r:M2,r,int}(T_{M2}-T_{r,int})+h_{c:M2,int}(T_{M2}-T_{int}) \tag{V-7}$$

The conductive heat transfer coefficient $h_{i,j}$ is calculated according to the thermal conductivity and thickness of each layer. The choice and approximation used for the calculation of the convective and radiation heat transfer and the mass flow rate are detailed in the following subsections.

V.2.2 Convective heat transfer consideration

V.2.2.1 External convective heat transfer coefficient: h_{cextg1}

The choice of an appropriate external convective heat transfer coefficient (CHTC) is crucial as it can induce a deviation of the thermal loads by up to 30% for cooling and 6% for heating in building energy simulation (Mirsadeghi et al., 2013). Existing approximations of the CHTC with the outdoor air are in function of the wind speed and direction. Other approximations consider the geometry of the building, the roughness of the surfaces, wind sheltering and urbanisation density. And some others depend on the wind boundary layer and may combine the CHTC from natural and forced convection distinctively. The most traditional form of wind-dependent CHCT is derived from the Nusselt-Jürges correlation:

$$h_{c:ext} = 5.678\left[a + b\left(\left(\frac{294.26}{273.16 + T_a}\right)\frac{V_{wind}}{0.3048}\right)^n\right] \quad \text{(V-8)}$$

Where a, b and n are parameters depending on the roughness of the surface and the wind velocity V_{wind}. The terms in the innermost parentheses indicate the temperature correction as the experiment was conducted at 294.26K (Palyvos, 2008). McAdams (1954) recast this formula and obtains for a smooth surface the following expression, which is used in several building models (Ong & Chow, 2003; Zanghirella et al., 2011):

$$h_{c:ext} = 5.7 + 3.8V \quad \text{(V-9)}$$

However, this correlation may contain free convection and radiation effects (Armstrong & Hurley, 2010; Kaplani & Kaplanis, 2014). Hence, the correlation given by Watmuff et al. (1977) was selected. It was also used in building and PV components modelling (Aste et al., 2008; Chow, 2003):

$$h_{c:ext} = 2.8 + 3V \quad \text{(V-10)}$$

V.2.2.2 Convective heat transfer coefficient in the air gap: h_{cg2f} et h_{cfM1}

The CHTC in the air gap was approximated by taking into account the nature of the air boundary layer through the Nusselt number correlation, with:

$$h_{c:gap} = Nu_{L_c}\frac{k_{air}}{L_c} \quad \text{(V-11)}$$

L_c is the characteristic length of the flow and k_{air} the air thermal conductivity. Nu_{L_c} the Nusselt number depends on the flow and is a function of dimensionless numbers such as the Reynolds Re, Rayleigh Ra and Prandtl Pr numbers (see Appendix A2.1.1). L_c can be either D_h the hydraulic diameter, d the thickness or L the height of the gap depending on the flow or the hypotheses of the modelling.

- **The airgap thickness or hydraulic diameter as the characteristic length**

Some approaches use the same CHTC for the two parallel surfaces forming the gap. For natural convection, Bar-Cohen and Rohsenow (1984) provide the Nusselt number depending on the heating constraint of the airgap. Agathokleous & Kalogirou (2018) suggest that isoflux plates with asymmetric heating are the closest to BIPV configuration by using the correlation:

$$Nu_{0,L/2} = \left[\frac{6}{Ra''} + \frac{1.88}{(Ra'')^{0.4}}\right]^{-0.5} \quad \text{(V-12)}$$

Here the subscript means that the Nusselt number is calculated at the mid-height of the plate. Ra'' is the gap modified Rayleigh number (see Appendix A2.1.1) and is a function of d and L.

Considering the air gap thickness d as the characteristic length of the flow, experimental analysis permits to obtain a more suitable Nusselt coefficient for the particular case of BIPV facade. Examples of those correlations can be found in the work of Agathokleous & Kalogirou (2018) and Fossa et al. (2008).

For forced convection, the Nusselt correlation depends on the Reynolds number. With the hypothesis of fully developed flow, the hydraulic diameter D_h is used as characteristic length. Considering the aspect ratio of the cross-section of the gap as infinite and an isoflux heat constraint, the Nusselt number for laminar flow ($Re_{Dh} \lesssim 2300$) is:

$$Nu_{Dh} = 8.23 \tag{V-13}$$

For turbulent flow, the below correlation can be used with $Re_{Dh} \gtrsim 10000$ and $L/d \gtrsim 10$ (Incropera et al., 2013):

$$Nu_{Dh} = 0.023 Re_{Dh}^{4/5} Pr^{0.4} \tag{V-14}$$

For mixed turbulent and laminar flow, Mei et al. (2003) suggest combining both flows by using the Nusselt expression:

$$Nu_{mix} = \sqrt{Nu_{lam}^2 + Nu_{turb}^2} \tag{V-15}$$

- **The height of the facade as the characteristic length**

Other approaches consider the air gap as two independent vertical surfaces as if the flow is external. The characteristic length corresponds to the height of the facade. For natural convection, several works have used the correlation proposed by Churchill & Chu (1975) (K. Kant et al., 2019; Ong & Chow, 2003; B. Yu et al., 2017):

$$Nu_{L,nat} = 0.68 + \frac{0.670 Ra^{\frac{1}{4}}}{\left(1 + (0.492/Pr)^{\frac{9}{16}}\right)^{2}} \text{ for } Ra \leq 10^9 \tag{V-16}$$

$$Nu_{L,nat} = \left[0.87 + \frac{0.387 Ra^{\frac{1}{6}}}{\left(1 + (0.492/Pr)^{\frac{9}{16}}\right)^{\frac{8}{27}}}\right]^2 \text{ for } Ra > 10^9 \tag{V-17}$$

For forced convection, the following expression can be considered for laminar flow:

$$Nu_{L,forced} = 0.664 Re^{\frac{1}{2}} Pr^{\frac{1}{3}} \tag{V-18}$$

And for mixed laminar-turbulent flow with $Re_L \geq Re_c = 10^5$ (Incropera et al., 2013):

$$Nu_{L,forced} = \left(0.037 Re^{\frac{4}{5}} - 871\right) Pr^{\frac{1}{3}} \tag{V-19}$$

Mei et al. (2003) suggested that mixed convection taking into account natural and forced convection, occurs in the gap as the flow is driven both by the buoyancy and the wind (see Equation (V-20)). For this, the Richardson number Ri (see Equation (V-21)) can be calculated to determine the nature of convection. If $Ri \gg 1$ the forced convection is negligible, whereas if $Ri \ll 1$ natural convection is negligible. In the modelling, mixed convection is considered for $0.25 \leq Ri \leq 4$.

$$Nu = \sqrt[m]{Nu_{nat}^m + \mathrm{Nu}_{forced}^m} \tag{V-20}$$

$$Ri = \frac{Gr}{Re^2} \tag{V-21}$$

The exponent m in Equation (V-20) should be determined, but according to Incropera et al. (2013), $m = 3$ gives a satisfactory approximation.

According to the model fitting performance with experimental data, the air gap is considered as two independent vertical walls for a naturally ventilated facade, and the correlations taking the facade height as the characteristic length of the flow are used (Equations (V-16) to (V-20)). For a mechanically ventilated air gap, the Nusselt number for forced convection in a fully developed flow is considered (Equations (V-13) to (V-15)).

V.2.2.3 Internal convective heat transfer coefficient: h_{cM2int}

With the assumption of natural convection on the inner surface of the facade, the internal CHTC $h_{c:M2int}$ is determined with the Nusselt correlation for natural convection on the vertical plate (equations (V-16) and (V-17)). As the experiment on the bioinspired facade prototype was performed indoors, I have also used those correlations for the estimation of CHCT between the indoor air and the front surface of the PV module (h_{cextg1}).

V.2.3 Radiation heat transfer consideration and PV power output calculation

V.2.3.1 Short wave radiation heat exchange and PV power output calculation

Incident direct and diffuse solar radiations are modelled separately since the glazing optical properties differ with the type of radiation. The variation of the absorptivity α and transmissivity τ of glazing according to the type of radiation and the incident angle θ_i are given in Table V-1 (Assoa, 2008). In this table, α_0 and τ_0 are the properties corresponding to direct solar radiation with $\theta_i = 0$, which can be calculated considering the extinction coefficient and the refraction index of the glazing (see Appendix A2.1.2) (Duffie & Beckman, 2006).

Table V-1: Variation of the optical properties of glazing according to the incident angle and the type of radiation

Optical properties of the glazing	*Direct solar radiation*	*Diffuse solar radiation*
Absorptivity α	$\alpha_{dir} = \alpha_0$ for all θ_i	$\alpha_{dif} = 1.12\alpha_0 - 0.175\alpha_0^2$
Transmissivity τ	If $\theta_i < 0.8$ then $\tau_{dir} = \tau_0$ Else, $\tau_{dir} = \tau_0 \cos\theta_i\,(2.5 - 1.56\cos\theta_i)$	$\tau_{dif} = 0.983\tau_0 - 0.068$
Reflectivity ρ	$\rho_{dir} = 1 - \alpha_{dir} - \tau_{dir}$	$\rho_{dif} = 1 - \alpha_{dif} - \tau_{dif}$

A single reflection of transmitted radiation by the wall is considered to model shortwave radiation (see Figure V-2). An effective absorptivity coefficient a_{i_n} of each surface node is then determined to calculate the absorbed radiation G_i^a, which general form is given by:

$$G_i^a = a_{i_{dir}} G_{dir} cos\theta_i + a_{i_{dif}} \left(\left(\frac{1 + cos\beta}{2} \right) G_{dif} + \left(\frac{1 - cos\beta}{2} \right) G_{albedo} \right) \quad \text{(V-22)}$$

Where β is the PV modules (the facade) tilt angle (90°). $\left(\frac{1+cos\beta}{2}\right)$ and $\left(\frac{1-cos\beta}{2}\right)$ are respectively the view factor of the facade with the sky f_{sky} and the ground f_{gr}. G_{albedo} is diffuse radiation reflected by the ground. For each node, the effective absorption coefficients are:

$$a_{g1_n} = a_{g1_n front} + a_{g1_n back} \quad \text{(V-23)}$$
$$a_{g1_n front} = \alpha_{g1_n}, a_{g1_n back} = \left(\xi^2 \tau_{g1_n} \tau_{g2_n}^2 \rho_{M1}\right) \alpha_{g1_n}$$

$$a_{PV_n} = a_{PV_nfront} + a_{PV_nback} \quad \text{(V-24)}$$
$$a_{PV_nfront} = (1-\xi)\left[(\tau\alpha)_{PV1_n} - \tau_{g1_n}\eta_{PV,f}\right]$$
$$a_{PV_nback} = (1-\xi)\left[\left((\tau\alpha)_{PV2_n} - \xi\tau_{g2_n}b_f\eta_{PV,f}\right)\tau_{g1_n}\tau_{g2_n}\rho_{M1}\right]$$

$$a_{g2_n} = a_{g2_nfront} + a_{g2_nback} \quad \text{(V-25)}$$
$$a_{g2_nfront} = \xi\tau_{g1}\alpha_{g2_n}, a_{g2_nback} = \xi\tau_{g1_n}\tau_{g2_n}\rho_{M1}\alpha_{g2_n}$$

$$a_{M1_n} = \xi\tau_{g1_n}\tau_{g2_n}\alpha_{M1} \quad \text{(V-26)}$$

The subscript n is either for direct or diffuse radiation. The module has effective absorption coefficients from the front and back to distinguish the flux absorbed from the incident irradiance and the reflected irradiance from the wall. $(\tau\alpha)_{PV1_n}$ and $(\tau\alpha)_{PV2_n}$ are the transmittance-absorptance products (Duffie & Beckman, 2006), respectively, for the front and back sides of the PV module. b_f the bifacial factor is the ratio between PV module efficiencies of the front ($\eta_{PV,f}$) and the back sides ($\eta_{PV,b}$) (Guerrero-Lemus et al., 2016).

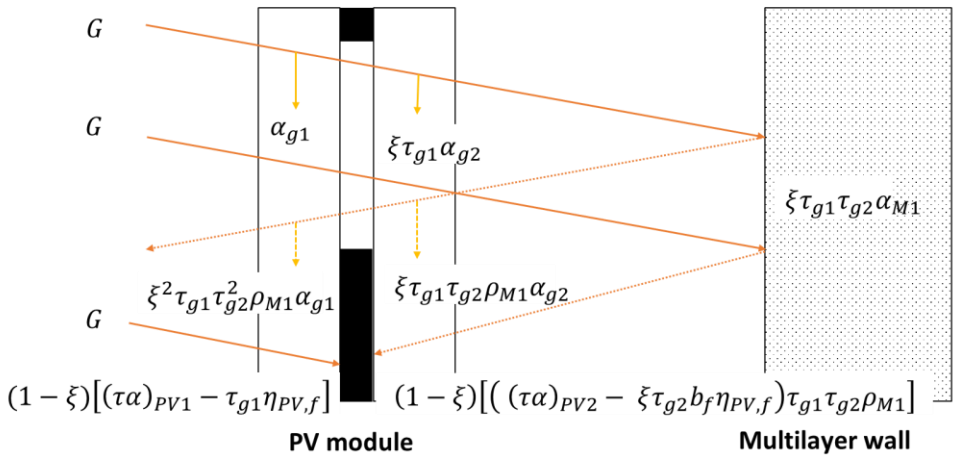

Figure V-2: Representation of the solar ray paths in the facade system

The PV power production is given by

$$E_{PV} = \sum_{n=\{dir,dif)} \left(\tau_{g1_n} + b_f\xi\tau_{g1_n}\tau_{g2_n}^2\rho_{M1}\right)\eta_{PV,f}G_n \quad \text{(V-27)}$$

Where the operating efficiency of the PV module is a function of β_r the cell temperature coefficient and T_r the reference temperature (Evans & Florschuetz, 1977):

$$\eta_{PV} = \eta_r\left[1 - \beta_r(T_{PV} - T_r)\right] \quad \text{(V-28)}$$

V.2.3.2 Longwave radiation heat exchange with the facade environment

Radiation heat transfer between the external or the internal surface of the facade with its environment is calculated considering the environment as a blackbody. Thus, radiation heat flux is given by:

$$q"_{rad} = \varepsilon_p\sigma\left(T_r^4 - T_p^4\right) = \varepsilon_p\sigma\left(T_r^2 + T_p^2\right)\left(T_r + T_p\right)\left(T_r - T_p\right) \quad \text{(V-29)}$$

Where p is the studied facade surface with an emissivity ε_p. T_r is the radiant temperature of the studied environment, and σ is the Stephan-Boltzmann coefficient. The radiation heat transfer coefficient (RHTC) is then given by :

$$h_{rpenv} = \varepsilon_{g1}\sigma\left(T_r^2 + T_p^2\right)\left(T_r + T_p\right) \quad \text{(V-30)}$$

The radiant temperature of the indoor environment is assumed to be equal to consigned ambient air temperature. The outdoor radiant temperature T_{env} is calculated with respect to the facade view factor to the ground f_{gr} and to the sky f_{sky}:

$$T_{env} = \left(f_{sky}T_{sky}^4 + f_{gr}T_{gr}^4\right)^{\frac{1}{4}} \quad \text{(V-31)}$$

The ground temperature is considered to be equal to the ambient air temperature. A detailed ground temperature model requires detailed data on the environment, such as the draining and evaporation cooling of the earth (Assoa, Mongibello, et al., 2017). As for the sky temperature, several models exist in the literature (Evangelisti et al., 2019). In this study, the approximation provided by the norm NF EN ISO 52016-1 (AFNOR, 2017) for intermediate climatic zones is selected, where:

$$T_{sky} = T_{ext} - 11 \quad \text{(V-32)}$$

V.2.3.3 Longwave Radiation heat exchange in the air gap

Considering the two surfaces delimiting the air gap as two infinite parallel plates, the radiation heat transfer coefficient is given by:

$$h_{r:g2,M1} = \sigma F_{g,M1}\left(T_{g2}^2 + T_{M1}^2\right)(T_{g2} + T_{M1}) \quad \text{(V-33)}$$

With:

$$F_{g,M1} = \frac{1}{\frac{1}{\varepsilon_{g2}} + \frac{1}{\varepsilon_{M1}} - 1} \quad \text{(V-34)}$$

Where ε_{g2} and ε_{M1} are respectively the emissivity of the rear glass and the external surface of the wall. The coefficient $F_{g,M1}$ is deduced by the study of the emittance and radiosity of the two surfaces.

V.2.4 Mass flow rate estimation

The pressure equilibrium within the openings of the air gap is established to estimate the airflow rate using four pressure nodes as in the work of Brinkworth et al. (2000) (see Figure V-3).

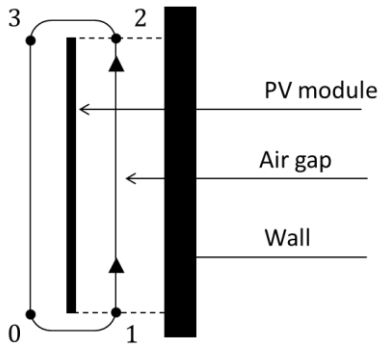

Figure V-3: Representation of the air circulation in the gap in a closed loop and the selected pressure nodes

The pressure balance can be written as follows:

$$(P_0 - P_1) + (P_1 - P_2) + (P_2 - P_3) = -(P_3 - P_0) \quad \text{(V-35)}$$

Where $(P_0 - P_1)$ and $(P_2 - P_3)$ are the pressure drop in the inlet and the outlet of the air gap:

$$(P_0 - P_1) = \frac{1}{2}K_{fin}\rho_{01}v_{01}^2 - \frac{1}{2}CP_0\rho_0 v_{windo}^2 \quad \text{(V-36)}$$

$$(P_2 - P_3) = \frac{1}{2}K_{fout}\rho_{23}v_{23}^2 + \frac{1}{2}CP_3\rho_0 v_{wind3}^2 \quad \text{(V-37)}$$

Where K_{fin} and K_{fout} are respectively the pressure drop coefficients at the inlet and the outlet of the air gap. CP_0 and CP_3 are the wind pressure coefficients at the two openings. ρ_i, v_i are the air density and the velocity in the given node.

$(P_3 - P_0)$ is the outdoor hydrostatic pressure difference at the level of the air inlet and outlet:

$$(P_3 - P_0) = -\rho_0 g L \tag{V-38}$$

$(P_1 - P_2)$ is the pressure loss in the air gap, is given by:

$$(P_1 - P_2) = \rho_{12} g L + \frac{1}{2} f \left(\frac{L}{D_{12}}\right) \rho_{12} v_{12}^2 \tag{V-39}$$

Where D_{12} is the hydraulic diameter (D_h) of the air gap.

For laminar flow, the approximation for a rectangular section is used to determine the friction coefficient f:

$$f = \frac{96}{Re} \tag{V-40}$$

For turbulent flow, the Blasius approximation is used:

$$f = 0.316 Re^{-0.25} \tag{V-41}$$

To extract the mass flow rate from the pressure balance, the following can be considered:

- the continuity equation while assuming the equality of the sections at the inlet, inside the gap and the outlet $S_{01} = S_{12} = S_{23} = S_{gap}$:

$$\dot{m} = \rho_i v_i S_i \tag{V-42}$$

- the Boussinesq approximation while considering a small variation of the air density in the gap:

$$(\rho_0 - \rho_m) = \rho_0 \beta_{th} (T_m - T_0) \text{ with } \beta_{th} = \frac{1}{T_m} \tag{V-43}$$

  T_m is as a function of the air temperature stratification in the gap, which is supposed to be equal to $S = 0.5$:

$$T_m = T_{in} + S(T_{f,out} - T_{f,in}) \text{ with } T_{f,in} = T_0 \tag{V-44}$$

- the expression of thermal energy transmitted to the air:

$$P_{th} = \dot{m} C_p \left(T_{f,out} - T_{f,in}\right) \tag{V-45}$$

Hence, equation (V-46) with which the air flow rate is deduced using Newton Raphson algorithm is obtained:

$$\left(K_{fin} + K_{fout} + f\left(\frac{L}{D_{12}}\right)\right)\dot{m}^3 - \rho_0 \left(CP_0 v_{windo}^2 - CP_3 v_{wind3}^2\right)\dot{m} - 2\left(\rho S_{gap}\right)^2 g L \beta S \frac{P_{th}}{C_p} = 0 \tag{V-46}$$

V.2.5 Algorithm of the coupled model resolution

The heat balance equations can be written as a single matrix equation:

$$\boldsymbol{A}T = Q \tag{V-47}$$

with $\boldsymbol{A}$ the heat transmission matrix, Q an array enclosing all the boundary conditions and heat capacitance and T the unknown is the array of temperatures on each node. The model gives as output the temperature on each node, the airflow rate and average velocity, the power transmitted to the air and the PV power production. It is solved iteratively according to the algorithm in Figure V-4. The stopping criteria for the iterations are $\epsilon_{\dot{m}} = 10^{-6} Kg/s$ for the airflow rate and $\epsilon_T = 10^{-5} °C$ for the temperature. For the calculation of the thermal loads of a building integrating the facade, this model is coupled with

building energy simulation in EnergyPlus. Details of the coupled facade and building model are given in Appendix A2.4.

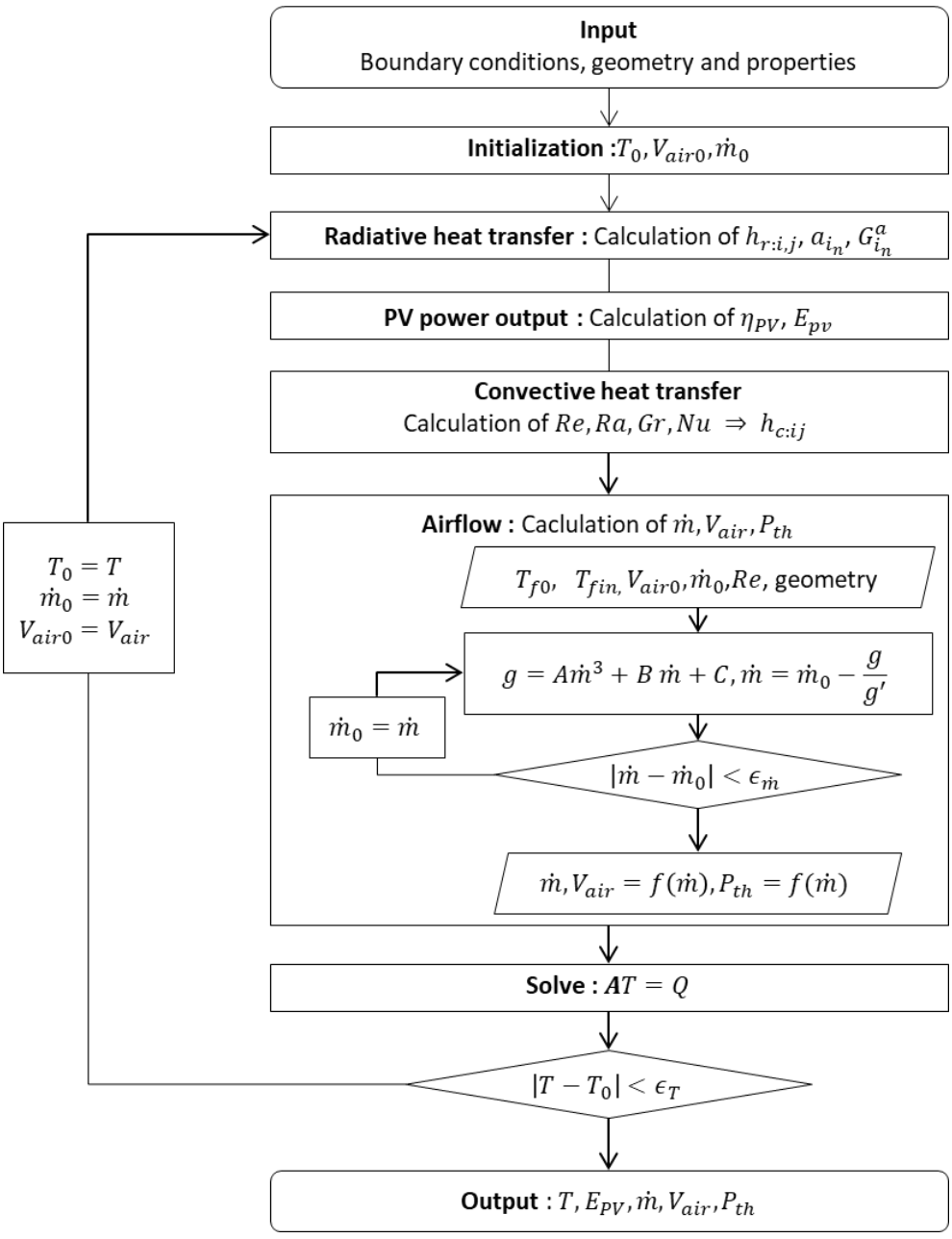

Figure V-4: Algorithm solving the thermal model of PV facade

V.3 Modifications of the facade model from the bilayer integration

The application of the bilayers on the facade modifies its behaviour, especially in their deformed state. In the model, the changes concern the heat transfer balances on the nodes T_{g2}, T_f and T_{M1} and the formulation of the airflow and the absorbed irradiance in the modules and the external surface of the wall. For this, several additional hypotheses are considered, and the details of those modifications are presented in the following subsections.

V.3.1 Changes in convective heat transfer

The bilayers are assimilated as extended rectangular fins to model convective heat transfer. Their effective length $L^e_{b|fin}$ that actually dissipates heat is shortened by their deflection y_b (see Figure V-5) to consider the air trapped near their mounting zone. This approximation was driven by the investigation of the work of Tonui et Tripanagnostopoulos (2007, 2008), in which fins were used to dissipate heat from a thermal collector.

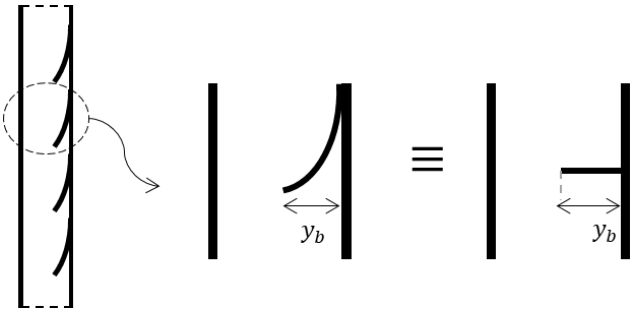

Figure V-5: Illustration of the approximation of the bilayers as extended fins

To study a bilayer as a fin, the following hypotheses are considered: one-dimensional steady-state heat transfer, no heat dissipation, uniform fin cross-section A_c (perimeter P_b), thermal conductivity and CHTC along the fin. In addition, its free end is considered to be adiabatic, and the temperatures of the fixed end and the wall are equal. With those hypotheses, the heat evacuated by the bilayer through convection equals the heat extracted from the wall through conduction at the wall-bilayer contact. This heat flux is determined by solving the fin equation (see Appendix A2.2.1) and can be expressed as a function of the CHTC h_c, the effective surface of the bilayer A^e_b (corresponding to the length of the fin) and its fin efficiency η_b:

$$q_e = \int_0^{L^e_{b|fin}} h_c P_b \big(T_b(x) - T_f\big) dx = -\lambda_b A_c \left.\frac{dT_b}{dx}\right|_{x=0} = h_c A^e_b \eta_b \big(T_{M1} - T_f\big) \tag{V-48}$$

The fin temperature along the position x is given by:

$$\big(T_b(x) - T_f\big) = \big(T_{M1} - T_f\big) \frac{\cosh\big(m(L^e - x)\big)}{\cosh(mL^e)} \tag{V-49}$$

And the fin efficiency by:

$$\eta_b = \frac{\tanh\big(mL^e_{b|fin}\big)}{mL^e_{b|fin}} \tag{V-50}$$

With those expressions, the heat transfer balances at the nodes (T_f) and (T_{M1}) become :

$$(T_f): \quad h_{c:g2,f}\big(T_{g2} - T_f\big) + h_{c:f,M1}\big(T_{M1} - T_f\big) + \frac{\mathrm{N} h_c A^e_b}{A} \eta_b \big(T_{M1} - T_f\big) = \frac{\dot{m} C_{pair}}{A} \big(T_{f,out} - T_{f,in}\big) \tag{V-51}$$

$$(T_{M1}): \quad h_{r:g2,M1}\big(T_{g2} - T_{M1}\big) + h_{c:f,M1}\big(T_f - T_{M1}\big) + \frac{\mathrm{N} h_c A^e_b}{A} \eta_b \big(T_f - T_{M1}\big) + G^a_{M1} = h_{M1,Ma}\big(T_{M1} - T_{Ma}\big) \tag{V-52}$$

where *N* is the number of bilayers along the height of the wall.

The presence of fins perpendicular to airflow on a wall can reduce the average CHTC due to air recirculation between them (air vortex), especially for natural convection (Tanda, 2008). However, they can also create turbulence enhancing the global CHTC (Bekele et al., 2011; Brinkworth & Sandberg,

2006). Using the Nusselt correlations for in-line rectangular fins might underestimate the convective heat transfer in the current case since the wetted surface from the main airflow is likely superior to that of rectangular fins (see Figure V-6). For this reason, the average CHTC on the wall and the bilayers (as fins) are considered equal ($h_{c:fM1} = h_c$) and is always enhanced proportionally to the increase of the thermal exchange surface while considering the deflection y_b of the bilayers. Thus:

$$h_{c:f,M1} = h^0_{c:f,M1} \frac{(L_0 + 2Ny_b)}{L_0} \tag{V-53}$$

With $h^0_{c:f,M1}$ the CHTC without bilayers and L_0 the height of the wall.

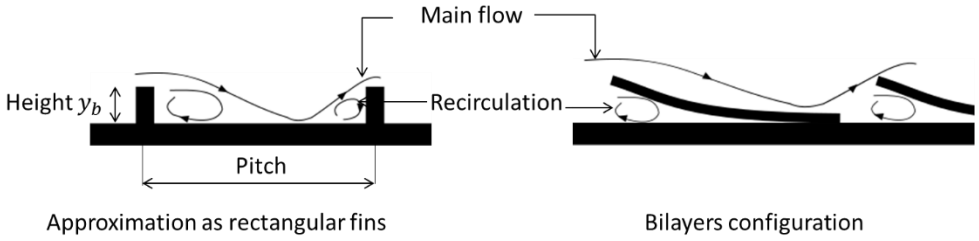

Figure V-6: Illustration of the airflow on the support with bilayers and its approximation taking the bilayers as rectangular fins

V.3.2 Changes in radiation heat transfer

V.3.2.1 Shortwave radiation heat transfer

The addition of bilayers requires the consideration of their shading and the multiple reflections in the gap. Based on the work of (Gomes et al., 2014) on radiation exchange in venetian blinds, the radiosity method is applied to model the radiation in the air gap while considering the bilayers as a shading layer between the module and the wall, as illustrated in Figure V-7. This shading layer has different effective absorptivity, reflectivity and transmitivity on its front surface (toward the module) and back surface (toward the wall) according to the deformation of the bilayers (Kotey et al., 2009).

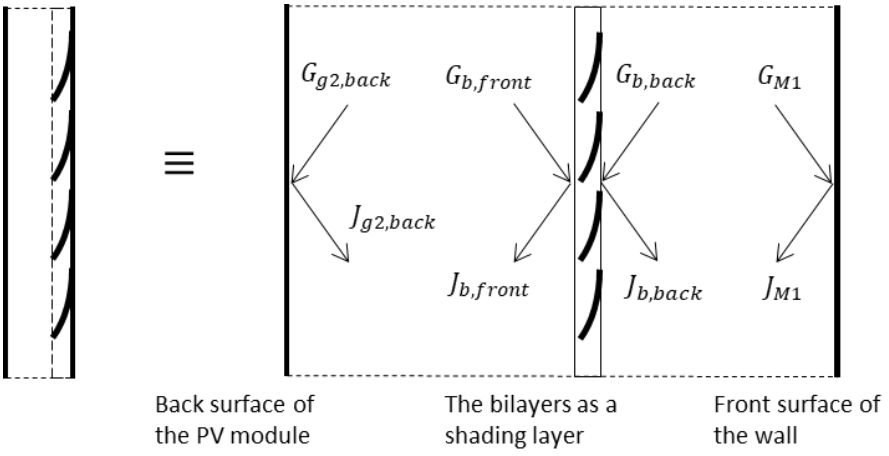

Figure V-7: Illustration of the approximation of the bilayers as a shading layer for radiation modelling

a) Determination of the absorbed irradiance at the surface in the air gap

The radiosity of one layer from its front surface is the total radiation leaving the surface, which is given by:

$$J_{i,front} = \varepsilon_{i,front} M^0_{i,front} + \rho_{i,front} G_{i,front} + \tau_{i,back} G_{i,back} \quad \text{(V-54)}$$

With ε_i, ρ_i and τ_i are respectively the emissivity, the reflectivity and the transmissivity of the surface according to the front or backside. The notion of front and back sides is important for transparent (semi-transparent) media, as the irradiance coming from the front $G_{i,front}$ is reflected while that coming from the back $G_{i,back}$ is transmitted to the front. The transmissivity is zero for an opaque surface, thus the term $\tau_{i,back} G_{i,back}$ in equation (V-54) is not included. M_i^0 the emittance of a black surface is neglected in shortwave radiation regarding the range of temperature of this study.

With the assumptions of diffuse surfaces on the bilayers and the wall, direct radiation can be transmitted as direct (leading to the transmissivity τ^{DD}) or diffuse radiation (leading to τ^{Dd}) but always reflected as diffuse radiation (leading to ρ^{Dd} and $\rho^{DD} = 0$). However, the diffuse radiation always remains diffuse (leading to the optical properties noted a^{dd}). Therefore, the radiation balance for direct radiation in the gap is:

$$J^D_{g2,back} = G^t_{dir} \quad \text{(V-55)}$$

$$J^D_{b,front} = 0 \quad \text{(V-56)}$$

$$J^D_{b,back} = \tau^{DD}_{b,front} J^D_{g2,back} \quad \text{(V-57)}$$

$$J^D_{M1} = 0 \quad \text{(V-58)}$$

With G^t_{dir} is the transmitted direct radiation from the module, is given by:

$$G^t_{dir} = \xi \tau_{g1,dir} \tau_{g2,dir} G_{dir} \quad \text{(V-59)}$$

Since a part of direct radiation becomes diffuse, diffuse radiation balance includes the radiosity calculated in direct radiation balance, leading to:

$$J^d_{g2,back} = \rho^{dd}_{g2} J^d_{b,front} + G^t_{dif} \quad \text{(V-60)}$$

$$J^d_{b,front} = \rho^{Dd}_{b,front} J^D_{g2,back} + \rho^{dd}_{b,front} J^d_{g2,back} + \tau^{dd}_{b,back} J^d_{M1} \quad \text{(V-61)}$$

$$J^d_{b,back} = \tau^{Dd}_{b,front} J^D_{g2,back} + \rho^{dd}_{b,back} J^d_{M1} + \tau^{dd}_{b,front} J^d_{g2,back} \quad \text{(V-62)}$$

$$J^d_{M1} = \rho^{dd}_{M1} J^d_{b,back} \quad \text{(V-63)}$$

With G^t_{dif} the transmitted diffuse radiation is determined in the same manner as G^t_{dir}.

Resolving those radiation balances allows the estimation of the absorbed radiation on each surface. For the PV modules, the radiation absorbed from the front side remains the same as in the basic model (see equations (V-23), (V-24) and (V-25)). Only the radiation absorbed from their back is modified:

$$G^a_{g1,back} = \xi \tau_{g2_{dif}} \alpha_{g1_{dif}} J^d_{b,front} \quad \text{(V-64)}$$

$$G^a_{PV,back} = (1-\xi)\left((\tau\alpha)_{PV2_n} - \xi \tau_{g2_{dif}} b_f \eta_{PV,f}\right) J^d_{b,front} \quad \text{(V-65)}$$

$$G^a_{g2,back} = \alpha_{g2_{dif}} J^d_{b,front} \quad \text{(V-66)}$$

The radiation absorbed by bilayers was assumed to be fully transmitted to the wall, which allows the addition of this flux to the node (T_{M1}) and obtain the radiation absorbed on the wall surface:

$$G^a_{M1} = \alpha_{M1}\left(J^D_{b,back} + J^d_{b,back}\right) + G^a_b \quad \text{(V-67)}$$

$$G^a_b = \alpha^D_{b,front} J^D_{g2,back} + \alpha^d_{b,front} J^d_{g2,back} + \alpha^d_{b,back} J^d_{M1} \quad \text{(V-68)}$$

b) Estimations of the effective optical properties of the shading layer

An elementary enclosure is considered to determine the effective optical properties of the bilayers as a shading layer (Kotey et al., 2009). The idea is to calculate the proportions of radiation transmitted, reflected and absorbed by this enclosure for a unit of irradiance. For this, bilayers are assumed to remain flat and rotate on the horizontal axis with a displacement equal to their deflection y_b (see Figure V-8). In addition, the following assumptions are considered:

- The thickness of the bilayers is negligible;
- Incident diffuse radiation is isotropic and uniform at the front surface of the shading layer despite the semi-transparency of the module and is diffused only by the part of the wall that is not covered by the projection of slats at the back surface of the enclosure;
- The bilayers and the walls have diffuse opaque surfaces with the same reflection properties for direct and diffuse radiation ($\rho^{Dd} = \rho^{dd}$);
- The air gap is considered to be formed by two infinite parallel surfaces.

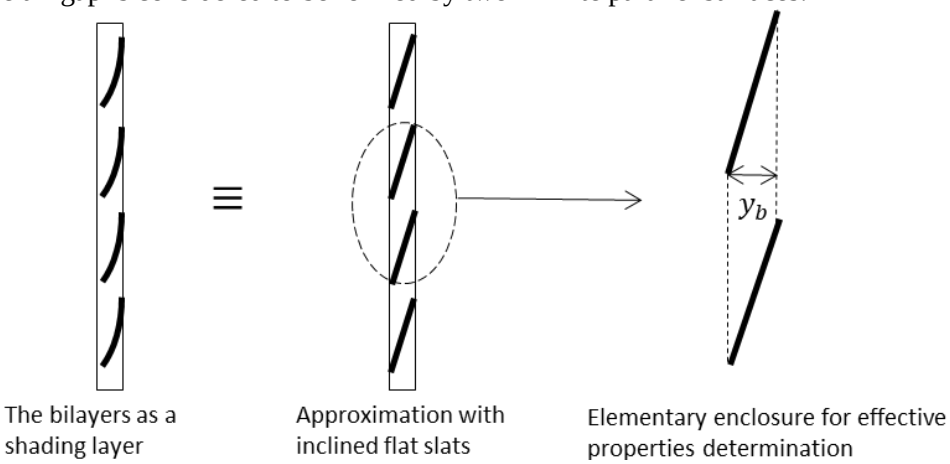

Figure V-8: Illustration of bilayers approximation as flat slats and the elementary enclosure of the shading layer

The following paragraphs address the method for the determination of the effective optical properties of the bilayers as a shading layer while considering the PV module as transparent glazing. The principle is the same for the consideration of the module semi-transparency, and the details are given in Appendix A2.2.2.

b.1) Effective properties for direct radiation

For direct radiation, with the assumption that the bilayers and the walls reflect radiation diffusely, the only direct-to-direct property is the transmission coefficient. Moreover, only the determination of the front properties is relevant. Thus, only the direct-to-direct transmissivity, direct-to-diffuse transmissivity and reflectivity are calculated. The direct absorptivity is deduced from those values as described in the equation below:

$$\alpha^{D}_{b,front} = 1 - \rho^{Dd}_{b,front} - \tau^{Dd}_{b,front} - \tau^{DD}_{b,front} \quad \text{(V-69)}$$

- **Direct-to-direct front transmissivity**

The direct-to-direct transmissivity from the front is the ratio of radiation passing through the enclosure at the back surface (S_2) and incident on the front surface (S_1). As described in Figure V-9, it is given by:

$$\tau^{DD}_{b,front} = \max\left(0, \frac{s-h}{s}\right) = \max\left(0, \frac{s' - L^{e}_{b}}{s'}\right) \quad \text{(V-70)}$$

Where s' is the projection of the surface s on the bottom slat according to the incident angle θ_i and the inclination of the slat ϕ_b:

$$s' = de = s\left|\frac{\cos(\theta_i)}{\sin(\theta_i + \phi_b)}\right| \quad \text{(V-71)}$$

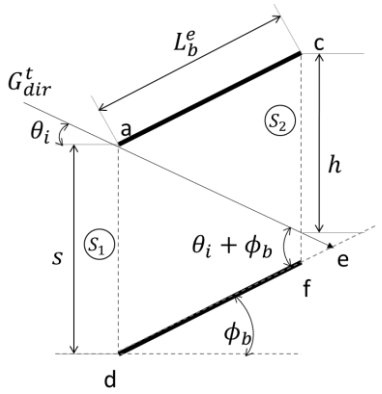

Figure V-9: Direct ray path in the enclosure for a transparent glazing

- **Direct-to-diffuse reflectivity and transmittance**

Reflectivity and transmitivity are calculated by considering the diffuse radiation balance in the enclosure. There are:

- Z_i a diffuse source due to the reflectance of direct incident irradiance $G_{dir,i}^t$. It is applied on the irradiated surface on the bottom slat and is zero for non-irradiated surfaces by direct radiation or for the calculation of diffuse-to-diffuse properties:

$$Z_i = \rho_{b,p}\frac{s}{s'}G_{dir}^t \quad \text{(V-72)}$$

- G_i the irradiance on surface i is defined by:

$$G_i = \sum_j^N F_{ij}J_i \quad \text{(V-73)}$$

With N the number of considered surfaces and F_{ij} the view factor from surface i to surface j. The view factor can be calculated using the cross-string method. Its determination is given in Appendix A2.2.3.

- J_i the radiosity of a given surface i. Its expressions are given in Equation (V-74) for the front and back of surfaces of the enclosure, in Equation (V-75) for irradiated surfaces with direct radiation and in Equation (V-76) for non-irradiated surfaces with direct radiation.

$$J_1 = J_2 = 0 \quad \text{(V-74)}$$

$$J_i = Z_i + \rho_i G_i \quad \text{(V-75)}$$

$$J_i = \rho_i G_i \quad \text{(V-76)}$$

The number of the studied surfaces increases with the number of diffuse radiation sources (see Figure V-10). The irradiance value of each surface is obtained from the resolution of the set of equations from (V-72) to (V-76). Considering that G_1 and G_2 the irradiance on the front and back surfaces of the enclosure, if the incident direct radiation is taken as unity $G_{dir}^t = 1$. The front direct-to-diffuse reflectivity and transmissivity of the shading layer are given by:

$$\rho_{b,front}^{Dd} = G_1, \qquad \tau_{b,front}^{Dd} = G_2 \quad \text{(V-77)}$$

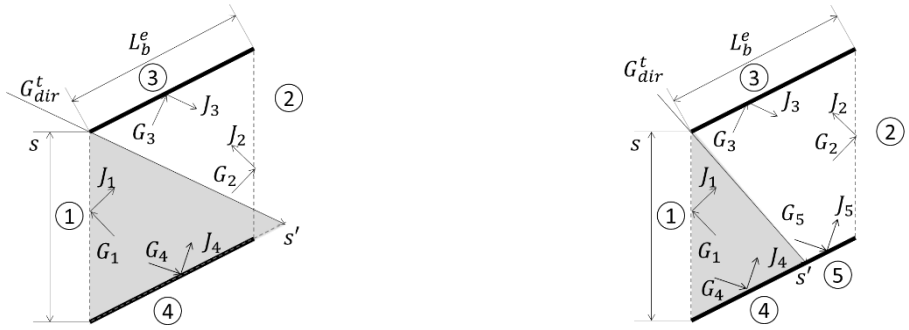

Figure V-10: Illustration of surface fragmentation in the enclosure according to the irradiated part by direct radiation

b.2) Effective properties for diffuse radiation

For diffuse radiation, the diffuse-to-diffuse reflectivity and transmissivity from the front and back surfaces of the shading layer are estimated. The absorptivity is deduced by those values and given by:

$$\alpha_{b,front}^{d} = 1 - \rho_{b,front}^{dd} - \tau_{b,front}^{dd}, \qquad \alpha_{b,back}^{d} = 1 - \rho_{b,back}^{dd} - \tau_{b,back}^{dd} \tag{V-78}$$

- **Front diffuse-to-diffuse reflectivity and transmissivity**

With the assumption of uniform diffuse radiation on the front surface of the enclosure, the front diffuse-to-diffuse properties can be determined considering a four-surface enclosure regardless of the module semi-transparency (see Figure V-11a) and by resolving the radiation balance in equations (V-73) and (V-76). The radiosity on the front and the back surfaces are given by:

$$J_1 = G_{dif}^t, \qquad J_2 = 0 \tag{V-79}$$

with G_{dif}^t the transmitted diffuse radiation. If $G_{dif}^t = 1$, similarly in the study of direct-to-diffuse reflectivity and transmissivity are given by:

$$\rho_{b,front}^{dd} = G_1, \qquad \tau_{b,front}^{dd} = G_2 \tag{V-80}$$

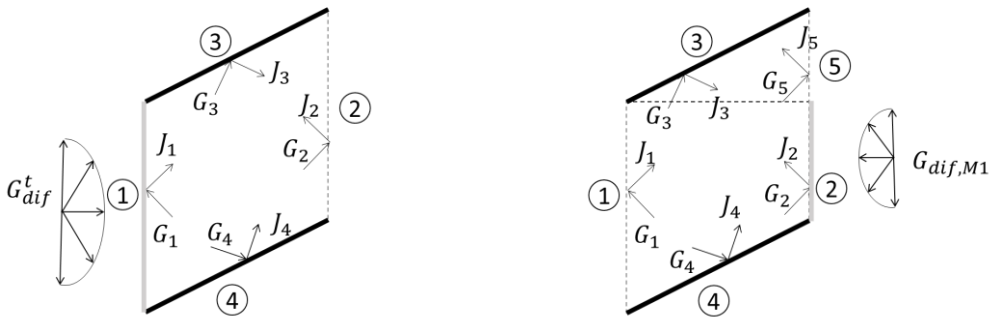

(a) (b)

Figure V-11: Illustration of the enclosure radiation balance for the determination of (a) the front diffuse-to-diffuse (b) and the back diffuse-to-diffuse optical properties of the shading layer

- **<u>Back diffuse-to-diffuse reflectivity and transmittance</u>**

When the bilayers are flat, only the parts of the wall that they do not cover irradiate. The wall surface that effectively irradiates increases gradually with the bilayers bending. Hence, to determine the back surface properties, I considered that the diffuse source at the back of the enclosure corresponds to the part of the wall that is not covered by the projection of the top slat on the back surface (see Figure V-11b). Thus, a five-surface enclosure is considered, and the value of radiosity on the front and back surfaces are:

$$J_1 = J_5 = 0, \qquad J_2 = G_{dif,M1} \tag{V-81}$$

Where $G_{dif,M1}$ is the supposedly diffuse radiation from the wall. If $G_{dif,M1} = 1$, then:

$$\rho_{b,back}^{dd} = G_2, \qquad \tau_{b,back}^{dd} = G_1 \tag{V-82}$$

This approximation enables obtaining $\tau_{b,back}^{dd} = 1$ when the bilayers are completely flat (maximum coverage of wall) and the integral radiosity of the wall is transmitted to the module.

V.3.2.2 Longwave radiation heat transfer

Longwave radiation heat transfer is modelled in the same manner as in the basic model. Nevertheless, an effective emissivity is calculated on the wall to take into account the presence of the bilayer. This emissivity is given by

$$\varepsilon_{M1}^{e} = \frac{L_c\, \varepsilon_b + L_u\, \varepsilon_{M1}}{L_c + L_u} \tag{V-83}$$

With L_c the part of the wall that is covered by the projection of the bilayers on it, and L_u the part of the wall that is uncovered.

V.3.3 Change in the mass flow rate calculation

The bending of the bilayers generates additional pressure losses in the air gap modifying the formulation of the mass flow rate. A constriction followed by a gradual expansion of the flow area can be observed at each bilayer. This phenomenon was approximated by considering the air gap as a pipe and the bilayers as a diaphragm reducing the pipe diameter by the deflection y_b (see Figure V-12).

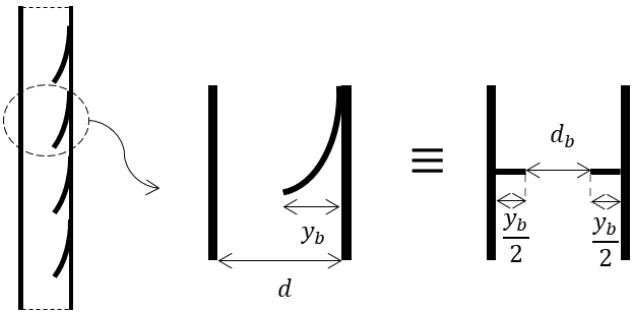

Figure V-12: Illustration of the approximation of the bilayer as a diaphragm for mass flow rate estimation

The local pressure loss at each bilayer is given by:

$$\Delta P = \frac{1}{2} K_b \rho v^2 \tag{V-84}$$

Where the loss coefficient K_b for a diaphragm with narrow edges in turbulent flow is:

$$K_b = \left(1 + 0.707\sqrt{1 - \frac{d_b}{d}} - \frac{d_b}{d}\right)^2 \left(\frac{d}{d_b}\right)^2 \tag{V-85}$$

With d is the air gap thickness and d_b is the reduced thickness due to the deflection of the bilayer:

$$d_b = d - y_b \tag{V-86}$$

The mass flow rate is determined by establishing the pressure equilibrium in the air gap (see Appendix A2.2.4 for more details). Considering the continuity equation, additional pressure drop from the bilayers, the Boussinesq approximation, the mean air velocity in the gap, and the assumption of the negligible edge of the bilayers, the same form of airflow equation is obtained:

$$\left(K_{fin} + K_{fout} + NK_b + f\left(\frac{L}{D_h}\right)\right)\dot{m}^3 - \rho_0\left(CP_0 v_{windo}^2 - CP_3 v_{wind3}^2\right)\dot{m} - 2\left(\rho S_{gap}\right)^2 gL\beta S\frac{P_{th}}{C_p} = 0 \quad \text{(V-87)}$$

V.4 Validation of the thermal models

One-year experimental data from a full-scale PV facade is used to validate the basic thermal model of the baseline facade. Transient heat transfer is considered in this validation. Experimental data from the reduced scale prototypes described in Chapter IV are used to validate the facade models with and without bilayers or the basic and the modified models. Steady-state heat transfer is considered in this validation. Thus, time-dependent terms are discarded in the equations. Details of those validations are described in this section.

V.4.1 Validation of transient heat transfer model of the facade without bilayers

V.4.1.1 Data set acquisition

In Chapter II, the experimental bench CONIPHER, which consisted of a full-scale BIPV facade, was used in the parametric study of a standard BIPV facade. For a short description, this facade comprised of semi-transparent bifacial photovoltaic modules arranged in rows of four and columns of two, a naturally ventilated air gap, ultra-high performance fibre concrete (UHPC) panels, rock wool insulation blocks and a concrete wall. The air gap was mounted in an open joint configuration or discontinuous with multiple openings at each module, leading the air to theoretically enter the two bottom openings and be exhausted at the two top openings. However, since the discontinuity was large (about 6 cm) compared to other studies on open joint ventilated facades in the literature (where the joint opening is about 1 cm)(Labat et al., 2012; Marinosci et al., 2014; Sanjuan et al., 2011), I assumed that the air circulation within each module is independent to apply the model of mass flow rate presented previously.

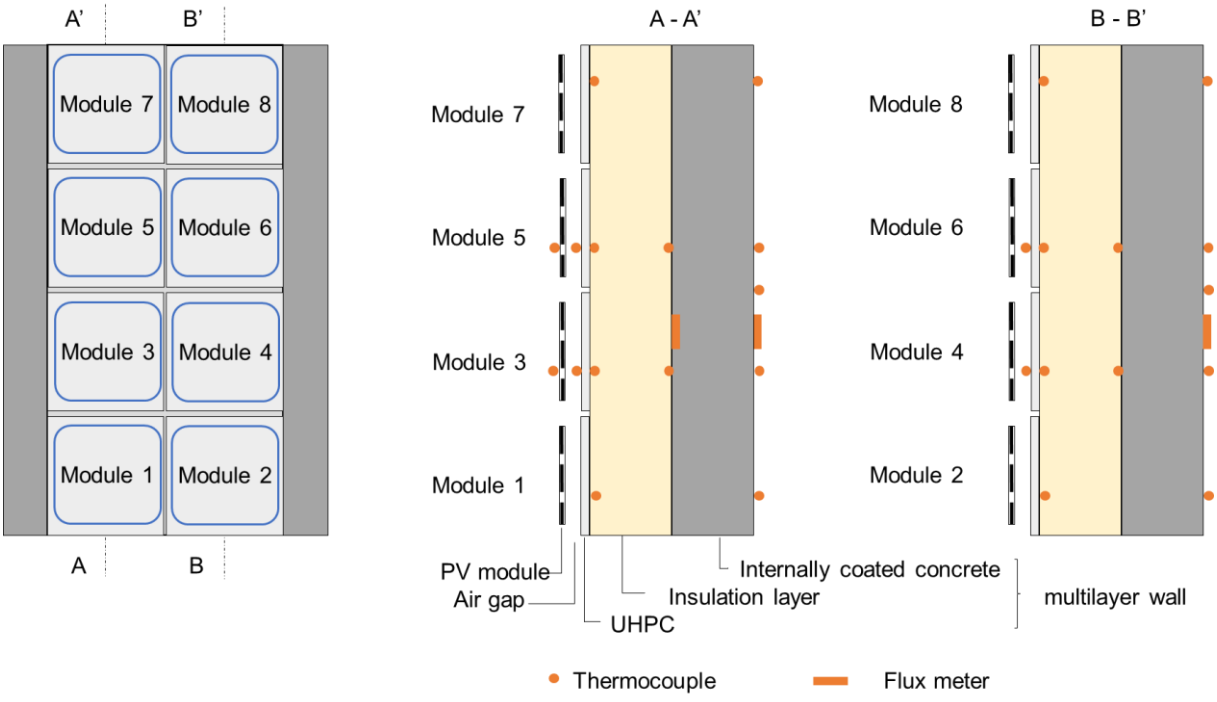

Figure V-13: Scheme of the front view of the photovoltaic facade and its vertical sections with the positions of the sensors within the facade

The measurement campaign on this facade was conducted from November 2018 to December 2019, considering the thermal, electrical and meteorological measurements. Here, only the description of the temperature and meteorological measurements used for the model validation are given. More details on the measurement campaign and the facade description can be found in the review article of Assoa et al. (2021).

T-type thermocouples (with an uncertainty of ±2%) have been used. They were positioned in four levels corresponding to the centre of each PV module to measure the temperature within the facade layers. The sensors were positioned on the inner and outer surfaces of the concrete and the inner and outer surfaces of UHPC panels. The temperature was measured only on the outer surface of the UHPC panels and the inner surface of the concrete on the first and fourth rows of modules. There were two (2) additional thermocouples in the mid-level of the inner wall. Modules 3 and 5 on the second column were also instrumented with one thermocouple each (see Figure V-13). The ambient air temperature was measured by three PT100 temperature sensors (with an accuracy of 0.1°C) positioned in the middle of the test cell at 0.9 m, 1.8 m and 2.6 m from the floor level. Three fluxmeters were stuck to the concrete wall, two on the inner side and one on the outer side.

The weather data were obtained from an existing weather station on the CEA site close to the experimental facade bench. They contained the ambient air temperature measured with a sheltered PT100 sensor, the global horizontal solar radiation and the direct normal radiation, and the wind velocity and direction. An additional pyranometer was mounted on the facade plane to measure the total vertical radiation. A local Agilent data logger recorded all measurements with a time step of one minute.

V.4.1.2 Principle of the model performance assessment

For the model validation, the temperatures measured on module 3 were used, which were the temperature of the front side of the module (T_{g1}), the temperature of the front surface of the UHPC panel (T_{M1}) and the temperature of the internal surface of the concrete wall (T_{M2}).

Before the validation, the experimental data was filtered to discard aberrant measurements such as very high or very low solar radiation, wind speed or ambient air temperature and illogical shifts between the meteorological and the facade temperatures data. The two data sets were not perfectly synchronized since they were not from the same data logger. The data filtering eliminates 66 days of data between January 3rd, 2019 to December 31st, 2019.

The mean bias error (MBE), mean absolute error (MAE), and root mean squared error (RMSE) at each node were estimated to evaluate the model performance (see Appendix A2.3). MBE is used to assess if the model globally overestimates or underestimates the temperature. MAE assesses the model reliability according to the average error magnitude. For the same purpose, the RMSE was also estimated, it penalizes higher absolute error. Hence, a significant difference between the MAE and RMSE indicates an important dispersion of the error magnitudes. The coefficient of determination R^2 is also calculated to assess the fitting of the model to the measurement.

V.4.1.3 Results and discussions

The simulated temperatures are plotted against measured temperatures in Figure V-14 for a general overview of the model accuracy. The figure shows that the points are clustered around the first bisector for the temperature T_{g1} and T_{M1} indicating a good model fitting. In effect, the coefficients of determination R^2 are 97%. The determination coefficient is also satisfactory for node T_{M2} ($R^2 = 95\%$), but the points are generally under the bisector, meaning that the simulated temperature is globally underestimated (see Table V-2).

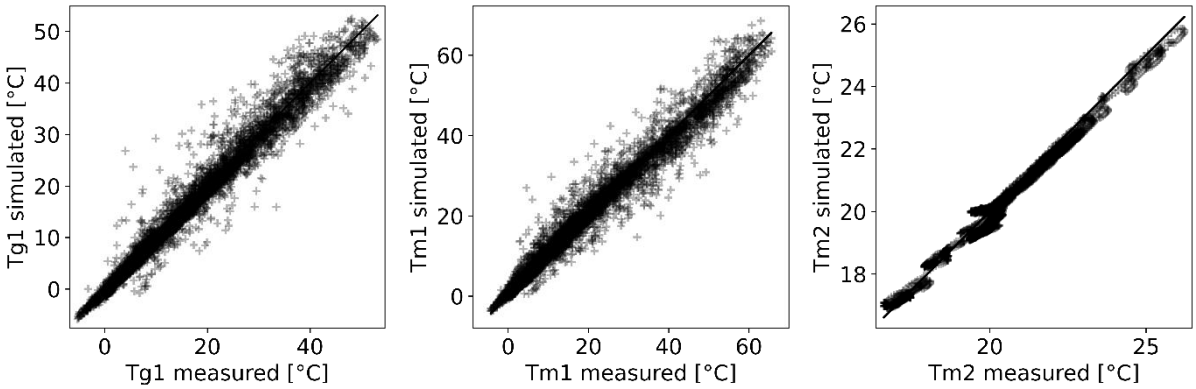

(a) (b) (c)

Figure V-14: Plotting of the simulated temperature against the measured temperature (a) Temperature on the front glass of the PV module T_{g1} (b) Temperature of the exterior surface of the wall T_{M1} (c) Temperature of the interior surface of the wall T_{M2}

Despite these high coefficients of determination, the maximum absolute errors go up to 22.8°C for $|\Delta T_{g1}|$ and 22.4°C for $|\Delta T_{M1}|$ in very few points. Figure V-15 shows the measured, simulated and outdoor ambient air temperatures over the day when those errors occur to understand their origin. A phase shift of one hour in the two compared temperatures is observed. Nonetheless, the peaks of the simulated temperature occur at the same instant as the pic of outdoor temperature. Thus, the errors might be due either to the neglect of PV module capacity or the synchronization of the meteorological and facade temperature data. Indeed, if this shift is corrected, the difference between the peaks of temperature on the nodes become respectively $\Delta T_{g1} = 5.1°C$ and $\Delta T_{M1} = 3.7°C$.

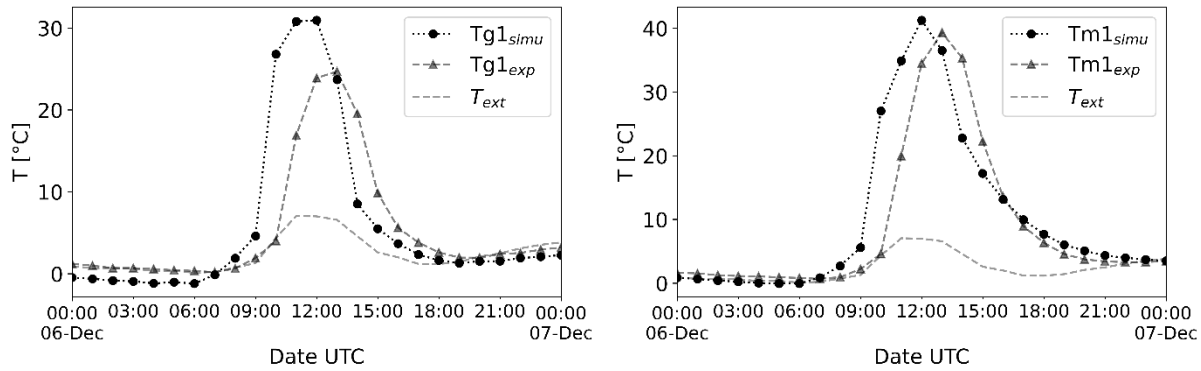

(a) (b)

Figure V-15: Plotting of the simulated, measured and outdoor air temperatures during the day when the maximum errors occur (a) Temperature on the front glass of the module T_{g1} (b) Temperature of the exterior surface of the wall T_{M1}

An enlarged analysis of the model behaviour is conducted by plotting the temperatures during seven days around the summer and winter solstices. Figure V-16 shows that during the summer period, the temperature at the node T_{g1} and T_{M1} closely fit against the measured data. The model underestimates the temperature on the node T_{g1} at night and on the node T_{M1} at higher peaks of temperature during the days. However, during winter, it overestimates the temperature during the day on both temperature nodes. Clear overestimation of the temperature on the node T_{g1} is observed in winter during the occurrence of sudden clear days. Apart from the lack of accuracy on the facade characteristic, those errors can be from the approximation of convection heat transfer coefficients and the external environment temperature. Indeed, the sky temperature does not consider the sky coverage and the ground temperature is assumed to be equal to the ambient air temperature.

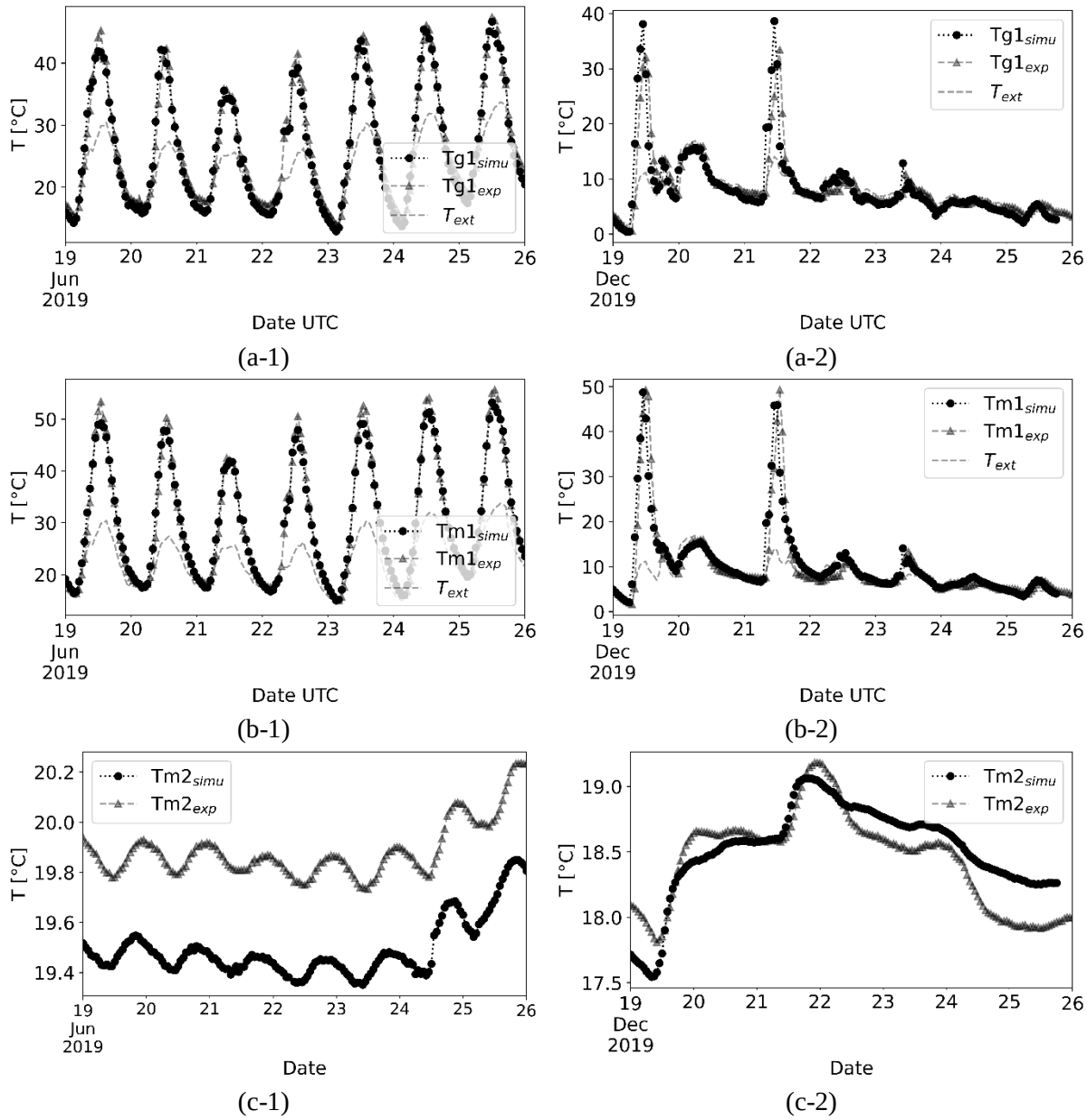

Figure V-16: Plotting of the simulated, measured and outdoor air temperatures during 7 days periods around (1) the summer solstice and (2) winter solstice (a) Temperature on the front glass of the PV module T_{g1} (b) Temperature of the exterior surface of the wall T_{M1} (c) Temperature of the interior surface of the wall T_{M2}

As for the temperature on T_{M2}, there is a slight bias in the model during the summer period. The model has the same trend as the measured temperature, but a quasi-constant error in the data set is observed (see Figure V-16c-1). The comparison of the data sets in June provides a mean bias error (MBE) of -0.4°C. The inaccuracy is probably due to the approximation of the interior radiant environment temperature. Nonetheless, the bias is lessened in winter, but the model loosely follows the measured temperature trend (see Figure V-16c-2).

Plotting the absolute temperature errors against the variation of the global solar radiation would enable the confirmation of the previous observations and the understanding of the limitations of the model. From Figure V-17, the maximum errors on nodes T_{g1} and T_{M1} are observed during low and mid-levels of solar radiation, which corresponds to cloudy days, winter periods and nighttimes. Thus, the model performs best in a period with a clear sky and high irradiance. However, the errors are rather scattered according to the irradiation, especially at the node T_{M2} which is less sensitive to exterior conditions due

to the highly insulated wall. However, in this node, the deviation tends to be slightly higher at high irradiance, whereas it is evenly distributed at low and mid-radiation levels (see Figure V-17c).

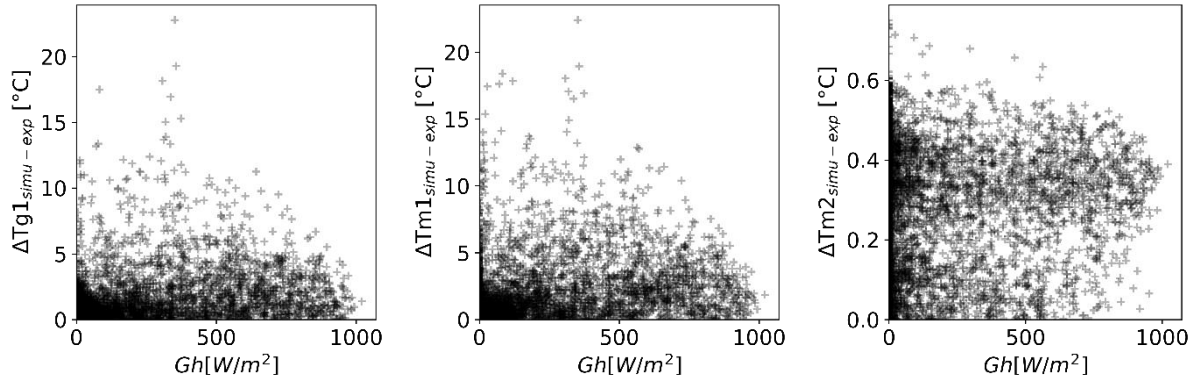

(a) (b) (c)

Figure V-17: Plotting of absolute difference between simulated and measured temperatures against global horizontal solar radiation (a) on the front glass of the module T_{g1} (b) on the exterior surface of the wall T_{M1} (c) on the interior surface of the wall T_{M2}

The variation of the error magnitudes leads to higher root mean squared errors (RMSE) compared to the mean absolute errors (MAE) at T_{g1} and T_{M1}. They are respectively 2.2°C and 1.4°C for T_{g1}, 2.7°C and 1.7°C for T_{M1}. The temperature at T_{g1} is underestimated, considering an MBE value of -0.5°C and that of T_{M2} is slightly overestimated with MBE = 0.2°C. At T_{M2} the error magnitudes vary a little in the model; hence, the values of RMSE and MAE are close (about 0.3°C on the hourly temperature). Those values are also close to the absolute value of MBE (-0.2°C) as the temperature is generally underestimated (with few compensations) (see Table V-2).

Table V-2: Evaluation of the model accuracy according to the hourly and daily temperature

		MAE [°C]	RMSE [°C]	MBE [°C]	R^2 [%]
Hourly temperature	T_{g1}	1.5	2.2	-0.5	97
	T_{M1}	1.7	2.7	0.2	97
	T_{M2}	0.3	0.3	-0.2	95
Mean daily temperature	T_{g1}	0.7	0.9	-0.5	99
	T_{M1}	0.7	1.1	0.2	98
	T_{M2}	0.3	0.3	-0.2	95

To conclude, the simulated temperatures follow the general trend of measured temperatures. The model is able to simulate the rapid fluctuations in the facade despite the importance of the errors in the lower and higher peaks of temperatures at the nodes T_{g1} and T_{M1}. Satisfactory values of MAE and RMSE are obtained in each node. In addition, those metrics are even smaller considering the daily average temperature, which means that the model is able to reproduce all the thermal phenomena occurring in the facade (see Table V-2).

V.4.2 Validation of the steady-state thermal model of the prototypes

V.4.2.1 Selection of the data set and model parameters

Experimental studies on two reduced-scale prototypes were conducted to validate the concept of the bioinspired facade (see Chapter IV). Prototype 1 is a double-skin facade with transparent glazing as the second skin, and Prototype 2 is the PV facade with the PV module as the second skin. The configurations with and without bilayers are investigated for each of those prototypes. The data set from those experimental studies was used to validate the steady-state heat transfer in the basic and modified facade model. Those facades were tested indoors under three levels of air velocity in the gap (natural ventilation, $V_{air} = 1\ m/s$ and $V_{air} = 2\ m/s$ at the inlet) and of solar simulator irradiance ($G = 400\ W/m^2$, $600\ W/m^2$ and $850\ W/m^2$) assumed to be diffuse in the validation.

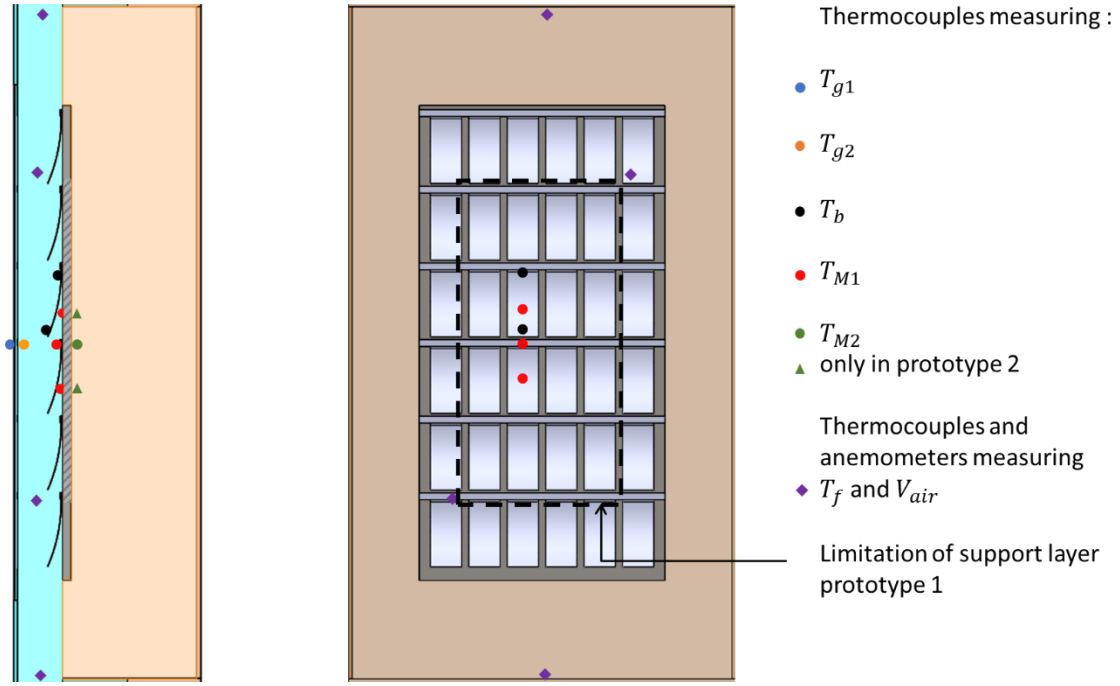

Figure V-18: Positions of the thermocouples and anemometers used for the validation of the model with prototype 2 and prototype 1 considering the limitation of its perimeter

Only the temperature data in the middle of the prototypes are used for the validation to avoid edge effects (see Figure V-18). To fit with the model temperature node, the temperature at the bilayer transversal interspace and on the wall behind the bilayers are averaged for the node T_{M1} at the external surface of the support layer, the same for the node T_{M2} at the internal surface of the support layer but only for prototype 2. The average initial deflections of all the bilayers are considered in the model input to calculate their deflection. The average of all the measurements is taken to account for the validation of the air temperature and velocity in the gap for natural ventilation. Those velocities are used as model input for forced ventilation ($V_{air} = 1\ m/s$ and $V_{air} = 2\ m/s$) to calculate the convective heat transfer coefficients in the gap and the airflow rate.

V.4.2.2 Validation of the model with the data from Prototype 1: the PV module as a transparent glazing

a) Validation of the model considering prototype 1 without bilayers

The plotting of measured and simulated temperatures in prototype 1 without bilayers in Figure V-19 shows a good fit with small deviations at each node. The maximum absolute error among all experiments

is $|\Delta T_{g1}| = 2.6°C$ observed at the node T_{g1} for $G = 850\ W/m^2$ and $V_{air} = 2\ m/s$. This error is an isolated case since most of the deviations are $|\Delta T| < 2°C$. The maximum mean absolute error (MAE) per test is $1.4°C$ (at $G = 850\ W/m^2$ and $V_{air} = 1\ m/s$). Average temperature in the prototype is slightly underestimated according to the value of MBE (see Table V-3).

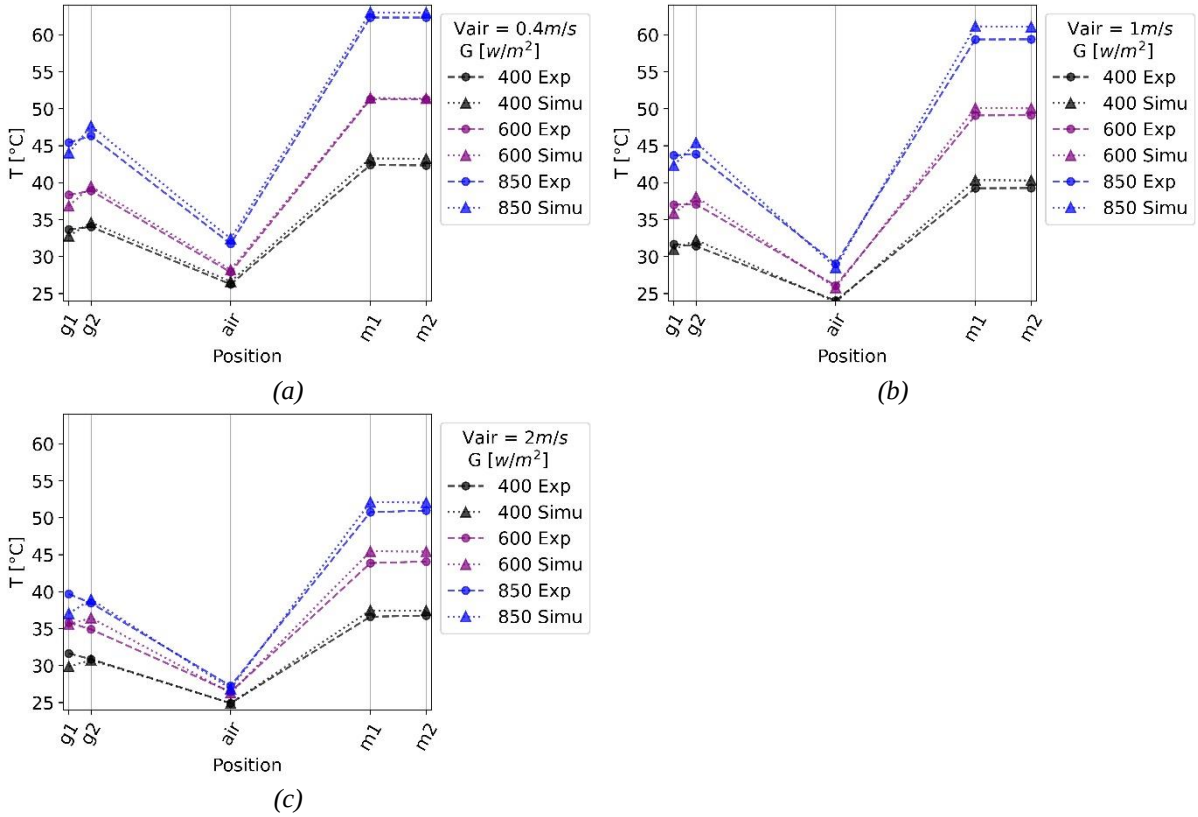

Figure V-19: Measured and simulated temperatures evolution in prototype 1 without bilayers (a) for natural ventilation in the air gap (b) for $V_{air} = 1\ m/s$ (c) for $V_{air} = 2\ m/s$ at the air gap entrance

Table V-3: Difference between the measured and simulated temperatures on the nodes of prototype 1 without bilayers

$V_{air}\ [m/s]$	0,4			1			2		
$G\ [W/m^2]$	400	600	850	400	600	850	400	600	850
$\Delta T_{g1}\ [°C]$	-0.9	-1.5	-1.4	-0.7	-1.2	-1.4	-1.7	-0.3	-2.6
$\Delta T_{g2}\ [°C]$	0.6	0.6	1.4	0.8	1.0	1.6	-0.2	1.5	0.5
$\Delta T_f\ [°C]$	0.4	0.4	0.7	-0.2	-0.3	-0.5	0.0	-0.2	-0.4
$\Delta T_{M1}\ [°C]$	0.9	0.2	0.7	1.1	1.0	1.8	0.9	1.6	1.4
$\Delta T_{M2}\ [°C]$	0.9	0.2	0.6	1.1	0.9	1.7	0.7	1.4	1.1
$MAE\ [°C]$	0.7	0.6	1.0	0.8	0.9	1.4	0.7	1.0	1.2
$MBE\ [°C]$	0.4	0.1	0.5	0.5	0.4	0.8	0.1	0.9	0.2

A higher temperature gradient in the glazing ($T_{g2} - T_{g1}$) is observed in the simulation compared to the experimentation. This is because the temperature T_{g1} ($\Delta T_{g1} < 0$) is underestimated, while that of T_{g2} is

overestimated (see Figure V-19). The deviations in the glazing can be mainly linked to the difficulty of temperature measurement on a transparent media exposed to short-wave irradiation. Radiation heat transfer around the thermocouple is strongly modified by its glueing with an aluminium scotch (see Figure V-20a).

Overestimation of the temperatures at T_{g2}, T_{M1} an T_{M2} can also be linked to an overestimation of the absorbed irradiance on the surfaces. The temperature T_f is also superior to the experiment for a naturally ventilated air gap. In forced convection, T_f underestimation can be from the CHCTs calculation, which only considers the air velocity and not the asymmetric temperatures in the gap. Hence, the error $|\Delta T_f|$ increases with the irradiance, even if it remains small $|\Delta T_f| < 1°C$. The neglect of the air gap asymmetric heating might have led to the overestimation of $h_{c:g2f}$ against an underestimation of $h_{c:fM1}$. Therefore, in the case of $G = 400\ W/m^2$ and $V_{air} = 2\ m/s$, the temperature T_{g2} is slightly underestimated.

The global analysis of the temperature deviations according to the irradiance level shows that the errors do not evolve uniformly with this constraint. However, the highest absolute deviations on each node are obtained with $G = 850\ W/m^2$. Only the glazing temperature estimation is significantly influenced by the rise of irradiance. There is no clear tendency for error evolution according to the change in the air velocity. Nonetheless, it is the model with natural ventilation that shows the best performance.

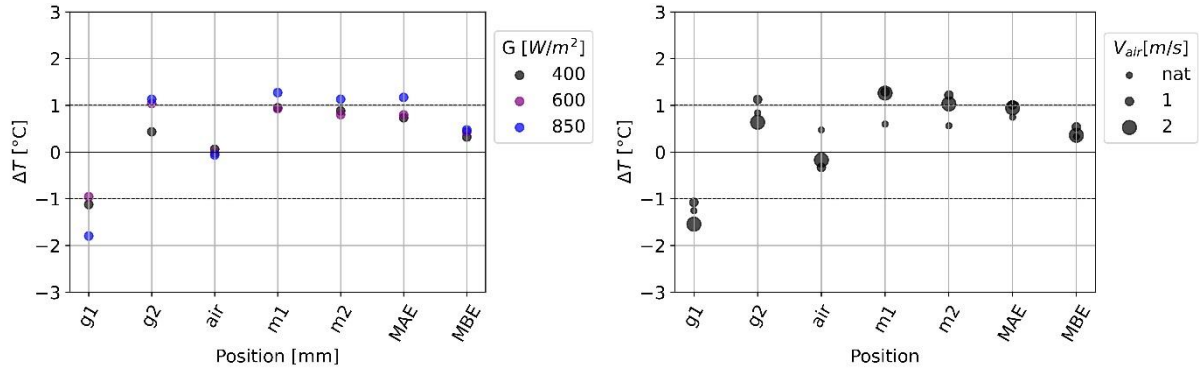

(a) *(b)*

Figure V-20: Difference between the measured and simulated temperatures on the nodes of prototype 1 without bilayers (a) according to the irradiance of the solar simulator (b) according to the air velocity in the gap

In this discussion, I have not suggested the mass flow rate as a possible source of errors. For the mechanically ventilated air gap, it is directly calculated with the experimental mean air velocity. For natural ventilation, the model gives good results, with a maximum error of $|\Delta V_{air}| = 0.01\ m/s$ corresponding to a relative error of 2.4% (see Table V-4).

Table V-4: Comparison of measured and calculated air velocity for natural ventilation in prototype 1 without bilayers

$G\ [W/m^2]$	400	600	850
$V_{air}(\text{meas})[m/s]$	0.32	0.38	0.42
$V_{air}(simu)[m/s]$	0.32	0.37	0.42
$\Delta V_{air}\ [m/s]$	0.003	-0.01	-0.002
$\delta V_{air}\ [\%]$	1.0	-2.4	-0.4

b) Validation of the model considering prototype 1 with bilayers

As in previous model validation, the simulated temperatures in prototype 1 with bilayers also follow the trend of the measured ones (see Figure V-21). The consideration of the bilayers leads to a higher level of temperature deviations. The maximum absolute error and MAE among all tests are lower than in the model without bilayers, respectively, 2.2°C and 1.1°C, both with $G = 850\ W/m^2$ and $V_{air} = 1\ m/s$. However, the recurrence of deviation superior to $|\Delta T| > 2°C$ is more frequent (see Table V-5).

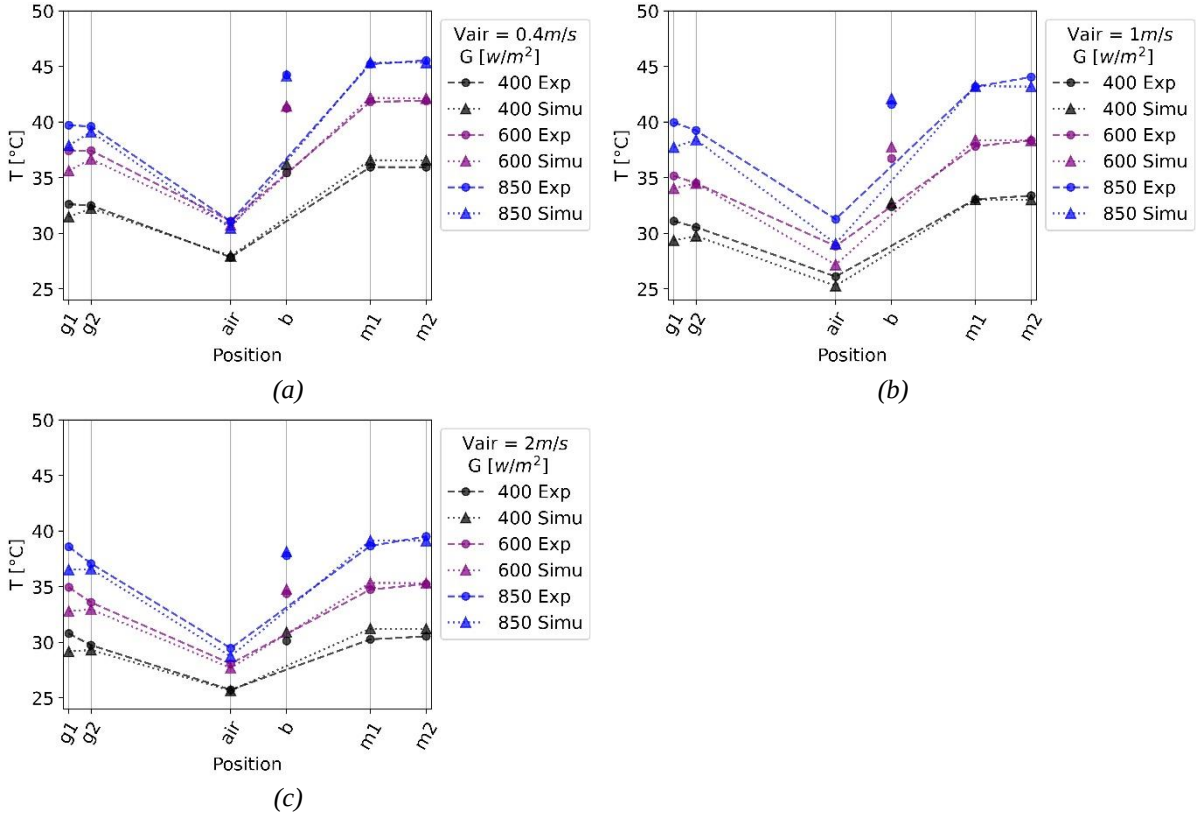

Figure V-21: Measured and simulated temperatures evolution in prototype 1 with bilayers (a) for natural ventilation in the air gap (b) for $V_{air} = 1\ m/s$ (c) for $V_{air} = 2\ m/s$ at the air gap entrance

Here, the underestimation of the glazing temperature is not only from the difficulty of its temperature measurement. Both T_{g1} and T_{g2} are underestimated, and the deviation on T_{g1} is rather significant. As in most cases, the temperature T_b and T_{M1} are superior to the measurement. The errors might come from the approximation of the radiation heat transfer coefficient, which should be improved to balance the temperatures at the boundary surfaces of the air gap. For forced convection, the neglect of facade asymmetric heating enhanced those deviations, as explained in the validation of the model without bilayers.

The temperature at T_f is always inferior to the measurement, with significant error magnitude at $V_{air} = 1\ m/s$. A mixt boundary layer of the flow occurs at this air velocity. Therefore, the errors might come from the approximation used to consider both laminar and turbulent flow. Either way, the proportional increase of $h_{c:fM1}$ with the bilayers bending might also bias the CHTC estimation. In contrast to the model without bilayers, the deviation trend at T_{M2} is not similar to that of T_{M1}. In prototype 1, there were no thermocouples at the internal support layer at the level of the bilayers. Hence, the temperature disparity due to the presence of the bilayers is not perceived at the T_{M2} in the measurement, resulting in its temperature underestimation in some cases. Finally, low deviation of bilayer temperature

($\max|\Delta T_b| = 1.0°C$) permits to defend their approximation as extended fins for convective heat transfer and as flat slats for radiation heat transfer.

Table V-5: Difference between the measured and simulated temperature on the nodes of prototype 1 with bilayers

$V_{air}\ [m/s]$	0,4			1			2		
$G\ [W/m^2]$	400	600	850	400	600	850	400	600	850
$\Delta T_{g1}\ [°C]$	-1.2	-1.8	-1.8	-1.8	-1.1	-2.2	-1.6	-2.2	-2.1
$\Delta T_{g2}\ [°C]$	-0.3	-0.8	-0.5	-0.8	-0.0	-0.9	-0.4	-0.6	-0.5
$\Delta T_f\ [°C]$	0.1	-0.4	-0.6	-0.8	-1.7	-2.2	-0.1	-0.4	-0.7
$\Delta T_b\ [°C]$	0.8	0.2	-0.1	0.4	1.0	0.5	0.8	0.4	0.4
$\Delta T_{M1}\ [°C]$	0.6	0.4	0.2	-0.1	0.6	0.0	1.0	0.6	0.5
$\Delta T_{M2}\ [°C]$	0.6	0.3	-0.2	-0.4	-0.0	-0.9	0.7	0.1	-0.4
$MAE\ [°C]$	0.6	0.6	0.6	0.7	0.7	1.1	0.8	0.7	0.8
$MBE\ [°C]$	0.2	-0.2	-0.4	-0.4	-0.1	-0.7	0.2	-0.2	-0.3

In this model, the evolution of the deviation according to the irradiance is more clearly depicted. The temperature errors tend to decrease with the irradiance (see Figure V-22a), which shows a possible underestimation of the absorbed irradiance, which can be due to the neglect of bilayers longitudinal interspace in the radiosity balance.

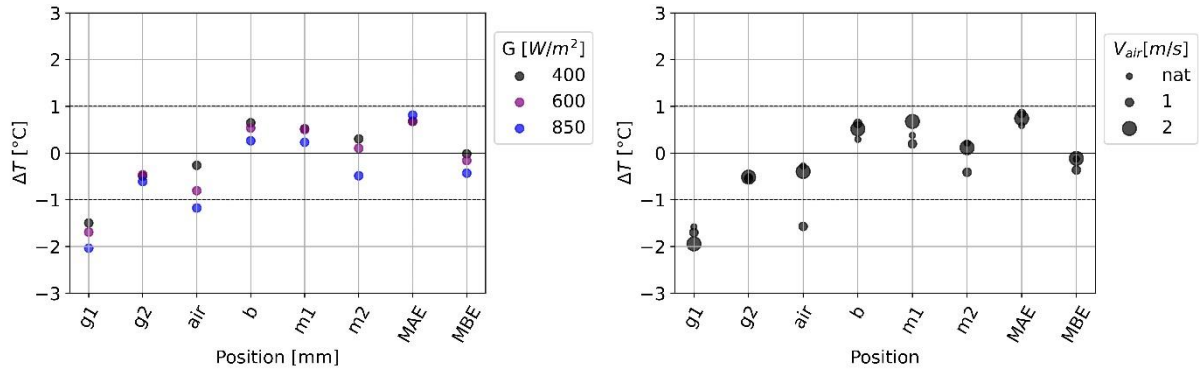

(a) *(b)*

Figure V-22: Difference between the measured and simulated temperatures on the nodes of prototype 1 with bilayers (a) according to the irradiance of the solar simulator (b) according to the air velocity in the gap

Furthermore, there is no obvious relation between model performance and air velocity (see Figure V-22b). The error magnitude per node remains the least inferior at natural ventilation despite a significant underestimation of the airflow rate, which also explains the temperature deviations. The maximum absolute error in air velocity simulation is $|\Delta V_{air}| = 0.11\ m/s$ corresponding to a relative error of $|\delta V_{air}| = 27.3\%$ (with $G = 600\ W/m^2$) (see Table V-6). The assumption of the bilayers as diaphragms might lead to excessive pressure losses considering that the longitudinal interspace between them is large in prototype 1. Thus the validation of prototype 2 with bilayers would enable providing more detail on the limitation of airflow rate estimation.

Table V-6: Comparison of measured and calculated air velocity for natural ventilation prototype 1 with bilayers

$G\ [W/m^2]$	400	600	850
$V_{air}(\text{meas})[m/s]$	0.32	0.39	0.43
$V_{air}(simu)[m/s]$	0.25	0.29	0.32
$\Delta V_{air}\ [m/s]$	-0.07	-0.11	-0.11
$\delta V_{air}\ [\%]$	-21.3	-27.3	-25.1

V.4.2.3 Validation of the model with the data from Prototype 2: with the PV module

a) Validation of the model considering prototype 2 without bilayers

Similarly to the study of prototype 1, the measured and simulated temperatures are compared in prototype 2 with the PV module as the second skin. For the prototype without bilayers, the model also reproduces well the measured temperatures (see Figure V-23). The maximum absolute error per test constraint is $|\Delta T_{g2}| = 2.4°C$ observed at the node T_{g2} with $G = 850\ W/m^2$ and $V_{air} = 1\ m/s$. The maximum MAE is 1.1 °C with the test performed with $G = 400\ W/m^2$ and $V_{air} = 1\ m/s$. The MBE values also indicate a global overestimation of the average temperature (see Table V-7), suggesting a possible overestimation of the absorbed irradiance.

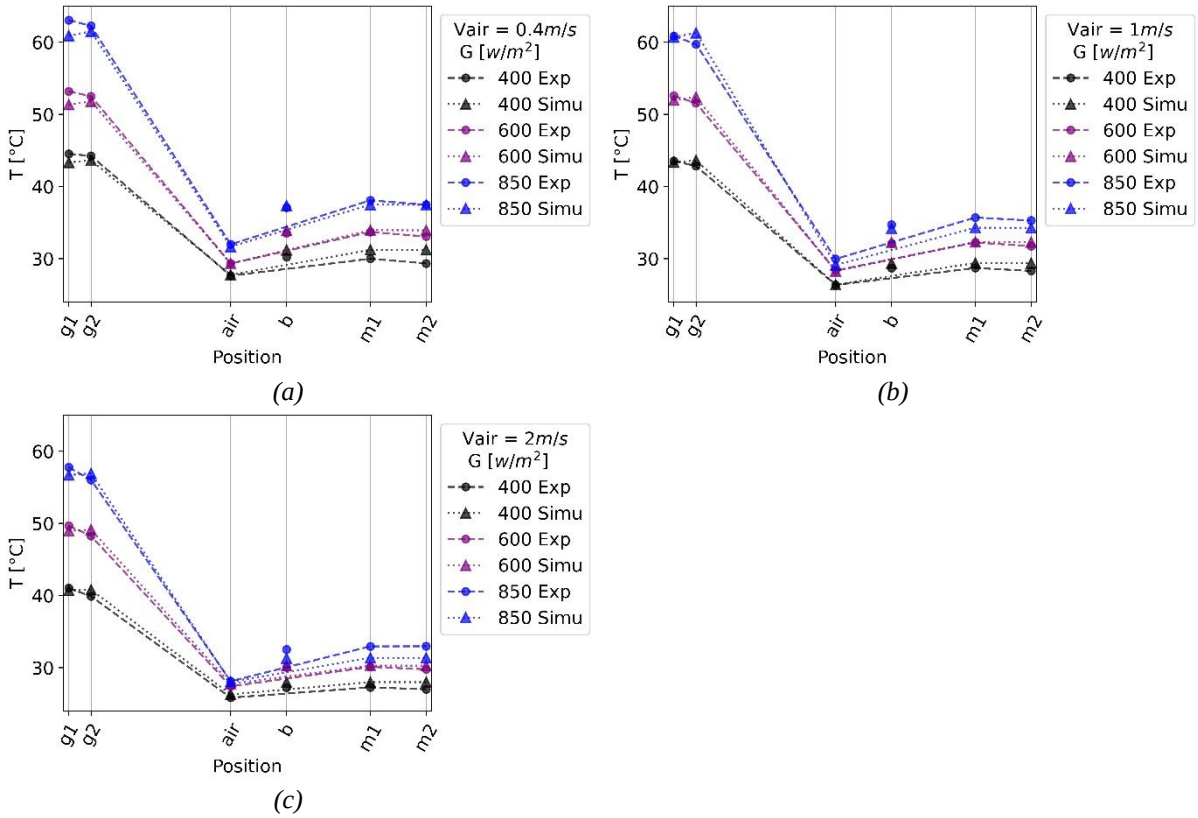

Figure V-23: Measured and simulated temperatures evolution in prototype 2 without bilayers (a) for natural ventilation in the air gap (b) for $V_{air} = 1\ m/s$ (c) for $V_{air} = 2\ m/s$ at the air gap entrance

In general, the temperature at the node T_{g1} is still underestimated but with less accentuated error. Only some measurements at $V_{air} = 2\ m/s$ are slightly overestimated. The temperature gradient in the glazing ($T_{g2} - T_{g1}$) is positive in the simulation but negative in the experiment (see Figure V-23). Despite their

non-uniform trend, the errors are likely to increase with the irradiance on T_{g2} while its decreases at T_{M1} and T_{M2} (see Figure V-24a).

Table V-7: Difference between the measured and simulated temperatures on the nodes of prototype 2 without bilayers

$V_{air}\ [m/s]$	0,4			1			2		
$G\ [W/m^2]$	400	600	850	400	600	850	400	600	850
$\Delta T_{g1}\ [°C]$	-1.0	-1.1	-0.8	-0.1	-0.6	-0.1	0.6	-0.4	0.2
$\Delta T_{g2}\ [°C]$	-0.4	-0.2	0.3	0.8	0.8	1.5	1.9	1.3	2.4
$\Delta T_{f}\ [°C]$	-0.1	0.6	1.0	0.1	-0.2	-0.3	0.2	-0.2	-0.2
$\Delta T_{M1}\ [°C]$	1.3	1.0	0.6	1.2	1.2	0.9	1.5	-0.3	-0.2
$\Delta T_{M2}\ [°C]$	1.4	1.1	0.7	1.2	1.2	0.7	1.4	-0.5	-0.6
$MAE\ [°C]$	0.9	0.8	0.7	0.8	0.8	0.7	1.2	0.5	0.7
$MBE\ [°C]$	0.4	0.4	0.4	0.7	0.5	0.6	1.2	0.1	0.4

For natural ventilation, as the deviation trend of the temperature T_f follows that of the warmer wall (T_{g2}), this compensating behaviour might be linked to the longwave radiation modelling in the gap, which evolves only the nodes T_{g2} and T_{M1}. For forced convection, the approximation of CHTC, which overlooks the asymmetric heating of the facade, can lead to an underestimation of $h_{c:g2f}$ at the PV module (the warmer surface) and an overestimation of $h_{c:fM1}$ at the support layer.

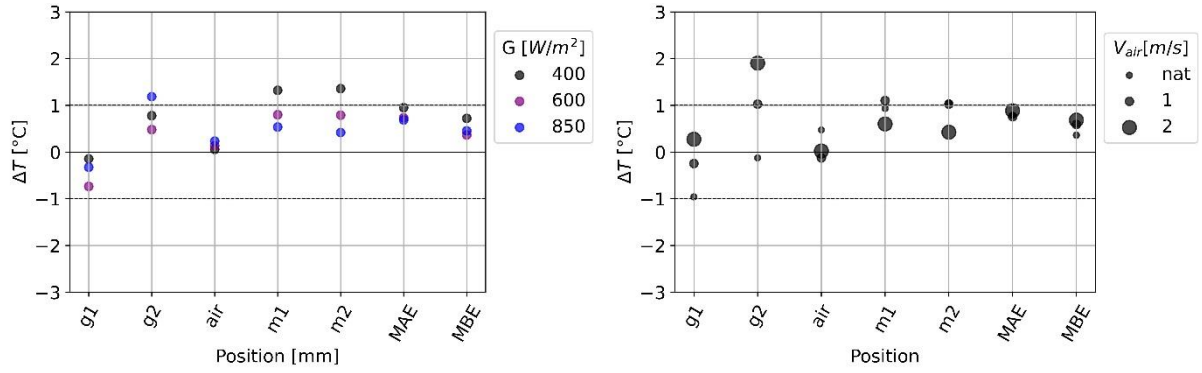

(a) (b)

Figure V-24: Difference between the measured and simulated temperatures on the nodes of prototype 2 without bilayers (a) according to the irradiance of the solar simulator (b) according to the air velocity in the gap

In a global analysis of the deviation according to the air velocity level, Figure V-24b shows that the temperature deviations are significantly influenced uniformly by the air velocity at the nodes T_{g1} and T_{g2}. This confirms the bias related to the choice of convective heat transfer. The model with natural ventilation gives the best approximation of temperature. Furthermore, a good fit with the measurement is obtained with the comparison of the air velocity in the naturally ventilated prototype. The maximum absolute error is just $|\Delta V_{air}| = 0.01\ m/s$ corresponding to a relative error of 3.0%. The errors increase with the irradiance level (see Table V-8).

Table V-8: Comparison of measured and calculated air velocity for natural ventilation prototype 2 without bilayers

$G\ [W/m^2]$	400		600		850	
$V_{air}(\text{meas})[m/s]$	0.30	0.32	0.38	0,36	0,42	0,43
$V_{air}(simu)[m/s]$	0.31	0.31	0.36	0,36	0,41	0,41
$\Delta V_{air}\ [m/s]$	0.01		-0.007		-0.01	
δV_{air} [%]	1.7		-1.9		-3.0	

Finally, the simulated PV power outputs are very close to the measured ones. The maximum deviation is just $\Delta P_{PV} = 0.9\,W$ corresponding to a relative error of 3.2% at $G = 400\,W/m^2$ with natural ventilation. The trend of error deviation according to the variation of the irradiance is closely similar to the tendency in the estimation of the temperature T_{g2}. However, considering that the PV power output is mainly influenced by the irradiance, a uniform error evolution with irradiance increase is expected. Thus, the non-uniform evolution of the deviation with the irradiance can be linked to the measurement error underestimating the irradiance at $G = 600\,W/m^2$ (see Table V-9). Hence, the model overestimates the temperature at glazing with the increase of irradiance, whereas it tends to underestimate the temperature at the wall and the PV power output with the increase of irradiance.

Table V-9: Difference between the measured and simulated PV power outputs for prototype 2 without bilayers

$G\ \left[\frac{W}{m^2}\right]$	$V_{air}\ \left[\frac{m}{s}\right]$	$P_{PV}\ [W]$		$\Delta P_{PV}\ [W]$	δP_{PV} [%]
		Meas	Simu		
400	0.4	27.9	28.8	0.9	3.2
		28.5	28.9	0.4	1.4
	1	28.7	29.1	0.4	1.1
		28.6	29.2	0.6	1.9
	2	29.0	29.8	0.8	2.5
		29.0	29.6	0.6	2.0
600	0.4	42.6	42.0	-0.6	-1.4
		42.7	42.1	-0.6	-1.4
	1	43.0	42.5	-0.5	-1.2
		42.9	42.5	-0.4	-1.0
	2	43.4	43.3	-0.1	-0.2
850	0.4	57.1	57.5	0.4	0.7
		57.0	57.2	0.2	0.4
	1	57.6	57.8	0.1	0.3
		57.8	57.7	-0.1	-0.3
	2	58.3	58.7	0.4	0.8

b) Validation of the model considering prototype 2 with bilayers

Finally, the validation of the model with a PV module and the bilayer components is presented here, considering the experimental result from prototype 2 with bilayers. As shown in Figure V-25, the general trend in the temperature evolution in the prototype layers is also respected. Per test constraints, the maximum absolute error was $|\Delta T_{M2}| = 2.2°C$ and the maximum MAE was 1.1 °C, both observed at the node T_{M2} at $G = 400\ W/m^2$ with natural ventilation. Globally the model tends to underestimate the temperature at high irradiance according to the value of MBE (see Table V-10).

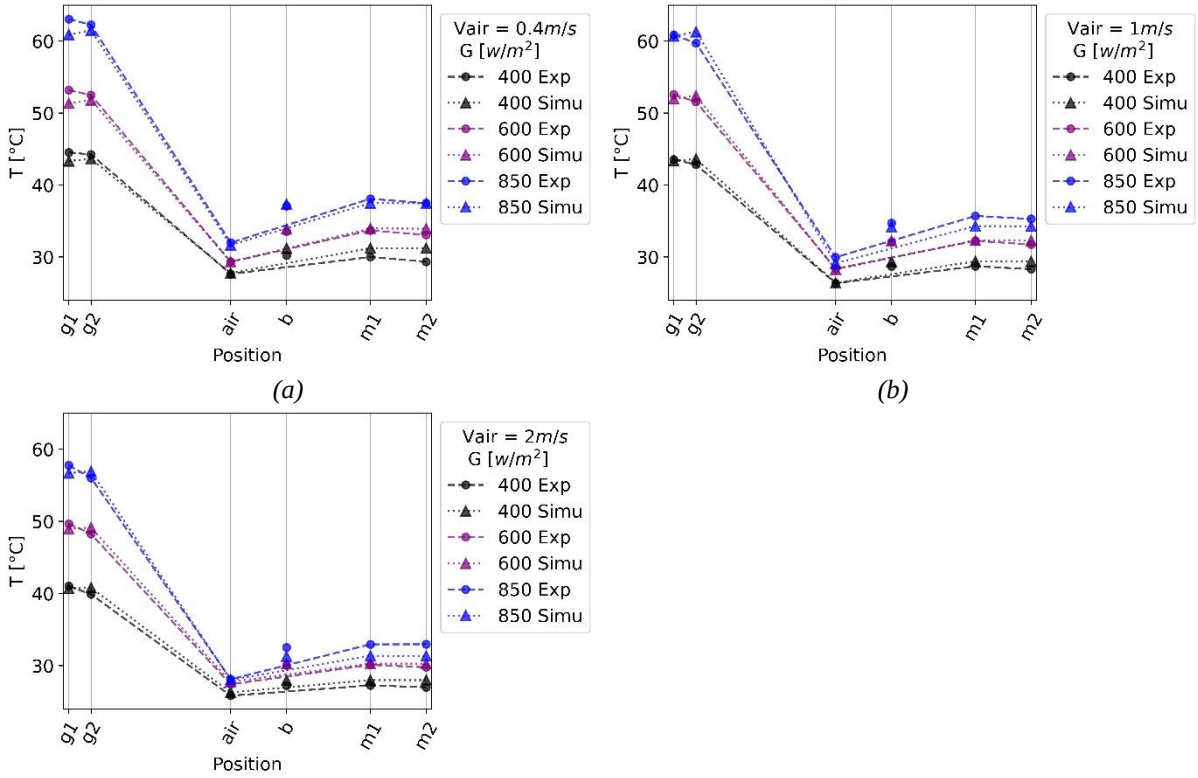

Figure V-25: Measured and simulated temperatures evolution in prototype 2 with bilayers (a) for natural ventilation in the air gap (b) for $V_{air} = 1\ m/s$ (c) for $V_{air} = 2\ m/s$ at the air gap entrance

The error tendency is closely similar to prototype 2 without bilayers but with different order of the deviation magnitudes. Those trends include:

- the underestimation of temperature T_{g1};
- decreasing errors at the wall against increasing errors at the PV module with the increase of irradiance at forced convection (see Figure V-25 and Table V-10);
- the high influence of the air velocity on the PV module temperature (see Figure V-26b);

and a good approximation of the PV power output that would likely decrease with the irradiance, considering a possible error of irradiance measurement at $G = 600\ W/m^2$ (see Table V-11).

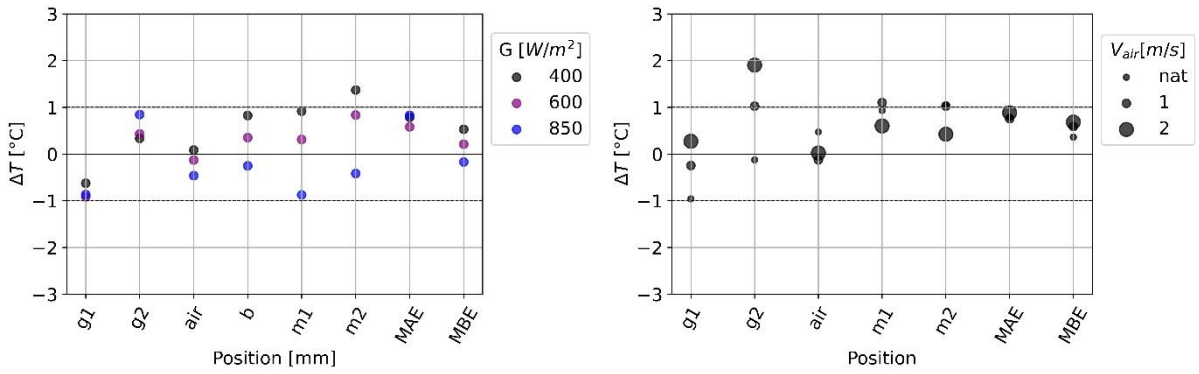

Figure V-26: Difference between the measured and simulated temperature on the nodes of prototype 2 with bilayers (a) according to the irradiance of the solar simulator (b) according to the air velocity in the gap

However, the error trend in the air gap boundary surfaces is not compensating for natural ventilation. The model generally tends to underestimate the temperature with the increase of irradiance. Hence, irradiance intake tends to be underestimated as it increases (see Table V-10). As for the bilayer temperature estimation, a good fit is obtained, with a maximum of $|\Delta T_b| = 1.2°C$ (at $G = 400\ W/m^2$ with a naturally ventilated air gap).

Table V-10: Difference between the measured and simulated temperatures on the nodes of prototype 2 with bilayers

$V_{air}\ [m/s]$	0,4			1			2		
$G\ [W/m^2]$	400	600	850	400	600	850	400	600	850
$\Delta T_{g1}\ [°C]$	-1.2	-1.5	-2.0	-0.3	-0.4	0.4	-0.4	-0.9	-1.0
$\Delta T_{g2}\ [°C]$	-0.6	-0.5	-0.7	0.7	1.1	2.1	0.9	0.8	1.1
$\Delta T_f\ [°C]$	-0.1	-0.2	-0.2	-0.0	-0.4	-1.1	0.4	0.1	-0.1
$\Delta T_b\ [°C]$	1.7	0.8	0.3	0.7	0.2	-0.2	0.7	0.1	-0.9
$\Delta T_{M1}\ [°C]$	1.5	0.8	-0.5	0.6	0.1	-1.0	0.6	0.0	-1.6
$\Delta T_{M2}\ [°C]$	2.2	1.6	0.2	1.0	0.6	-0.4	0.9	0.3	-1.1
$MAE\ [°C]$	1.1	0.9	0.7	0.6	0.4	1.0	0.6	0.4	0.9
$MBE\ [°C]$	0.6	0.3	-0.3	0.5	0.2	0.1	0.5	0.1	-0.3

Table V-11: Difference between the measured and simulated PV power output for prototype 2 with bilayers

$G\ \left[\frac{W}{m^2}\right]$	$V_{air}\ \left[\frac{m}{s}\right]$	$P_{PV}\ [W]$		$\Delta P_{PV}\ [W]$	δP_{PV}
		Meas	Simu		
400	0.4	28.4	29.3	0.9	3.0
		28.9	29.2	0.3	1.0
	1	29.2	29.4	0.2	1.0
		29.1	29.2	0.1	0.4
	2	29.4	29.7	0.3	1.1
		29.6	29.7	0.1	0.3

600	0.4	43.3	42.8	-0.5	-1.0
		43.2	42.4	-0.8	-1.8
	1	44.1	42.6	-1.5	-3.4
		43.7	42.5	-1.2	-2.8
	2	44.1	43.1	-1.0	-2.2
		44.3	43.4	-0.9	-2.0
850	0.4	58.1	58.2	0.1	0.1
		57.8	57.7	-0.1	-0.0
	1	58.4	58.3	-0.1	-0.2
		58.0	57.8	-0.2	-0.4
	2	59.6	59.2	-0.4	-0.6
		58.8	58.7	-0.1	-0.1

Finally, unlike in prototype 1 with bilayers, the errors in the calculated air velocity are less pronounced. It also evolves with the irradiance and reaches a maximum of $|\Delta V_{air}| = 0.06\, m/s$ as average at $G = 850\, W/m^2$ corresponding to a relative error of 14.6%. This order of error magnitude is acceptable, especially for lower radiation levels. In effect, the approximation of the bilayers as diaphragms in prototype 2 for the airflow calculation is more accurate than in prototype 1 because their longitudinal interspaces are very narrow and can be neglected (see Table V-12). Thus, the bilayer approximation is relevant only for narrowly packed bilayers in the transverse direction.

Table V-12: Comparison of measured and calculated air velocity for natural ventilation prototype 2 with bilayers

$G\ [W/m^2]$	400		600		850	
$V_{air}(\text{meas})[m/s]$	0.28	0.30	0.32	0.33	0.40	0.40
$V_{air}(simu)[m/s]$	0.27	0.27	0.31	0.31	0.34	0.34
$\Delta V_{air}\ [m/s]$	-0.02		-0.02		-0.06	
δV_{air} [%]	-6.08		-5.96		-14.55	

V.5 Conclusions

In summary, this chapter presents the modelling and the validation of the thermal model of PV facades studied in this work. The dynamic model corresponding to the ordinary PV facade is validated with one-year experimental data from a real-scale PV facade. Satisfactory results are obtained. The model performs the best during clear sky days with high irradiance in consecutive periods. Nonetheless, its dependence on solar irradiance is small, and the highest errors occur at lower and higher picks of daily temperature. Some improvements of the model can be undertaken in the estimation of environment radiant temperature, the consideration of the PV model heat capacity and the choice of convective heat transfer coefficient.

Experimental data from reduced-scale prototypes are used to validate the steady-state thermal model of the ordinary PV facade without bilayers and the bioinspired facade with bilayers. The models also give a good fit with the temperature measurements in overall cases. For the facade with the glazing, the model without bilayers tends to overestimate the temperature as the irradiance rises. The opposite behaviours

are observed with the model with bilayers. However, in the PV prototype, an overestimation of PV temperature against an underestimation of wall temperature is observed with the increase of irradiance. This is accompanied by an underestimation of PV power output with the rise of irradiance. In the range of studied irradiance, the errors are satisfactory. However, those features should be taken into account in further parametric studies of the facade.

The models give the best estimation for a naturally ventilated facade. Narrow longitudinal interspaces between the bilayers are required to obtain a good approximation of the airflow rate. A two-dimensional thermal model can be considered for better airflow and radiation heat transfer modelling. Also, the asymmetric heating of the airgap can be considered to enhance the accuracy of the thermal model.

Chapter VI. Assessment of the bioinspired facade performance

VI.1 Introduction

The bioinspired PV facade designed in this project uses thermosensitive bilayers to modulate its heat exchange and enhance PV power production. The investigations presented in previous chapters have confirmed the relevance of those components in reducing the facade temperature in summer and slightly enhancing PV power production. Quantification of those improvements on the yearly based building thermal loads and electricity production is necessary to validate the concept performance. This issue is discussed in this chapter by assessing the energy performance of a building integrating the facade according to the region of its implementation.

For this, a fictive tertiary building is investigated by assessing the improvement brought by the bioinspired facade compared to standard BIPV facades and multilayer walls. Integration of those facades on the southern side of the building is considered. Their models are developed in Python (see Chapter V) and are coupled with a building energy model simulated on EnergyPlus. Yearly cooling and heating loads and PV electricity production are then compared for each configuration. This chapter is divided into two parts. The first part describes the facade and the building model. The second part provides and discusses the results of the simulations conducted.

VI.2 Description of the facades and the building

VI.2.1 Description of the facade

The bioinspired facade is compared to two types of standard multilayer walls and BIPV facades to evaluate its potential to improve the building energy performance (see Figure VI-1).

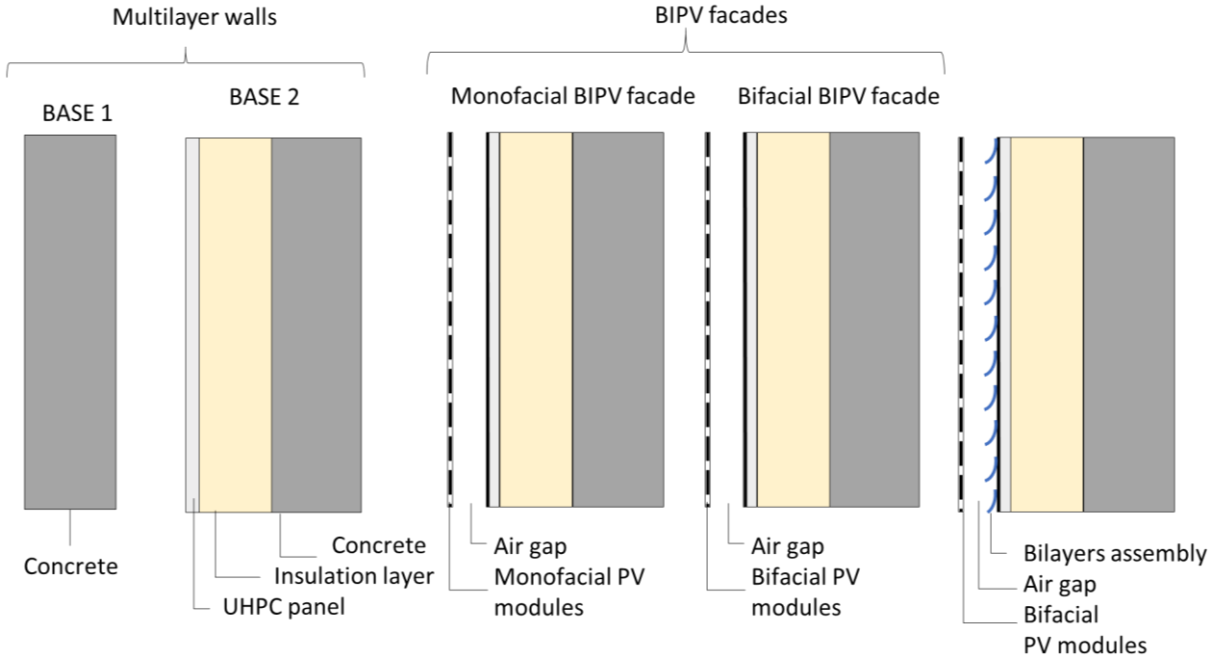

Figure VI-1: Composition of the compared facades: uninsulated concrete wall (BASE 1) - standard insulated concrete facade (BASE 2) – Monofacial BIPV facade – Bifacial BIPV facade – Bifacial BIPV facade with bilayers (DYNABIOSOL)

For the multilayer walls, the first one is an uninsulated concrete wall, supposed to be composed only of a 20 cm thick concrete layer and referenced as BASE 1. The comparative study with this facade enables assessing the bioinspired facade performance in the case of building refurbishment framework.

The second facade noted BASE 2 is an ordinary insulated facade composed of an external coating made of 2 cm thick ultra-high performance fibre concrete (UHPC) panels, a 12 cm thick rock wool insulation layer and a 20 cm thick concrete wall (as in the facade BASE 1) (see Table VI-1). This composition constitutes the multilayer wall in the BIPV facades and the bioinspired facade. Only a minimum thickness of insulation is analysed to focus on standard thermal performances of building facades because the impact of the bilayers can not be evaluated if the insulation is too thick. The comparison with this facade highlights if the concept improves an insulated facade that should be thermally performant in standard configuration.

Table VI-1: Composition of the multilayer wall: the facade BASE 2

Layers	Material	Thickness [cm]	Thermal conductivity k [W/mK]	Density ρ [kg/m^3]	Specific heat Cp [J/kgK]	Heat transfer coefficient U [W/m^{2}K]
Exterior	UHPC panel	2	0.16	880	2500	0.27
|	Rock wool insulation	12	0.035	20	1030	
Interior	Concrete	20	2.32	880	2500	

The BIPV facades are constituted by semi-transparent PV modules, a 10 cm thick airgap opened on its top and bottom at each floor and the multilayer wall. Both the integration of the monofacial and bifacial PV modules are studied to analyse the relevance of bifacial PV modules in building facades. Therefore, there are the facade mono-BIPV with monofacial PV modules and the facade bi-BIPV with bifacial ones.

The bioinspired facade is noted as DYNABIOSOL. It has the same configuration as the bi-BIPV facade but with the bilayer components mounted on the UHPC panels. Two scenarios of air gap opening control are considered with this facade to study the necessity of air control modulation as the bilayers tend to cool the facade regardless of the season:

- First, in DYNABIOSOL 1, the air gap is opened and naturally ventilated without any control operation;
- Second, in DYNABIOSOL 2, the air gap is opened or closed according to the outdoor and PV module temperatures. The ventilation in the air gap can be forced or natural to optimise the PV cooling and heat dissipation. For this, the following schedule is considered:
    - The airgap is closed if the outdoor temperature $T_{ext} < 10°C$;
    - During winter:
        - The air gap is closed at night from 6 pm to 6 am, and when the outdoor temperature is $T_{ext} < 19°C$ and $T_{PV} < 25°C$;
        - When $T_{PV} > 25°C$, the air gap is opened with natural ventilation to obtain a module efficiency always close to the reference (the Standard testing conditions STC with $T_{STC} = 25°C$ and $G_{STC} = 1000\ W/m^2$);
    - During summer, the air gap is always open; it operates:
        - With natural ventilation if $T_{PV} < 25°C$;
        - With mechanical ventilation of 2 m/s if $T_{PV} > 25°C$.

For all BIPV facades, the PV modules have 30% of semi-transparency. The electrical efficiency of the PV cells is 20% at STC and has a temperature coefficient $\beta = 0.0045/°C$. The bifacial PV modules have a bifaciality factor of 90%.

In the DYNABIOSOL facade, the bilayers have an effective length of 15.5 cm and a width of 7 cm. They are supposed to be arranged behind the PV cells. As the facade thermal model is one-dimensional, both the PV cells and the bilayers are assumed to be closely packed according to the facade width direction. The total width of the bilayers is then equal to the width of the facade. Only the number of rows of the bilayers in the facade height is relevant in the model. It equals 9 rows of bilayers per 2 m of facade height according to the PV module semi-transparency factor.

VI.2.2 Description of the building and its model

Those facades are integrated into a three-floor fictive tertiary building with a square area of 15 m x 15 m. Each floor is 2.5 m in height and has the same configuration. Three sides of the building are highly glazed with double-glazing windows and are oriented respectively to the east, the west and the north. The southern side encloses the tested facades (see Figure VI-2).

The assessment of the DYNABIOSOL facade is conducted considering the southern orientation only because the concept is designed mainly for this orientation. Changes in the bilayer disposition should be considered for optimal integration of the components on other orientations, namely the choice of the direction of the bilayer deflection to fit the sun path.

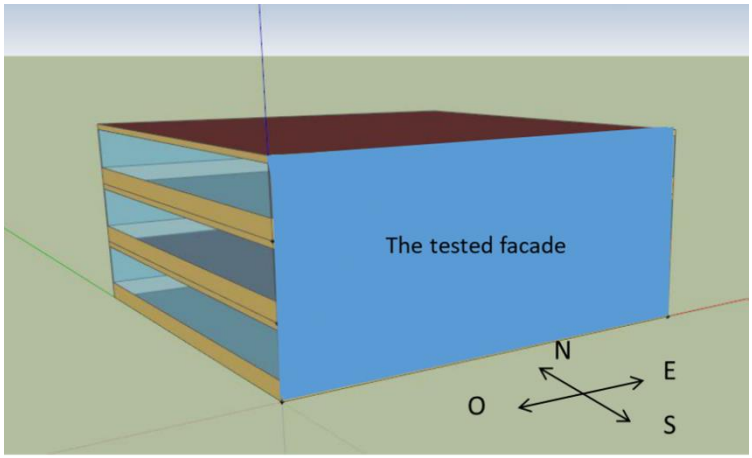

Figure VI-2: Architecture of the modelled building

Three implementations of the building are considered to explore the adequacy of the facade to operate in different climates in France. Those are Paris (48.857° N, 2.351° E), Lyon (45.760° N, 4.840° E) and Nice (43.703° N, 7.27° E).

In effect, there are 8 climatic zones in France. They are distinguished by the indication H1, H2, and H3 according to the severity of the temperature in winter (with H1 the coldest). These indications are followed by the letters a,b,c or d according to the temperature in summer, with the letter “a” the least warm and with moderate solar irradiance. Hence, Paris in zone H1a would represent a climate with a cold winter with lower solar irradiance. Lyon in zone H1c would represent a cold winter and warm summer region. Nice in zone H3 would represent a region with mild winter, warm summer and high solar irradiance.

VI.2.2.1 Building wall compositions

This subsection details the compositions of the other walls of the building apart from the tested facade.

- Opaque walls

The opaque walls on the north, east and west orientations and the floors are constituted by insulated concrete layers. Details on the compositions of those walls are given in Table VI-2.

- Glazed walls

The glazings on the north, west and east sides cover the width of the building and are 1.4 m in height. They are double-glazing windows with a heat transfer coefficient of 1.1 W/m^{2}K, a solar heat gain coefficient (SHGT) of 0.5 and a visible light transmittance (VT) of 0.7. The sill of those windows is 0.9 m in height.

Table VI-2: Composition of the other opaque walls

Type of wall	Material	Thickness [cm]	Thermal conductivity k [W/mK]	Density ρ [kg/m3]	Specific heat Cp [J/kgK]	Heat transfer coefficient U [W/m^{2}K]
Exterior wall	Exterior coating	1.5	1.00	1450	500	0.144
	Extruded polystyrene	20	0.03	35	1400	
	Concrete wall	25	2.5	2500	1000	
Low floor	Extruded polystyrene	20	0.03	35	1400	0.140
	Reinforced concrete slab	25	2.5	2500	1000	
Intermediate floor	Reinforced concrete slab	25	2.5	2500	1000	4
Roof terrace	Extruded polystyrene	20	0.03	35	1400	0.140
	Reinforced concrete slab	25	2.5	2500	1000	

VI.2.2.2 Modelling of the building

A building model developed in EnergyPLus from a previous project of the CEA laboratory is used in this investigation. The model uses a nodal or multizone approach in which neighbouring building spaces with the same aero-thermal solicitations, such as the temperature, ventilation rate and internal loads, can be represented as a zone. Thus, each zone is considered a homogenous volume characterised by the same variable states and described by a unique node (Foucquier et al., 2013). Each floor is considered as a unique zone to ease the building energy modelling. Thus, the same temperature thermostat would be allocated. The entire building is, therefore, modelled with three zones. The energy systems and the internal heat gains in the building are detailed in the following subsection.

VI.2.3 Description of the energy systems and the scenarios

VI.2.3.1 Temperature set point

The building simulation aims to determine the energy needs of the building according to the southern facade configuration. Explicit modelling of the energy production systems for heating and cooling is not

required. Energyplus can determine those needs with the temperature setpoint. Here, a temperature setpoint of 19°C is considered during the heating season and a temperature setpoint of 26°C during the cooling season.

VI.2.3.2 Ventilation

A balanced ventilation system with a heat exchanger and a bypass system is considered in the building. The bypass is for directly supplying outdoor air into the building space without using the heat exchanger. Therefore, it is used when the outdoor air temperature allows for meeting the thermal requirement with minimal energy use. The heat exchange is used to precool or preheat the outdoor temperature with the exhaust air before its injection. The exchange/bypass scenario used is illustrated in Figure VI-3.

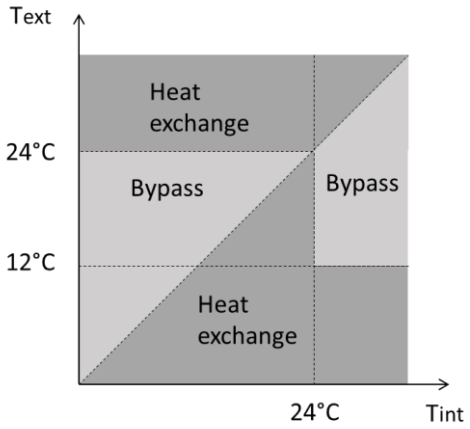

Figure VI-3: Principle of the dual flow ventilation operation

The ventilation system is modelled using a simplified "equivalent flow" method in EnergyPlus. In bypass mode, the flow rate is the nominal flow rate of 18 m^3 per hour per occupant. When there is a heat exchange, the equivalent flow rate injected in the model is reduced by 60% to consider the exchanger efficiency. Night ventilation is considered on summer nights to provide free cooling. An air flow rate four times higher than the nominal air flow rate during the occupancy period is considered.

VI.2.3.3 Internal heat gain

Internal heat gains in the building are from the heat dissipation from the occupants, electronic equipment (such as office equipment like computers), artificial lighting, and domestic hot water use. They are modelled according to the scenario of their occurrences as follows:

- **Occupancy scenario**

A building occupancy of 23 people per floor is considered, leading to 0.1 person/m² in the offices. Each person is considered to emit an internal heat input of 90W and occupy the building only during weekdays from 8 am to 6 pm.

- **Equipment**

An identical scenario is considered for the internal heat gain from the equipment on each floor. It is assumed to be 16 W/m² during the building occupancy, meaning during weekdays from 8 am to 6 pm. The rest of the time, it is 1.6W/m².

- **Lighting**

Similarly, internal heat gain from artificial lighting is considered only during building occupancy (from 8 am to 6 pm on weekdays). The artificial lighting control follows illuminance in each zone. The

luminaries are on if daylighting does not provide an illuminance of 500 lux in each zone at the height of 80 cm. Internal heat gain related to the luminaries is 7 W/m^2 when they are on.

- **Domestic hot water**

Heat gain from hot water is estimated to be 65 W per Heater.

VI.2.3.4 Electricity needs

As the building, energy and ventilation systems are not explicitly designed, the electricity needed from those systems and their auxiliaries (like fans and pumps) is not calculated. However, to assess the percentage of electricity coverage from the PV production, I have referred to the mean electricity consumption observed in office buildings labelled BBC (low energy consumption building) studied in the PREBAT project in France (CEREMA, 2022). Hence, on average, the electricity needs in primary energy according to a conversion coefficient of 2.58 are for :

- a dual flux mechanical ventilation is 18.5 kWh/m^2/year,
- the auxiliaries for the conditioning energy and hot water consumptions are 6.5 kWh/m^2/year,
- the equipment for the occupant circulation (introduced in the new French environmental regulatory calculation RE2020), such as the lift, is between 0.4 to 3 kWh/m^2/year.

The maximum sum of those needs is 28 kWh/m^2/year in primary energy or 11 kWh/m^2/year of end-use electrical energy (electricity need for lightning excluded as calculated with the building model). The end-use electricity is compared here with the local electricity production by the PV modules.

The building model is simulated with those parameters. It gives as output the cooling and heat loads of the building and the PV production of the facade, which are presented and compared for each facade configuration in the following part of this chapter.

VI.3 Results and discussions

This section focuses on the impact of the facade DYNABIOSOL, considering the building cooling and heating energy demand and the PV power production according to the region of building implementation. The assessment of the thermal performance (cooling and heating) is conducted by taking the building with the facade BASE 1 with the uninsulated concrete and the facade BASE 2 as references. Comparisons with the other types of BIPV facades are also undertaken. The PV power production is assessed by comparing the three scenarios of PV module integration. The results are presented in kWh per m^2 of the conditioned building area and in kWh per m^2 of PV module for PV power production to provide a global insight into energy use.

VI.3.1 Impact of the bioinspired facade on cooling performance

The cooling load per conditioned area of the building are presented in Table VI-3 according to its implementation and the configuration of the southern facade.

Table VI-3: Yearly cooling load per conditioned building area according to the implementation and the configuration of the facade

	Cooling load per conditioned building area [kWh/m^2/year]		
Facade	Paris	Nice	Lyon
BASE 1	24.56	49.59	30.57
BASE 2	26.07	47.66	31.09
Mono-BIPV	25.80	47.41	30.83

Bi-BIPV	25.82	47.41	30.93
DYNABIOSOL 1	25.68	47.07	30.69
DYNABIOSOL 2	25.53	46.84	30.52

Small differences in the cooling loads are observed from the five facade configurations. Indeed, change in the southern facade configuration entails an insignificant contribution to cooling load variation because heat gains mostly come from the building occupancy and the irradiation from the windows. Insulating the facade, in the case of Paris and Lyon, even increases the cooling load with the building configuration and energy scenarios (facades BASE 2, Mono-BIPV, Bi-BIPV and DYNABIOSOL against BASE 1). More optimised management of the ventilation scenarios should be suggested in those locations. Since the building is tightly sealed, insulation traps heat indoors, while thermal exchange with outdoor air would lessen cooling demand. Hence, it is more relevant to compare the facade BASE 1 only with the building implemented in Nice.

Table VI-4: Percentage of cooling load reduction by taking as reference the facade BASE 1 in Nice

	Cooling load reduction [%]				
	BASE 2	Mono-BIPV	Bi-BIPV	DYNABIOSOL 1	DYNABIOSOL 2
Nice	-3.9	-4.4	-4.4	-5.1	-5.6

Table VI-4 shows that the facade DYNABIOSOL can effectively reduce the cooling consumption in Nice by up to 5.1% against 3.9% with the insulated facade BASE 2. As reported in the literature, cooling performance improvement with air gap ventilation is confirmed. The BIPV facades decrease the cooling load by 4.4% (Ibañez-Puy, 2017; Saadon, 2015). The application of the bilayers enables to reach further improvement, especially with the use of mechanical ventilation. This improvement is up to 5.6% and corresponds to a cooling load reduction of 2.75 kWh/m². As the facade is insulated, this cooling gain can be attributed to the limitation of external heat gain from the insulation itself, the reflectance of the bilayers and their bending that increases the thermal exchange with the air and mechanical ventilation.

Table VI-5: Percentage of cooling load reduction by taking as reference the facade BASE 2 according to the building implementation

	Cooling load reduction [%]		
Facade	Paris	Nice	Lyon
Mono-BIPV	-1.0	-0.5	-0.9
Bi-BIPV	-0.9	-0.5	-0.5
DYNABIOSOL 1	-1.5	-1.2	-1.3
DYNABIOSOL 2	-2.0	-1.7	-1.8

Even if the insulation could trap heat inside the building (in the case of Lyon and Paris), the result suggests that ventilating the facade and applying the bilayers would lessen this negative impact. Airflow in the facade and the bending of bilayers allow the facade to dissipate its heat outdoors. The comparison of the BIPV facade and DYNABIOSOL facades with the facade BASE 2 highlights this observation in Table VI-5. Up to 2.0%, 1.7% and 1.8% of cooling load reduction are reached in Paris, Nice and Lyon with DYNABIOSOL 2. The maximum absolute reduction of 0.84 kWh/m² is observed in Nice.

The improvement reported from the comparison with the facade BASE 2 is marginal. Nonetheless, this does not contradict the study in previous chapters. The external temperature of the facade significantly falls by applying the bilayers. In effect, the decreases of peak temperature on the surface of the wall (behind the PV modules) are up to 16.5°C, 19.1°C and 17.2°C respectively, in Paris, Nice and Lyon by

comparing the facade BASE 2 with DYNABIOSOL 1. A further decrease of up to 24°C can be reached with DYNABIOSOL 2, considering the climate of Lyon. The temperature decrease in the range of 5°C, as estimated in Chapter II and observed in the experimental study in Chapter IV, is also obtained by comparing DYNABIOSOL 1 with the facade bi-BIPV (see Table VI-6). The small percentage of cooling load reduction is because the facade is not an essential source of the building cooling energy consumption.

Table VI-6: Peak temperature observed on the external surface of the wall according to the facade configuration and the building implementation

	The yearly maximum temperature on the wall surface [°C]		
Facade	Paris	Nice	Lyon
BASE 2	64.6	64.3	67.3
Mono-BIPV	52.1	50.7	54.2
Bi-BIPV	52.0	50.6	54.1
DYNABIOSOL 1	48.1	45.2	50.0
DYNABIOSOL 2	40.9	43.3	43.4

In summary, the concept of DYNABIOSOL has the potential to improve the cooling load of the building compared to standard insulated facades and other BIPV solutions, especially in warm regions. Insulation of the envelope can nonetheless deteriorate the summer comfort and increase cooling load if the building is tightly sealed. Applying bilayer components can help increase the facade heat removal capacity in that scope.

The improvement brought by design on the cooling performance is slight, taking as a reference a facade that is already insulated. However, the scale of performance enhancement might change depending on the building since the concept effectively reduces the external temperature of the wall. The facade DYNABIOSOL 2 outperforms DYNABIOSOL 1 due to the active use of mechanical ventilation. However, it can induce additional electrical needs and the installation of a fan system on the facade, which should be considered in energy load calculation and the facade cost-effectiveness.

VI.3.2 Impact of the bioinspired facade on heating performance

Similarly to the study of cooling load, the heating load of the building according to its implementation and the type of facade are presented in Table VI-7.

With the studied building configuration and the internal heat gains, the heating load is significantly smaller than the cooling load. Even with the uninsulated facade (southern facade), it represents at most 27% of overall conditioning energy. In effect, the building has large glazed areas, allowing the admission of solar heat gain. The ventilation system also enables it to preserve heat, and the occupancy scenarios can be oversized.

Table VI-7: Heating load per conditioned building area according to the implementation and the configuration of the facade

	Heating load per conditioned building area [kWh/m^2]		
Facade	Paris	Nice	Lyon
BASE 1	8.80	0.38	10.58
BASE 2	3.11	0.09	4.91
Mono-BIPV	3.13	0.09	4.96
Bi-BIPV	3.13	0.09	4.97

DYNABIOSOL 1	3.17	0.10	5.02
DYNABIOSOL 2	3.09	0.09	4.90

Mainly, the presence of insulation contributes to the heating load reduction. Its implementation leads to a decrease in heating energy load by respectively 65%, 77% and 54% in Paris, Nice and Lyon. Therefore, the four facades with external insulation (BASE 2, the BIPV facades, DYNABSIOL 1 and 2) have a very small difference in their heating performance (less than 0.08 kWh/m² considering the absolute difference). Nonetheless, a closer look at this difference shows that ventilating the facade slightly increases the heating loads. Enhanced convective heat transfer with air circulation and reduced incident irradiance from the PV cells shading have a cooling effect on the wall. The presence of the bilayers enhances the cooling effect in the facade DYNABIOSOL 1 since the bilayers are designed for heat removal. This observation joins the results discussed in Chapter IV. Closing the air gap enables the bioinspired facade to limit heat loss from ventilation, bending and the reflectance of the bilayers. The air gap opening control enables the facade DYNABIOSOL 2 to have an equivalent or better heating performance than the facade BASE 2.

VI.3.2.1 Quantification of useful heat

In previous results, significant improvement in heating performance can be achieved in the framework of building refurbishment from the bioinspired facade (comparison with uninsulated facade BASE 1). Nevertheless, even if the difference is insignificant, the design can underperform the standard insulted wall (BASE 2) in heating efficiency. Closing the air gap allows the facade to limit or overcome this performance loss. However, for further performance gain, the useful heat removed from the facade ventilation can be recovered by valorising preheated air in the ventilation supply of the building space. This subsection presents the quantification of this useful heat considering the four facades with an air gap. The sum of useful heat is calculated as a function of the instantaneous heating demand of the building and is presented in Table VI-8.

Table VI-8: Useful heat from the facade ventilation reported to the conditioned surface of the building according to the implementation

	Useful heat per conditioned building area [kWh/m^2]		
Facade	Paris	Nice	Lyon
Mono-BIPV	0.33	0.01	0.61
Bi-BIPV	0.33	0.01	0.61
DYNABIOSOL 1	0.30	0.01	0.56
DYNABIOSOL 2	0.07	0.01	0.17

The results in Table VI-8 show that heat recovery is the lowest with the facade DYNABIOSOL 2 in all regions. This is because the air gap is closed when the temperature is low. During the airgap opening period, the building does not necessarily have an instantaneous heating demand.

Conventional integration of PV modules (mono-BIPV and bi-BIPV) provides the highest gain in heat recovery from the facade. This result is contradictory to that of the experimental study on the facade prototypes. In Chapter IV, the facade DYNABIOSOL 1 (with an open air gap) allows higher heat recovery from air ventilation than a bi-BIPV facade without bilayers. The contradiction can be linked to the inaccuracy of the numerical model. At low solar irradiance and natural ventilation (conditions in which the present comparison is relevant), the facade model with the bilayers tends to underestimate the air velocity up to 6.1%. Meanwhile, the facade model without the bilayers slightly overestimates the air velocity by 1.7%. Those errors sum up by comparing the capacity of the two facades to recover heat. Thus, it is plausible that the heat recovery in conventional BIPV facades and DYNABIOSOL 1 can be

more or less the same, as concluded in the experimental study in Chapter IV. However, low heat recovery in DYNABIOSOL 1 can also be from a lower wall temperature. Thus, heat removal potential is also low despite the increased thermal exchange surface with the air.

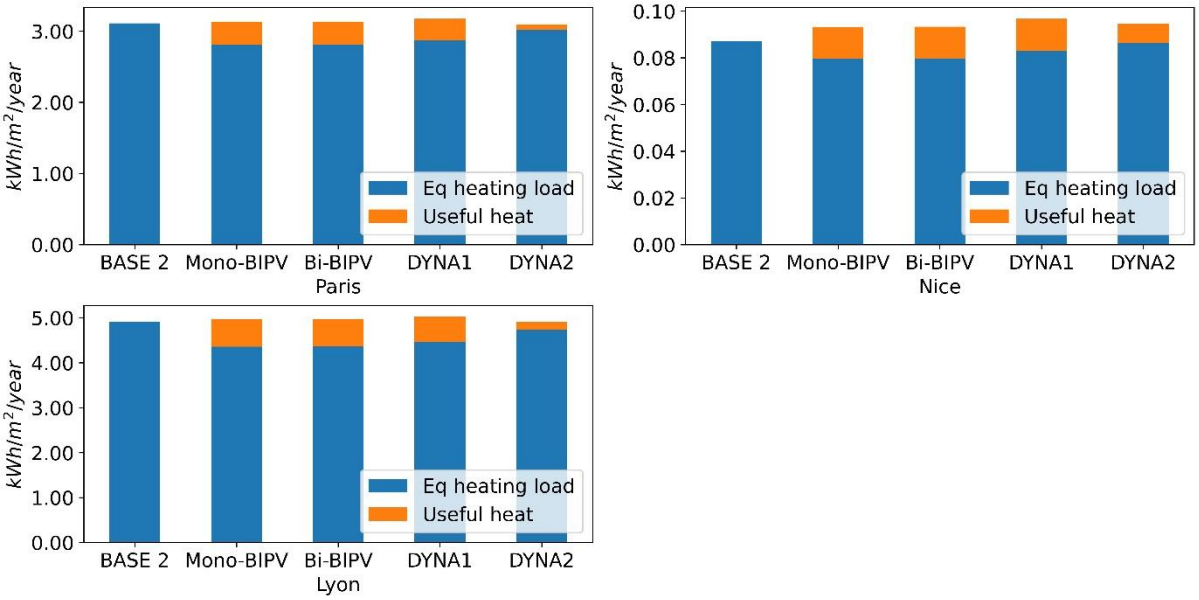

Figure VI-4: Equivalent heating load and the part covered by the heat recovery from the facade ventilation

An equivalent heating load can be calculated by subtracting the useful heat gain from the building heating load. Only the facades DYNABIOSOL and BASE 2 are investigated in detail considering this operation since further improvement on the numerical model is required to consider other BIPV facades. Nonetheless, in a global overview of the equivalent heating loads, Figure VI-4 shows that all the ventilated BIPV facades would have the same or higher heating performance than the facade BASE 2 if the heat recovery is considered.

Table VI-9 shows that the facade DYNABIOSOL 1 has a higher heat collection capacity since its air gap is always open. If useful heat is considered in the heating load estimation, up to 7.7%, 4.8%, and 9.1% of heating load gain can be achieved in Paris, Nice and Lyon. This gain is smaller with DYNABIOSOL 2, at most 3.6% in Lyon and less than 1% in Nice.

Table VI-9: Percentage of equivalent heating energy gain after heat recovery – comparison with the facade BASE 2 according to the implementation

	Reduction of heating load [%]		
Facade	Paris	Nice	Lyon
DYNABIOSOL 1	-7.7	-4.8	-9.1
DYNABIOSOL 2	-2.9	-0.8	-3.6

Those results show that the recovery of useful heat from the air gap is the most relevant in cold regions with high heating demand (here in Lyon). In mild winter climates (such as in Nice), the facade ventilation removes a significant amount of heat, but only a limited part of it is valuable as the heating demand is low. The function of the facade as a heat collector is pertinent as its vertical inclination and southern orientation are in accordance with the solar path in winter.

This study only provides an overview of the potential heat gain through air heat recovery. The actual heating load in the case of air preheating would be different from the calculated equivalent heating load since the ventilation system changes basically. Therefore, the heat recovery is not taken into account in further analysis.

VI.3.2.2 Conclusions

In summary, the DYNABIOSOL solution improves the heating performance for building refurbishment by up to 73%. However, it does not outperform standard facade solutions regarding heating load reduction. Both the ventilation and the bilayers within the facade induce a cooling effect. Closing the air gap allows the facade to mitigate performance loss and compete with standard ones. Nevertheless, the most effective approach to maximising the heating performance is to recover the useful heat from the air gap. Up to a 9% reduction in heating load can be achieved. Nonetheless, the cost of additional subsystems and the adequacy of this solution to the building policy should be assessed for its adoption.

VI.3.3 Impact of the bioinspired facade on global conditioning performance

An overview of the overall conditioning performance of the building according to the facade configuration is investigated to conclude the investigation of the thermal performance. For this, the required energy for heat and cold production is assumed to be equivalent. The conditioning load calculated is given in Table VI-10.

Table VI-10: Conditioning load per conditioned building area according to the implementation and the configuration of the facade

	Conditioning load per conditioned building area [kWh/m^2]		
Facade	Paris	Nice	Lyon
BASE 1	33.36	49.97	41.15
BASE 2	29.18	47.75	36.00
Mono-BIPV	28.93	47.50	35.79
Bi-BIPV	28.96	47.51	35.89
DYNABIOSOL 1	28.86	47.17	35.71
DYNABIOSOL 2	28.63	46.93	35.43

The case study assesses a building with high cooling demand. Therefore, all the ventilated facades outperform the facades BASE 1 and BASE 2. The performance differences in the insulated facades (including BASE 2) are small. Both DYNABIOSOL facades (1 and 2) have the highest performance, which supports the potential of the design to improve thermal performance. DYNABIOSOL 2 provides higher performance than DYNABIOSOL 1 because of its reinforced cooling in summer with mechanical ventilation and the control of air gap opening in winter.

The highest absolute conditioning energy gain is observed in Nice with DYNABIOSOL 2 (3.04 kWh/m² and 0.83 kWh/m², compared to BASE 1 and BASE 2). These performance gains decrease with the severity of the climate in winter, as the heating performance of DYNABIOSOL can be slightly lower than that of other insulated facades. Nevertheless, in terms of the percentage, up to 14.2% of conditioning load reduction can be achieved in Paris by implementing the facade DYNABIOSOL 2 compared to facade BASE 1 (see Table VI-11). Therefore, the climate is not the only reason for adopting the DYNABIOSOL solution but also the thermal loading of the building (linked to its usage and configuration).

Table VI-11: Percentage of conditioning load reduction compared to the facade BASE 1 according to the building implementation

	The difference in conditioning load [%]		
Facade	Paris	Nice	Lyon
DYNABIOSOL 1	-13.5	-5.6	-13.2
DYNABIOSOL 2	-14.2	-6.1	-13.9

The results of the conditioning load calculation closely join that of the cooling load analysis. The energy gain is just reduced because of performance loss in heating. The conclusion remains the same: the suitability of DYNABIOSOL in warm climates or with buildings with high cooling demands and the extension of the concept with air gap operation control or mechanical ventilation for further performance gain.

VI.3.4 Impact of the bioinspired facade on electrical performance

VI.3.4.1 Impact on electrical performance according to PV power output

Finally, the electrical performance of the bioinspired facade is assessed by comparing it with the mono-BIPV and bi-BIPV facades.

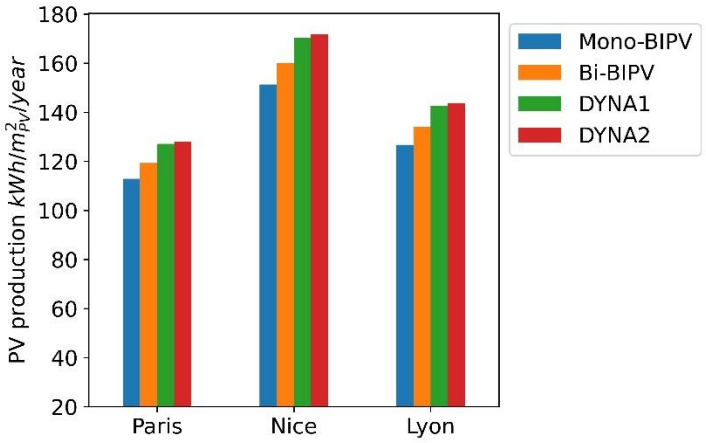

Figure VI-5: Yearly electricity production per PV area according to the facade configuration and the building implementation

Figure VI-5 shows yearly electricity production from the PV modules per meter square of their area according to the facade and the building implementation. As expected, electrical production in all cases is higher in Nice, and then in Lyon because of a high yearly solar irradiance in those regions. The DYNABIOSOL facades improve electrical production from both the mono-BIPV and bi-BIPV facades. The facade DYNABIOSOL 2 slightly outperforms DYNABIOSOL 1, thanks to the use of mechanical ventilation in summer for PV cooling.

The quantification of the electrical performance improvement from the design is given in Table VI-12. It shows that integrating the bifacial PV module alone increases the electrical performance by at least 5.7%. This result shows a significant potential in bifacial PV module application since a substantial gain is made even without optimising their integration (through a reflective back wall, for instance). Combining the bifacial PV module with the application of the bilayers increases the electrical performance of the facade mono-BIPV by at least 12.6%. Applying airflow modulation in DYNABIOSOL 2 leads to a further increase of 13.5% in Paris and Nice and 13.4% in Lyon.

Table VI-12: Increase in electricity production according to the facade configuration and the building implementation

Reference facade	Studied facade	Paris	Nice	Lyon
Mono-BIPV	Bi-BIPV	5.7%	5.8%	5.7%
	DYNABIOSOL 1	12.6%	12.6%	12.6%
	DYNABIOSOL 2	13.5%	13.5%	13.4%
Bi-BIPV	DYNABIOSOL 1	6.5%	6.5%	6.5%
	DYNABIOSOL 2	7.3%	7.3%	7.2%

If the facade bi-BIPV is taken as a reference, implementing the bilayer components increases electrical performance by up to 6.5%. The resulting PV power enhancement is more important than the result in the experimental study in Chapter IV. In that chapter, the study focuses on punctual measurements. Therefore, the power enhancement scale corresponds to the specific environmental conditions during the measurements. As reported in the current analysis, a more significant impact can be achieved on a yearly-based assessment.

Adding mechanical ventilation in DYNABIOSOL 2 leads to a further increase in power production by up to 7.3% compared to the bi-BIPV facade. The results from the facades DYNABIOSOL confirm the importance of PV cooling and irradiance reflection at the back surface of bifacial PV modules to maximise the PV power output of bifacial modules, as reported in the work of (Tina et al., 2021).

Table VI-13: Peak temperature observed on the PV modules according to the facade configuration and the building implementation

	The yearly maximum temperature on the wall surface [°C]		
Facade	Paris	Nice	Lyon
Mono-BIPV	56.1	56.2	58.6
Bi-BIPV	55.9	56.0	58.5
DYNABIOSOL 1	56.1	56.3	58.6
DYNABIOSOL 2	50.5	55.5	53.4

During the concept development, disturbance of the airflow from the mere presence of the bilayer was intended to produce a cooling effect on the PV module as convection heat exchange increased. However, this objective is not reached. Conversely, more irradiance reaches the PV modules with the reflective bilayers and increases their temperature (comparison of bi-BIPV and DYNABIOSOL 1 PV modules temperature). However, without a reflective back wall, the temperature of bifacial PV modules would decrease as part of the back irradiance is converted to electricity (comparison of mono-BIPV to bi-BIPV PV modules temperature). Thus, the reflective properties of the bilayers are the main reason for the power increase in DYNABIOSOL 1. In DYNABIOSOL 2, PV cooling from ventilation reinforces the performance enhancement as mechanical ventilation reduces the maximum temperature of the PV modules up to 5°C in Lyon and Paris in DYNABIOSOL 2 compared to the Mono-BIPV and bi-BIPV facades (see Table VI-13).

VI.3.4.2 Impact on electrical performance according to specific electricity need

The assessment of the yearly electrical performance of the bioinspired facade shows significant potential for its performance gain. It is also necessary to quantify the scale of this improvement on the coverage of the energy demand on the building. As a first step, the capacity of the DYNABIOSOL facade to cover the electricity needs of the building is analysed. For this, the lighting need is simulated. The end-use electricity, including the air ventilation, the energy system auxiliaries and other circulation equipment,

is assumed to equal 11 kWh/m^2. The simulation result is presented in Figure VI-6, showing the electricity need of the building and PV energy production of the facade per meter square of the conditioned building area.

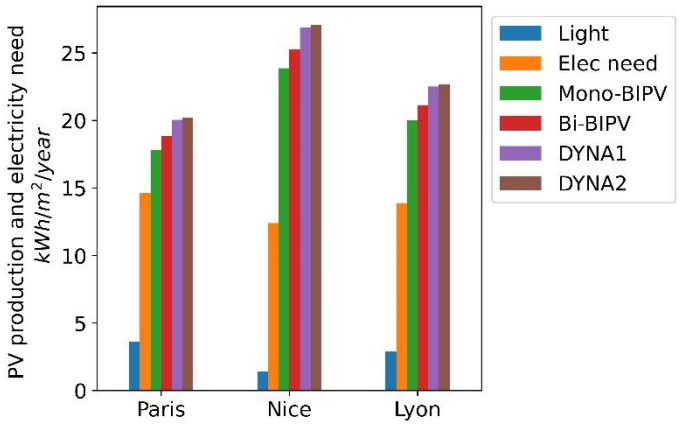

Figure VI-6: Yearly specific electricity need of the building and the PV production per conditioned area according to the facade configuration and the building implementation

The integration of PV modules on the facade broadly covers the specific electricity needs of the building regardless of the typology of PV modules in the facades. The PV modules cover ¼ of the overall facade area and are oriented in a direction with high solar potential (south). Even if the electricity needs are not precisely simulated, this result shows relevance in applying PV modules in building facades. The predominance of the DYNABIOSOL facades over mono-BIPV and bi-BIPV has already been discussed in previous analyses. Nonetheless, for information purposes, Table VI-14 reports the ratio of specific electricity needs of the building to the electricity production of the PV facades. With the application of the facade DYNABIOSOL 2, only 72.3%, 53.0% and 67.6% of the PV power output are assigned for specific electricity demands, respectively, in Paris, Nice and Lyon. Up to 82.1%, 60.1% and 76.7% of the PV production would be assigned to specific electricity demand in the three regions with the mono-BIPV facade.

Table VI-14: Percentage of specific electricity needed against PV production according to the facade configuration and the building implementation

	[%]		
Facade	Paris	Nice	Lyon
Mono-BIPV	82.1	60.1	76.7
Bi-BIPV	77.6	56.8	72.5
DYNABIOSOL 1	72.9	53.4	68.1
DYNABIOSOL 2	72.3	53.0	67.6

VI.3.4.3 Impact on electrical performance according to overall energy need

A second analysis can be undertaken considering that the thermal energy is produced with electrical energy through the heat pump, for instance. The PV power production and overall electricity need (with conditioning energy included) are compared. As in the work of (Saadon, 2015), I consider the production of conditioning energy with a heat pump with a coefficient of performance (COP) (for heat production) and the coefficient EER (Energy Efficiency Ratio for cold production) approximated by overall COP equal to 3. A loss of system heat emission of 0.87 is also considered, and the end-use conditioning electricity is deduced from the division with those coefficients.

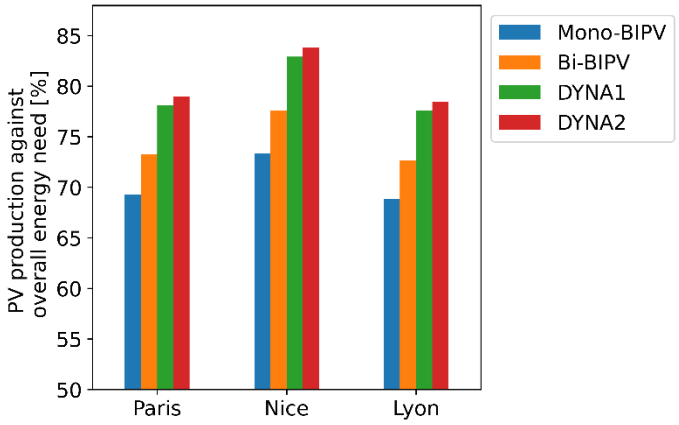

Figure VI-7: Percentage of the PV production coverage of overall energy need (conditioning and specific electricity needs) according to the facade configuration and the building implementation

As a result, Figure VI-7 displays the coverage of overall energy needs by the PV module in percentage. This figure shows that integrating PV modules leads to coverage of at least 68.8 % of the building energy requirement with monofacial PV modules in Lyon. Using a bifacial PV module increases the energy coverage by 4%. The application of the bilayer leads to a further enhancement, increasing 9% with the facade DYNABIOSOL 1 and 9.9% with DYNABIOSOL 2. In Nice, the coverage of the energy requirement by PV electricity production is the highest, up to 83.8%. In effect, even if the conditioning energy is the highest in Nice (because of the high demand for cooling), the solar potential is also high, leading to higher coverage of energy load. These results are only for general insight into the energy performance of the concept as they are based on strong assumptions about the heat pump performance and the direct distribution of the produced electricity.

VI.3.4.4 Conclusions

The results show the relevance of the integration of PV modules on the building facade. Applying bifacial PV modules with the bilayer components reinforces the potential of this technology. Modulating the airflow in the air gap through mechanical ventilation allows further electrical performance improvement. The cooling and the high irradiance reflection at the back of the bifacial PV modules significantly enhance the facade performance. Nonetheless, as stated in the thermal performance study, mechanical ventilation can reduce the performance of the facade DYNABIOSOL 2 through additional electricity demand. Moreover, building energy efficiency is already increased with the most generic configuration of the developed concept, DYNABIOSOL 1.

VI.4 Conclusions

This chapter presents the performance assessment of the bioinspired facade by confronting its integration impact with conventional building walls and BIPV facades. The investigation is conducted on the southern side facade of a tertiary building, which is highly glazed on its east, west and north sides.

The global building thermal efficiency assessment has shown a significant improvement in thermal efficiency in a building refurbishment framework from the bioinspired facade concept. The concept is adapted to buildings with high cooling since the bilayers have a cooling effect on the facade. In this case, a positive but small impact can be achieved compared to standard facade or other BIPV facade configurations, which are already well-insulated. The concept can, therefore, help improve summer thermal comfort, a crucial concern in tightly insulated buildings. Nonetheless, the cooling effect from the bilayer application induces a decrease in heating efficiency. A subordinary system should be

implemented to recover heat from the facade ventilation. Either way, the air gap should be closed at night or during cloudy periods in winter to limit heat loss.

In a yearly period, applying bilayers with or without airflow modulation in the gap significantly enhances electricity production. The bioinspired facade can improve up to 13% of the performance of the monofacial facade and 7% of the bifacial facade. Those improvements allow better coverage of the building energy needs.

This study also indicates the suitability of the facade to provide energy economy in different climatic conditions. Nonetheless, due to the design cooling effect, the highest energy gain is obtained in warm with high solar irradiation regions. In overall energy performance, modulating the ventilation rate and air gap opening in the facade leads to the highest energy performance, regardless of the region of building implementation. However, due to the possible implementation of additional subsystems, it can be roughly concluded that the bioinspired facade with or without mechanical ventilation has an equivalent performance.

General conclusions and Perspectives

Summary of results

This thesis focused on the design of a bioinspired photovoltaic (PV) facade with evolutive functionalities. The developed solution aims to improve the thermal and electrical efficiencies of a PV facade element by adjusting its functions to the energy requirement of the buildings and the outdoor climatic conditions. This work ranged from the development of the concept to its validation with experimental prototypes and numerical performance assessment.

As a first step, a literature review was conducted to identify the advantages and limitations of existing PV facades and the innovation opportunities for their improvement. This study highlights that a simultaneous maximisation of the cooling and heating performances leads to a trade-off between the two performances in buildings. In the case of a PV facade integration, the maximisation of electricity production is added to this trade-off. Adaptive envelope solutions enable lessening those compromises since they are designed as an interface that exchanges and benefits from the building outdoor environment to reach the energy requirements and maintain a good indoor environment quality. However, these technologies often use highly complex mechanical systems with high maintenance costs. Hence, exploring the application of smart materials and bioinspiration approaches is among current research trends to develop low-tech and efficient envelopes to overcome these drawbacks. From this analysis, the bioinspiration approach is adopted in this work. A ventilated opaque photovoltaic facade is chosen as a starting point for the design. Additionally, this facade comprises semi-transparent bifacial PV modules as a first step of optimisation, considering the reported electrical performance of this technology in the literature.

Following a technology-pull bioinspiration approach, the second chapter details the design process of the bioinspired PV facade. The approach involves identifying the thermal and electrical limitations of the baseline facade to search for corresponding analogic biological strategies. By getting inspired by the thermal exchange in mammal skins and cacti, irradiation reflection in diverse organisms and plant motion, thermosensitive bilayers are applied on the facade wall. The idea is to adapt the facade cooling to the thermal demand by: controlling the air gap opening and modulating the heat exchange area in the gap with the progressive deformation of the bilayers with temperature. The reflective properties and movement of bilayers are also employed to develop adaptive strategies towards solar radiation availability through shading of the wall and reflection of sun rays to the back of the bifacial PV modules. In order to reach a significant thermal and electrical performance improvement, preliminary sizing of the concept identifies that the bilayers should be thermally conductive and have a deflection capacity between 0.6 mm/°C to 1.43 mm/°C. This result is valid for bilayers of 15.5 cm in length and an air gap thickness of 10 cm thick.

Potential candidates of bilayers for the design were identified and characterised in Chapter III according to their deflection with the temperature changes. They are assemblies of the couples Aluminium-PMMA and Invar-PMMA. The epoxy adhesive was always identified to bind each couple of layers without blocking its movement. The results show that the manufactured bilayers undergo linear deformations under cyclic heating solicitation in their elastic deformation zone. They can be assumed to quasi-return in their initial state without precisely measuring possible residual deformation. The couple Alumnium-PMMA was selected for this application because it deforms mainly along its length and not on its width. The deformation can be approximated with a one-dimensional equation in the function of the applied temperature difference. The determined equation is essential for this study to determine the bilayer deflection only with the changes in their temperature. Thus, it enables avoiding the use of a displacement

measuring device in higher-scale experiments. This equation also models the bilayer in the facade coupled thermal model.

Experiments on two reduced-scale prototypes of the facade have been performed to validate the concept and presented in Chapter IV. This study consisted of a parametric investigation of an elementary facade unit and provided several findings. First, the adequacy of the bilayer Aluminium-PMMA over that of Invar-PMMA was confirmed to fit the application. The investigations validated the potential of the bilayers to cool down the external surface of the facade wall at high irradiation and to increase the PV power output compared to the conventional bifacial PV facade. Increased heat exchange area from the bilayer deformation plays a small role in heat removal on the facade. The reflectivity of bilayers was found to be the main reason for the PV power enhancement, while shading and irradiance reflection are the main components of wall cooling. Thus, arranging the bilayers in line behind the PV cells leads to the highest reduction of the wall temperature. In addition, applying the bilayers on a conductive support layer limits the temperature disparity induced by the shading. An increase in air gap thickness hardly enhanced the heat removal, as the bilayers were sized to perform with a 10 cm thick air gap. Their application was equivalent to using mechanical ventilation with a velocity inferior to or equal to 2 m/s in a conventional PV facade.

The results of the experimental study in Chapter IV were used to validate the thermal models of conventional BIPV facades and the bioinspired facades in a steady state of heat transfer in Chapter V. The transient heat transfer model of the conventional BIPV facade was also validated in this chapter. The models developed provide satisfactory accuracy. They provide insight into the facade performance and can be coupled to a building energy model to assess the energy performance at a building scale. However, as the bilayer application integrally modifies the heat transfer and the airflow in the gap, the accuracy of the model decreases during their consideration, especially for airflow estimation. Therefore, further improvement is needed to enhance the precision of the model.

The assessment of the bioinspired facade performance at a building scale is presented in Chapter VI with the developed thermal models. The study focused on the energy performance of a fictive tertiary building, considering three implementations in France. It confronted the thermal and electrical performance of the building with the bioinspired facade to uninsulated and insulated conventional walls and standard BIPV facades considering southern orientation.

The concept enables a significant gain in thermal performance in building refurbishment. The case study showed up to a 75% gain in heating load and a 5% gain in cooling load, noting that the building has a high cooling demand. The comparison with insulated walls and standard BIPV facades joins the findings in the experimental study conducted on the facade prototypes. The design slightly but positively impacted the cooling load in all comparison cases. A well-designed control of the air gap opening or recovery of the preheated air is necessary to surpass the heating performance of conventional insulated building walls. The facade fits all studied implementations in France if the modulation of the air gap is considered. Nonetheless, it performs the best in high-cooling demand buildings or climates.

The predominance of bioinspired PV facade energy performance over conventional walls is evident due to electricity production. Meanwhile, the bioinspired facade solution also substantially enhances PV power output over conventional BIPV facades. In a yearly period, the case studied showed up to 13% electricity production increase compared to monofacial PV facade and 7% to bifacial facade. Those improvements would lead to better coverage of the building energy needs and confirm the relevance of the design as a pathway solution for positive energy building.

Recommendations and perspectives

This work has shown a promising example of bioinspiration approach application in building envelope design. It demonstrated that using smart materials in a BIPV facade would provide adaptive features in its functionalities and enhance its electrical and thermal performances. The design is now at a reduced-

scale prototype stage and opens to several perspectives. Some perspectives and recommendations are presented here according to each study step.

- **The bioinspired design development**

The development of the concept mainly followed the methodology steps linearly. This process defines perimeters or preselects the facade features that should be addressed in each design stage. In further work, introducing a loop in the design process to go back and forth to each stage would improve the methodology. In effect, in the problem definition stage, for instance, the literature review allowed selecting and analysing few relevant properties predicted to influence the baseline PV facade in the parametric study. However, other facade properties, such as the wall thermal inertia and the air gap height, were also found to be relevant in the course of the design development. Therefore, another loop of parametric study can be conducted starting from the developed concept.

The parametric study methodology can also be improved to understand the variation of facade properties, considering their interaction. In that scope, an adimensional analysis enables the identification of some characteristic properties that limit the facade with static functionalities.

Furthermore, classification studies and literature reviews on bioinspiration in buildings have helped tremendously in the search and analysis of biological strategies. In addition to these resources, cooperation with biologists and interdisciplinary collaboration are very beneficial for a deeper investigation and the abstraction of biological mechanisms.

The preliminary study was conducted to provide general sizing and characteristics of the bioinspired components to move forward with experimental validation of the concept. Some of the facade features were chosen by relying on predictive physical phenomena, such as the length and the longitudinal interspaces between the bilayers, to match those of PV cells. Further investigation can be undertaken to optimize these features by considering the analysis of sunray paths in the facade.

- **The experimental validation**

Investigations of the bilayer samples are a core step of the concept validation. Their analysis mainly addresses the capacity of the bilayer to undergo cyclic deformation. Hence, investigations of the presence of hysteresis, residual deformation and the fatigue of the bilayers constitute some perspectives of this work. Understanding these thermomechanical phenomena is essential to advancing the readiness level of bilayer application technology in buildings. Therefore, a long-term experimental campaign should be conducted to validate the operation of the bilayers, considering the building lifetime.

The bilayer deformation is considered one-dimensional in this study. This assumption can not be applied to all cases according to the composition or the geometry of the bilayer. Exploring the limit of this hypothesis would allow the consideration of various types of bilayers. A broader investigation can be carried out on the manufacturing, the influence of the bonding material and the thermomechanical behaviour to optimise the deformation of the bilayers considering their intended functions.

Several parameters have been studied during the concept validation on the reduced-scale prototype of the facade. The results have given guidance on the application of the bilayers. The study can be extended further by analysing the impact of the reflectivity of the support layer and the bilayers, the PV module semi-transparency and the transversal interspaces of the bilayers.

An exhaustive experimental investigation of the airflow in the gap would also help map the velocity field in the air gap to understand its variation and effect along the prototype width and height. This investigation would highlight the airflow disturbance due to the bilayers' presence and their impact on the pressure loss. Such analysis can be done considering no-intrusive measuring methods such as particle image velocimetry (PIV). The effect of the air movement on the bilayers' deformation should also be

investigated, whether the airflow induces the bilayers to bend further upward and its impact on the simplified deflection equation determined.

Finally, the major perspective of the experimental validation is conducting an experimental campaign on a full-scale prototype integrated into a building. The investigation of the influence of the facade thermal insulation can also be pertinent at this scale for a direct study of building energy consumption. The experimentation should last at least a year to cover the behaviour of the building in winter, summer and mid-season.

- **The numerical validation**

Numerical simulation and performance assessment are often adopted over experimental studies due to their lower cost (of time and resources) and efficiency in handling parametric investigations. Here, numerical models of tertiary buildings simulated in three regions in France helped assess the bioinspired facade performance. Boarding this analysis to other global locations would enable the understanding of the design impact at lower latitudes and in different climates, such as tropical and equatorial climates. Previously cited parameters in the experimental study perspectives can also be analysed numerically.

Finally, some improvements of the numerical model can also be suggested to strengthen its reliability, namely, in the choice of empirical correlations for the estimation of sky temperature and convective heat transfer and the consideration of the PV module capacity. With the presence of the bilayers, two-dimensional modelling would be more adapted for the consideration of airflow and radiation exchange.

In conclusion, many perspectives are open with the aim of considering the cost-effectiveness and the introduction of the bioinspired facade to the industry. These include improving the concept in a new iteration, the thermomechanical behaviour analysis of the bilayers and the full-scale prototyping of the facade.

References

Aburas, M., Soebarto, V., Williamson, T., Liang, R., Ebendorff-Heidepriem, H., & Wu, Y. (2019). Thermochromic smart window technologies for building application : A review. *Applied Energy*, *255*, 113522. https://doi.org/10.1016/j.apenergy.2019.113522

Aelenei, D., Aelenei, L., & Vieira, C. P. (2016). Adaptive Façade : Concept, Applications, Research Questions. *Energy Procedia*, *91*, 269-275. https://doi.org/10.1016/j.egypro.2016.06.218

Aflaki, A., Mahyuddin, N., Al-Cheikh Mahmoud, Z., & Baharum, M. R. (2015). A review on natural ventilation applications through building façade components and ventilation openings in tropical climates. *Energy and Buildings*, *101*, 153-162. https://doi.org/10.1016/j.enbuild.2015.04.033

AFNOR. (2016). *Photovoltaics in buildings—Part 1 : BIPV modules* (NF EN 50583-1).

AFNOR. (2017). *Energy performance of buildings—Energy needs for heating and cooling, internal temperatures and sensible and latent heat loads—Part 1 : Calculation procedures* (NF EN ISO 52016-1). https://viewerbdc.afnor.org/pdf/viewer/mFvXQArpfHY1?proxy=true

Agathokleous, R. A., & Kalogirou, S. A. (2016). Double skin facades (DSF) and building integrated photovoltaics (BIPV) : A review of configurations and heat transfer characteristics. *Renewable Energy*, *89*, 743-756. https://doi.org/10.1016/j.renene.2015.12.043

Agathokleous, R. A., & Kalogirou, S. A. (2018a). Part I : Thermal analysis of naturally ventilated BIPV system: Experimental investigation and convective heat transfer coefficients estimation. *Solar Energy*, *169*, 673-681. https://doi.org/10.1016/j.solener.2018.02.048

Agathokleous, R. A., & Kalogirou, S. A. (2018b). Part II : Thermal analysis of naturally ventilated BIPV system: Modeling and Simulation. *Solar Energy*, *169*, 682-691. https://doi.org/10.1016/j.solener.2018.02.057

Ahmed, O. K., Hamada, K. I., Salih, A. M., & Daoud, R. W. (2020). A state of the art review of PV-Trombe wall system : Design and applications. *Environmental Progress & Sustainable Energy*, *39*(3), e13370. https://doi.org/10.1002/ep.13370

Al Dakheel, J., & Tabet Aoul, K. (2017). Building Applications, Opportunities and Challenges of Active Shading Systems : A State-of-the-Art Review. *Energies*, *10*(10), 1672. https://doi.org/10.3390/en10101672

Almosni, S., Delamarre, A., Jehl, Z., Suchet, D., Cojocaru, L., Giteau, M., Behaghel, B., Julian, A., Ibrahim, C., Tatry, L., Wang, H., Kubo, T., Uchida, S., Segawa, H., Miyashita, N., Tamaki, R., Shoji, Y., Yoshida, K., Ahsan, N., … Guillemoles, J.-F. (2017). Material challenges for solar cells in the twenty-first century : Directions in emerging technologies. *Science and Technology of Advanced Materials*, *18*(NRG2), 336-369. https://doi.org/10.1080/14686996.2018.1433439

Arens, E. A., & Zhang, H. (2006). *The Skin's Role in Human Thermoregulation and Comfort*. 51.

Armand Decker, S. (2015). *Développement d'une méthode d'optimisation multiobjectif pour la construction bois : Prise en compte du confort des usagers, de l'impact environnemental et de la sécurité de l'ouvrage* [These de doctorat, Bordeaux]. https://theses.fr/2015BORD0189

Armstrong, S., & Hurley, W. G. (2010). A thermal model for photovoltaic panels under varying atmospheric conditions. *Applied Thermal Engineering*, *30*(11), 1488-1495. https://doi.org/10.1016/j.applthermaleng.2010.03.012

Ascione, F., De Masi, R. F., de Rossi, F., Ruggiero, S., & Vanoli, G. P. (2016). Optimization of building envelope design for nZEBs in Mediterranean climate : Performance analysis of residential case study. *Applied Energy*, *183*, 938-957. https://doi.org/10.1016/j.apenergy.2016.09.027

Assoa, Y. B. (2008). *Performances de capteurs solaires PV/T hybrides bi-fluides intégrables à l'enveloppe des bâtiments. Etude expérimentale et modélisation adaptée*.

Assoa, Y. B., Mongibello, L., Carr, A., Kubicek, B., Machado, M., Merten, J., Misara, S., Roca, F., Sprenger, W., Wagner, M., Zamini, S., Baenas, T., & Malbranche, P. (2017). Thermal analysis of a BIPV system by various modelling approaches. *Solar Energy*, *155*, 1289-1299. https://doi.org/10.1016/j.solener.2017.07.066

Assoa, Y. B., Sauzedde, F., Boillot, B., & Boddaert, S. (2017). Development of a building integrated solar photovoltaic/thermal hybrid drying system. *Energy*, *128*, 755-767. https://doi.org/10.1016/j.energy.2017.04.062

Assoa, Y. B., Thony, P., Messaoudi, P., Schmitt, E., Bizzini, O., Gelibert, S., Therme, D., Rudy, J., & Chabuel, F. (2021). Study of a building integrated bifacial photovoltaic facade. *Solar Energy*, *227*, 497-515. https://doi.org/10.1016/j.solener.2021.09.004

Aste, N., Chiesa, G., & Verri, F. (2008). Design, development and performance monitoring of a photovoltaic-thermal (PVT) air collector. *Renewable Energy*, *33*(5), 914-927. https://doi.org/10.1016/j.renene.2007.06.022

Aste, N., Leonforte, F., & Piccolo, A. (2018). Color rendering performance of smart glazings for building applications. *Solar Energy*, *176*, 51-61. https://doi.org/10.1016/j.solener.2018.10.026

Athienitis, A. K., Bambara, J., O'Neill, B., & Faille, J. (2011). A prototype photovoltaic/thermal system integrated with transpired collector. *Solar Energy*, *85*(1), 139-153. https://doi.org/10.1016/j.solener.2010.10.008

Athienitis, A. K., Barone, G., Buonomano, A., & Palombo, A. (2018). Assessing active and passive effects of façade building integrated photovoltaics/thermal systems : Dynamic modelling and simulation. *Applied Energy*, *209*, 355-382. https://doi.org/10.1016/j.apenergy.2017.09.039

Attia, S., Bilir, S., Safy, T., Struck, C., Loonen, R., & Goia, F. (2018). Current trends and future challenges in the performance assessment of adaptive façade systems. *Energy and Buildings*, *179*, 165-182. https://doi.org/10.1016/j.enbuild.2018.09.017

Badarnah Kadri, L. (2012). *Towards the LIVING envelope : Biomimetics for building envelope adaptation* [Delft University of Technology]. https://doi.org/10.4233/UUID:4128B611-9B48-4C8D-B52F-38A59AD5DE65

Badarnah, L. (2017). Form Follows Environment : Biomimetic Approaches to Building Envelope Design for Environmental Adaptation. *Buildings*, *7*(2), Article 2. https://doi.org/10.3390/buildings7020040

Bar-Cohen, A., & Rohsenow, W. M. (1984). Thermally Optimum Spacing of Vertical, Natural Convection Cooled, Parallel Plates. *Journal of Heat Transfer*, *106*(1), 116-123. https://doi.org/10.1115/1.3246622

Baumeister, D., Tocke, R., Dwyer, J., Benyus, J. M., & Ritter, S. (2014). *Biomimicry Resource Handbook : A Seed Bank of Best Practices*. Biomimicry 3.8.

Baumgärtner, L., Krasovsky, R. A., Stopper, J., & von Grabe, J. (2017). Evaluation of a solar thermal glass façade with adjustable transparency in cold and hot climates. *Energy Procedia*, *122*, 211-216. https://doi.org/10.1016/j.egypro.2017.07.347

Bekele, A., Mishra, M., & Dutta, S. (2011). Effects of Delta-Shaped Obstacles on the Thermal Performance of Solar Air Heater. *Advances in Mechanical Engineering*, *3*, 103502. https://doi.org/10.1155/2011/103502

Bhamare, D. K., Rathod, M. K., & Banerjee, J. (2019). Passive cooling techniques for building and their applicability in different climatic zones—The state of art. *Energy and Buildings*, *198*, 467-490. https://doi.org/10.1016/j.enbuild.2019.06.023

BIPVBoost. (2019). *D9.1 BIPV market and stakeholder analysis*.

Biyik, E., Araz, M., Hepbasli, A., Shahrestani, M., Yao, R., Shao, L., Essah, E., Oliveira, A. C., del Caño, T., Rico, E., Lechón, J. L., Andrade, L., Mendes, A., & Atlı, Y. B. (2017). A key review of building integrated photovoltaic (BIPV) systems. *Engineering Science and Technology, an International Journal*, *20*(3), 833-858. https://doi.org/10.1016/j.jestch.2017.01.009

Breed, M. D., & Moore, J. (2016). Chapter 4—Homeostasis and Time Budgets. In M. D. Breed & J. Moore (Éds.), *Animal Behavior (Second Edition)* (p. 109-144). Academic Press. https://doi.org/10.1016/B978-0-12-801532-2.00004-0

Brinkworth, B. J., Marshall, R. H., & Ibarahim, Z. (2000). A validated model of naturally ventilated PV cladding. *Solar Energy*, *69*(1), 67-81. https://doi.org/10.1016/S0038-092X(99)00076-6

Brinkworth, B. J., & Sandberg, M. (2006). Design procedure for cooling ducts to minimise efficiency loss due to temperature rise in PV arrays. *Solar Energy*, *80*(1), 89-103. https://doi.org/10.1016/j.solener.2005.05.020

Capeluto, G., & Ochoa, C. E. (2017). What Is a Real Intelligent Envelope? In G. Capeluto & C. E. Ochoa (Éds.), *Intelligent Envelopes for High-Performance Buildings : Design and Strategy* (p. 1-20). Springer International Publishing. https://doi.org/10.1007/978-3-319-39255-4_1

CEREMA. (2022). *Bâtiments démonstrateurs à basse consommation d'énergie—Enseignements opérationnels tirés de 166 constructions et rénovations du programme PREBAT 2012—2019*. https://www.cerema.fr/system/files/product/publication/2022/06/prebat_2012-2019-web.pdf

Charkoudian, N. (2010). Mechanisms and modifiers of reflex induced cutaneous vasodilation and vasoconstriction in humans. *Journal of Applied Physiology*, *109*(4), 1221-1228. https://doi.org/10.1152/japplphysiol.00298.2010

Chesné, L. (2012). *Vers une nouvelle méthodologie de conception des bâtiments, basée sur leurs performances bioclimatiques*.

Chiu, I., & Shu, L. H. (2007). Biomimetic design through natural language analysis to facilitate cross-domain information retrieval. *Artificial Intelligence for Engineering Design, Analysis and Manufacturing*, *21*(1), 45-59. https://doi.org/10.1017/S0890060407070138

Chow, T. T. (2003). Performance analysis of photovoltaic-thermal collector by explicit dynamic model. *Solar Energy*, *75*(2), 143-152. https://doi.org/10.1016/j.solener.2003.07.001

Chow, T. T., Chan, A. L. S., Fong, K. F., Lin, Z., He, W., & Ji, J. (2009). Annual performance of building-integrated photovoltaic/water-heating system for warm climate application. *Applied Energy*, *86*(5), 689-696. https://doi.org/10.1016/j.apenergy.2008.09.014

Chow, T. T., Hand, J. W., & Strachan, P. A. (2003). Building-integrated photovoltaic and thermal applications in a subtropical hotel building. *Applied Thermal Engineering*, *23*(16), 2035-2049. https://doi.org/10.1016/S1359-4311(03)00183-2

Churchill, S. W., & Chu, H. H. S. (1975). Correlating equations for laminar and turbulent free convection from a vertical plate. *International Journal of Heat and Mass Transfer*, *18*(11), 1323-1329. https://doi.org/10.1016/0017-9310(75)90243-4

Coelho, M., & Zigelbaum, J. (2011). Shape-changing interfaces. *Personal and Ubiquitous Computing*, *15*(2), 161-173. https://doi.org/10.1007/s00779-010-0311-y

Cruz, E., Hubert, T., Chancoco, G., Naim, O., Chayaamor-Heil, N., Cornette, R., Menezo, C., Badarnah, L., Raskin, K., & Aujard, F. (2021). Design processes and multi-regulation of biomimetic building skins : A comparative analysis. *Energy and Buildings*, *246*, 111034. https://doi.org/10.1016/j.enbuild.2021.111034

Čurpek, J., & Čekon, M. (2020). Climate response of a BiPV façade system enhanced with latent PCM-based thermal energy storage. *Renewable Energy*, *152*, 368-384. https://doi.org/10.1016/j.renene.2020.01.070

de Gracia, A., Navarro, L., Castell, A., Ruiz-Pardo, Á., Alvárez, S., & Cabeza, L. F. (2013). Experimental study of a ventilated facade with PCM during winter period. *Energy and Buildings*, *58*, 324-332. https://doi.org/10.1016/j.enbuild.2012.10.026

de Gracia, A., Navarro, L., Castell, A., Ruiz-Pardo, Á., Álvarez, S., & Cabeza, L. F. (2013). Thermal analysis of a ventilated facade with PCM for cooling applications. *Energy and Buildings*, *65*, 508-515. https://doi.org/10.1016/j.enbuild.2013.06.032

Diarce, G., Urresti, A., García-Romero, A., Delgado, A., Erkoreka, A., Escudero, C., & Campos-Celador, Á. (2013). Ventilated active façades with PCM. *Applied Energy*, *109*, 530-537. https://doi.org/10.1016/j.apenergy.2013.01.032

Drezner, T. D. (2011). Cactus surface temperatures are impacted by seasonality, spines and height on plant. *Environmental and Experimental Botany*, *74*, 17-21. https://doi.org/10.1016/j.envexpbot.2011.04.006

Drezner, T. D. (2017). Shape and size adjustments of a cactus with rib and furrow morphology. *Journal of Arid Environments*, *138*, 1-8. https://doi.org/10.1016/j.jaridenv.2016.11.004

Duan, S., Wang, L., Zhao, Z., & Zhang, C. (2021). Experimental study on thermal performance of an integrated PCM Trombe wall. *Renewable Energy*, *163*, 1932-1941. https://doi.org/10.1016/j.renene.2020.10.081

Duffie, J. A., & Beckman, W. A. (2006). *Solar engineering of thermal processes*. Wiley. https://books.google.fr/books?id=tPayQgAACAAJ

Duigou, A., & Castro, M. (2016). Evaluation of force generation mechanisms in natural, passive hydraulic actuators. *Scientific Reports*, *6*, 18105. https://doi.org/10.1038/srep18105

El-Dabaa, R. and S. A. (2019). HMTM : Hygromorphic-Thermobimetal Composites as a Novel Approach to Enhance Passive Actuation of Adaptive Façades. *Ji-Hyun Lee (Eds.) « Hello, Culture! » [18th International Conference, CAAD Futures 2019, Proceedings / ISBN 978-89-89453-05-5] Daejeon, Korea, pp. 290-300*. http://papers.cumincad.org/cgi-bin/works/BrowseTree=series=AZ/Show?cf2019_038

European Commission. (2016). COMMISSION RECOMMENDATION (EU) 2016/ 1318—Of 29 July 2016—On guidelines for the promotion of nearly zero-energy buildings and best practices to ensure that, by 2020, all new buildings are nearly zero-energy buildings. *Official Journal of the European Union*.

European Commission. (2021). *Proposal for a DIRECTIVE OF THE EUROPEAN PARLIAMENT AND OF THE COUNCIL on energy efficiency (recast) COM/2021/558 final*. https://eur-lex.europa.eu/legal-content/EN/TXT/?uri=COM%3A2021%3A558%3AFIN

Evangelisti, L., Guattari, C., & Asdrubali, F. (2019). On the sky temperature models and their influence on buildings energy performance : A critical review. *Energy and Buildings*, *183*, 607-625. https://doi.org/10.1016/j.enbuild.2018.11.037

Evans, D. L., & Florschuetz, L. W. (1977). Cost studies on terrestrial photovoltaic power systems with sunlight concentration. *Solar Energy*, *19*(3), 255-262. https://doi.org/10.1016/0038-092X(77)90068-8

Fayemi, P. E., Wanieck, K., Zollfrank, C., Maranzana, N., & Aoussat, A. (2017). Biomimetics : Process, tools and practice. *Bioinspiration & Biomimetics*, *12*(1), 011002. https://doi.org/10.1088/1748-3190/12/1/011002

Foged, I. W., & Pasold, A. (2015). *Thermal Activated Envelope*. 11.

Formentini, M., & Lenci, S. (2018). An innovative building envelope (kinetic façade) with Shape Memory Alloys used as actuators and sensors. *Automation in Construction*, *85*, 220-231. https://doi.org/10.1016/j.autcon.2017.10.006

Fossa, M., Ménézo, C., & Leonardi, E. (2008). Experimental natural convection on vertical surfaces for building integrated photovoltaic (BIPV) applications. *Experimental Thermal and Fluid Science*, *32*(4), 980-990. https://doi.org/10.1016/j.expthermflusci.2007.11.004

Foucquier, A., Robert, S., Suard, F., Stephan, L., & Jay, A. (2013). State of the art in building modelling and energy performances prediction : A review. *Renewable and Sustainable Energy Reviews*, *23*, 272. https://doi.org/10.1016/j.rser.2013.03.004

Franco, A. C., & Nobel, P. S. (1989). Effect of Nurse Plants on the Microhabitat and Growth of Cacti. *Journal of Ecology*, *77*(3), 870-886. https://doi.org/10.2307/2260991

Freitas, S., & Brito, M. C. (2019). Solar façades for future cities. *Renewable Energy Focus*, *31*, 73-79. https://doi.org/10.1016/j.ref.2019.09.002

Frontini, F., Bonomo, P., Chatzipanagi, A., & Verberne, G. (2015). BIPV PRODUCT OVERVIEW FOR SOLAR FAÇADES AND ROOFS. *Report 2015, SUPSI-SEAC*, 47.

Frontini, F., Caccuvio, M., Renken, C., & Moll, C. (2019). *Guide des modules bifaciaux—Utilisation des modules solaires bifaciaux – possibilités d'application sur les bâtiments et dimensionnement des composants des installations*. https://www.swissolar.ch/fileadmin/user_upload/Fachleute/Photovoltaik_Leitfaeden/9897-2019.08.09_Leitfaden_bifaziale_Module_Final_FR.pdf

Garde, F., & Donn, M. (2014). *Solution Sets and Net Zero Energy Buildings : A review of 30 Net ZEBs case studies worldwide*. IEA Solar Heating and Cooling Programme. https://doi.org/10.18777/ieashc-task40-2014-0002

Gebeshuber, I. C., & Drack, M. (2008). An attempt to reveal synergies between biology and mechanical engineering. *Proceedings of the Institution of Mechanical Engineers, Part C: Journal of Mechanical Engineering Science*, *222*(7), 1281-1287. https://doi.org/10.1243/09544062JMES890

Gilbert, C., Robertson, G., Le Maho, Y., Naito, Y., & Ancel, A. (2006). Huddling behavior in emperor penguins : Dynamics of huddling. *Physiology & Behavior*, *88*(4), 479-488. https://doi.org/10.1016/j.physbeh.2006.04.024

Goel, A., Rugaber, S., & Vattam, S. (2009). Structure, Behavior and Function of Complex Systems : The SBF Modeling Language. *Artificial Intelligence for Engineering Design, Analysis and Manufacturing*, 44.

Goia, F., Perino, M., & Serra, V. (2014). Experimental analysis of the energy performance of a full-scale PCM glazing prototype. *Solar Energy*, *100*, 217-233. https://doi.org/10.1016/j.solener.2013.12.002

Gomes, M. G., Santos, A. J., & Rodrigues, A. M. (2014). Solar and visible optical properties of glazing systems with venetian blinds : Numerical, experimental and blind control study. *Building and Environment*, *71*, 47-59. https://doi.org/10.1016/j.buildenv.2013.09.003

Gu, W., Ma, T., Ahmed, S., Zhang, Y., & Peng, J. (2020). A comprehensive review and outlook of bifacial photovoltaic (bPV) technology. *Energy Conversion and Management*, *223*, 113283. https://doi.org/10.1016/j.enconman.2020.113283

Gu, W., Ma, T., Li, M., Shen, L., & Zhang, Y. (2020). A coupled optical-electrical-thermal model of the bifacial photovoltaic module. *Applied Energy*, *258*, 114075. https://doi.org/10.1016/j.apenergy.2019.114075

Guerrero-Lemus, R., Vega, R., Kim, T., Kimm, A., & Shephard, L. E. (2016). Bifacial solar photovoltaics – A technology review. *Renewable and Sustainable Energy Reviews*, *60*, 1533-1549. https://doi.org/10.1016/j.rser.2016.03.041

Guiavarch, A., & Peuportier, B. (2006). Photovoltaic collectors efficiency according to their integration in buildings. *Solar Energy*, 13. https://doi.org/10.1016/j.solener.2005.07.004

Helms, M., Vattam, S. S., & Goel, A. K. (2009). Biologically inspired design : Process and products. *Design Studies*, *30*(5), 606-622. https://doi.org/10.1016/j.destud.2009.04.003

Hofer, J., Groenewolt, A., Jayathissa, P., Nagy, Z., & Schlueter, A. (2016). Parametric analysis and systems design of dynamic photovoltaic shading modules. *Energy Science & Engineering*, *4*(2), 134-152. https://doi.org/10.1002/ese3.115

Holstov, A., Bridgens, B., & Farmer, G. (2015). Hygromorphic materials for sustainable responsive architecture. *Construction and Building Materials*, *98*, 570-582. https://doi.org/10.1016/j.conbuildmat.2015.08.136

Holstov, A., Farmer, G., & Bridgens, B. (2017). Sustainable Materialisation of Responsive Architecture. *Sustainability*, *9*(3), 435. https://doi.org/10.3390/su9030435

Ibañez-Puy, M. (2017). Opaque Ventilated Façades_ Thermal and energy performance review. *Renewable and Sustainable Energy Reviews*, 12.

Ibrahim, M., Wurtz, E., Anger, J., & Ibrahim, O. (2017). Experimental and numerical study on a novel low temperature façade solar thermal collector to decrease the heating demands : A south-north pipe-embedded closed-water-loop system. *Solar Energy*, *147*, 22-36. https://doi.org/10.1016/j.solener.2017.02.036

Ilevbare, I. M., Probert, D., & Phaal, R. (2013). A review of TRIZ, and its benefits and challenges in practice. *Technovation*, *33*(2), 30-37. https://doi.org/10.1016/j.technovation.2012.11.003

Incropera, F. P., Lavine, A. S., Bergman, T. L., & DeWitt, D. P. (2013). *Principles of heat and mass transfer*. CERN Document Server. https://cds.cern.ch/record/1556016

Infuso, A., Corrado, M., & Paggi, M. (2014). Image analysis of polycrystalline solar cells and modelling of intergranular and transgranular cracking. *Journal of the European Ceramic Society*, *34*(11), 2713-2722. https://doi.org/10.1016/j.jeurceramsoc.2013.12.051

ISO 18458:2015. (2015). *Biomimetics—Terminology, concepts and methodology*. https://www.iso.org/obp/ui/#iso:std:iso:18458:ed-1:v1:en

Jiang, B., Ji, J., & Yi, H. (2008). The influence of PV coverage ratio on thermal and electrical performance of photovoltaic-Trombe wall. *Renewable Energy*, *33*(11), 2491-2498. https://doi.org/10.1016/j.renene.2008.02.001

Jie, J., Wei, H., & Lam, H. N. (2002). The annual analysis of the power output and heat gain of a PV-wall with different integration mode in Hong Kong. *Solar Energy Materials and Solar Cells*, *71*(4), 435-448. https://doi.org/10.1016/S0927-0248(01)00098-8

Jun, J. W. S. (2017). Remembrane : A Shape Changing Adaptive Structure. *Gülen Çagdas, Mine Özkar, Leman F. Gül and Ethem Gürer (Eds.) Future Trajectories of Computation in Design [17th International Conference, CAAD Futures 2017, Proceedings / ISBN 978-975-561-482-3] Istanbul, Turkey, July 12-14, 2017, pp. 180-198.* http://papers.cumincad.org/cgi-bin/works/Show?cf2017_180

Kant, K., Pitchumani, R., Shukla, A., & Sharma, A. (2019). Analysis and design of air ventilated building integrated photovoltaic (BIPV) system incorporating phase change materials. *Energy Conversion and Management*, *196*, 149-164. https://doi.org/10.1016/j.enconman.2019.05.073

Kant, N., & Singh, P. (2021). Review of next generation photovoltaic solar cell technology and comparative materialistic development. *Materials Today: Proceedings*. https://doi.org/10.1016/j.matpr.2021.11.116

Kaplani, E., & Kaplanis, S. (2014). Thermal modelling and experimental assessment of the dependence of PV module temperature on wind velocity and direction, module orientation and inclination. *Solar Energy*, *107*, 443-460. https://doi.org/10.1016/j.solener.2014.05.037

Karlessi, T., & Santamouris, M. (2015). Improving the performance of thermochromic coatings with the use of UV and optical filters tested under accelerated aging conditions. *International Journal of Low-Carbon Technologies*, *10*(1), 45-61. https://doi.org/10.1093/ijlct/ctt027

Kellogg, D. L. (2012). Chapter 93. Thermoregulation. In L. A. Goldsmith, S. I. Katz, B. A. Gilchrest, A. S. Paller, D. J. Leffell, & K. Wolff (Éds.), *Fitzpatrick's Dermatology in General Medicine* (8e éd.). The McGraw-Hill Companies. accessmedicine.mhmedical.com/content.aspx?aid=56052148

Khaled, K., & Berardi, U. (2021). Current and future coating technologies for architectural glazing applications. *Energy and Buildings*, *244*, 111022. https://doi.org/10.1016/j.enbuild.2021.111022

Kim, C., Jeong, M. S., Ko, J., Ko, M., Kang, M. G., & Song, H.-J. (2021). Inhomogeneous rear reflector induced hot-spot risk and power loss in building-integrated bifacial c-Si photovoltaic modules. *Renewable Energy*, *163*, 825-835. https://doi.org/10.1016/j.renene.2020.09.020

Kim, M., Kim, B., Koh, J., & Yi, H. (2023). Flexural biomimetic responsive building façade using a hybrid soft robot actuator and fabric membrane. *Automation in Construction*, *145*, 104660. https://doi.org/10.1016/j.autcon.2022.104660

Knippers, J., & Speck, T. (2012). Design and construction principles in nature and architecture. *Bioinspiration & Biomimetics*, *7*(1), 015002. https://doi.org/10.1088/1748-3182/7/1/015002

Kotey, N., Collins, M., Wright, J., & Jiang, T. (2009). A Simplified Method for Calculating the Effective Solar Optical Properties of a Venetian Blind Layer for Building Energy Simulation. *Journal of Solar Energy Engineering-transactions of The Asme - J SOL ENERGY ENG*, *131*. https://doi.org/10.1115/1.3090822

Krauter, S., Araújo, R. G., Schroer, S., Hanitsch, R., Salhi, M. J., Triebel, C., & Lemoine, R. (1999). Combined photovoltaic and solar thermal systems for facade integration and building insulation. *Solar Energy*, *67*(4), 239-248. https://doi.org/10.1016/S0038-092X(00)00071-2

Kuhn, T. E., Erban, C., Heinrich, M., Eisenlohr, J., Ensslen, F., & Neuhaus, D. H. (2021). Review of technological design options for building integrated photovoltaics (BIPV). *Energy and Buildings*, *231*, 110381. https://doi.org/10.1016/j.enbuild.2020.110381

Kuru, A., Oldfield, P., Bonser, S., & Fiorito, F. (2019). Biomimetic adaptive building skins : Energy and environmental regulation in buildings. *Energy and Buildings*, *205*, 109544. https://doi.org/10.1016/j.enbuild.2019.109544

Labat, M., Woloszyn, M., Garnier, G., Rusaouen, G., & Roux, J. J. (2012). Impact of direct solar irradiance on heat transfer behind an open-jointed ventilated cladding : Experimental and numerical investigations. *Solar Energy*, *86*(9), 2549-2560. https://doi.org/10.1016/j.solener.2012.05.030

Lee, C., Lee, H., Choi, M., & Yoon, J. (2019). Design optimization and experimental evaluation of photovoltaic double skin facade. *Energy and Buildings*, *202*, 109314. https://doi.org/10.1016/j.enbuild.2019.07.031

Lee, T. D., & Ebong, A. U. (2017). A review of thin film solar cell technologies and challenges. *Renewable and Sustainable Energy Reviews*, *70*, 1286-1297. https://doi.org/10.1016/j.rser.2016.12.028

Lewis, D. A., & Nobel, P. S. (1977). Thermal Energy Exchange Model and Water Loss of a Barrel Cactus, Ferocactus acanthodes 1. *Plant Physiology*, *60*(4), 609-616. https://doi.org/10.1104/pp.60.4.609

Li, D., Wu, Y., Wang, B., Liu, C., & Arıcı, M. (2020). Optical and thermal performance of glazing units containing PCM in buildings : A review. *Construction and Building Materials*, *233*, 117327. https://doi.org/10.1016/j.conbuildmat.2019.117327

Li, M., Ma, T., Liu, J., Li, H., Xu, Y., Gu, W., & Shen, L. (2019). Numerical and experimental investigation of precast concrete facade integrated with solar photovoltaic panels. *Applied Energy*, *253*, 113509. https://doi.org/10.1016/j.apenergy.2019.113509

Li, Y., Darkwa, J., Kokogiannakis, G., & Su, W. (2019). Phase change material blind system for double skin façade integration : System development and thermal performance evaluation. *Applied Energy*, *252*, 113376. https://doi.org/10.1016/j.apenergy.2019.113376

Lienhard, J., Schleicher, S., Poppinga, S., Masselter, T., Milwich, M., Speck, T., & Knippers, J. (2011). Flectofin : A hingeless flapping mechanism inspired by nature. *Bioinspiration & Biomimetics*, *6*(4), 045001. https://doi.org/10.1088/1748-3182/6/4/045001

Loonen, R. C. G. M. (2015). Bio-inspired Adaptive Building Skins. In F. Pacheco Torgal, J. A. Labrincha, M. V. Diamanti, C.-P. Yu, & H. K. Lee (Éds.), *Biotechnologies and Biomimetics for Civil Engineering* (p. 115-134). Springer International Publishing. https://doi.org/10.1007/978-3-319-09287-4_5

Loonen, R. C. G. M., Rico-Martinez, J. M., Favoino, F., Brzezicki, M., Menezo, C., La Ferla, G., & Aelenei, A., L. L. (2015). *Design for façade adaptability : Towards a unified and systematic characterization*. 1284-1294. https://pure.tue.nl/ws/files/8287122/15_abs_loonen.pdf

Loonen, R. C. G. M., Trčka, M., Cóstola, D., & Hensen, J. L. M. (2013). Climate adaptive building shells : State-of-the-art and future challenges. *Renewable and Sustainable Energy Reviews*, *25*, 483-493. https://doi.org/10.1016/j.rser.2013.04.016

López Jaimes, A., Zapotecas-Martínez, S., & Coello, C. (2011). *An Introduction to Multiobjective Optimization Techniques* (p. 29-57).

López, M., Rubio, R., Martín, S., & Ben Croxford. (2017). How plants inspire façades. From plants to architecture : Biomimetic principles for the development of adaptive architectural envelopes. *Renewable and Sustainable Energy Reviews*, *67*, 692-703. https://doi.org/10.1016/j.rser.2016.09.018

Lüttge, U. (2004). Ecophysiology of Crassulacean Acid Metabolism (CAM). *Annals of Botany*, *93*(6), 629-652. https://doi.org/10.1093/aob/mch087

Maghrabie, H. M., Abdelkareem, M. A., Elsaid, K., Sayed, E. T., Radwan, A., Rezk, H., Wilberforce, T., Abo-Khalil, A. G., & Olabi, A. G. (2022). A review of solar chimney for natural ventilation of residential and non-residential buildings. *Sustainable Energy Technologies and Assessments*, *52*, 102082. https://doi.org/10.1016/j.seta.2022.102082

Marinosci, C., Semprini, G., & Morini, G. L. (2014). Experimental analysis of the summer thermal performances of a naturally ventilated rainscreen façade building. *Energy and Buildings*, *72*, 280-287. https://doi.org/10.1016/j.enbuild.2013.12.044

Matthieu Bouchaud. (2015). *Réalisation d'un module de façade en bilame permettant la ventilation d'un bâtiment*. https://seminairemateriaux.wordpress.com/2016/02/29/le-couple-bilame-tissu-imper-respirant-vers-une-ventilation-naturelle-biomimetique-des-batiments-lien-vers-le-memoire/

Mazzucchelli, E. S., Alston, M., Brzezicki, M., & Doniacovo, L. (2018). Study of a BIPV Adaptive System. *Journal of Facade Design and Engineering*, *6*(3), 149-162. https://doi.org/10.7480/jfde.2018.3.2602

McAdams, W. H. (1954). *Heat Transmission* (Third ed. McGraw-Hill).

McEwen, B. S. (2016). Chapter 5 - Central Role of the Brain in Stress and Adaptation : Allostasis, Biological Embedding, and Cumulative Change. In G. Fink (Éd.), *Stress : Concepts, Cognition, Emotion, and Behavior* (p. 39-55). Academic Press. https://doi.org/10.1016/B978-0-12-800951-2.00005-4

Mei, L., Infield, D., Eicker, U., & Fux, V. (2003). Thermal modelling of a building with an integrated ventilated PV façade. *Energy and Buildings*, *35*(6), 605-617. https://doi.org/10.1016/S0378-7788(02)00168-8

Mesquita, D. de B., Lucas de S. Silva, J., Moreira, H. S., Kitayama, M., & Villalva, M. G. (2019). A review and analysis of technologies applied in PV modules. *2019 IEEE PES Innovative Smart*

Grid Technologies Conference - Latin America (ISGT Latin America), 1-6. https://doi.org/10.1109/ISGT-LA.2019.8895369

Mirsadeghi, M., Cóstola, D., Blocken, B., & Hensen, J. L. M. (2013). Review of external convective heat transfer coefficient models in building energy simulation programs : Implementation and uncertainty. *Applied Thermal Engineering*, *56*(1), 134-151. https://doi.org/10.1016/j.applthermaleng.2013.03.003

Modjinou, M., Ji, J., Yuan, W., Zhou, F., Holliday, S., Waqas, A., & Zhao, X. (2019). Performance comparison of encapsulated PCM PV/T, microchannel heat pipe PV/T and conventional PV/T systems. *Energy*, *166*, 1249-1266. https://doi.org/10.1016/j.energy.2018.10.007

Moloney, J. (2011). *Designing Kinetics for Architectural Facades : State Change* (1re éd.). Routledge. https://doi.org/10.4324/9780203814703

Nagy, Z., Svetozarevic, B., Jayathissa, P., Begle, M., Hofer, J., Lydon, G., Willmann, A., & Schlueter, A. (2016). The Adaptive Solar Facade : From concept to prototypes. *Frontiers of Architectural Research*, *5*(2), 143-156. https://doi.org/10.1016/j.foar.2016.03.002

Nghana, B., Tariku, F., & Bitsuamlak, G. (2022). Numerical assessment of the impact of transverse roughness ribs on the turbulent natural convection in a BIPV air channel. *Building and Environment*, *217*, 109093. https://doi.org/10.1016/j.buildenv.2022.109093

Ning, X., Wang, X., Zhang, Y., Yu, X., Choi, D., Zheng, N., Kim, D. S., Huang, Y., Zhang, Y., & Rogers, J. A. (2018). Assembly of Advanced Materials into 3D Functional Structures by Methods Inspired by Origami and Kirigami : A Review. *Advanced Materials Interfaces*, *5*(13), 1800284. https://doi.org/10.1002/admi.201800284

Nobel, P. S. (1978). Surface Temperatures of Cacti—Influences of Environmental and Morphological Factors. *Ecology*, *59*(5), 986-995.

Nobel, P. S. (1980). Interception of photosynthetically active radiation by cacti of different morphology. *Oecologia*, *45*(2), 160-166. https://doi.org/10.1007/BF00346455

Nobel, P. S., Geller, G. N., Kee, S. C., & Zimmerman, A. D. (1986). Temperatures and thermal tolerances for cacti exposed to high temperatures near the soil surface. *Plant, Cell & Environment*, *9*(4), 279-287. https://doi.org/10.1111/1365-3040.ep11611688

Oliveira, M. C. C. de, Diniz Cardoso, A. S. A., Viana, M. M., & Lins, V. de F. C. (2018). The causes and effects of degradation of encapsulant ethylene vinyl acetate copolymer (EVA) in crystalline silicon photovoltaic modules : A review. *Renewable and Sustainable Energy Reviews*, *81*, 2299-2317. https://doi.org/10.1016/j.rser.2017.06.039

Ong, K. S., & Chow, C. C. (2003). Performance of a solar chimney. *Solar Energy*, *74*(1), 1-17. https://doi.org/10.1016/S0038-092X(03)00114-2

Palyvos, J. A. (2008). A survey of wind convection coefficient correlations for building envelope energy systems' modeling. *Applied Thermal Engineering*, *28*(8), 801-808. https://doi.org/10.1016/j.applthermaleng.2007.12.005

Perez, G., Allegro, V. R., Alonso, C., Martín-Consuegra, F., Oteiza, I., Frutos, B., & Guerrero, A. (2019). Selection of suitable materials for the development of an innovative thermochromic Trombe wall. *Advances in Building Energy Research*, 1-15. https://doi.org/10.1080/17512549.2019.1684364

Raina, G., & Sinha, S. (2021). A simulation study to evaluate and compare monofacial Vs bifacial PERC PV cells and the effect of albedo on bifacial performance. *Materials Today: Proceedings*, *46*, 5242-5247. https://doi.org/10.1016/j.matpr.2020.08.632

Ramzy, N., & Fayed, H. (2011). Kinetic systems in architecture : New approach for environmental control systems and context-sensitive buildings. *Sustainable Cities and Society*, *1*(3), 170-177. https://doi.org/10.1016/j.scs.2011.07.004

Ratovonkery, J., Assoa, Y. B., & Ménézo, C. (2020). Bio-Inspired Design of a Dynamic Solar Photovoltaic Envelope with Evolving Functionalities. *37th European Photovoltaic Solar Energy Conference and Exhibition*, 1951-1955. https://doi.org/10.4229/EUPVSEC20202020-6CV.2.26

Reichert, S., Menges, A., & Correa, D. (2015). Meteorosensitive architecture : Biomimetic building skins based on materially embedded and hygroscopically enabled responsiveness. *Computer-Aided Design*, *60*, 50-69. https://doi.org/10.1016/j.cad.2014.02.010

Ritter, V., Matschi, C., & Schwarz, D. (2015). Assessment of five control strategies of an adjustable glazing at three different climate zones. *Journal of Facade Design and Engineering*, *3*(2), 129-141. https://doi.org/10.3233/FDE-130036

Romano, R., Aelenei, L., Aelenei, D., & Mazzucchelli, E. S. (2018). What is an adaptive façade? Analysis of Recent Terms and definitions from an international perspective. *Journal of Facade Design and Engineering*, *6*(3), 65-76. https://doi.org/10.7480/jfde.2018.3.2478

Romero-Puertas, M., Ortega-Galisteo, A., Rodríguez, M., & Sandalio, L. (2011). Insights into Cadmium Toxicity : Reactive Oxygen and Nitrogen Species Function. In *Metal Toxicity in Plants : Perception, Signaling and Remediation* (p. 91-117). https://doi.org/10.1007/978-3-642-22081-4_5

Rounis, E. D., Athienitis, A. K., & Stathopoulos, T. (2016). Multiple-inlet Building Integrated Photovoltaic/Thermal system modelling under varying wind and temperature conditions. *Solar Energy*, *139*, 157-170. https://doi.org/10.1016/j.solener.2016.09.023

Saadon, S. (2015). *Modeling and simulation of ventilated building integrated photovoltaic/thermal (BIPV/T) envelope*. Institut National des Sciences Appliquées de Lyon.

Saadon, S., Gaillard, L., Giroux-Julien, S., & Ménézo, C. (2016). Simulation study of a naturally-ventilated building integrated photovoltaic/thermal (BIPV/T) envelope. *Renewable Energy*, *87*, 517-531. https://doi.org/10.1016/j.renene.2015.10.016

Salomon, L. (2021). *Introduction to Multiobjective Optimization*. 87.

Sanjuan, C., Suárez, M. J., González, M., Pistono, J., & Blanco, E. (2011). Energy performance of an open-joint ventilated façade compared with a conventional sealed cavity façade. *Solar Energy*, *85*(9), 1851-1863. https://doi.org/10.1016/j.solener.2011.04.028

Schleicher, S., Lienhard, J., Poppinga, S., Speck, T., & Knippers, J. (2015). A methodology for transferring principles of plant movements to elastic systems in architecture. *Computer-Aided Design*, *60*, 105-117. https://doi.org/10.1016/j.cad.2014.01.005

Shahin, H. S. M. (2019). Adaptive building envelopes of multistory buildings as an example of high performance building skins. *Alexandria Engineering Journal*, *58*(1), 345-352. https://doi.org/10.1016/j.aej.2018.11.013

Shu, L. H. (2010). A natural-language approach to biomimetic design. *Artificial Intelligence for Engineering Design, Analysis and Manufacturing*, *24*(4), 507-519. https://doi.org/10.1017/S0890060410000363

Shukla, A. K., Sudhakar, K., & Baredar, P. (2016). A comprehensive review on design of building integrated photovoltaic system. *Energy and Buildings*, *128*, 99-110. https://doi.org/10.1016/j.enbuild.2016.06.077

Sisodia, R., & Bhatla, S. C. (2018). Plant Movements. In S. C. Bhatla & M. A. Lal, *Plant Physiology, Development and Metabolism* (p. 907-935). Springer Singapore. https://doi.org/10.1007/978-981-13-2023-1_29

Soria, B., Gerritsen, E., Lefillastre, P., & Broquin, J.-E. (2016). A study of the annual performance of bifacial photovoltaic modules in the case of vertical facade integration. *Energy Science & Engineering*, *4*(1), 52-68. https://doi.org/10.1002/ese3.103

Souayfane, F., Fardoun, F., & Biwole, P.-H. (2016). Phase change materials (PCM) for cooling applications in buildings : A review. *Energy and Buildings*, *129*, 396-431. https://doi.org/10.1016/j.enbuild.2016.04.006

Soudi, N., Nanayakkara, S., Jahed, N. M. S., & Naahidi, S. (2020). Rise of nature-inspired solar photovoltaic energy convertors. *Solar Energy*, *208*, 31-45. https://doi.org/10.1016/j.solener.2020.07.048

Speck, T., & Speck, O. (2008). Process sequences in biomimetic research. *Design and Nature IV*, *I*, 3-11. https://doi.org/10.2495/DN080011

Suresh, C., Kumar Hotta, T., & Saha, S. K. (2022). Phase change material incorporation techniques in building envelopes for enhancing the building thermal Comfort-A review. *Energy and Buildings*, *268*, 112225. https://doi.org/10.1016/j.enbuild.2022.112225

Svetozarevic, B., Begle, M., Jayathissa, P., Caranovic, S., Shepherd, R. F., Nagy, Z., Hischier, I., Hofer, J., & Schlueter, A. (2019). Dynamic photovoltaic building envelopes for adaptive energy and comfort management. *Nature Energy*, *4*(8), Article 8. https://doi.org/10.1038/s41560-019-0424-0

Tällberg, R., Jelle, B. P., Loonen, R., Gao, T., & Hamdy, M. (2019). Comparison of the energy saving potential of adaptive and controllable smart windows : A state-of-the-art review and simulation studies of thermochromic, photochromic and electrochromic technologies. *Solar Energy Materials and Solar Cells*, *200*, 109828. https://doi.org/10.1016/j.solmat.2019.02.041

Tanda, G. (2008). Natural convective heat transfer in vertical channels with low-thermal-conductivity ribs. *International Journal of Heat and Fluid Flow*, *29*(5), 1319-1325. https://doi.org/10.1016/j.ijheatfluidflow.2008.05.004

Timoshenko, S. (1925). Analysis of Bi-Metal Thermostats. *Journal of the Optical Society of America*, *11*(3), 233. https://doi.org/10.1364/JOSA.11.000233

Tina, G. M., Bontempo Scavo, F., Aneli, S., & Gagliano, A. (2020). A novel building ventilated façade with integrated bifacial photovoltaic modules : Analysis of the electrical and thermal performances. *2020 5th International Conference on Smart and Sustainable Technologies (SpliTech)*, 1-6. https://doi.org/10.23919/SpliTech49282.2020.9243810

Tina, G. M., Scavo, F. B., Aneli, S., & Gagliano, A. (2021). Assessment of the electrical and thermal performances of building integrated bifacial photovoltaic modules. *Journal of Cleaner Production*, *313*, 127906. https://doi.org/10.1016/j.jclepro.2021.127906

Tonui, J. K., & Tripanagnostopoulos, Y. (2007). Air-cooled PV/T solar collectors with low cost performance improvements. *Solar Energy*, *81*(4), 498-511. https://doi.org/10.1016/j.solener.2006.08.002

Tonui, J. K., & Tripanagnostopoulos, Y. (2008). Performance improvement of PV/T solar collectors with natural air flow operation. *Solar Energy*, *82*(1), 1-12. https://doi.org/10.1016/j.solener.2007.06.004

Vattam, S., Helms, M. E., & Goel, A. K. (2007). *Biologically-Inspired Innovation in Engineering Design : A Cognitive Study* [Technical Report]. Georgia Institute of Technology. https://smartech.gatech.edu/handle/1853/14346

Vattam, S., Wiltgen, B., Helms, M., Goel, A. K., & Yen, J. (2011). DANE : Fostering creativity in and through biologically inspired design. In *Design Creativity 2010* (p. 115-122). Springer.

Vazquez, E., Randall, C., & Duarte, J. P. (2019). Shape-changing architectural skins : A review on materials, design and fabrication strategies and performance analysis. *Journal of Facade Design and Engineering*, *7*(2), 93-114. https://doi.org/10.7480/jfde.2019.2.3877

Verma, S., & Devadass, P. (2013). adaptive [skins] : Responsive building skin systems based on tensegrity principles. *AA School of Architecture*.

Vicente, R., & Silva, T. (2014). Brick masonry walls with PCM macrocapsules : An experimental approach. *Applied Thermal Engineering*, *67*(1), 24-34. https://doi.org/10.1016/j.applthermaleng.2014.02.069

Vincent, J. F. V., Bogatyreva, O. A., Bogatyrev, N. R., Bowyer, A., & Pahl, A.-K. (2006). Biomimetics : Its practice and theory. *Journal of The Royal Society Interface*, *3*(9), 471-482. https://doi.org/10.1098/rsif.2006.0127

Vulkan, A., Kloog, I., Dorman, M., & Erell, E. (2018). Modeling the potential for PV installation in residential buildings in dense urban areas. *Energy and Buildings*, *169*, 97-109. https://doi.org/10.1016/j.enbuild.2018.03.052

Wang, J. (2014). *Integrating Acclimated Kinetic Envelopes into Sustainable Building Design* [Thesis]. https://oaktrust.library.tamu.edu/handle/1969.1/152455

Wanieck, K., Fayemi, P.-E., Maranzana, N., Zollfrank, C., & Jacobs, S. (2017). Biomimetics and its tools. *Bioinspired, Biomimetic and Nanobiomaterials*, *6*(2), 53-66. https://doi.org/10.1680/jbibn.16.00010

Watmuff, J., Charters, W. W. S., & Proctor, D. (1977). Solar and wind induced external coefficients—Solar collectors. *Undefined*. https://www.semanticscholar.org/paper/Solar-and-wind-induced-external-coefficients-Solar-Watmuff-Charters/2705119fba76d0ed96c3444d353afd565082a27a

Willmer, P., Stone, G., & Johnston, I. A. (2005). *Environmental physiology of animals* (2nd ed). Blackwell Pub.

Willot, Q., Simonis, P., Vigneron, J.-P., & Aron, S. (2016). Total Internal Reflection Accounts for the Bright Color of the Saharan Silver Ant. *PLOS ONE*, *11*(4), e0152325. https://doi.org/10.1371/journal.pone.0152325

Xu, L., Luo, K., Ji, J., Yu, B., Li, Z., & Huang, S. (2020). Study of a hybrid BIPV/T solar wall system. *Energy*, *193*, 116578. https://doi.org/10.1016/j.energy.2019.116578

Xu, S., Liao, W., Huang, J., & Kang, J. (2014). Optimal PV cell coverage ratio for semi-transparent photovoltaics on office building façades in central China. *Energy and Buildings*, *77*, 130-138. https://doi.org/10.1016/j.enbuild.2014.03.052

Yang, H., Burnett, J., & Ji, J. (2000). Simple approach to cooling load component calculation through PV walls. *Energy and Buildings*, *31*(3), 285-290. https://doi.org/10.1016/S0378-7788(99)00041-9

Yen, J., Weissburg, M. J., Helms, M., & Goel, A. K. (2011). Biologically Inspired Design : A Tool for Interdisciplinary Education. *Biomimetics : Nature-Based Innovation*, 351-380. https://doi.org/10.1201/b11230-15

Yi, H., Kim, D., Kim, Y., Kim, D., Koh, J., & Kim, M.-J. (2020). 3D-printed attachable kinetic shading device with alternate actuation : Use of shape-memory alloy (SMA) for climate-adaptive responsive architecture. *Automation in Construction*, *114*, 103151. https://doi.org/10.1016/j.autcon.2020.103151

Yi, H., & Kim, Y. (2021a). Prototyping of 4D-printed self-shaping building skin in architecture : Design, fabrication, and investigation of a two-way shape memory composite (TWSMC) façade panel. *Journal of Building Engineering*, *43*, 103076. https://doi.org/10.1016/j.jobe.2021.103076

Yi, H., & Kim, Y. (2021b). Self-shaping building skin : Comparative environmental performance investigation of shape-memory-alloy (SMA) response and artificial-intelligence (AI) kinetic control. *Journal of Building Engineering*, *35*, 102113. https://doi.org/10.1016/j.jobe.2020.102113

Yoon, J. (2018). SMP Prototype Design and Fabrication for Thermo-responsive Façade Elements. *Journal of Facade Design and Engineering*, *7*(1), 41-62. https://doi.org/10.7480/jfde.2019.1.2662

Yu, B., He, W., Li, N., Wang, L., Cai, J., Chen, H., Ji, J., & Xu, G. (2017). Experimental and numerical performance analysis of a TC-Trombe wall. *Applied Energy*, *206*, 70-82. https://doi.org/10.1016/j.apenergy.2017.08.171

Yu, G., Yang, H., Yan, Z., & Kyeredey Ansah, M. (2021). A review of designs and performance of façade-based building integrated photovoltaic-thermal (BIPVT) systems. *Applied Thermal Engineering*, *182*, 116081. https://doi.org/10.1016/j.applthermaleng.2020.116081

Zalewski, L., Joulin, A., Lassue, S., Dutil, Y., & Rousse, D. (2012). Experimental study of small-scale solar wall integrating phase change material. *Solar Energy*, *86*(1), 208-219. https://doi.org/10.1016/j.solener.2011.09.026

Zanetti, I., Bonomo, P., Frontini, F., Saretta, E., Macé, P., & Bosch, E. (2020). *Building Integrated Photovoltaics : A pratical hanbook for solar buildings' stakeholders—Status Report 2020*. SUPSI -Becquerel Institute. https://solarchitecture.ch/wp-content/uploads/2020/11/201022_BIPV_web_V01.pdf

Zanetti, I., Bonomo, P., Frontini, F., Saretta, E., van den Donker, M., Vossen, F., & Folkerts, W. (2017). *Building Integrated Photovoltaics : Product overview for solar building skins—Status Report 2017*. SUPSI - SEAC. https://www.solaxess.ch/wp-content/uploads/2018/04/Report-2017_SUPSI_SEAC_BIPV.pdf

Zanghirella, F., Perino, M., & Serra, V. (2011). A numerical model to evaluate the thermal behaviour of active transparent façades. *Energy and Buildings*, *43*(5), 1123-1138. https://doi.org/10.1016/j.enbuild.2010.08.031

Zhang, T., Tan, Y., Yang, H., & Zhang, X. (2016). The application of air layers in building envelopes : A review. *Applied Energy*, *165*, 707-734. https://doi.org/10.1016/j.apenergy.2015.12.108

Zhang, T., & Yang, H. (2019). Flow and heat transfer characteristics of natural convection in vertical air channels of double-skin solar façades. *Applied Energy*, *242*, 107-120. https://doi.org/10.1016/j.apenergy.2019.03.072

Zhang, W., Gong, T., Ma, S., Zhou, J., & Zhao, Y. (2021). Study on the Influence of Mounting Dimensions of PV Array on Module Temperature in Open-Joint Photovoltaic Ventilated Double-Skin Façades. *Sustainability*, *13*(9), Article 9. https://doi.org/10.3390/su13095027

Zhou, D., Zhao, C. Y., & Tian, Y. (2012). Review on thermal energy storage with phase change materials (PCMs) in building applications. *Applied Energy*, *92*, 593-605. https://doi.org/10.1016/j.apenergy.2011.08.025

ZigZagsolar. (s. d.). *ZigZagsolar Home—ZigZagSolar solarfacades*. ZigZagSolar. Consulté 18 août 2022, à l'adresse https://www.zigzagsolar.com/

List of figures

List of tables

APPENDICES

A1 Summary of bioinspiration approaches

A1.1 Technology pull approaches

Table A1.1: Process of technology pull approaches, based on the work of Badarnah Kadri (2012)

General phases	**(Shu, 2010)**	**BID method**[1]	**(Speck & Speck, 2008)**	**BioTRIZ (Vincent et al., 2006)**	**Biomimicry 3.8 (Baumeister et al., 2014)**	**(Badarnah Kadri, 2012)**
Problem definition : *Technological domain*	Problem definition	- Problem definition - Reframing the problem	definition of the technical problem	-Problem definition -Analyse and understand the problem	- Function identification - Context definition - Integration of Life's Principles into design brief	Identify, functions, challenges
Exploration and investigation : *Biology to technology*	- Search for biological analogies - Assessment of biological analogies	- Biological solution search - Biological solution definition - Principle extraction	- Search for biological analogies - Identify appropriate principles - Abstraction: detachment from biological model	- Find functional analogy in biology - Compare solutions from biology and TRIZ	- Discover natural models - Abstract biological strategies into design principles	- Explore and investigate - Discover and extract - Elaborate and analyse - Classify - Abstract
Solution development : *New technical solution*	Application of biological analogies	Principle application	Implementation: test technical feasibility and prototyping	- List principles from biology and technical domains - Develop ideas	- Brainstorm bioinspired idea - Emulate design principle - Measure using Life's Principle	-Develop concept -Transform and evaluate -Prototype and validate

[1] The BID method is proposed by researchers in CBID (Center for biologically inspired design) in Georgia Tech, Atlanta, GA 30332-0230. The processus is citied in the works of Helms et al. (2009); Vattam et al. (2007); Yen et al. (2011)

A1.2 Biology push approaches

Table A1.2: Process of biology push approaches, based on the work of Badarnah Kadri (2012)

General phases	**Bioinspiration 3.8 (Baumeister et al., 2014)**	**Processus BID**	**(Speck & Speck, 2008)**	**(López et al., 2017)**
Biological domain	Discover natural model	Biological solution identification Biological solution definition Principles extraction	Identify a biological system Analyse biomechanics functional morphology and anatomy Understand the principles	Data collection according to Choice of climatic context
Transfer phase: *Biology to technology*	Abstract biological strategies into design principles Identify function Define context Brainstorm bioinspired idea	Reframe the solution	Abstraction: detachment from biological model	Analyse explored biological organisms by answering the following: What? ⇨ description Why? ⇨ challenges How? ⇨ functions
Technological domain	Integrate Life's Principles Emulate design principles Measure using Life's Principles	Problem search Problem definition Principle application	Technical implementation	Application ideas Innovation and design concept generation

A2 Thermal modelling of the facades

A2.1 Modelling of the facade without bilayers

A2.1.1 Dimensionless numbers for Nusselt correlation

Table A2.1: Dimensionless number for Nusselt correlation

Dimensionless numbers	*Expressions*	*Parameters*
Reynolds number	$Re_{Dh} = \frac{\nu V}{D_h}$	ν kinematic viscosity $[m^2/s]$ V velocity $[m/s]$ D_h hydraulic diameter $[m]$ $D_h = \frac{4S}{P}$ S pipe section $[m^2]$ P pipe perimeter $[m]$
Prandtl number	$Pr = \frac{\nu}{\alpha}$	α fluid thermal diffusivity $[m^2/s]$
Rayleigh number	$Ra_L = \frac{\rho^2 g \beta_{th} L^3 (\mathrm{T_p} - T_\infty)}{\mu k}$	β_{th} volumetric coefficient of thermal expansion $[°K^{-1}]$ μ dynamic viscosity $[kg/m.s]$ ρ density $[kg/m^3]$ d channel thickness $[m]$ g gravitational acceleration $[m/s^2]$ k thermal conductivity $[W/m^2\,°K]$ L collector height $[m]$ T_p wall temperature $[°K]$ T_∞ air temperature $[°K]$ q'' heat flux $[W/m^2]$
Channel Rayleigh number	$Ra'_d = \frac{\rho^2 g \beta_{th} C_p d^4 (\mathrm{T_p} - T_\infty)}{\mu L}$	
Modified channel Rayleigh number	$Ra''_d = \frac{\rho^2 g \beta_{th} C_p d^5 q''}{\mu L k^2}$	

A2.1.2 Optical properties for direct normal irradiation

The absorptivity α_0 and transmitivity τ_0 of glazing at a normal incident angle $\theta_i = 0$ can be calculated according to the extinction coefficient and the refraction index of the glazing (Duffie & Beckman, 2006). In effect, the absorption coefficient can be approximated by:

$$\alpha \cong 1 - \tau_a \tag{A2.1}$$

with τ_a is the transmission coefficient considering only the absorption loss. It depends on the extinction coefficient K, the glazing thickness δ and the glazing refraction angle θ_2:

$$\tau_a = \exp\left(-\frac{K\delta}{\cos\theta_2}\right) \tag{A2.2}$$

With a normal direct solar radiation $\theta_2 = 0$ and $\tau_a(0) = \exp(-K\delta)$.

The transmissivity is given by:

$$\tau = \tau_a \tau_r \tag{A2.3}$$

Where τ_r is the transmission coefficient considering only the reflection loss. It is given by:

$$\tau_r = \frac{1}{2}\left(\frac{1-r_{\parallel}}{1+r_{\parallel}} + \frac{1-r_{\perp}}{1+r_{\perp}}\right) \quad \text{(A2.4)}$$

With $r_{\parallel}$ and $r_{\perp}$ represent respectively the parallel and perpendicular components of unpolarized radiation. They depend on the refractive index of the media through which the rays are passing. They are equal in the case of normal radiation (or the incident angle $\theta_i = 0$), $r(0) = r_{\parallel} = r_{\perp}$, thus:

$$\tau_r(0) = \left(\frac{1-r(0)}{1+r(0)}\right) \quad \text{(A2.5)}$$

Since the refractive index of the air is nearly unity, $r(0)$ depends only on the refractive index of the glazing and is given by:

$$r(0) = \left(\frac{n-1}{n+1}\right)^2 \quad \text{(A2.6)}$$

Thus,

$$\alpha_0 \cong 1 - \tau_a(0) \quad \text{(A2.7)}$$

$$\tau_0 = \tau_a(0)\tau_r(0) \quad \text{(A2.8)}$$

$$\rho_0 = 1 - \tau_0 - \alpha_0 \quad \text{(A2.9)}$$

A2.2 Modelling of the facade with bilayers

A2.2.1 Heat transfer from fins

Let us consider a rectangular fin with a uniform cross-section A_c, a length L_b^e, a cross-section perimeter P_b and a thermal conductivity λ_b. The heat transfer along the fin is one-dimensional. It exchanges with surrounding air with a convection heat transfer coefficient h_c. The heat balance from the fin can be established by considering a differential element, as given in Figure A2.1.

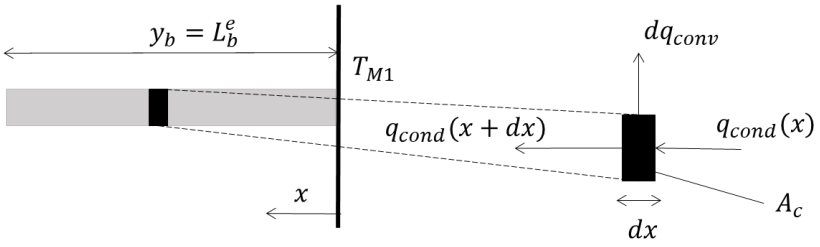

Figure A2.1: Heat balance in a differential element of a fin

Therefore, the following heat balance is obtained :

$$q_{cond}(x+dx) = q_{cond}(x) + dq_{conv} \quad \text{(A2.10)}$$

With

$$q_{cond}(x) = -\lambda_b A_c \left.\frac{dT_b}{dx}\right|_x \quad \text{(A2.11)}$$

$$q_{cond}(x+dx) = -\lambda_b A_c \left.\frac{dT_b}{dx}\right|_{x+dx} \quad \text{(A2.12)}$$

$$dq_{conv} = h_c P_b \big(T_b(x) - T_f\big) dx \tag{A2.13}$$

Leading to the following differential equation:

$$\frac{d^2 T_b}{dx^2} - \frac{h_c P_b}{\lambda_b A_c}\big(T_b(x) - T_f\big) = 0 \tag{A2.14}$$

Taking $m^2 = \frac{h_c P_b}{\lambda_b A_c}$ and $\theta = \big(T_b(x) - T_f\big)$, the equation can be simplified as follows :

$$\frac{d^2\theta}{dx^2} - m^2\theta = 0 \tag{A2.15}$$

And its general solution is given by:

$$\theta(x) = C_1 e^{mx} + C_2 e^{-mx} \tag{A2.16}$$

To solve this equation, let us assume boundary conditions of an adiabatic free end and equal temperatures at the fin-to-wall contact:

$$\begin{cases} -\lambda_b A_c \dfrac{dT_b}{dx}\Big|_{x=L^e_{b|fin}} = -\lambda_b A_c \dfrac{d\theta}{dx}\Big|_{x=L^e_{b|fin}} = 0 \\ T_b(x=0) = T_{M1} \; or \; \theta_0 = (T_b(x=0) - T_{M1}) = 0 \end{cases} \tag{A2.17}$$

With those boundary conditions, the solution of the differential equation is:

$$\big(T_b(x) - T_f\big) = \big(T_{M1} - T_f\big)\frac{\cosh\big(m(L^e_b - x)\big)}{\cosh(mL^e_b)} \tag{A1.18}$$

The heat flux evacuated by the fin through convection is equal to the heat extracted from the wall through conduction at the fin-wall contact:

$$q_e = \int_0^{L^e_{b|fin}} h_c P_b \big(T_b(x) - T_f\big) dx = -\lambda_b A_c \frac{dT_b}{dx}\Big|_{x=0} \tag{A2.19}$$

With the solution of the fin equation, this heat flux is given by:

$$q_e = h_c P_b \frac{\tanh\big(mL^e_{b|fin}\big)}{m} = h_c A^e_b \eta_b \big(T_{M1} - T_f\big) \tag{A2.20}$$

Where η_b the fin efficiency.

A2.2.2 Effective optical properties of the bilayers considering the PV module semi-transparency

The effective optical properties of the bilayers are calculated considering an elementary enclosure delimitated by two consecutive bilayers (considered as flat slats). Those properties are given in subsection V.3.2.1 while considering the PV module as transparent glazing. To take into account the module semi-transparency, the properties expressions on the front surface slightly change for direct radiation. Several expressions are obtained depending on the incident angle and the entrance position of direct rays in the elementary shading layer enclosure.

The following approximations are established considering:

- The PV cells and bilayer are facing each other. The lengths of the PV cells and the bilayers are equal.

- The interspaces between the bilayers at the close configuration and the PV cells are also equal.
- The thickness of the back cover of the PV modules is neglected.

- **Direct-to-direct transmissivity**

For the studied geometry, incident direct radiation on the front surface passes through L_i corresponding to the interspace between the modules (or the bilayers). Thus, the reference surface for the calculation of transmitivity becomes L_i (instead of s). To calculate the direct-to-direct transmissivity, the first step is to identify the position of the rays' entrance within the enclosure which is described with the points A and B. Three cases of ray path are identified depending on the location of those points and depending on the value of L_a the projection of the slat surface at the back side of the enclosure, d the airgap thickness, L_i and y_b (see Figure A2.2). With:

$$L_a = L_b^e \sin \phi_b \tag{A2.21}$$

The reference values for the determination of A and B are:

$$A = \left((d - y_b) \tan \theta_i \,\%s\right) \tag{A2.22}$$

$$B = \left((d - y_b) \tan \theta_i \,\%s\right) - L_i \tag{A2.23}$$

According to the position A and B, the direct-to-direct front transmissivity is given in Table A2.2.

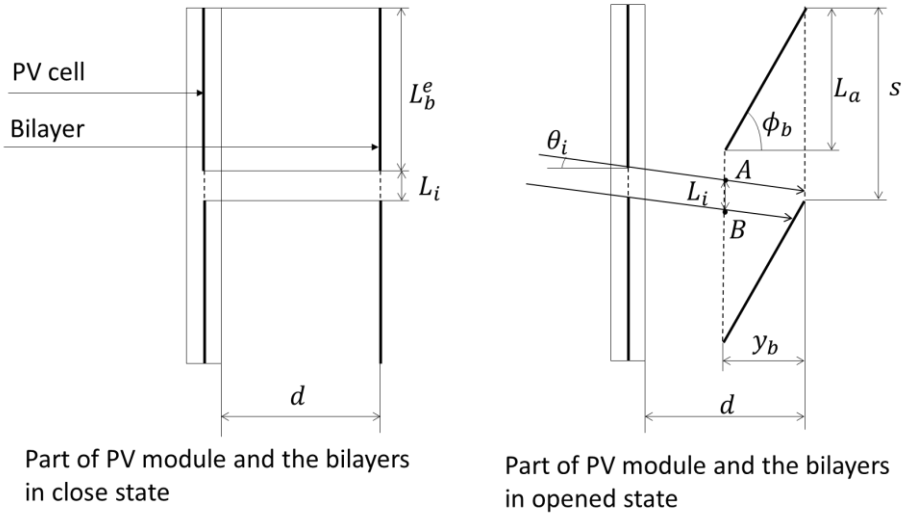

Figure A2.2: Illustration of the principle for the calculation of $\tau_{b,front}^{DD}$ in the PV facade

- **Direct-to-diffuse reflectivity and transmissivity**

The direct-to-diffuse reflectivity and transmissivity are determined by considering possible cases of the irradiated bilayer surfaces by direct radiation (see Table A2.3). With the expressions of J_i and G_i on each surface of enclosure and the transmitted direct irradiance $G_{dir}^t = 1$, those properties are given by:

$$\rho_{b,front}^{Dd} = G_1, \qquad \tau_{b,front}^{Dd} = G_2 \tag{A2.24}$$

Table A2.2: Value of $\tau_{b,front}^{DD}$ according to the entrance of the ray in the reference bilayers enclosure

Case	$[A < (L_a + L_i) \cup A = 0] \cap [B \leq L_a]$	$A \geq (L_a + L_i)$	$[A < (L_a + L_i) \cup A = 0] \cap [B > L_a]$
	$A > B$		$A < B$
Figure	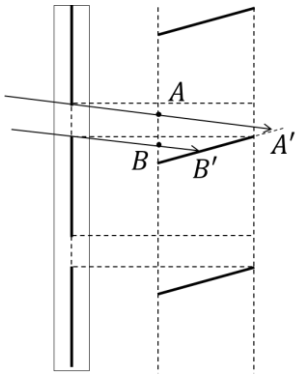	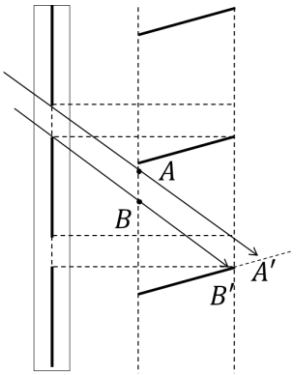	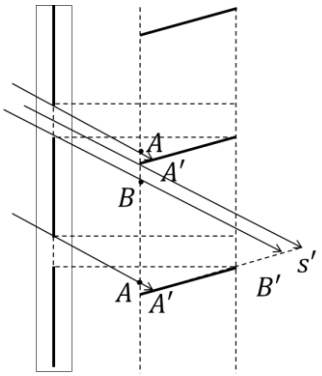
A	$L_a + L_i - A$	$s - (A - L_a + L_i)$	$L_a + L_i - A$
B	$L_a - B = A - L_i$	$A - L_i$	$s - (B - L_a)$
$\tau_{b,front}^{DD}$	$\max\left(0, \frac{A' - L_b^e}{L_i'}\right)$	$\max\left(0, \frac{A' - L_b^e}{L_i'}\right)$	$\max\left(0, \frac{s' - \max(B', L_b^e)}{L_i'}\right)$

Table A2.3: Value of the diffuse source Z_i while considering the semi-transparency of the module

For semi-transparent PV module			
$A > B$		$A < B$	
$A' \geq L_b^e$	$A' < L_b^e$	$s' \geq L_b^e$	$s' < L_b^e$
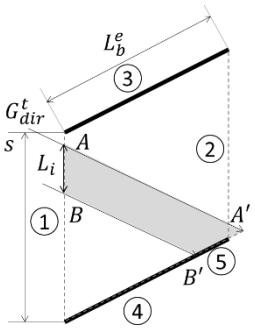	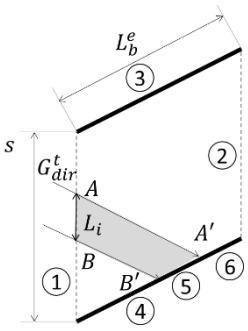	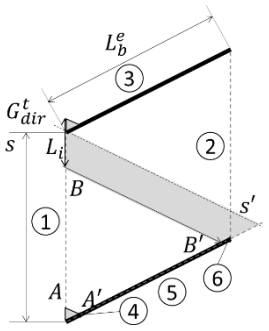	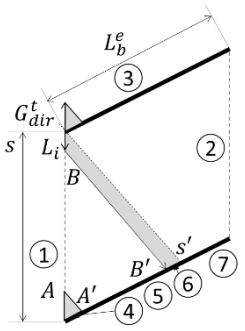
$N_{max} = 5$	$N_{max} = 6$	$N_{max} = 6$	$N_{max} = 7$
$Z_5 = \rho_{b,p} \frac{L_b^e - B'}{L_i'} G_{dir}^t$	$Z_5 = \rho_{b,p} \frac{A' - B'}{L_i'} G_{dir}^t$	$Z_4 = \rho_{b,p} \frac{A'}{L_i'} G_{dir}^t$ $Z_6 = \rho_{b,p} \frac{L_b^e - B'}{L_i'} G_{dir}^t$	$Z_4 = \rho_{b,p} \frac{A'}{L_i'} G_{dir}^t$ $Z_6 = \rho_{b,p} \frac{A' - B'}{L_i'} G_{dir}^t$

A2.2.3 Determination of the view factor of the bilayer enclosure

The view factor F_{ij} of the surface i to the surface j in the considered enclosure is calculated according to the Hottel cross-string method. Considering 2 facing surfaces of random shape, the view factor F_{12} of surface 1 to surface 2 can be approximated by:

$$F_{12} = \frac{\sum_{k=1}^{2} CS_k + \sum_{k=1}^{2} US_k}{2S_1} \tag{A2.25}$$

With CS_k are the diagonal surfaces joining the ends of the two surfaces and crossing each other. US_k are the surfaces joining the two facing ends of the studied surfaces and are uncrossed.

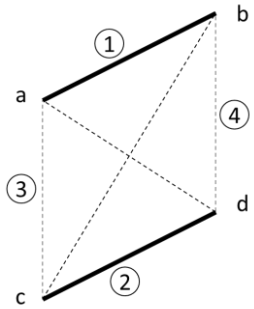

Figure A2.3: Illustration of the four-surface enclosure for view factor calculation using the cross-string method

Hence, considering the geometry of the considered enclosure (see Figure A2.3), the view factor of surface 1 to the three other surfaces as follows:

$$F_{12} = \frac{(ad + bc) - (ac + bd)}{2ab} \tag{A2.26}$$

$$F_{13} = \frac{(ab + ac) - bc}{2ab} \tag{A2.27}$$

$$F_{14} = \frac{(ab + bd) - ad}{2ab} \tag{A2.28}$$

Some useful relations for the determination of the view factor in a given enclosure with N surfaces are the complementarity of the view factor of one surface i to the other surfaces j to the unity:

$$\sum_{j=1}^{n} F_{ij} = 1 \tag{A2.29}$$

And the reciprocity of the view factors from i to j and j to i according to their area:

$$S_{ij} F_{ij} = S_{ji} F_{ji} \tag{A2.30}$$

The view factor of a flat or convex surface to itself is:

$$F_{ii} = 0 \tag{A2.31}$$

As approximation, the surfaces are considered flat.

A2.2.4 Details of the mass flow rate estimation

The flow rate estimation considers intermediate pressure nodes upstream and downstream of each bilayer end to determine the pressure equilibrium. Figure A2.4 shows the localisation of those nodes for a wall with two bilayers. Thus, the pressure equilibrium can be written as follows:

$$(P_0 - P_1) + (P_1 - P_2) + (P_2 - P_3) + (P_3 - P_4) + (P_4 - P_5) + (P_5 - P_6) + (P_6 - P_7) = -(P_7 - P_0) \quad \text{(A2.32)}$$

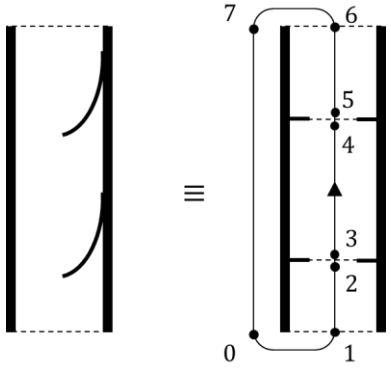

Figure A2.4: Illustration of the air circulation in the gap in a closed loop and the selected pressure nodes considering the approximation of the bilayers as a diaphragm

$(P_7 - P_0)$ the outdoor hydraulic pressure drop corresponding to the height of the air gap.

$$(P_7 - P_0) = -\rho_0 g L \quad \text{(A2.33)}$$

$(P_0 - P_1)$ and $(P_6 - P_7)$ are the pressure drops in the inlet and the outlet of the air gap. They have the same expression as in the facade without bilayers.

$$(P_0 - P_1) = \frac{1}{2} K_{fin} \rho_{01} v_{01}^2 - \frac{1}{2} C P_0 \rho_0 v_{windo}^2 \quad \text{(A2.34)}$$

$$(P_6 - P_7) = \frac{1}{2} K_{fout} \rho_{67} v_{67}^2 + \frac{1}{2} C P_7 \rho_0 v_{wind7}^2 \quad \text{(A2.35)}$$

$(P_1 - P_2)$, $(P_3 - P_4)$ and $(P_5 - P_6)$ are the pressure drops due to friction loss at the linear part of the air gap. By taking into account the continuity relation, equality of airflow section, and mean air density at those air gap parts, we have:

$$v_{12} = v_{34} = v_{56} = \frac{\dot{m}}{\rho_m S_{gap}} \quad \text{(A2.36)}$$

By noting the pressure losses $(P_1 - P_2), (P_3 - P_4)$ and $(P_5 - P_6)$ globally as $\left(P_{2(i+1)} - P_{2(i+1)}\right)$, the general expression of the pressure losses is:

$$\left(P_{2(i+1)} - P_{2(i+1)}\right) = \rho_m g L_{2(i+1)-2(i+1)} + \frac{1}{2} f \left(\frac{L_{2(i+1)-2(i+1)}}{D_h}\right) \frac{\dot{m}^2}{\rho_m S_{gap}^2} \quad \text{(A2.37)}$$

where $i \in [0, N+1]$ and N is the number of bilayers.

With the assumption that the thickness of bilayers is negligible, then

$$\sum_{i=0}^{N+1} L_{2(i+1)-2(i+1)} \approx L \quad \text{(A2.38)}$$

With L the height of the air gap. Therefore,

$$\sum_{i=0}^{N+1} \left(P_{2(i+1)} - P_{2(i+1)}\right) \approx \rho_m g L + \frac{1}{2} f \left(\frac{L}{D_h}\right) \frac{\dot{m}^2}{\rho_m S_{gap}^2} \quad \text{(A2.39)}$$

$(P_2 - P_3)$, $(P_4 - P_5)$ are the pressure drop due to the bilayer bending, which is considered equivalent to that of a diaphragm with a diameter narrow by y_b. A pressure drop coefficient K_b is then considered at each bilayer. By assuming that y_{bi} is the same for all bilayers ($d_{bi} = d_{23} = d_{45}$), we also have equal velocity ($v_{23} = v_{45}$) and the pressure drop at those levels is:

$$(P_2 - P_3) = (P_4 - P_5) = (P_{2i} - P_{2i+1}) = \frac{1}{2} K_b \frac{\dot{m}^2}{\rho_m S_{gap}^2} \tag{A2.40}$$

And

$$\sum_{i=1}^{N} (P_{2i} - P_{2i+1}) = \frac{1}{2} N K_{b_i} \frac{\dot{m}^2}{\rho_m S_{gap}^2} \tag{A2.41}$$

Thus the generalized form of the pressure equilibrium in an air gap with N bilayers is:

$$\begin{aligned}(P_0 - P_1) + \sum_{i=0}^{N+1} \left(P_{2(i+1)} - P_{2(i+1)}\right) + \sum_{i=1}^{N} (P_{2i} - P_{2i+1}) + \left(P_{2(N+1)} - P_{2(N+1)+1}\right) \\ = -\left(P_{2(N+1)+1} - P_0\right)\end{aligned} \tag{A2.42}$$

With the Boussinesq approximation while considering a small variation of the air density in the gap:

$$(\rho_0 - \rho_m) = \rho_0 \beta_{th} (T_m - T_0) \text{ with } \beta_{th} = \frac{1}{T_m} \tag{A2.43}$$

T_m is as a function of the air temperature stratification in the gap, which is supposed to be equal to $S = 0.5$:

$$T_m = T_{in} + S(T_{f,out} - T_{f,in}) \text{ with } T_{f,in} = T_0 \tag{A2.44}$$

And the expression of thermal energy transmitted to the air:

$$P_{th} = \dot{m} C_p \left(T_{f,out} - T_{f,in}\right) \tag{A2.45}$$

Hence:

$$\sum_{i=0}^{N+1} \left(P_{2(i+1)} - P_{2(i+1)}\right) + \left(P_{2(N+1)+1} - P_0\right) = -gL\beta_{th} \frac{P_{th}}{\dot{m} C_p} + \frac{1}{2} f \left(\frac{L}{D_h}\right) \frac{\dot{m}^2}{\rho_m S_{gap}^2} \tag{A2.46}$$

Leading to the mass flow rate equation:

$$\begin{aligned}\left(K_{fin} + K_{fout} + N K_b + f\left(\frac{L}{D_h}\right)\right) \dot{m}^3 - \rho_0 \left(CP_0 v_{windo}^2 - CP_3 v_{wind3}^2\right) \dot{m} \\ - 2\left(\rho S_{gap}\right)^2 gL\beta_{th} S \frac{P_{th}}{C_p} = 0\end{aligned} \tag{A2.47}$$

A2.3 Error metrics for the model validation

The difference between the model output and the measurement are calculated to evaluate the developed model performance to fit experimental data. For instance, for the temperature at a given node $k \in \{T_{g1}, \dots, T_{M2}\}$, the difference ΔT_k is:

$$\Delta T_k = T_{k,simu} - T_{k,exp} \tag{A2.48}$$

ΔT_k is used to determine if the temperature is overestimated ($\Delta T_k > 0$) or underestimated ($\Delta T_k < 0$) at the studied node.

The absolute error $|\Delta T_k|$ is calculated to assess the error magnitude between the two temperatures. Considering the dataset obtained during the measurement period, the mean bias error (MBE), mean absolute error (MAE), and root mean squared error (RMSE) at each node or in the facade layers are calculated for a global assessment of the model performance. Those metrics are given by :

$$MBE = \frac{1}{n}\sum_{i=1}^{n} \Delta T_{k,i} \tag{A2.49}$$

$$MAE = \frac{1}{n}\sum_{i=1}^{n} \left|\Delta T_{k,i}\right| \tag{A2.50}$$

$$RMSE = \sqrt{\frac{1}{n}\sum_{i=1}^{n} \left(\Delta T_{k,i}\right)^2} \tag{A2.51}$$

With n the number of measurements conducted at the analysed temperature node or the number of the node for the steady-state measurement.

There is the relation, $MBE \leq MAE \leq RMSE$. However, if their absolute values are close $|MBE| \approx MAE \approx RMSE$, there is a constant bias in the model, indicating a general overestimation or underestimation of the measurement.

The coefficient of determination R^2 is also calculated to assess the fitting of the model to the measurement. It is given by :

$$R^2 = 1 - \frac{\sum_i \left(\Delta T_{k,i}\right)^2}{\sum_i \left(T_{k,exp_i} - \overline{T_{k,exp_i}}\right)^2} \tag{A2.52}$$

With $\overline{T_{k,exp_i}}$ the average measured temperature in the considered period:

$$\overline{T_{k,exp_i}} = \frac{1}{n}\sum_{i=1}^{n} T_{k,exp_i} \tag{A2.53}$$

A2.4 Facade thermal model and building energy model coupling

The software EnergyPlus is used to calculate the thermal loads of the building, integrating the PV facade through a building energy simulation. A thermal model of the facade is developed separately in Python for a deeper understanding of the thermal exchange in the air gap. The EnergyPlus model and the facade model are coupled.

In EnergyPLus, only the multilayer wall is modelled. The air gap and the PV modules are not considered. The external temperature of this wall (the wall surface behind the module T_{M1}) is taken as the boundary condition of the multilayer wall. Their specified value is determined in Python with the PV façade model. Therefore, Python provides the external wall temperature to EnergyPlus as input in the model coupling.

The indoor air temperature T_{int} is according to the temperature setpoint and a shared input for the two models. However, since the radiant air temperature also depends on other surface temperatures, EnergyPlus provides their value as input for the façade model in Python. The temperature of the internal

surface of the multilayer wall (T_{M2}) calculated by the two models is used to control if the two simulations give the same output. For this purpose, the simulations are run in loops until the average difference between the internal wall temperatures calculated by EnergyPlus and Python is smaller than $\epsilon < 10^{-3}°C$.

The Python code runs first. Hence, the radiant indoor temperature is initialized as equal to the setpoint temperature (air temperature) in the first loop. Throughout the loops, the two models exchange the external wall temperature and indoor radiant temperature until the condition of the internal wall temperature is met. The illustration of the model coupling is given in Figure A2.5.

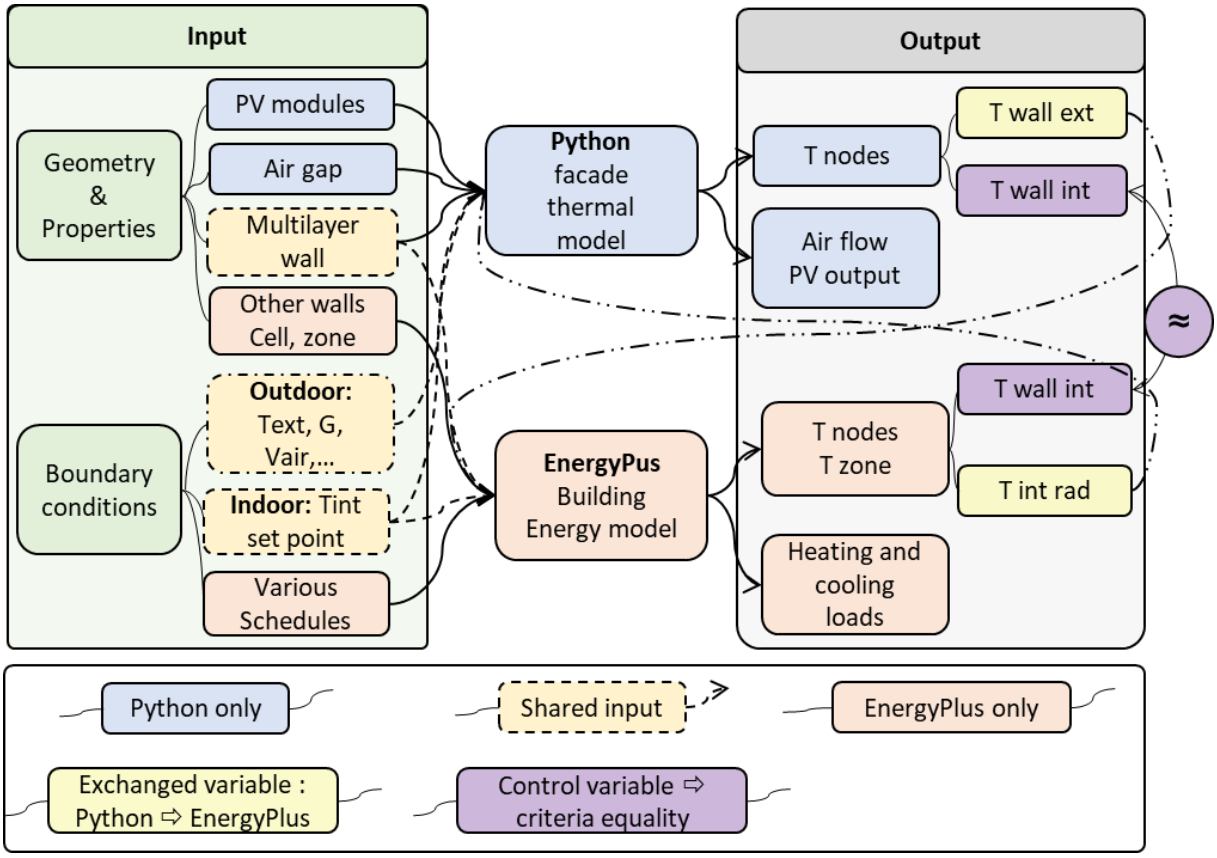

Figure A2.5: Coupling principle of the facade model on Python and the building model on EnergyPlus